FORGE

Fate Of Repository Gases

European Commission FP7

Numerical modelling of the PGZ1 in-situ test - 3D and 1D modelling

FORGE Report D5.12R and D5.13

	Name	Organisation	Signature	Date
Compiled	R. Charlier	University of Liege		3/5/2012
Verified	RP Shaw	BGS		8th November 2013
Approved	RP Shaw	BGS		8th November 2013

Keywords.

Mont Terri URL; HG-A experiment; Opalinus Clay; Gas flow; modelling

Bibliographical reference

R. CHARLIER, F. COLLIN, P. GERARD, J.P. RADU. 20132 Numerical modelling of the PGZ1 in-situ test - 3D and 1D modelling

FORGE Reports D5.12R and D5.13. 109pp.

Euratom 7th Framework Programme Project: FORGE

EURATOM

Fate of repository gases (FORGE)

The multiple barrier concept is the cornerstone of all proposed schemes for underground disposal of radioactive wastes. The concept invokes a series of barriers, both engineered and natural, between the waste and the surface. Achieving this concept is the primary objective of all disposal programmes, from site appraisal and characterisation to repository design and construction. However, the performance of the repository as a whole (waste, buffer, engineering disturbed zone, host rock), and in particular its gas transport properties, are still poorly understood. Issues still to be adequately examined that relate to understanding basic processes include: dilational versus visco-capillary flow mechanisms; long-term integrity of seals, in particular gas flow along contacts; role of the EDZ as a conduit for preferential flow; laboratory to field up-scaling. Understanding gas generation and migration is thus vital in the quantitative assessment of repositories and is the focus of the research in this integrated, multi-disciplinary project. The FORGE project is a pan-European project with links to international radioactive waste management organisations, regulators and academia, specifically designed to tackle the key research issues associated with the generation and movement of repository gasses. Of particular importance are the long-term performance of bentonite buffers, plastic clays, indurated mudrocks and crystalline formations. Further experimental data are required to reduce uncertainty relating to the quantitative treatment of gas in performance assessment. FORGE will address these issues through a series of laboratory and field-scale experiments, including the development of new methods for up-scaling allowing the optimisation of concepts through detailed scenario analysis. The FORGE partners are committed to training and CPD through a broad portfolio of training opportunities and initiatives which form a significant part of the project.

Further details on the FORGE project and its outcomes can be accessed at www.FORGEproject.org.

Contact details:

R. Charlier, F. Collin, P. Gerard, J.P. Radu

Université de Liège – ArGEnCo

Secteur Géotechnologies, Hydrogéologie, Prospection géophysique (GEO³)

Institut de Mécanique et de Génie Civil, Chemin des Chevreuils 1, Bât. B52/3 B 4000

Liège 1 - Sart Tilman

Belgique

Tél.: 04/366.93.34

Fax: 04/366.93.26

E-mail: robert.charlier@ulg.ac.be

www.argenco.ulg.ac.be

Faculté des Sciences Appliquées
Département d'Architecture, Géologie, Environnement & Constructions
Secteur GEO³
Prof. R. CHARLIER

Numerical modelling of the PGZ1 in-situ test - 3D and 1D modelling

Final report

03/05/2012

R. Charlier, F. Collin, P. Gerard, J.P. Radu

Université de Liège – ArGEnCo
www.argenco.ulg.ac.be
Secteur Géotechnologies, Hydrogéologie, Prospection géophysique (GEO³)

Institut de Mécanique et de Génie Civil, Chemin des Chevreuils 1, Bât. B52/3 B 4000 Liège 1 - Sart Tilman– Belgique
Tél.: 04/366.93.34 ; Fax: 04/366.93.26
E-mail : Robert.Charlier@ulg.ac.be

TABLE OF CONTENTS

1 INTRODUCTION 1

2 IN-SITU TEST DESCRIPTION 1

3 MATHEMATIC MODEL 4

3.1 Model of biphasic transfer 4
3.1.1 Advection of liquid water – dissolved nitrogen mixing 5
3.1.2 Advection of gas N_2 – water vapour mixing 6
3.1.3 Diffusion in the gas mixing nitrogen – water vapour 7
3.1.4 Diffusion of dissolved nitrogen in water 8

3.2 Mechanical model 9

3.3 Balance equations 11
3.3.1 Momentum conservation 11
3.3.2 Water mass conservation 11
3.3.3 Nitrogen mass conservation 12
3.3.4 Porosity variation 12

4 HYDRAULIC AND MECHANICAL MODELS PARAMETERS 13

4.1 Water and nitrogen 13

4.2 Argillite 14

4.3 Injection chamber 14

4.4 Retention curve and water and gaz permeabilities 15
4.4.1 Argillite 15
4.4.2 Injection chamber 17

5 DISCRETISATION, INITIAL AND BOUNDARY CONDITIONS OF THE 3D SIMULATIONS 18

5.1 Meshing 18

5.2 Initial and boundary conditions 21

6 3D NUMERICAL RESULTS AND COMPARISONS WITH IN-SITU MEASUREMENTS 25

6.1 Phase 1 and 2: after boring 25

6.2 Phase 4: gas injection 25

6.3 Phase 4: gas injection – influence of argillite permeability and injection compressibility 29

6.4 Phase 3: waiting phase – influence of PGZ1031 borehole drainage 31

6.5 Phase 3: waiting phase – influence of leakage in the injection chamber 35

6.6 Phase 4: gas injection –decreasing of argillite permeability after 3rd peak 38

6.7 Phase 4: gas injection – influence of unresined space betwwen packers.....41

6.8 Phase 3: waiting phase – influence of PGZ1031 borehole drainage – new independent mesh 44

6.9 Phase 4: gas injection – influence of EDZ.....48

7 DISCRETISATION, INITIAL AND BOUNDARY CONDITIONS OF THE 1D SIMULATIONS (SET 1)..... 52

7.1 Meshing, initial and boundary conditions.....52

7.2 Considered cases (set 1) 52

8 1D NUMERICAL RESULTS (SET 1) AND COMPARISONS WITH IN-SITU MEASUREMENTS 53

9 3D NUMERICAL RESULTS (SET 1) AND COMPARISONS WITH IN-SITU MEASUREMENTS 72

9.1 Phase 4: gas injection 72

10 DISCRETISATION, INITIAL AND BOUNDARY CONDITIONS OF THE 1D SIMULATIONS (SET 2)..... 75

10.1 Considered cases (set 2) 75

11 1D NUMERICAL RESULTS (SET 2) AND COMPARISONS WITH IN-SITU MEASUREMENTS 76

12 3D NUMERICAL RESULTS (SET 2) AND COMPARISONS WITH IN-SITU MEASUREMENTS 91

12.1 Phase 4: gas injection 91

13 CONCLUSIONS..... 98

List of figures

Figure 1 : 3D view of the PGZ borings in-situ tests. 2
Figure 2 : Location of PGZ1 boreholes in a horizontal plane XY. 3
Figure 3 : Location of measurement points in a horizontal plane XY. 3
Figure 4 : Location of PGZ1 boreholes. 4
Figure 5 : Biphasic transfer model. 9
Figure 6 : Water saturation $S_{r,w}$ evolution with the capillary pressure p_c for the argillite. 16
Figure 7 : Water permeability K_w evolution with the water saturation $S_{r,w}$ for the argillite. 17
Figure 8 : Gas permeability K_g evolution with the water saturation $S_{r,w}$ for the argillite. 17
Figure 9 : Water saturation $S_{r,w}$ evolution with the capillary pressure p_c for the injection chamber. 18
Figure 10 : Geometry around the PGZ1201 borehole. 19
Figure 11 : Half a 3D mesh around the PGZ1201 borehole. 20
Figure 12 : Zoom on the perspective view – Injection chamber (interval 2). 20
Figure 13 : Boundary conditions – Half a 3D mesh around the PGZ1201 borehole. 21
Figure 14 : Boundary conditions – Imposed anisotropic normal stresses. 22
Figure 15 : Boundary conditions – Phasing. 23
Figure 16 : Boundary conditions – Phasing of the gas injection in the chamber (Phase 4). 24
Figure 17 : Water pore pressure and wall radial stress at the end of the phase 2. 25
Figure 18 : Water pore pressure near the injection chamber during the phase 4. 26
Figure 19 : Water pore pressure at the end of the 3rd gas injection level of the phase 4. 27
Figure 20 : Gas pressure at the end of the 3rd gas injection level of the phase 4. 27
Figure 21 : Water pressure evolution during the phase 4. 28
Figure 22 : Gas pressure evolution during the phase 4. 28
Figure 23 : Water pressure evolution during the phase 4 in the PGZ1202 borehole. 29
Figure 24 : Pore pressure evolution during the phase 4 – Influence of permeability. 30
Figure 25 : Pore pressure evolution during the phase 4 – Influence of compressibility. 30
Figure 26 : Experimental pore pressure evolution during the phase 3. 32
Figure 27 : Perspective and x-y plane views with location of the PGZ1031 borehole. 32
Figure 28 : Water pore pressure at the end of the phase 3. 33
Figure 29 : Numerical water pressure evolution during the phase 3, with drainage effect of the PGZ1031 borehole. 33
Figure 30 : Comparison of numerical and experimental pore pressure evolutions during the phase 3, with drainage effect of the PGZ1031 borehole. 34

Figure 31 : Comparison of numerical and experimental pore pressure evolutions in the PGZ1201 borehole during the phases 3 and 4, with drainage effect of the PGZ1031 borehole. 34

Figure 32 : Comparison of numerical and experimental pore pressure evolutions in the PGZ1202 borehole during the phases 3 and 4, with drainage effect of the PGZ1031 borehole. 35

Figure 33 : Experimental pore pressure evolutions during the phase 3......36

Figure 34 : Comparison of numerical and experimental pore pressure evolutions during the phase 3, with leakage in the injection chamber......36

Figure 35 : Comparison of numerical and experimental pore pressure evolutions in the PGZ1201 borehole during the phases 3 and 4, with drainage leakage in the injection chamber. 37

Figure 36 : Comparison of numerical and experimental pore pressure evolutions in the PGZ1202 borehole during the phases 3 and 4, with leakage in the injection chamber. 37

Figure 37 : Comparison of numerical pore pressure evolutions during the phase 4, with and without leakage in the injection chamber. 38

Figure 38 : Comparison between numerical and experimental water pressure evolutions in the PGZ1201 borehole during the beginning of the phase 4. 39

Figure 39 : Comparison between numerical and experimental water pressure evolutions in the PGZ1201 borehole during the phase 4, with modification of argillite permeabilities after 3rd peak. 39

Figure 40 : Comparison between numerical and experimental water pressure evolutions in the PGZ1202 borehole during the beginning of the phase 4. 40

Figure 41 : Comparison between numerical and experimental water pressure evolutions in the PGZ1202 borehole during the phase 4, with modification of argillite permeabilities after 3rd peak. 40

Figure 42 : Schematic view of the end of PGZ1201 borehole, with 3 intervals, packers and unresined volumes. 41

Figure 43 : Comparison of numerical and experimental pore pressure evolutions during the phase 3, with influence of unresined volume. 42

Figure 44 : Comparison of numerical and experimental pore pressure evolutions in the PGZ1201 borehole during the phases 3 and 4, with influence of unresined volume. 42

Figure 45 : Comparison of numerical and experimental pore pressure evolutions in the PGZ1202 borehole during the phases 3 and 4, with influence of unresined volume. 43

Figure 46 : Comparison of numerical and experimental pore pressure evolutions in the PGZ1201 borehole during the phases 3 and 4, with influence of unresined volume and with "leakage" no stopped after 3rd peak. 43

Figure 47 : Half a 3D mesh around the PGZ1031 borehole. 44

Figure 48 : Locations of PGZ1201 and PGZ1202 boreholes measurements intervals in the mesh around the PGZ1031 borehole......45

Figure 49 : Simulations of PGZ1031 borehole drainage - Numerical results of sensitivity study for PGZ1201 borehole intervals. 46

Figure 50 : Simulations of PGZ1031 borehole drainage - Numerical results of sensitivity study for PGZ1202 borehole intervals. 47

Figure 51 : Simulations of PGZ1031 borehole drainage - Numerical results of the fitted case for PGZ1201 and PGZ1202 borehole intervals. 48

Figure 52 : Zoom on the EDZ in the perspective view around the injection chamber.. 49

Figure 53 : Retention curves used for EDZ, argillite and injection chamber. 49

Figure 54 : Numerical results of the phase 4 only, for PGZ1201 and PGZ1202 borehole intervals, with and without EDZ, and comparison with experimental data. 50

Figure 55 : Determination of experimental slopes due to drainage of PGZ1031 borehole. 51

Figure 56 : Numerical results of the phase 4 only, for PGZ1201 and PGZ1202 borehole intervals, with and without EDZ, and comparison with corrected experimental data. 51

Figure 57 : Scheme of the grid and boundary conditions for the 1D simulations. 52

Figure 58 : Time evolution of water and gas pressures, for case 1 of 1D simulations (set 1). 55

Figure 59 : Time evolution of gas saturation and space evolutions of gas flows, water saturation, water and gas pressures, for case 1 of 1D simulations (set 1). 55

Figure 60 : Time evolution of water and gas pressures, for case 2 of 1D simulations (set 1). 56

Figure 61 : Time evolution of gas saturation and space evolutions of gas flows, water saturation, water and gas pressures, for case 2 of 1D simulations (set 1). 56

Figure 62 : Time evolution of water and gas pressures, for case 3 of 1D simulations (set 1). 57

Figure 63 : Time evolution of gas saturation and space evolutions of gas flows, water saturation, water and gas pressures, for case 3 of 1D simulations (set 1). 57

Figure 64 : Time evolution of water and gas pressures, for case 5 of 1D simulations (set 1). 59

Figure 65 : Time evolution of gas saturation and space evolutions of gas flows, water saturation, water and gas pressures, for case 5 of 1D simulations (set 1). 59

Figure 66 : Time evolution of water and gas pressures, for case 6 of 1D simulations (set 1). 60

Figure 67 : Time evolution of gas saturation and space evolutions of gas flows, water saturation, water and gas pressures, for case 6 of 1D simulations (set 1). 60

Figure 68 : Time evolution of water and gas pressures, for case 7 of 1D simulations (set 1). 62

Figure 69 : Time evolution of gas saturation and space evolutions of gas flows, water saturation, water and gas pressures, for case 7 of 1D simulations (set 1). 62

Figure 70 : Time evolution of water and gas pressures, for case 8 of 1D simulations (set 1). 63

Figure 71 : Time evolution of gas saturation and space evolutions of gas flows, water saturation, water and gas pressures, for case 8 of 1D simulations (set 1). 63

Figure 72 : Time evolution of water and gas pressures, for case 9 of 1D simulations (set 1). 64

Figure 73 : Time evolution of gas saturation and space evolutions of gas flows, water saturation, water and gas pressures, for case 9 of 1D simulations (set 1). 64

Figure 74 : Time evolution of water and gas pressures, for case 10 of 1D simulations (set 1). 66

Figure 75 : Time evolution of gas saturation and space evolutions of gas flows, water saturation, water and gas pressures, for case 10 of 1D simulations (set 1). 66

Figure 76 : Time evolution of water and gas pressures, for case 11 of 1D simulations (set 1). 67

Figure 77 : Time evolution of gas saturation and space evolutions of gas flows, water saturation, water and gas pressures, for case 11 of 1D simulation (set 1)s. 67

Figure 78 : Time evolution of water and gas pressures, for case 13 of 1D simulations (set 1). 68

Figure 79 : Time evolution of gas saturation and space evolutions of gas flows, water saturation, water and gas pressures, for case 13 of 1D simulations (set 1). 68

Figure 80 : Time evolution of water and gas pressures, for case 15 of 1D simulations (set 1). 70

Figure 81 : Time evolution of gas saturation and space evolutions of gas flows, water saturation, water and gas pressures, for case 15 of 1D simulations (set 1). 70

Figure 82 : Time evolution of water and gas pressures, for case 13 of 1D simulations (set 1), with gas extraction phase. 71

Figure 83 : Time evolution of water and gas pressures, for case 13 of 1D simulation (set 1), with gas extraction phase. 71

Figure 84 : Numerical results of the phase 4 only, for PGZ1201 borehole intervals, and comparison with experimental data. 73

Figure 85 : Numerical results of the phase 4 only, for PGZ1202 borehole intervals, and comparison with experimental data. 73

Figure 86 : Numerical results of the phase 4 only, for PGZ1201 borehole intervals, and comparison with experimental data. 74

Figure 87 : Numerical results of the phase 4 only, for PGZ1202 borehole intervals, and comparison with experimental data. 74

Figure 88 : Time evolution of water and gas pressures, for case 1' of 1D simulations (set 2). 77

Figure 89 : Time evolution of gas saturation and space evolutions of gas flows, water saturation, water and gas pressures, for case 1' of 1D simulations (set 2). 77

Figure 90 : Time evolution of water and gas pressures, for case 2' of 1D simulations (set 2). 78

Figure 91 : Comparison of time evolution of gas pressure, between case 1' and case 2'. 79

Figure 92 : Time evolution of gas saturation and space evolutions of gas flows, water saturation, water and gas pressures, for case 2' of 1D simulations (set 2). 79

Figure 93 : Time evolution of water and gas pressures, for case 6' of 1D simulations (set 2). 80

Figure 94 : Comparison of time evolution of gas pressure, between case 2' and case 6'. 81

Figure 95 : Time evolution of gas saturation and space evolutions of gas flows, water saturation, water and gas pressures, for case 6' of 1D simulations (set 2). 81

Figure 96 : Time evolution of water and gas pressures, for case 11' of 1D simulations (set 2). ... 82

Figure 97 : Comparison of time evolution of gas pressure, between case 6' and case 11'. 83

Figure 98 : Time evolution of gas saturation and space evolutions of gas flows, water saturation, water and gas pressures, for case 11' of 1D simulations (set 2). 83

Figure 99 : Time evolution of water and gas pressures, for case 11b' of 1D simulations (set 2). . 84

Figure 100 : Comparison of time evolution of gas pressure, between case 11' and case 11b'. 85

Figure 101 : Time evolution of gas saturation and space evolutions of gas flows, water saturation, water and gas pressures, for case 11b' of 1D simulations (set 2). 85

Figure 102 : Comparison of Mualem and cubic laws for gas relative permeability. 86

Figure 103 : Time evolution of water and gas pressures, for case 15' of 1D simulations (set 2). .87

Figure 104 : Comparison of time evolution of gas pressure, between case 11b' and case 15'. 87

Figure 105 : Time evolution of gas saturation and space evolutions of gas flows, water saturation, water and gas pressures, for case 15' of 1D simulations (set 2). 88

Figure 106 : Summary of time ranges related to the effect of the chamber, of the EDZ and of the argillite. 88

Figure 107 : Gas flows profiles at different gas injection peaks, for case 15' of 1D simulations (set 2). 89

Figure 108 : Time evolution of water and gas pressures, for case 15' of 1D simulations (set 2) with extraction phase. 90

Figure 109 : Time evolution of water and gas pressures, for case 15' of 1D simulations (set 2) with extraction phase (zoom). 90

Figure 110 : Numerical results of 3D simulation PGZ1_70, for PGZ1201 borehole intervals, and comparison with experimental data. 93

Figure 111 : Numerical results of 3D simulation PGZ1_70, for PGZ1201 borehole 1 and 3 intervals, and comparison with experimental data. 93

Figure 112 : Numerical results of 3D simulation PGZ1_70, for PGZ1202 borehole intervals, and comparison with experimental data. 94

Figure 113 : Numerical results of 3D simulation PGZ1_70, for PGZ1202 borehole intervals, and comparison with experimental data. 94

Figure 114 : Numerical results of 3D simulation PGZ1_70, for PGZ1202 borehole 1 and 3 intervals, and comparison with experimental data. 95

Figure 115 : Numerical results of 3D simulation PGZ1_74, for PGZ1201 borehole intervals, and comparison with experimental data. 95

Figure 116 : Numerical results of 3D simulation PGZ1_74 (with gas extraction phase), for PGZ1201 borehole intervals, and comparison with experimental data. 96

Figure 117 : Numerical results of 3D simulation PGZ1_74 (with gas extraction phase), for PGZ1201 borehole 1 and 3 intervals, and comparison with experimental data. 96

Figure 118 : Numerical results of 3D simulation PGZ1_74 (with gas extraction phase), for PGZ1202 borehole intervals, and comparison with experimental data. 97

Figure 119 : Numerical results of 3D simulation PGZ1_74 (with gas extraction phase), for PGZ1202 borehole intervals, and comparison with experimental data. 97

Figure 120 : Numerical results of 3D simulation PGZ1_74 (with gas extraction phase), for PGZ1202 borehole 1 and 3 intervals, and comparison with experimental data. 98

List of tables

Table 1: Water and nitrogen properties. 13
Table 2 : Hydraulic parameters of argillite. 14
Table 3 : Mechanical parameters of argillite. 14
Table 4 : Hydraulic parameters of the injection chamber. 15
Table 5: Considered cases for the 1D simulations (set 1). 53
Table 6: Considered cases for the 1D simulations (set 2). 75
Table 7: 3D simulations main parameters. 92

1 INTRODUCTION

The main objective of the PGZ1 in-situ test is to understand and quantify the gas behaviour of the argillite bedrock below the fracture pressure. This gas injection test in host rock is called "PGZ1 test". Thus, it will determine in priority the gas inlet pressure threshold and the pressure value at which microcracking could appear.

This report is mainly based on presentations given at the FORGE, "GL gaz" or Andra meetings (Châtenay September 16, 2010, Prague November 30, 2010, Barcelona May 17, 2011, Châtenay January 25 & 26, 2012, Liège March 7 & 8, 2012), and therefore only some of the most significant results are given to the reader, the rest of them being of course available on request.

Most data come from the Andra reports "*Expérimentation PGZ. Installation et premiers résultats*" *D.NT.AMFS.09.0085.B*, 19/07/2010 and "*Expérimentation PGZ. Essai PGZ1. Analyse de la phase d'injection de gaz GAS1" D.NT.AMFS.11.0084*, 11/08/2011.

2 IN-SITU TEST DESCRIPTION

The test consists of injection borehole (PGZ1201), a borehole monitoring of pore pressures parallel to injection borehole (PGZ1202) and a borehole monitoring deformations of the rock (PGZ1031). This borehole is perpendicular to the PGZ1201 and is located approximately 1 m above the last.

The PGZ1031 borehole was performed in front of the GEX gallery. This borehole is tilted downward and equipped with an extensometer to 20 measurement points. Boreholes PGZ1201 and PGZ1202 have been performed in the GED gallery between 20-21 and 19-20 hangers respectively. These two inclined boreholes are approximately 28 m long and descendant with 2 multi-plugs completions to 3 chambers each.

Figure 1 shows a 3D view of all the PGZ borings and, in particular, boreholes of PGZ1 test.

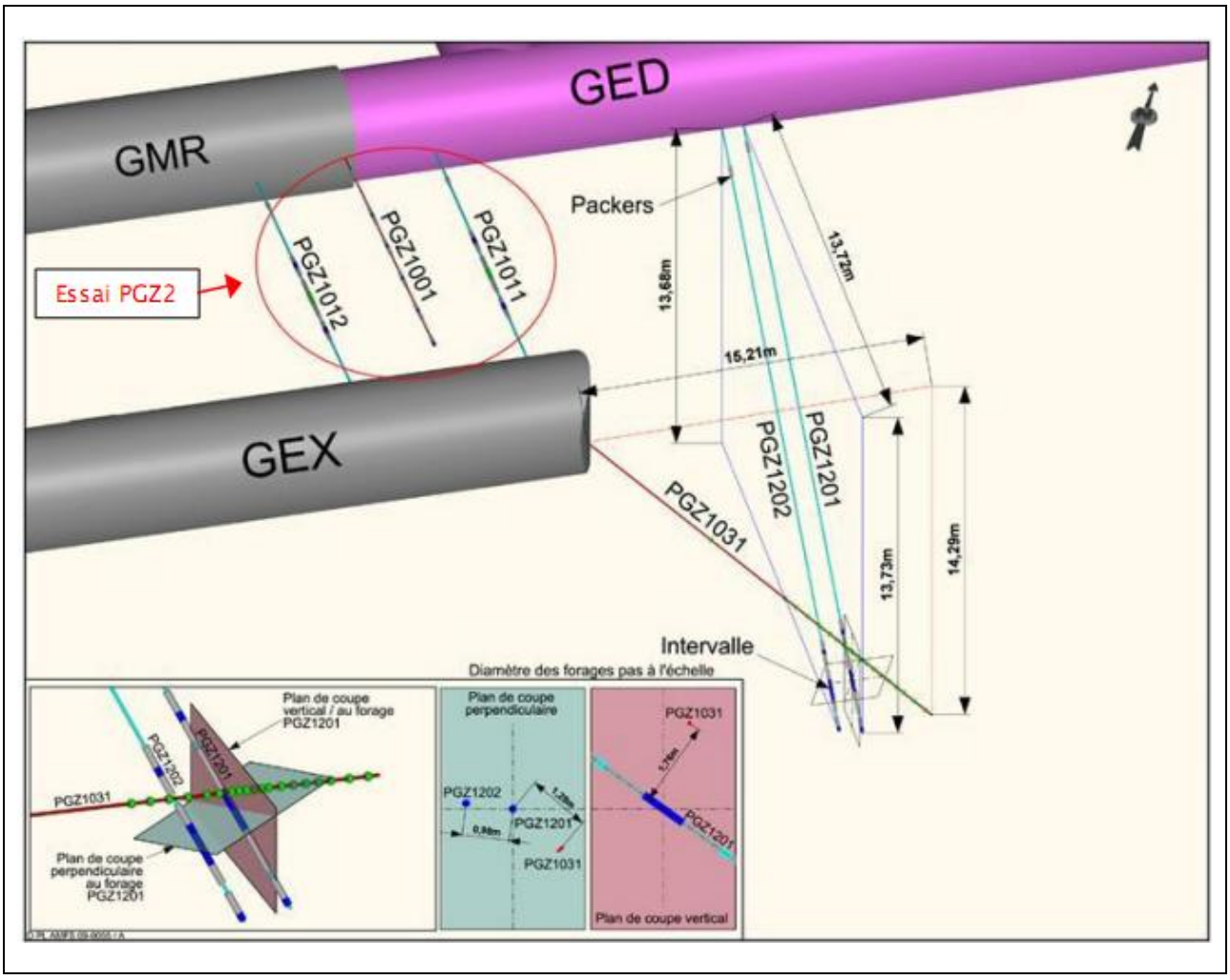

Figure 1 : 3D view of the PGZ borings in-situ tests.

The PGZ1201 borehole is equipped with a complete multi plugs to 3 chambers. The injection chamber of the PGZ1201 borehole has a length of 1 m and the two other measuring chambers, which are located of both sides of the interval 2, are 0.2 m long.

The chamber 2 of PGZ1201 is the interval in which various hydraulic (water and gas) tests will be performed. ***Figure 2*** and ***Figure 3*** show the position of the PGZ1 test boring in a horizontal plane XY.

Figure 4 presents a horizontal plane view, two vertical cross sections and a 3D view of the PGZ1 boreholes with GED and GEX galleries.

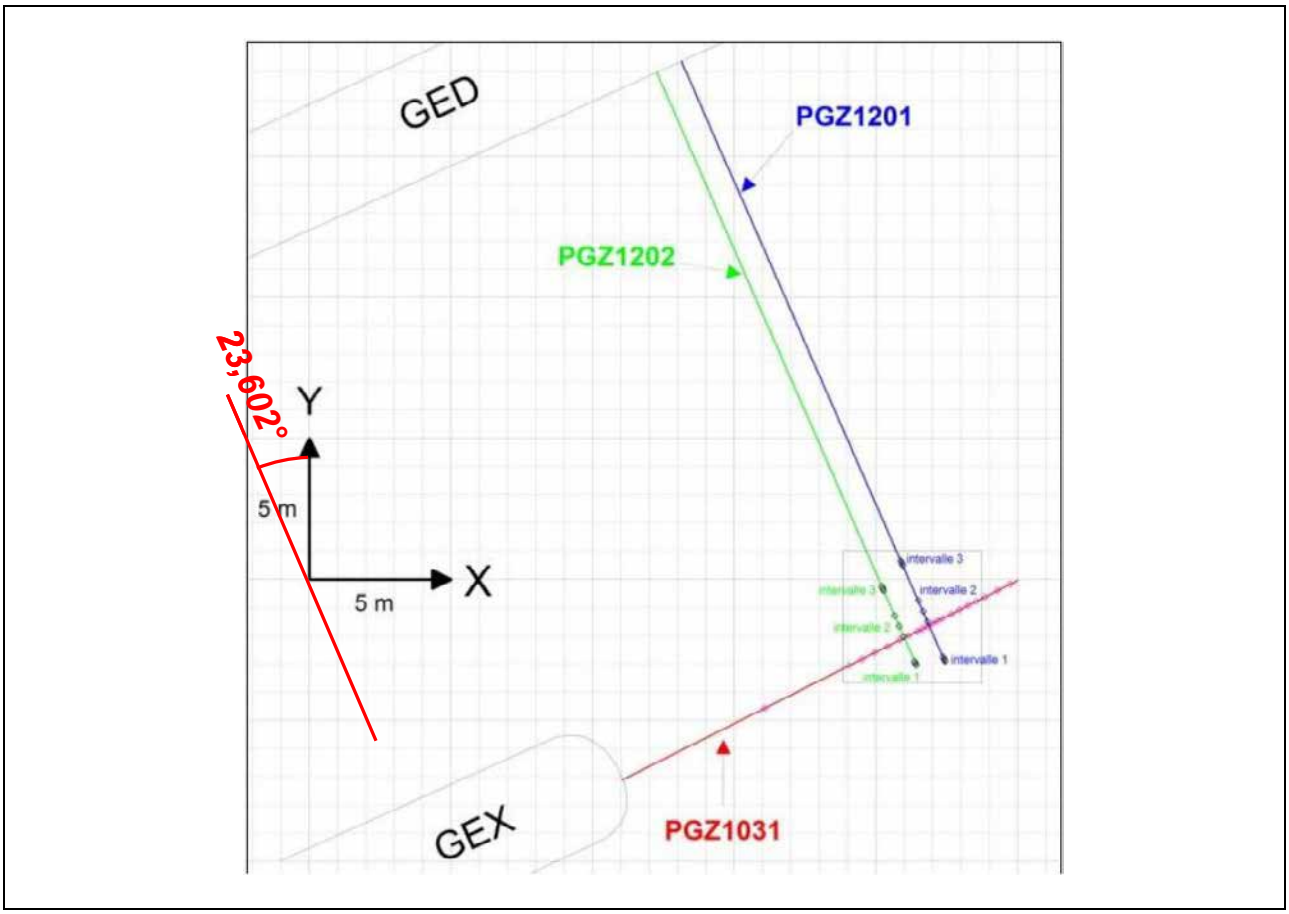

Figure 2 : Location of PGZ1 boreholes in a horizontal plane XY.

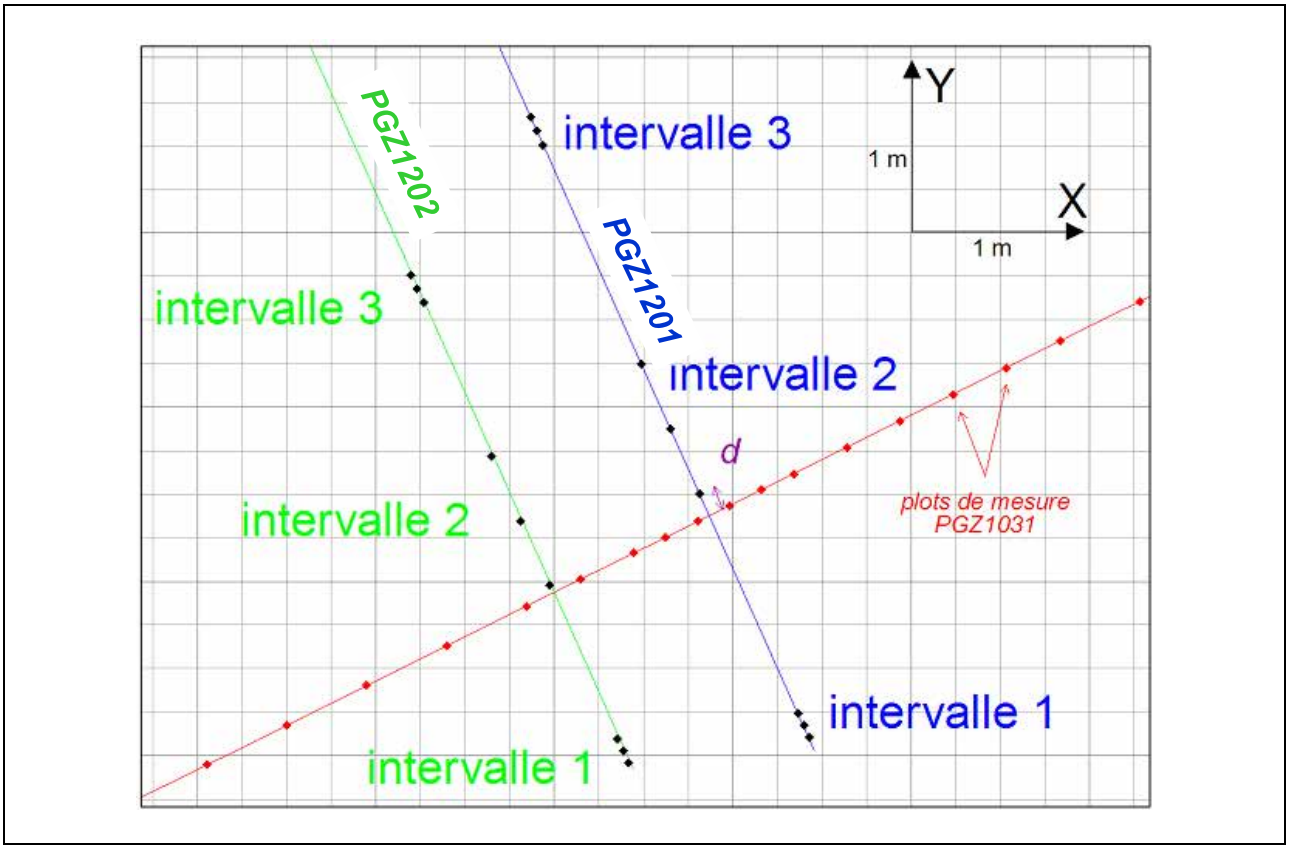

Figure 3 : Location of measurement points in a horizontal plane XY.

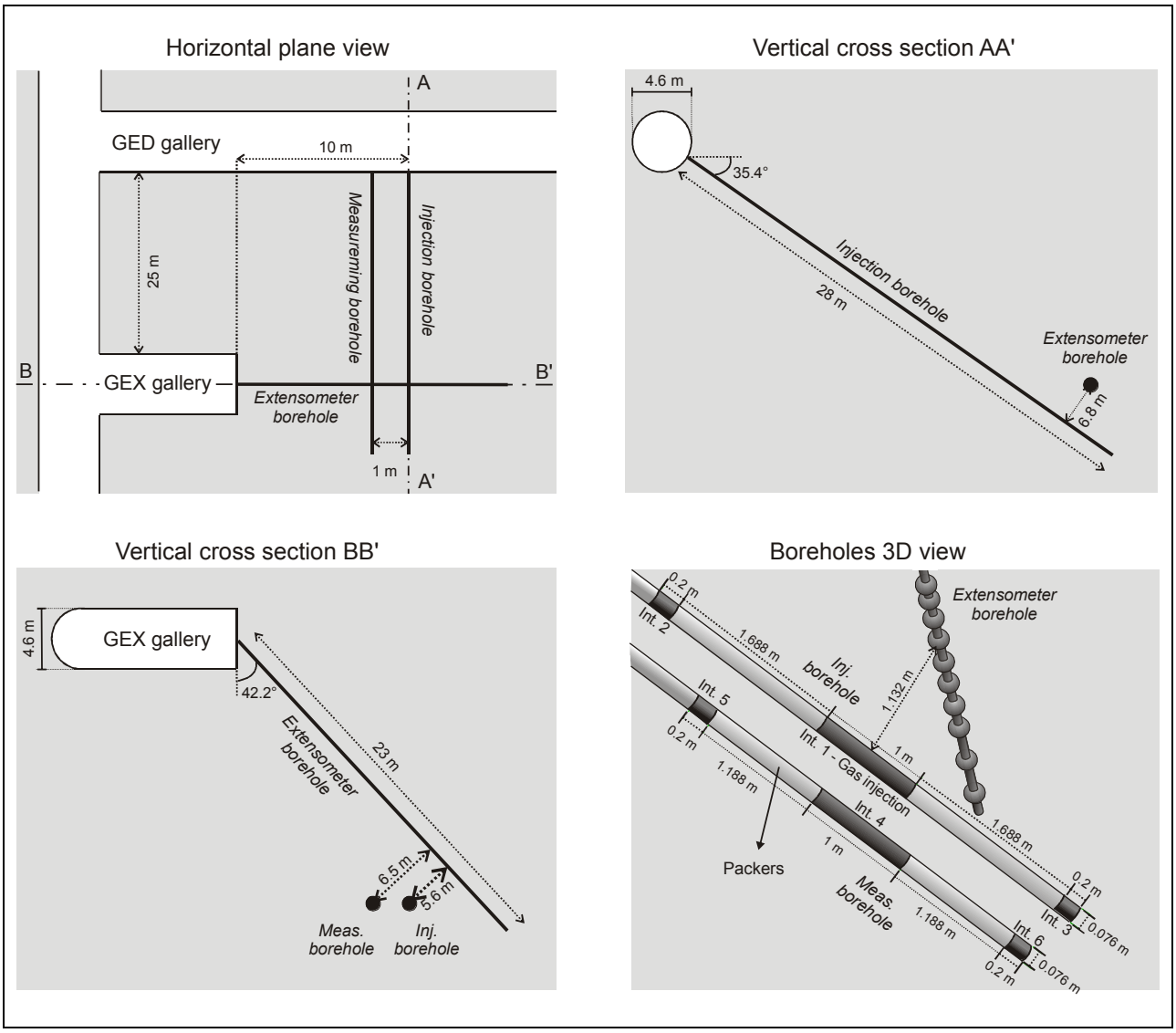

Figure 4 : Location of PGZ1 boreholes.

3 MATHEMATIC MODEL

3.1 Model of biphasic transfer

The biphasic transfer model presented below was first developed in the frame of the benchmark *"Simulation hydro-mécanique du transfert de gaz autour d'une alvéole de stockage"*, for water - hydrogen mixing. In the case of the PGZ tests, the gas component being nitrogen, the model was adjusted accordingly, particularly as regards the viscosity of the gas component or the different diffusion coefficients.

In the frame of these calculations, we consider the gas phase consists only of water and nitrogen vapour. We assume that there is no more air in the gas phase during the nitrogen production and this prevents to model its transfer.

In the water – nitrogen biphasic transfer model, the following phenomena are taken into consideration:

- advection of mixing liquid water – dissolved nitrogen;
- advection of mixing gas nitrogen – water vapour;
- diffusion in the gas mixing nitrogen – water vapour;
- diffusion of dissolved nitrogen in water.

3.1.1 Advection of liquid water – dissolved nitrogen mixing

We neglect the influence of dissolved nitrogen on the properties of liquid water - dissolved nitrogen mixing. Therefore, mixing advection is defined by the water advection within the porous medium, represented by the generalized Darcy's law:

$$\underline{q}_l = -\frac{k k_r^w(S_{r,w})}{\mu_w}(\underline{\nabla} p_w + \rho_w g \underline{\nabla} z) \tag{1}$$

with k the intrinsic permeability [m²], k_r^w the water relative permeability [-], $S_{r,w}$ the water saturation [-], μ_w the water viscosity [kg.m^{-1}.s^{-1}], ρ_w the water density [kg.m^{-3}], g the gravity acceleration [m.s^{-2}] and z the vertical upward directed coordinate [m].

The water is assumed to be compressible and obeys the following behaviour:

$$\frac{d\rho_w}{\rho_w} = \frac{dp_w}{\chi_w} \tag{2}$$

The water saturation of the medium $S_{r,w}$ is expressed as a function of the capillary pressure using the Van Genuchten's model:

$$S_{r,w} = S_{res} + \frac{S_{\max} - S_{res}}{\left[1 + \left(\frac{p_c}{P_r}\right)^n\right]^m} \tag{3}$$

with p_c (= $p_g - p_w$) the capillary pressure [Pa], S_{max} the maximum water saturation [-], S_{res} the residual saturation [-], n and m coefficients of the Van Genuchten's law as: $m = 1 - 1/n$ and P_r a parameter of the Van Genuchten's law [Pa].

The water relative permeability is expressed by integrating the predictive model proposed by Mualem in the Van Genuchten's capillary model. Then we have:

$$k_{r,w} = \sqrt{S_{r,w}}\left[1 - \left(1 - S_{r,w}^{1/m}\right)^m\right]^2 \tag{4}$$

3.1.2 Advection of gas N_2 – water vapour mixing

The gas phase consists of a mixing of nitrogen and water vapour. The flow of each component depends to a part of the advection flow of the gas phase. Before specifying the expression of this flow of advection, it is necessary to know the properties of the N2 - water vapour mixing.

- The *density of the gas mixing* ρ_g is the sum of component densities (approximation of Dalton's law):

$$\rho_g = \rho_{N_2}^g + \rho_{H_2O}^g \tag{5}$$

with $\rho_{N_2}^g$ the density of the nitrogen gas [kg.m^{-3}], $\rho_{H_2O}^g$ the density of the water vapour [kg.m^{-3}].

Each gas present in the mixing follows the ideal gas law:

$$p_{N_2}^g = \frac{\rho_{N_2}^g}{M_{N_2}} RT \quad \text{and} \quad p_{\mathrm{H_2O}}^{\mathrm{g}} = \frac{\rho_{H_2O}^g}{M_{H_2O}} RT \tag{6}$$

with M_{N_2} the nitrogen molar mass [=0.028 kg.mol^{-1}], M_{H_2O} the water molar mass [=0.018 kg.mol^{-1}] and R the ideal gas constant [=8.313 J.mol^{-1}.K^{-1}].

In particular, the water vapour density is defined by the following expression:

$$\rho_{H_2O}^g = \rho_{H_2O,0}^g . \exp\left(\frac{(p_w - p_g) M_{H_2O}}{\rho_w RT} \right) \tag{7}$$

with $\rho_{H_2O,0}^g$ the saturated vapour density [kg.m^{-3}].

For temperatures between 293 and 331° K, the saturation vapour density can be obtained from the following expression:

$$\frac{1}{\rho_{H_2O,0}^g} = 194.4 \ \exp\left(0.06374 \left(T - 273 \right) + 0.1634 \, 10^{-3} \left(T - 273 \right)^2 \right) \tag{8}$$

- The *gas mixing viscosity* μ_g can be estimated by the following simplified formula:

$$\mu_g = \frac{1}{\frac{X^g_{N_2}}{\mu^g_{N_2}} + \frac{X^g_{H_2O}}{\mu^g_{H_2O}}} \tag{9}$$

with $\mu^g_{N_2}$ and $\mu^g_{H_2O}$ the viscosities of nitrogen gas and water vapour [kg.m^{-1}.s^{-1}]; $X^g_{N_2}$ and $X^g_{H_2O}$ the mass fractions of nitrogen gas and water vapour [-] defined as:

$$X^g_{N_2} = \frac{\rho^g_{N_2}}{\rho_g} \quad \text{and} \quad X^g_{H_2O} = \frac{\rho^g_{H_2O}}{\rho_g} \tag{10}$$

Knowing the gas mixing properties, it is now possible to define the expression of the gas advection within the porous medium. It is represented by the generalised Darcy's law:

$$\underline{q}_g = -\frac{k k^g_r(S_{r,g})}{\mu_g}(\underline{\nabla} p_g + \rho_g g \underline{\nabla} z) \tag{11}$$

with k the intrinsic permeability [m²], k^g_r the gas relative permeability [-], $S_{r,g} = 1 - S_{r,w}$ the gas saturation [-], μ_g the viscosity of the gas N_2 – water vapour mixing [kg.m^{-1}.s^{-1}], ρ_g the gas mixing density [kg.m^{-3}], g the gravity acceleration [m.s^{-2}] and z the vertical upward directed coordinate [m].

The gas relative permeability is expressed by a cubic law as follow:

$$k_{r,g} = A.\ 1 - S_{r,w}{}^{3} \tag{12}$$

where A is a multiplication coefficient.

3.1.3 Diffusion in the gas mixing nitrogen – water vapour

Diffusion of nitrogen in the mixing N_2 – water vapour is expressed by the Fick's law:

$$\underline{i}_{(N_2)_g} = -\rho_g(1 - S_{r,w})\varphi\tau \quad D^{vapeur}_{N_2} \underline{\nabla}\left(\frac{\rho^g_{N_2}}{\rho_g}\right) = -\underline{i}_{(H_2O)_g} \tag{13}$$

with φ the porosity [-], τ the tortuosity [-], $D^{vapeur}_{N_2}$ the diffusion coefficient of N_2 in water vapour [m². s^{-1}], which is expressed through the following relationship:

$$D^{vapeur}_{N_2} = D_0\left(\frac{P_0}{P_g}\right)\left(\frac{T}{T_0}\right)^{1.75} \tag{14}$$

with $D_0 = 2.42\ 10^{-5}$ m².s^{-1}, $P_0 = 101$ kPa and $T_0 = 303$ K

3.1.4 Diffusion of dissolved nitrogen in water

Diffusion of dissolved nitrogen is also incorporated into the model using Fick's law.

$$\underline{i}_{(N_2)_d} = -\rho_w S_{r,w} \quad \varphi \quad \tau \quad D_{N_2}^{H_2O} \underline{\nabla} \left(\frac{\rho_{N_2}^w}{\rho_w} \right) \tag{15}$$

with $\rho_{N_2}^w$ the dissolved nitrogen density [kg.m^{-3}], $D_{N_2}^{H_2O}$ the diffusion coefficient of nitrogen gas in the liquid water [m².s^{-1}].

The dissolved nitrogen density is given by the Henry's law:

$$\rho_{N_2}^w = H_{N_2}(T).\rho_{N_2}^g \tag{16}$$

with H_{N_2} the Henry's constant for nitrogen [-].

The diffusion coefficient of nitrogen gas in water is given by:

$$D_{N_2}^{H_2O} = 2\ 10^{-9} \text{ m²/s} \tag{17}$$

All the phenomena considered for the biphasic transfer model are summarised in ***Figure 5***:

2 chemical species : water – nitrogen / 2 phases : liquid - gas

Liquid phase: *Liquid water + N_2 dissolved*

- Advection of the liquid phase $$\underline{q}_l = -\frac{K_{w,sat} k_r^w(S_{r,w})}{\mu_w}(\underline{\nabla} p_w + \rho_w g \underline{\nabla} z)$$
- Diffusion of N_2 dissolved in water $$\underline{i}_{(N_2)_d} = -\rho_w S_{r,w} D_{N_2}^{H_2O} \underline{\nabla}\left(\frac{\rho_{N_2}^w}{\rho_w}\right)$$

Henry's law $$\rho_{N_2}^w = H_{N_2}(T).\rho_{N_2}^g$$

Gas phase: *Water vapour + N_2 gas*

- Advection of the gas phase $$\underline{q}_g = -\frac{K_{g,\sec} k_r^g(S_{r,g})}{\mu_g}(\underline{\nabla} p_g + \rho_g g \underline{\nabla} z)$$
- Diffusion of N_2 – vapour water $$\underline{i}_{(N_2)_g} = -\rho_g S_{r,g} D_{N_2}^{vapeur} \underline{\nabla}\left(\frac{\rho_{N_2}^g}{\rho_g}\right) = -\underline{i}_{(H_2O)_g}$$

Figure 5 : Biphasic transfer model.

3.2 Mechanical model

The argillite has an elasto-plastic behaviour and it is proposed to use a Van-Eekelen's model.

The behaviour law chosen for argillite is a linear elastic perfectly plastic model with a yield Van-Eekelen's surface given by the following equation (material strength convention):

$$F \equiv II_{\hat{\sigma}} + m\left(I_\sigma - \frac{3c}{\tan\phi_C}\right) = 0 \tag{18}$$

where $II_{\hat{\sigma}} = \sqrt{\frac{1}{2}\hat{\sigma}_{ij}\hat{\sigma}_{ij}}$ is the second invariant of the deviatoric stresses, $\hat{\sigma}_{ij} = \sigma_{ij} - \frac{I_\sigma}{3}\delta_{ij}$ is the deviatoric stresses tensor, $I_\sigma = \sigma_{ij}\delta_{ij}$ is the first invariant of the stresses, ϕ_C is the compressive friction angle and c is the cohesion.

The m coefficient is defined by:

$$m = a(1 + b\sin 3\beta)^n \tag{19}$$

which is function of the Lode's angle given by:

$$\sin 3\beta = -\left(\frac{3\sqrt{3}}{2} \frac{III_{\hat{\sigma}}}{II_{\hat{\sigma}}^{3}} \right) \tag{20}$$

where $III_{\hat{\sigma}} = \frac{1}{3}\hat{\sigma}_{ij}\hat{\sigma}_{jk}\hat{\sigma}_{ki}$ is the third invariant of the deviatoric stresses.

The three parameters *a*, *b* and *n* must verify the following conditions:

$$\begin{aligned} &a > 0, \\ &bn > 0, \\ &-1 < b < 1 \end{aligned} \tag{21}$$

The value of the parameter *n*, which controls the convexity of the yield surface, is chosen conventionally to -0.229 (the default value in Van Eekelen model) and the two coefficients *a* and *b* allow for a independent choice for ϕ_C and ϕ_E (the extensive friction angle):

$$\begin{aligned} b &= \frac{\left(\frac{r_C}{r_E}\right)^{\frac{1}{n}} - 1}{\left(\frac{r_C}{r_E}\right)^{\frac{1}{n}} + 1} \\ a &= \frac{r_C}{1+b^{\,n}} \end{aligned} \tag{22}$$

where the reduced radius in compression r_C and extension r_E are given by:

$$\begin{aligned} r_C &= \frac{1}{\sqrt{3}}\left(\frac{2\sin\phi_C}{3-\sin\phi_C} \right) \\ r_E &= \frac{1}{\sqrt{3}}\left(\frac{2\sin\phi_E}{3+\sin\phi_E} \right) \end{aligned} \tag{23}$$

3.3 Balance equations

We have three conservation equations to respect to solve our problem: the momentum conservation equation, the mass conservation equations of water and nitrogen.

3.3.1 Momentum conservation

This equation is written in quasi-static conditions by:

$$div(\sigma_{ij}) + \rho g_i = 0 \tag{24}$$

where σ_{ij} is the total stresses tensor [Pa], ρ is the homogenised density [kg.m^{-3}] et g_i is the gravity vector [m.s^{-2}].

The total stress is expressed by:

$$\sigma_{ij} = \sigma'_{ij} + b.(p_w S_{r,w} + p_g S_{r,g}).\delta_{ij} \tag{25}$$

with b the Biot's coefficient [-].

3.3.2 Water mass conservation

The water is in the liquid phase and gas phase. By writing the conservation of the mass of liquid water and water vapour, we get:

$$\dot{S}_{(H_2O)_l} + div(\underline{f}_{(H_2O)_l}) + \dot{E}^{l\to g}_{H_2O} = Q_{(H_2O)_l} \tag{26}$$

$$\dot{S}_{(H_2O)_g} + div(\underline{f}_{(H_2O)_g}) - \dot{E}^{l\to g}_{H_2O} = Q_{(H_2O)_g} \tag{27}$$

where $\dot{S}_{(H_2O)_l}$ is the liquid water storage term [kg.m^{-3}.s^{-1}], $\underline{f}_{(H_2O)_l}$ is the liquid water mass flow [kg.m^{-2}.s^{-1}], $\dot{E}^{l\to g}_{H_2O}$ is the exchange term from the liquid phase to the gas phase [kg.m^{-3}.s^{-1}] and $Q_{(H_2O)_l}$ is a production/consummation term of liquid water [kg.m^{-3}.s^{-1}] (respectively for the water vapour).

$$\underline{f}_{(H_2O)_l} = \rho_w.\underline{q}_l \tag{28}$$

$$\underline{f}_{(H_2O)_g} = \rho^g_{H_2O}.\underline{q}_g + \underline{i}_{(H_2O)_g} \tag{29}$$

where $\underline{q}_l$ and $\underline{q}_g$ are the average velocities of liquid and gas phases with respect to the solid phase [m.s^{-1}] and $\underline{i}_{(H_2O)_g}$ is the diffusive vapour flux [kg.m^{-2}.s^{-1}].

Both balance equations (31) and (32) can be combined into a single equation where the evaporation term disappears. Including relations (33) and (34), we get:

$$\frac{\partial}{\partial t}(\rho_w.\phi.S_{r,w} + \rho^g_{H_2O}.\phi.S_{r,g}) + div(\rho_w.\underline{q}_l) + div(\underline{i}_{(H_2O)_g} + \rho^g_{H_2O}.\underline{q}_g) - Q_{H_2O} = 0 \tag{30}$$

where Q_{H_2O} is the total production/consummation term of water [kg.m^{-3}.s^{-1}].

3.3.3 Nitrogen mass conservation

The nitrogen is in the liquid phase and gas phase. By writing the mass conservation of dissolved nitrogen and nitrogen, we get:

$$\dot{S}_{(N_2)_g} + div(\underline{f}_{(N_2)_g}) + \dot{E}^{g\to d}_{N_2} = Q_{(N_2)_g} \tag{31}$$

$$\dot{S}_{(N_2)_d} + div(\underline{f}_{(N_2)_d}) - \dot{E}^{g\to d}_{N_2} = Q_{(N_2)_d} \tag{32}$$

where $\dot{S}_{(N_2)_g}$ the nitrogen storage term [kg.m^{-3}.s^{-1}], $\underline{f}_{(N_2)_g}$ is the nitrogen mass flow [kg.m^{-2}.s^{-1}], $\dot{E}^{g\to d}_{N_2}$ is the exchange term from the liquid phase to the gas phase [kg.m^{-3}.s^{-1}] and $Q_{(N_2)_l}$ is a production/consummation term of nitrogen [kg.m^{-3}.s^{-1}] (respectively for the dissolved nitrogen).

$$\underline{f}_{(N_2)_g} = \rho^g_{N_2}.\underline{q}_g + \underline{i}_{(N_2)_g} \tag{33}$$

$$\underline{f}_{(N_2)_d} = \rho^g_{N_2}.H_{N_2}.\underline{q}_l + \underline{i}_{(N_2)_d} \tag{34}$$

where $\underline{q}_l$ and $\underline{q}_g$ [m.s^{-1}] are the average velocities of liquid and gas phases with respect to the solid phase and $\underline{i}_{(N_2)_g}$ and $\underline{i}_{(N_2)_d}$ are the diffusive flows of nitrogen gas and dissolved nitrogen [kg. m^{-3}.s^{-1}].

We can group the balance equations (36) and (37), the exchange term from the gas phase to the liquid phase disappears:

$$\begin{aligned}&\frac{\partial}{\partial t}(\rho^g_{N_2}.\varphi.S_{r,g} + \rho^g_{N_2}.H_{N_2}.\varphi.S_{r,w}) + div\ \underline{i}_{(N_2)_g} + \rho^g_{N_2}.\underline{q}_g \\ &+ div\ \underline{i}_{(N_2)_d} + \rho^g_{N_2}.H_{N_2}.\underline{q}_l - Q_{N_2} = 0\end{aligned} \tag{35}$$

with Q_{N_2} the nitrogen production/consummation term [kg.m^{-3}.s^{-1}].

3.3.4 Porosity variation

The evolution of porosity takes into account the compressibility of the skeleton and solid grains:

$$d\varphi = (b-\varphi).(\varepsilon_v + \frac{S_{r,w}.dp_w + S_{r,g}.dp_g}{K_s}) \tag{36}$$

where b is the Biot's coefficient [-], $\varepsilon_v = \varepsilon_{ii}$ and K_s the bulk modulus of the grains [Pa], which is calculated from the Biot's cioefficient and the drained bulk modulus of the skeleton K_0 [Pa] by :

$$b = 1 - \frac{K_0}{K_s} \tag{37}$$

where $K_0 = \frac{E_0}{3(1-2\upsilon_0)}$, E_0 and υ_0 being the drained Young's modulus [Pa] and the drained Poisson's coefficient of the skeleton [-].

4 HYDRAULIC AND MECHANICAL MODELS PARAMETERS

Here are first the different properties of water and nitrogen, which are both components of the gas phase. Then we give the value of the parameters that are used in the biphasic transfer and mechanical laws characterizing each material.

4.1 Water and nitrogen

The properties of the various components are given below for a temperature of 303° K and a pressure of 0.1 MPa.

	Name	Value	Unit
μ_w	Water dynamic viscosity	0.001	Pa.s
ρ_w	Water density	1000	kg.m^{-3}
$1/\chi_w$	Water compressibility	5 10^{-10}	Pa^{-1}
$\mu^g_{N_2}$	Nitrogen dynamic viscosity	17.9 10^{-6}	Pa.s
$\mu^g_{H_2O}$	Water vapour dynamic viscosity	10^{-5}	Pa.s
$\rho^g_{N_2}$	Nitrogen density	1.25	kg.m^{-3}
H_{N_2}	Henry's coefficient	0.0176	-

Table 1: Water and nitrogen properties.

4.2 Argillite

	Name	Value	Unit
$k_{xx}=k_{yy}$	Horizontal intrinsic permeabilities	$4\ 10^{-20}$	m²
k_{zz}	Vertical intrinsic permeability	$1.33\ 10^{-20}$	m²
φ	Porosity	0.18	-
m	Van Genuchten's coefficient	0.55	-
n	Van Genuchten's coefficient	1.49	-
P_r	Van Genuchten's parameter	15	MPa
S_{max}	Maximal saturation	1	-
S_{res}	Residual saturation	0.01	-
τ	Tortuosity	0.25	-
A	Multiplication coefficient of $k_{r,g}$	25	-

Table 2 : Hydraulic parameters of argillite.

	Name	Value	Unit
E_0	Drained Young's modulus	4000	MPa
υ_0	Drained Poisson's coefficient	0.30	-
c	Cohesion	3	MPa
Φ	Friction angle	20	°
b	Biot's coefficient	0.6	-

Table 3 : Mechanical parameters of argillite.

Theses hydraulic and mechanical parameters used for argillite are similar to those used for preceding numerical modelling of PGZ2 in-situ test (2008 and 2010)

4.3 Injection chamber

	Name	Value	Unity
k	Intrinsic permeability	10^{-12}	m²
φ	Porosity	1	-
m	Van Genuchten's coefficient	0.33333	-
n	Van Genuchten's coefficient	1.5	-
P_r	Van Genuchten's parameter	0.05	MPa

S_{max}	Maximal saturation	1	-
S_{res}	Residual saturation	0	-
τ	Tortuosity	1	-
$1/\chi$	Compressibility	$1\ 10^{-8}$	Pa^{-1}

Table 4 : Hydraulic parameters of the injection chamber.

4.4 Retention curve and water and gaz permeabilities

4.4.1 Argillite

We give below for the argillite the evolution curves of the water saturation $S_{r,w}$ with the capillary pressure p_c (***Figure 6***) and the curves of the water K_w and gas K_g permeabilities with the water saturation $S_{r,w}$ (***Figure 7*** et ***Figure 8***).

Theses hydraulic parameters and these chosen curves are similar to those used for the preceding numerical modelling of PGZ2 in-situ test (2008 and 2010)

Water saturation of the medium $S_{r,w}$ is expressed according to the capillary pressure p_c through the Van Genuchten's model:

$$S_{r,w} = S_{res} + \frac{S_{\max} - S_{res}}{\left[1 + \left(\frac{p_c}{P_r}\right)^n\right]^{\frac{1}{n}-1}} \tag{44}$$

with here the values of S_{max} = 1, S_{res} = 0.01, n = 1.49 and P_r = 15 MPa. (Cfr *provisional report ULg – Argillite parameters synthesis*)

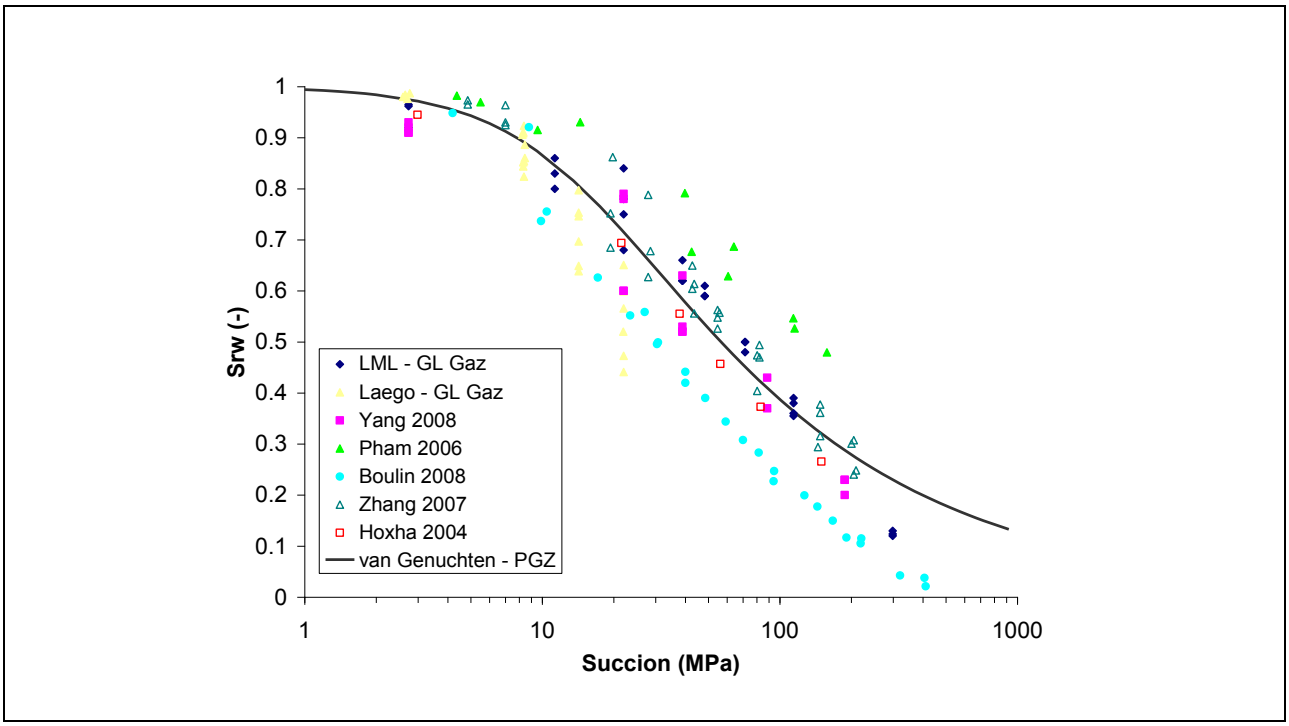

Figure 6 : Water saturation $S_{r,w}$ evolution with the capillary pressure p_c for the argillite.

The water permeability is expressed by:

$$K_w = k.\sqrt{S_{r,w}}\left[1-\ 1-S_{r,w}^{1/m}\ ^{m}\right]^2 = k.k_{w,r} \tag{45}$$

with here k = 4 10^{-20} m^2 (horizontal direction) and 1.33 10^{-20} m^2 (vertical direction) (the intrinsic permeability k is equal to 4 10^{-20} m² on the ***Figure 7***) and m = 0.55.

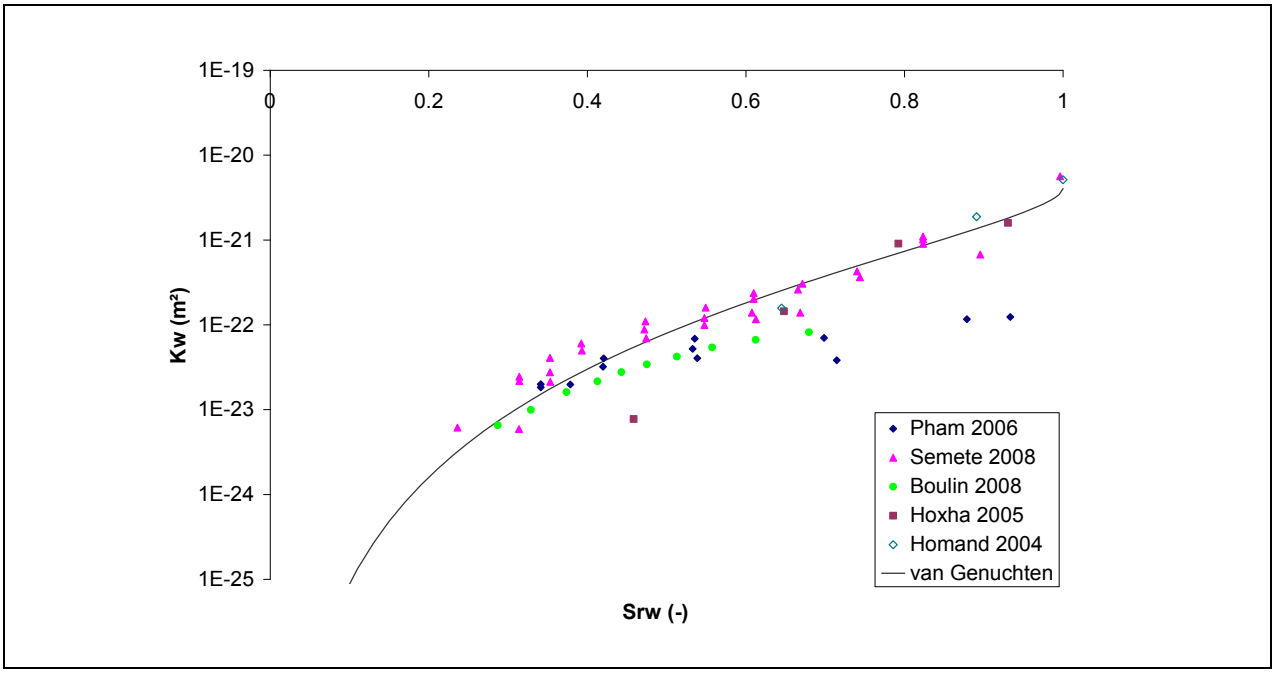

Figure 7 : Water permeability K_w evolution with the water saturation $S_{r,w}$ for the argillite.

The gas permeability is expressed by a cubic law as follows:

$$K_g = K_{g,\sec} . \ 1 - S_{r,w}{}^{3} = k.A. \ 1 - S_{r,w}{}^{3} \tag{46}$$

where A is a multiplication coefficient and $K_{g,sec}$ is the dry gas permeability for $S_{r,w} = 0$. Choosing $K_{g,sec} = 1\ 10^{-18}$ m^2, we obtain $A = 25$ for an intrinsic permeability k de $4\ 10^{-20}$.

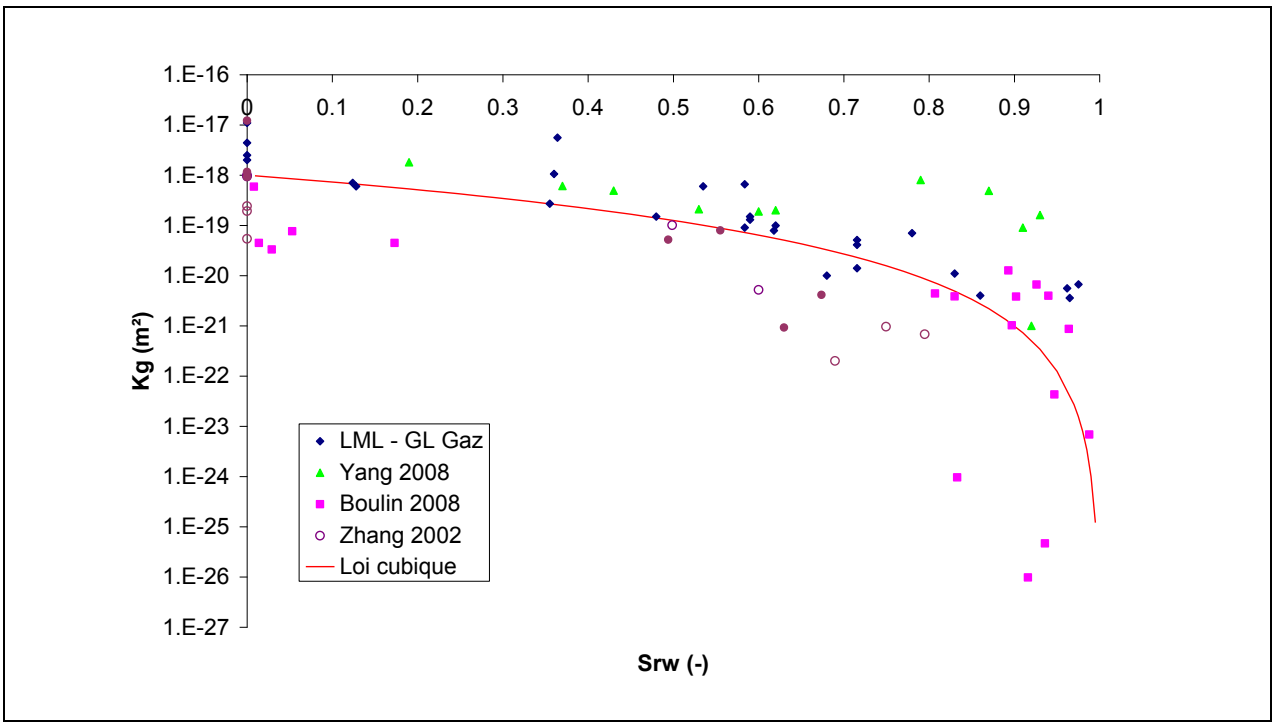

Figure 8 : Gas permeability K_g evolution with the water saturation $S_{r,w}$ for the argillite.

4.4.2 Injection chamber

We give now for the injection chamber the evolution curve of the water saturation $S_{r,w}$ with the capillary pressure p_c (***Figure 9***).

Water saturation of the medium $S_{r,w}$ is expressed according to the capillary pressure p_c through the Van Genuchten's model:

$$\frac{S_{r,w} - S_{res}}{S_{\max} - S_{res}} = \left[1 + \left(\frac{p_c}{P_r} \right)^n \right]^{-m} \tag{47}$$

with here the values of $S_{max} = 1$, $S_{res} = 0$, $m = 0.333$, $n = 1.5$ et $P_r = 0.05$ MPa.

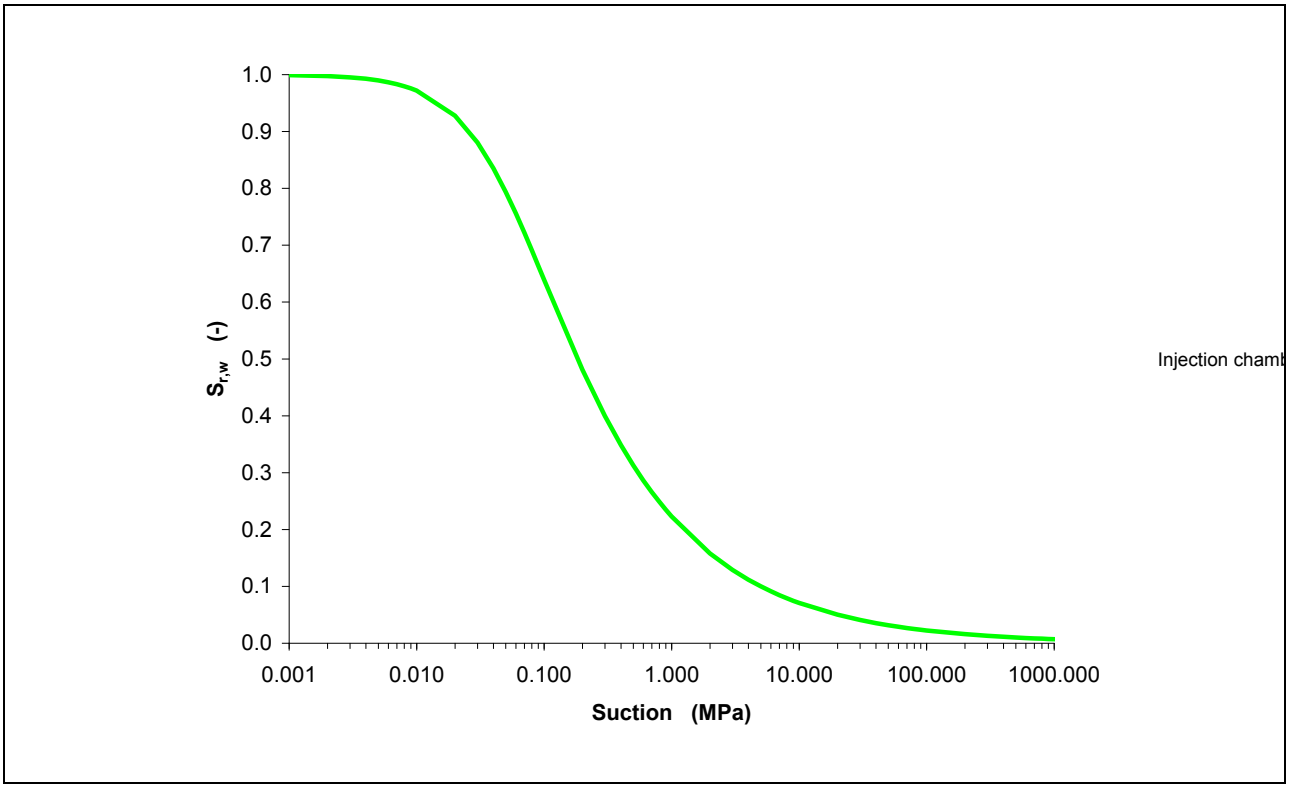

Figure 9 : Water saturation $S_{r,w}$ evolution with the capillary pressure p_c for the injection chamber.

For the injection chamber, water and gas relative permeability curves are not used: the intrinsic permeability is so supposed independent of the saturation.

5 DISCRETISATION, INITIAL AND BOUNDARY CONDITIONS OF THE 3D SIMULATIONS

5.1 Meshing

Several fully coupled (mechanical - water - gas) simulations were performed with the non linear finite elements code LAGAMINE developed at the University of Liège.

For symmetry reasons, half a 3D mesh is used around the PGZ1201 borehole, inclined in x, y, z according the actual axis of the borehole. ***Figure 11*** shows a perspective view of this studied domain.

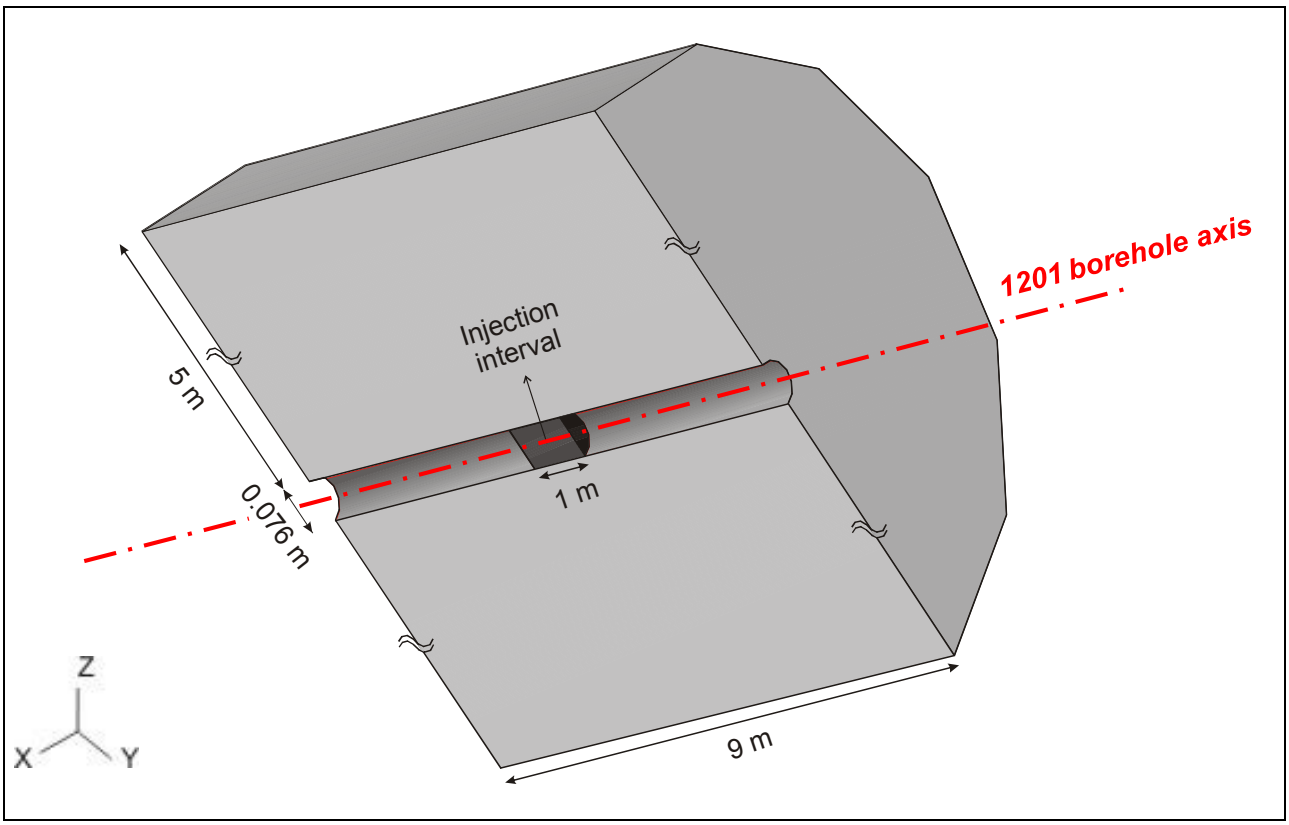

Figure 10 : Geometry around the PGZ1201 borehole.

Figure 11 presents the 3 plane views (x-y, y-z and z-x) and the perspective view of this mesh. The mesh includes 16478 nodes for 13614 8-nodes brick elements and 5803 boundary conditions/loading elements. The total number of equation is 79511 (with 5 degrees of freedom per node (x, y, z, p_w, p_g))

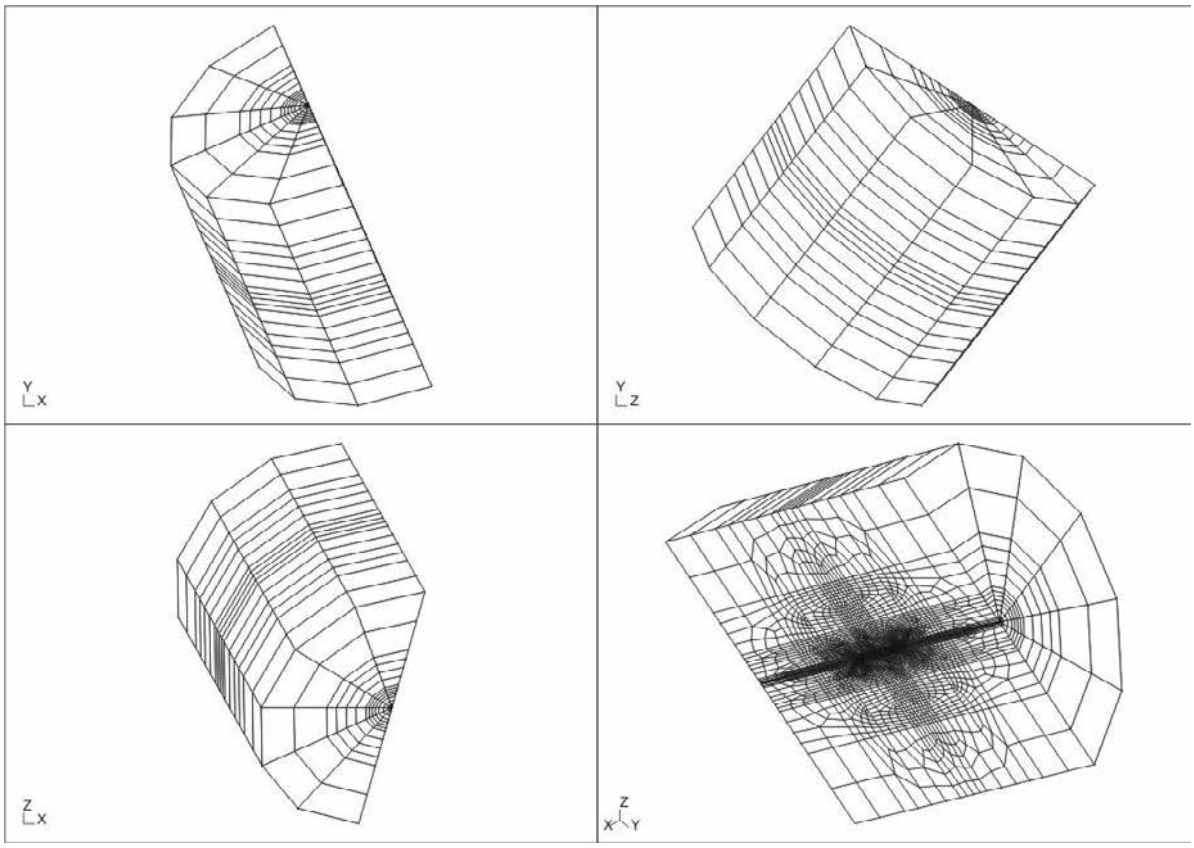

Figure 11 : Half a 3D mesh around the PGZ1201 borehole.

Figure 12 presents a zoom of the mesh perspective view in the injection chamber zone (1m length). The volume of the injection chamber has been taken to 4.48 dm³ (cylindrical chamber of 1 m length and 3.78 cm of radius (after boring).

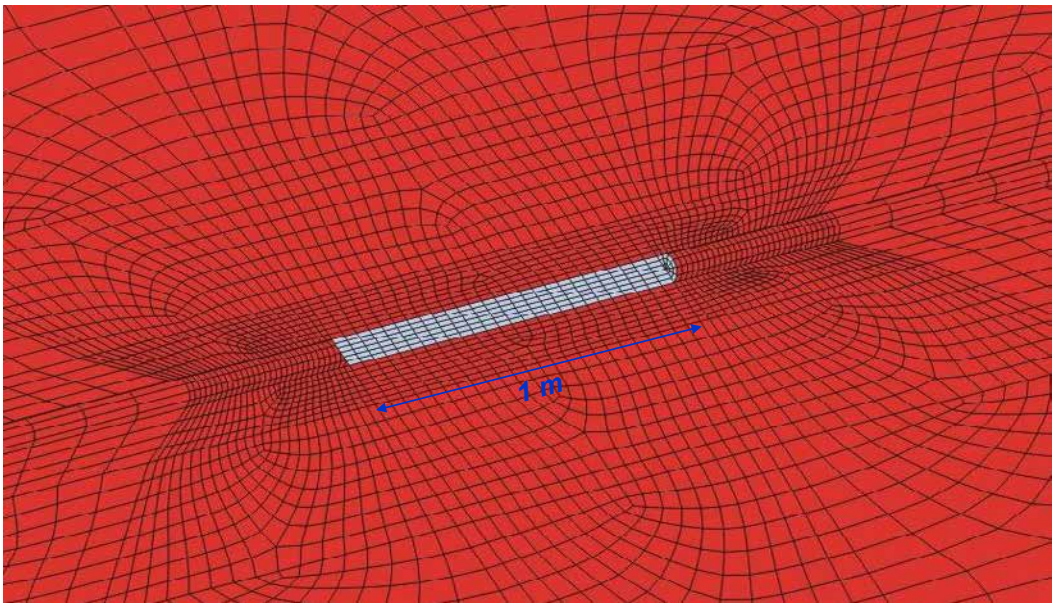

Figure 12 : Zoom on the perspective view – Injection chamber (interval 2).

The extend of the mesh will be taken equal to 9 m longitudinally in the direction of the PGZ1201 borehole axis and 5 m radially from that borehole axis. The radius of the borehole is equal to 3.8 cm. (***Figure 13***)

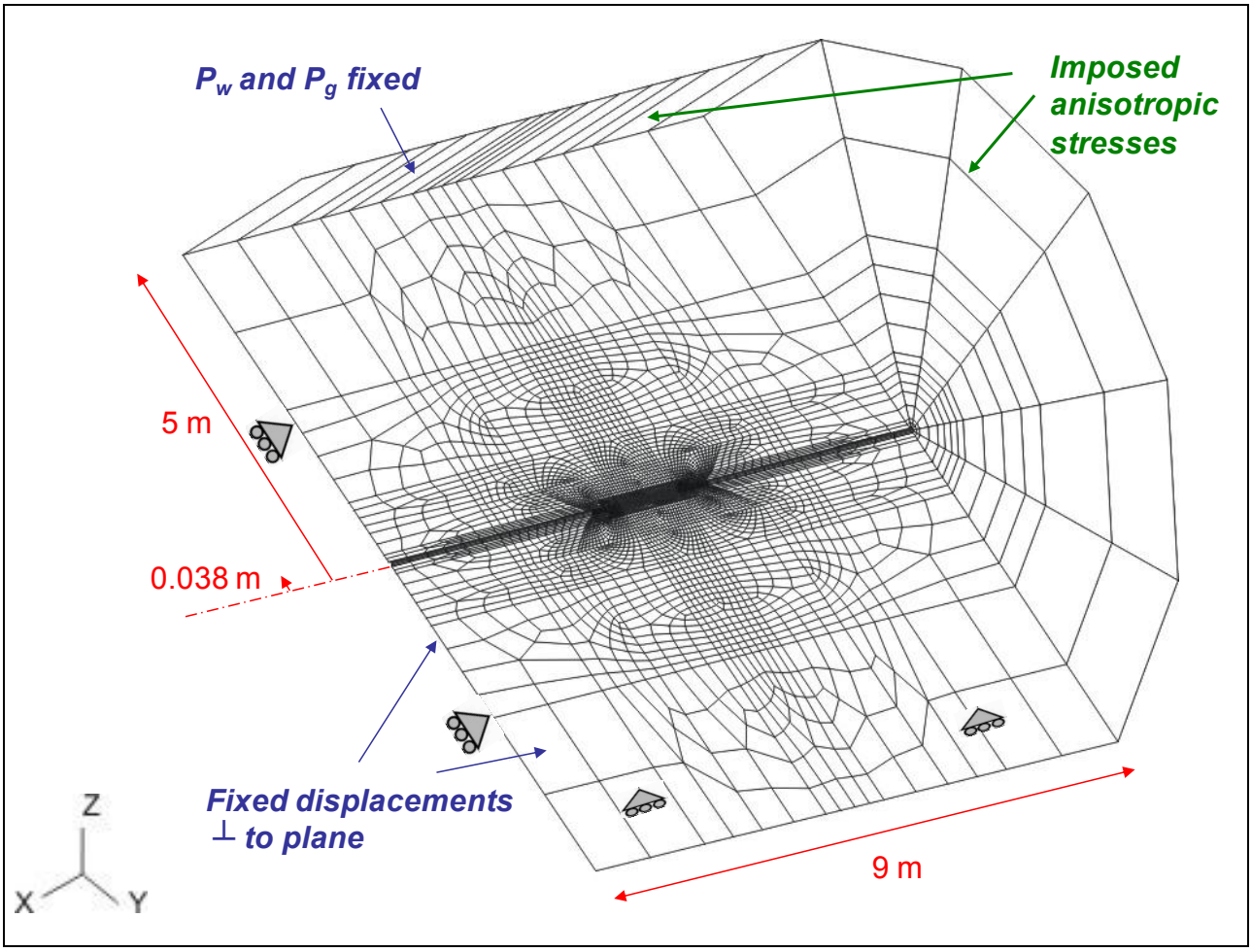

Figure 13 : Boundary conditions – Half a 3D mesh around the PGZ1201 borehole.

5.2 Initial and boundary conditions

Some displacements are fixed for symmetry reason, and stresses are imposed at the distant boundary conditions of the mesh (***Figure 13***)

Figure 14 presents the anisotropic normal stresses imposed at the distant boundary conditions and at the PGZ1201 borehole wall.

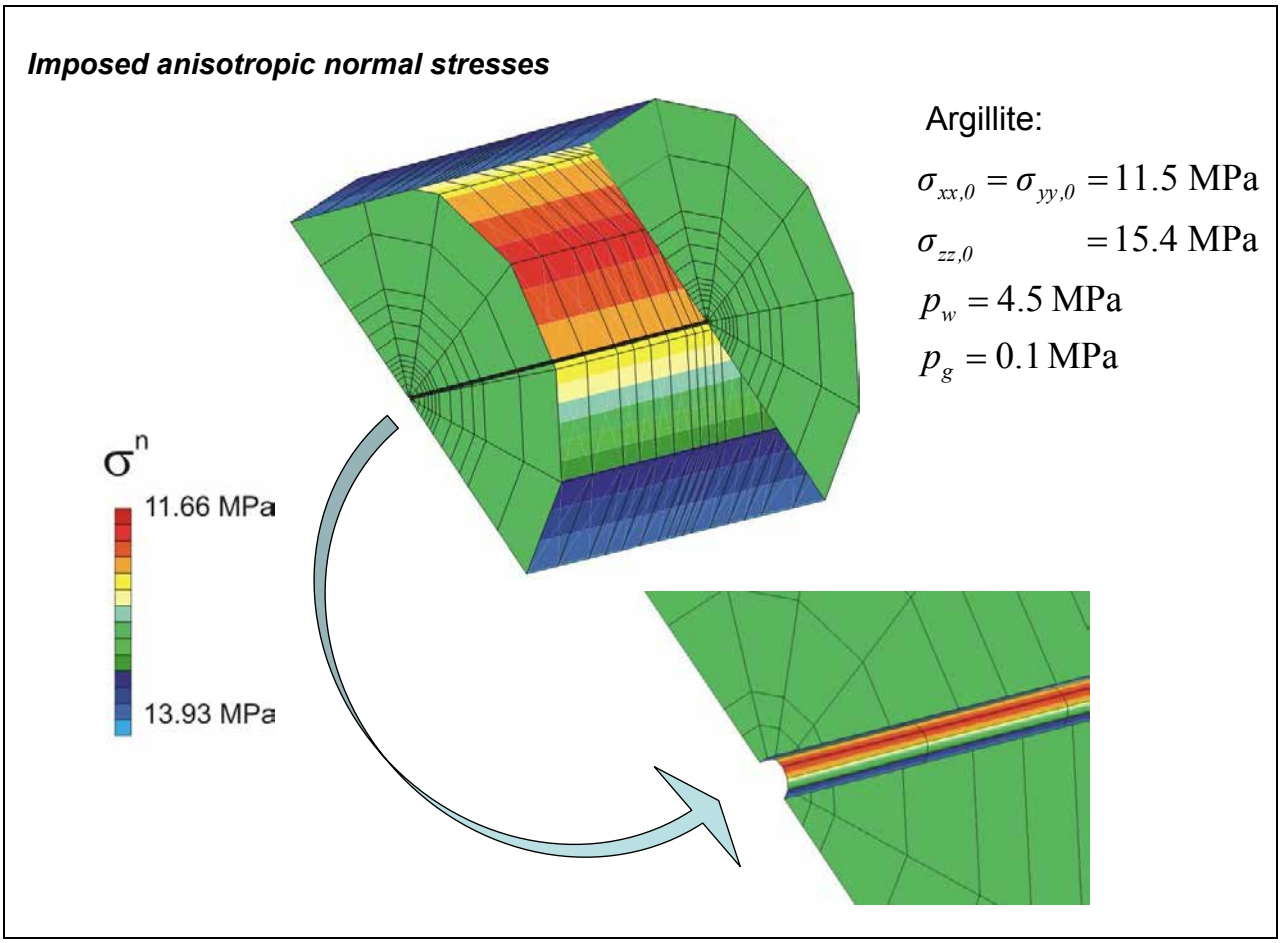

Figure 14 : Boundary conditions – Imposed anisotropic normal stresses.

The initial conditions in argillite correspond to the in situ site, namely:

$\sigma_{xx,0} = \sigma_{yy,0}$=11.5 MPa
$\sigma_{zz,0}$ =15.4 MPa
$p_w = 4.5$ MPa
$p_g = 0.1$ MPa
$T = 303$ °K

The stress state is assumed anisotropic and the effect of gravity is not considered. Even if a gas is not initially present, it is still necessary to define an initial value of the gas pressure. By default, we take the atmospheric pressure.

Figure 15 presents the summary of the 4 phases of the simulation:

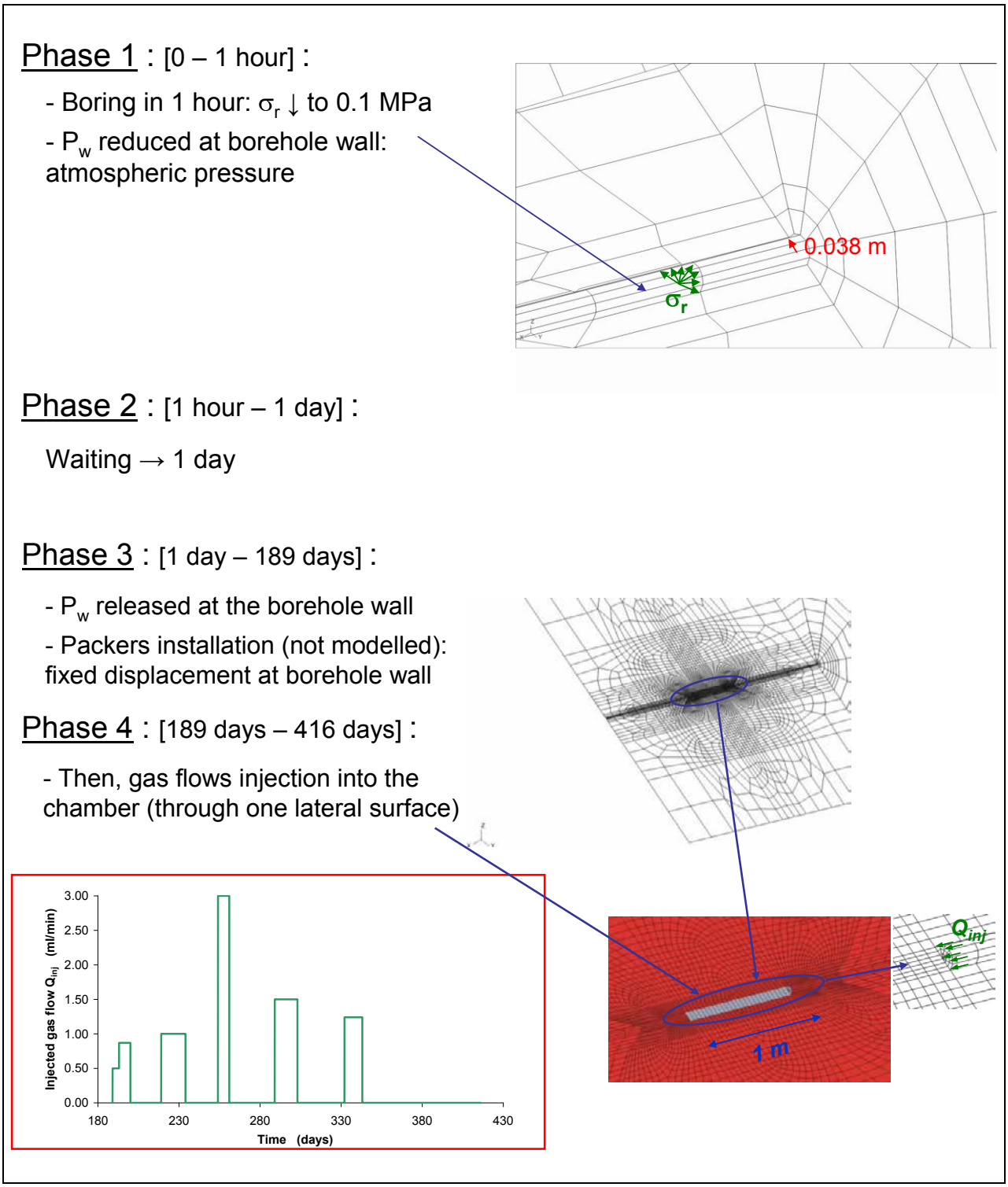

Figure 15 : Boundary conditions – Phasing.

Phase 1: The excavation of the borehole is done in 1 hour by decreasing at the wall the radial total stress and the pore water pressure to 0.1 MPa (atmospheric pressure). The gas pressure is fixed at its initial value constant throughout the model.

Phase 2: Then the water pressure and the total radial stress at the wall of the borehole are kept constant for 1 day. The gas pressure is always maintained at its initial value constant throughout the model.

Phase 3: During that phase, from 1 day to 189 days, the water pressure is released at the borehole wall. At the beginning of the phase, packers (not modelled here) are installed in the borehole: consequently we fixed all the displacements at the borehole wall. The gas pressure is always maintained at its constant initial value.

Phase 4: That phase is comprised between 189 and 416 days. During that phase, gas flow injection is performed according phasing given in ***Figure 16***. The gas is injected through a lateral surface of the chamber. Five rises (and five drops) of gas pressure (GRI1a to GRI5) are so performed, with between theses some no-injection periods (GRIS1b to GRIS5).

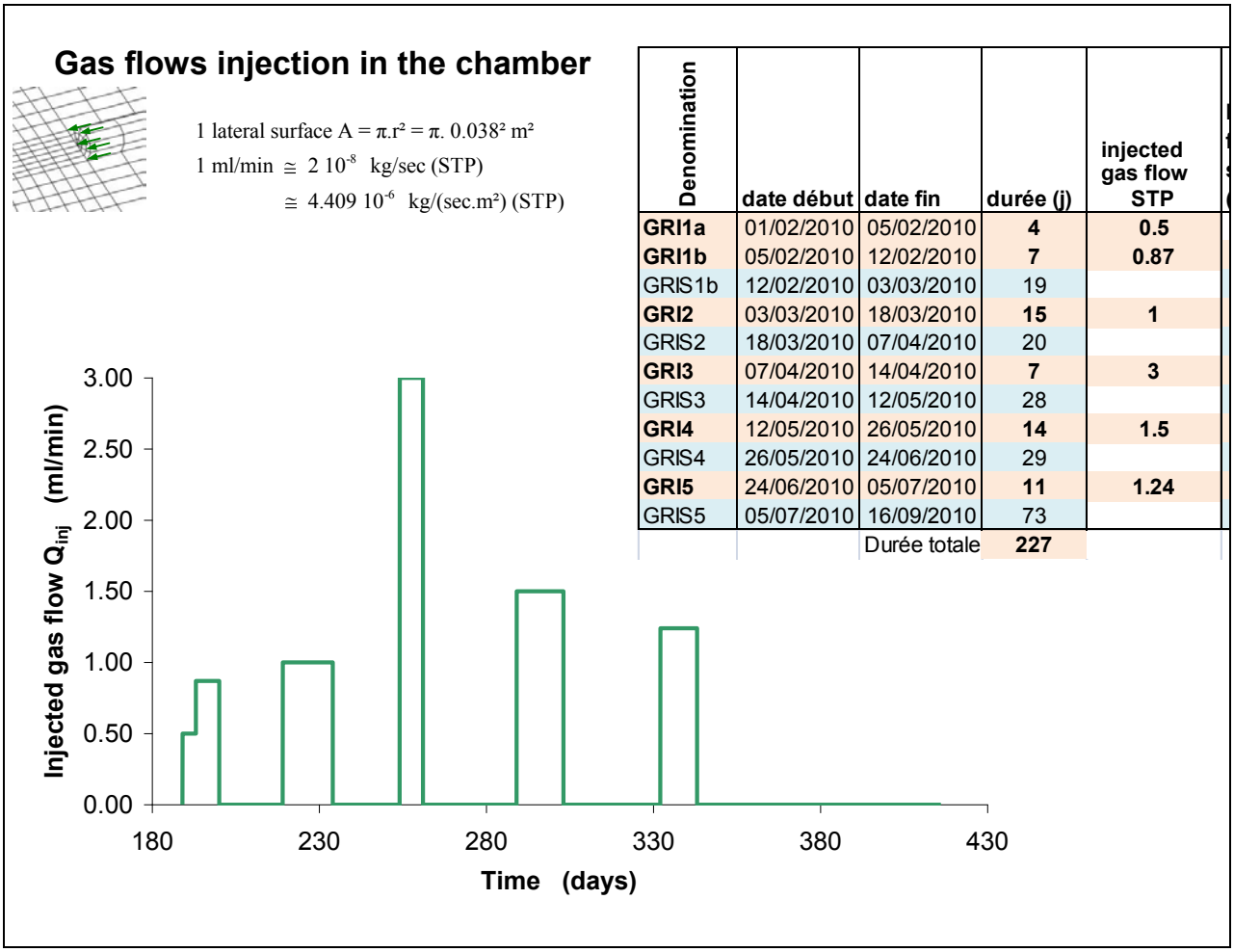

Denomination	date début	date fin	durée (j)	injected gas flow STP
GRI1a	01/02/2010	05/02/2010	**4**	**0.5**
GRI1b	05/02/2010	12/02/2010	**7**	**0.87**
GRIS1b	12/02/2010	03/03/2010	19	
GRI2	03/03/2010	18/03/2010	**15**	**1**
GRIS2	18/03/2010	07/04/2010	20	
GRI3	07/04/2010	14/04/2010	**7**	**3**
GRIS3	14/04/2010	12/05/2010	28	
GRI4	12/05/2010	26/05/2010	**14**	**1.5**
GRIS4	26/05/2010	24/06/2010	29	
GRI5	24/06/2010	05/07/2010	**11**	**1.24**
GRIS5	05/07/2010	16/09/2010	73	
		Durée totale	**227**	

Figure 16 : Boundary conditions – Phasing of the gas injection in the chamber (Phase 4).

6 3D NUMERICAL RESULTS AND COMPARISONS WITH IN-SITU MEASUREMENTS

6.1 Phase 1 and 2: after boring

Figure 17 gives the results of the water pore pressure and the wall total radial normal stress obtained at the end of the phase 2, after 1 day. The water pressure has decreased to 0.1 MPa at the borehole wall and the total radial stress imposed at the borehole wall is also reduced to about 0.1 MPa.

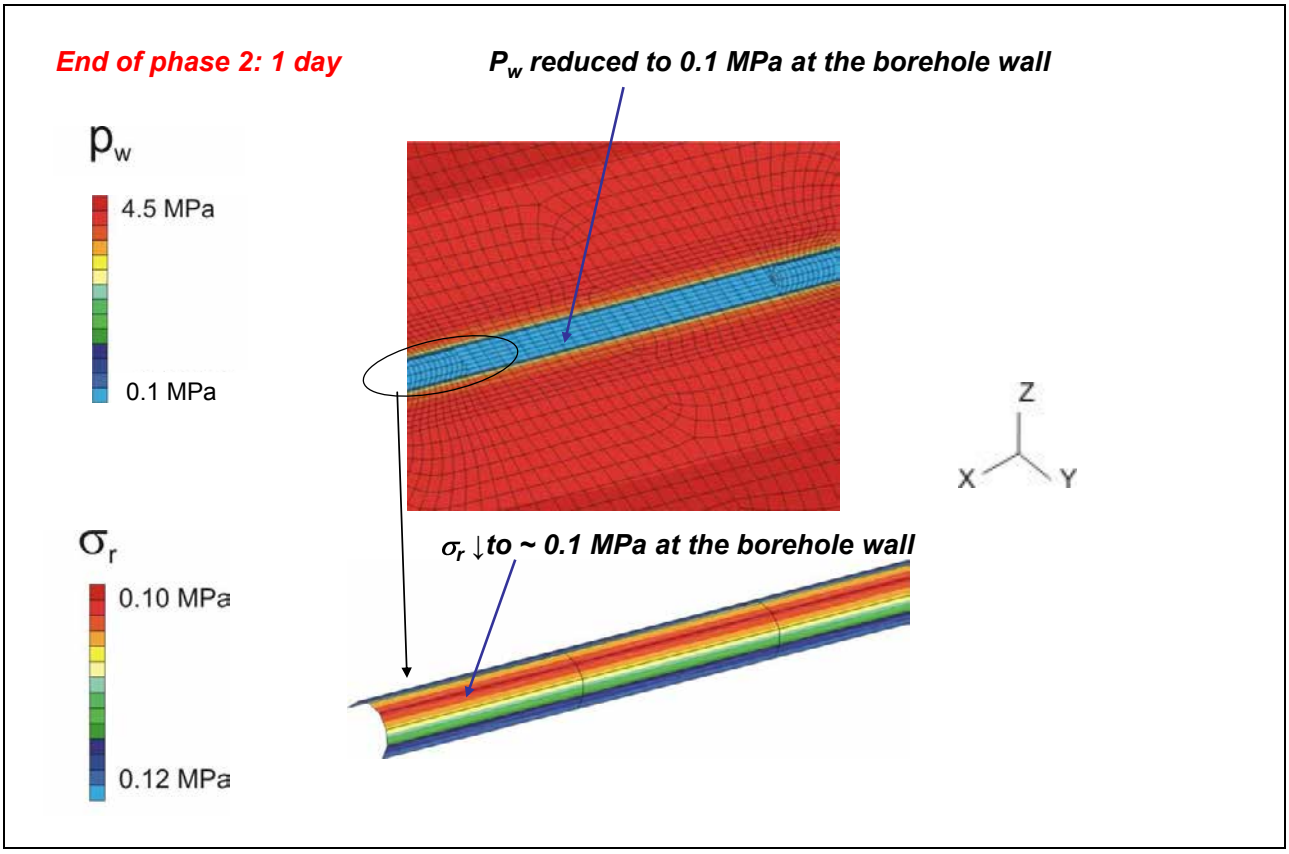

Figure 17 : Water pore pressure and wall radial stress at the end of the phase 2.

6.2 Phase 4: gas injection

On ***Figure 18*** are presented, in the injection chamber zone, the evolution of the water pressure repartition during the phase 4, at the end of each injection level (five red points on ***Figure 18***).

Figure 19 and ***Figure 20*** give, for the whole of the mesh, the repartition of the water pore pressure and the gas pressure respectively at the end of the 3rd gas injection level of the phase 4. On ***Figure 18*** and ***Figure 19***, we can clearly observe the effect of the anisotropy of the permeability

tensor. We can also see on ***Figure 20*** that the influence zone of the gas pressure rising is very reduced and limited to the injection chamber zone.

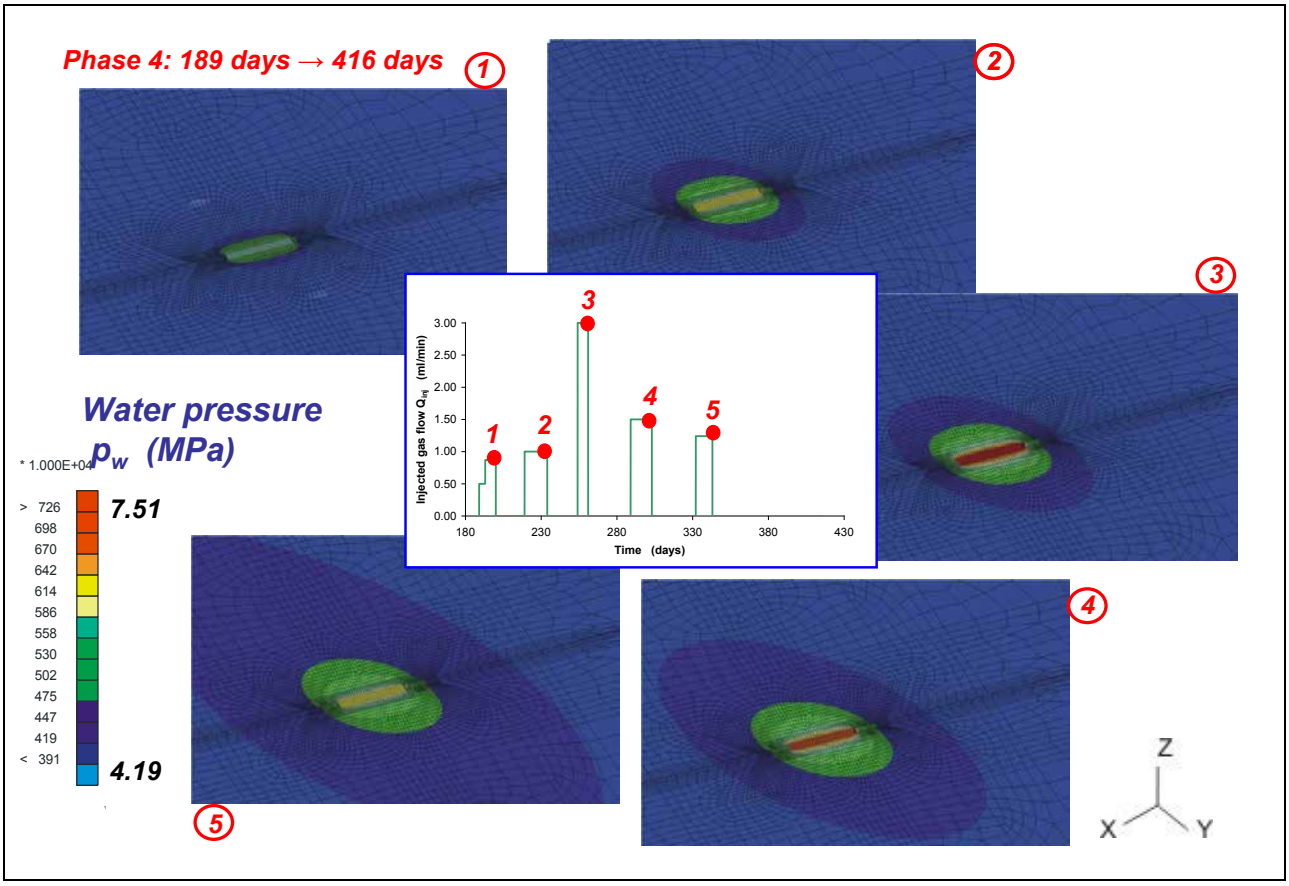

Figure 18 : Water pore pressure near the injection chamber during the phase 4.

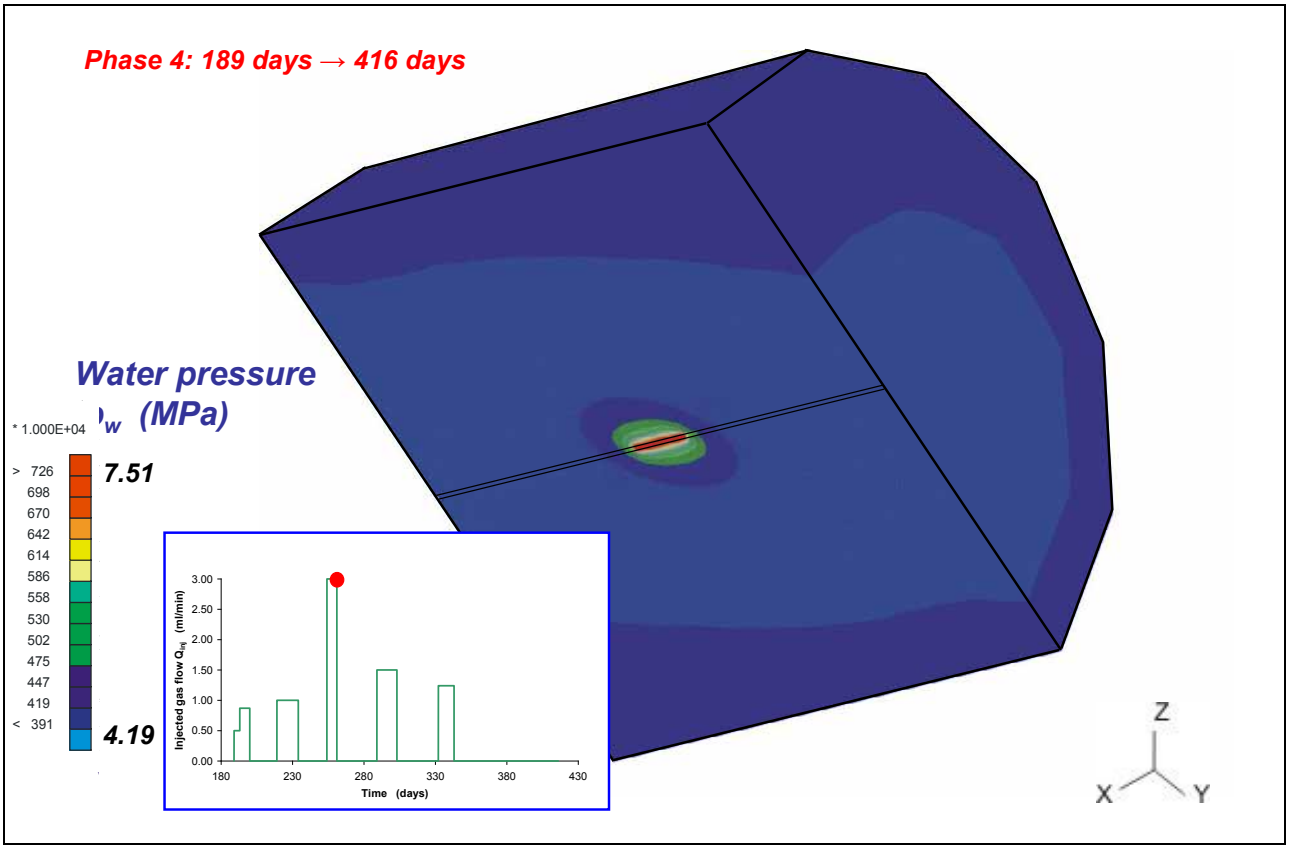

Figure 19 : Water pore pressure at the end of the 3rd gas injection level of the phase 4.

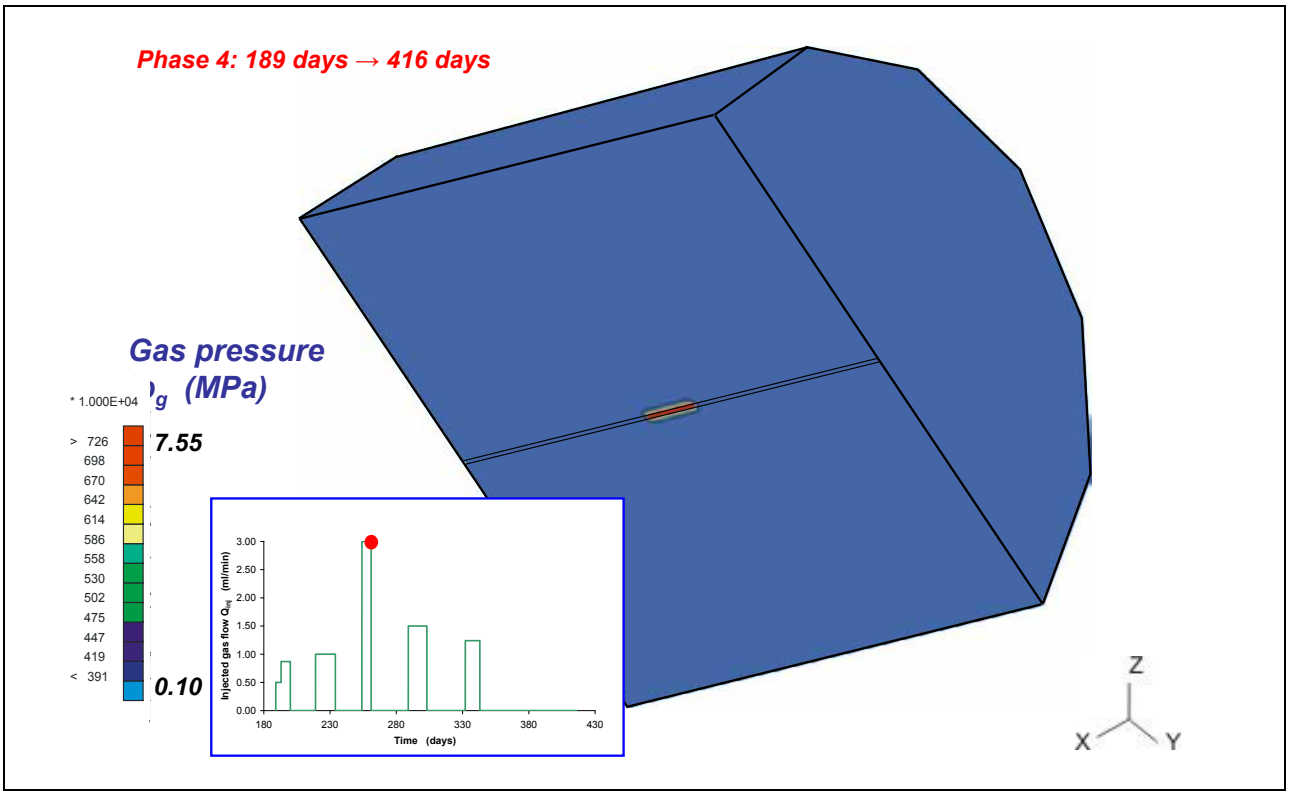

Figure 20 : Gas pressure at the end of the 3rd gas injection level of the phase 4.

Figure 21 and ***Figure 22*** present, for the 3 intervals, the evolution of the water and the gas pressures respectively during the phase 4. On these figures and for comparison with the numerical results, the in-situ measurements of the pore pressure in the interval 2 (injection chamber) are also presented. The five levels of injected gas flow are also plotted on these figures.

Figure 23 present, for the 3 intervals in the PGZ1202 borehole, the comparison between the numerical and experimental water pore pressure during the phase 4.

It clearly appears the evolutions in the interval 2 of the water and gas pressure are identical. Gas pressure increases are lower at the intervals 1 and 3. We note also that the three first level of gas injection (just before the drop of the 3rd level) are reasonably well reproduced, with however peak values higher numerically than experimentally. On the other hand, the end of the experimental curve is not correctly reproduced with the used parameters.

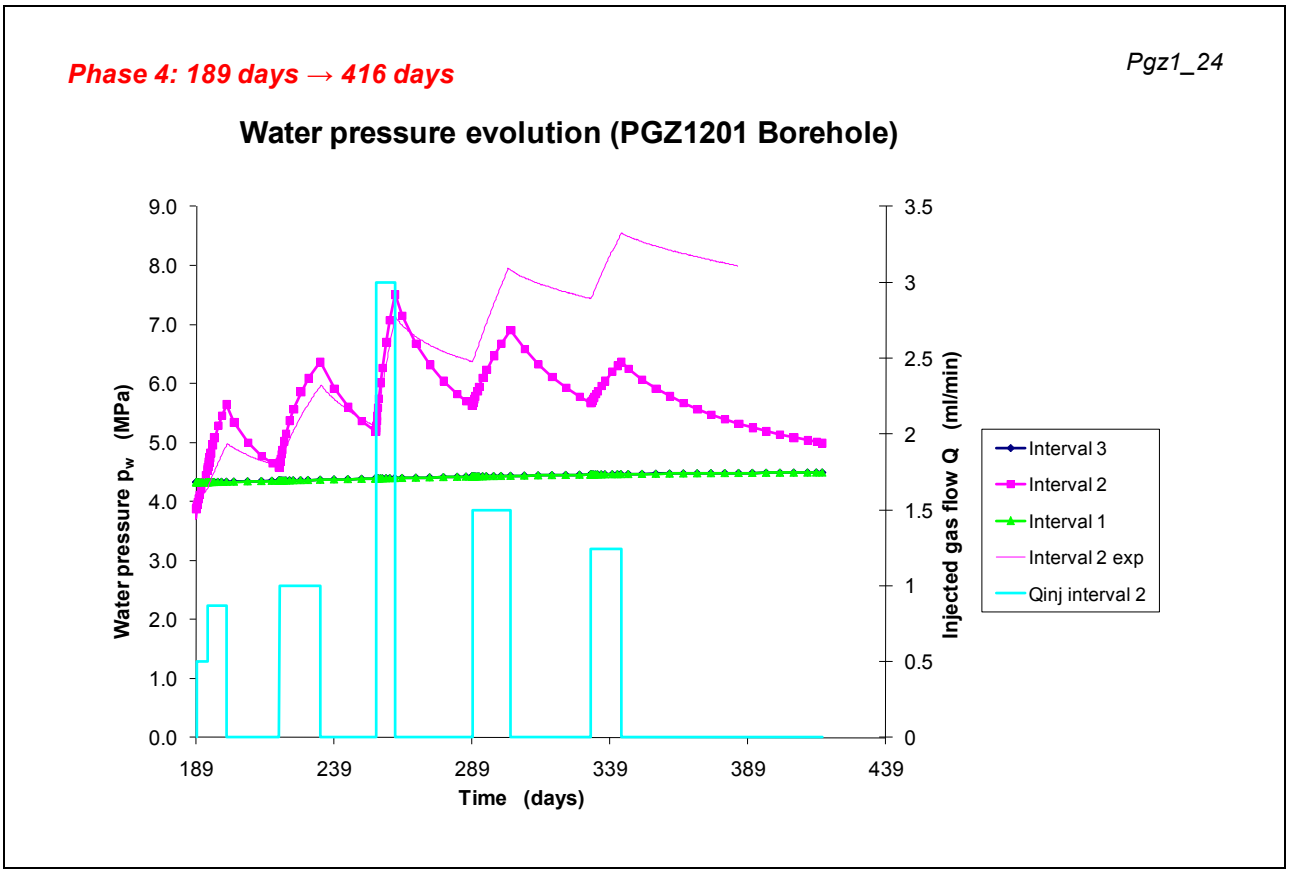

Figure 21 : Water pressure evolution during the phase 4.

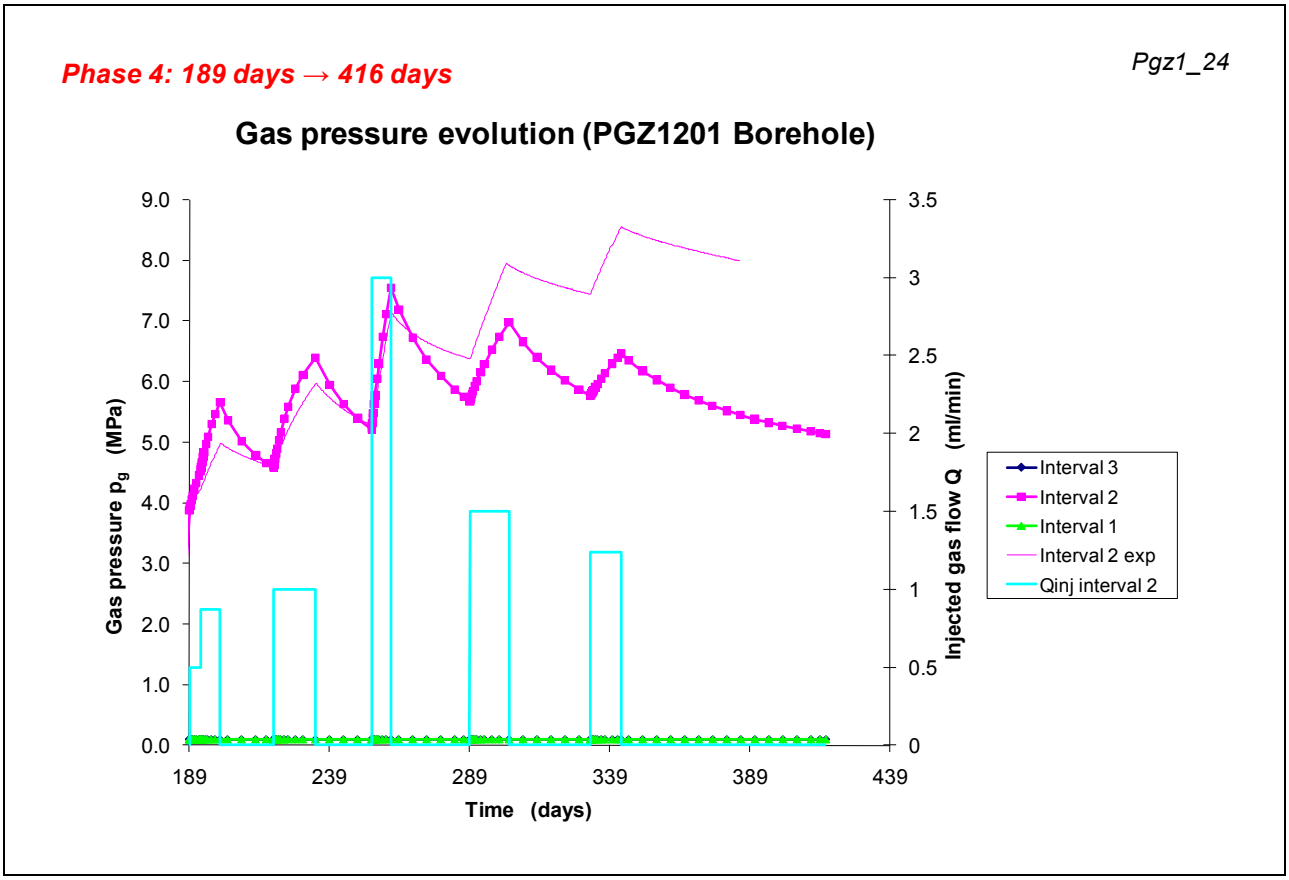

Figure 22 : Gas pressure evolution during the phase 4.

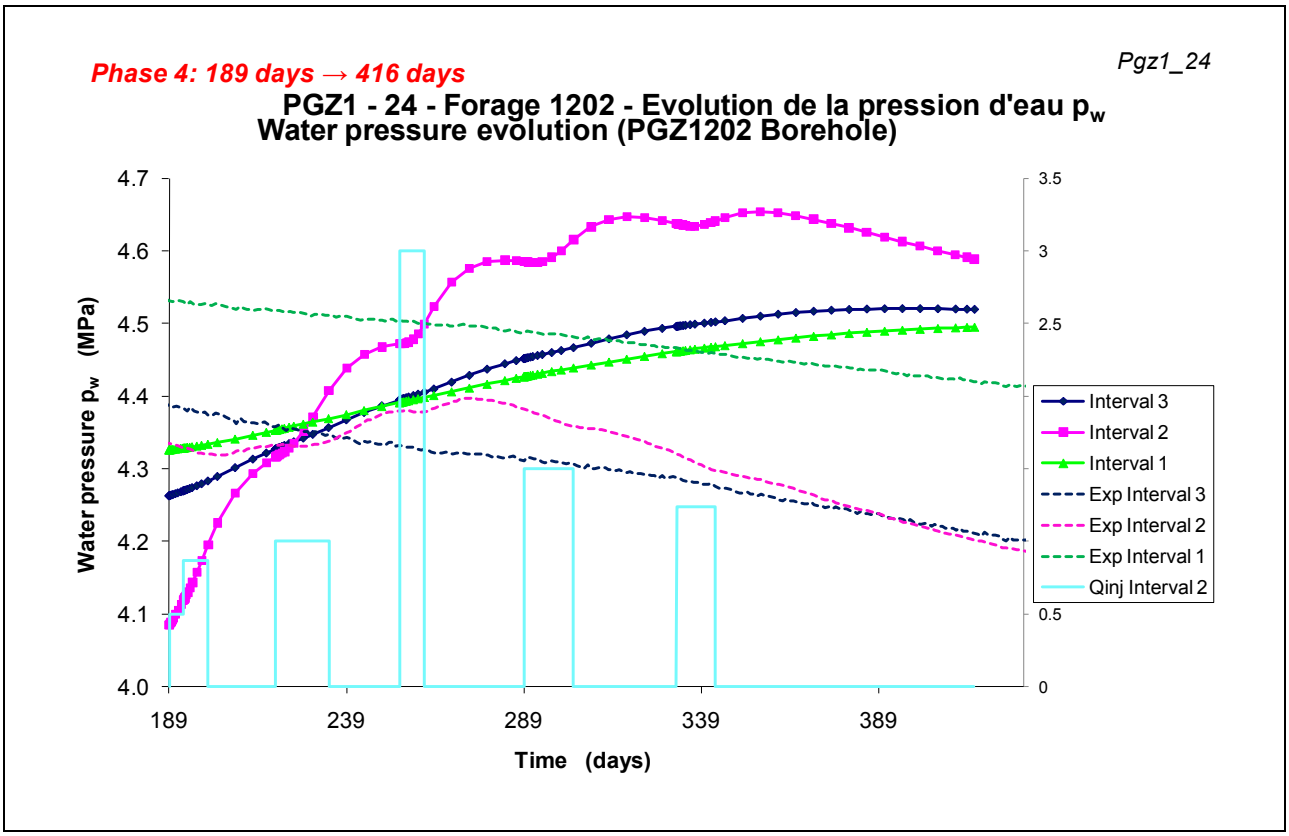

Figure 23 : Water pressure evolution during the phase 4 in the PGZ1202 borehole.

6.3 Phase 4: gas injection – influence of argillite permeability and injection compressibility

Two other sets of argillite permeability were then tested (1.10^{-20} m² (horizontally) + 0.33 10^{-20} m² (vertically) and 4.10^{-21} m² (horizontally) + 1.33 10^{-21} m² (vertically)). The results obtained with these two permeability sets are plotted on ***Figure 24***, with also the preceding results obtained with permeabilities given in Table 2 (4.10^{-20} m² (horiz) + 1.33 10^{-20} m² (vert)). We can note that the argillite permeability fit the general shape of the pore pressure evolution curve (in red on ***Figure 24***), and especially the low points of the curve. To fit the first part of the experimental curve, the best choice of permeability set seems thus to remain that given in Table 2.

Peak heights can be adapted modifying the compressibility of the injection chamber. ***Figure 25*** shows the influence of that compressibility of the curve: a compressibility of 3 10^{-8} Pa^{-1} allows to correctly fit the beginning of the experimental curve (always just before the drop after the 3rd peak). For that figure, the used argillite permeability is 4.10^{-20} m² horizontally and 1.33 10^{-20} m² vertically (cfr Table 2).

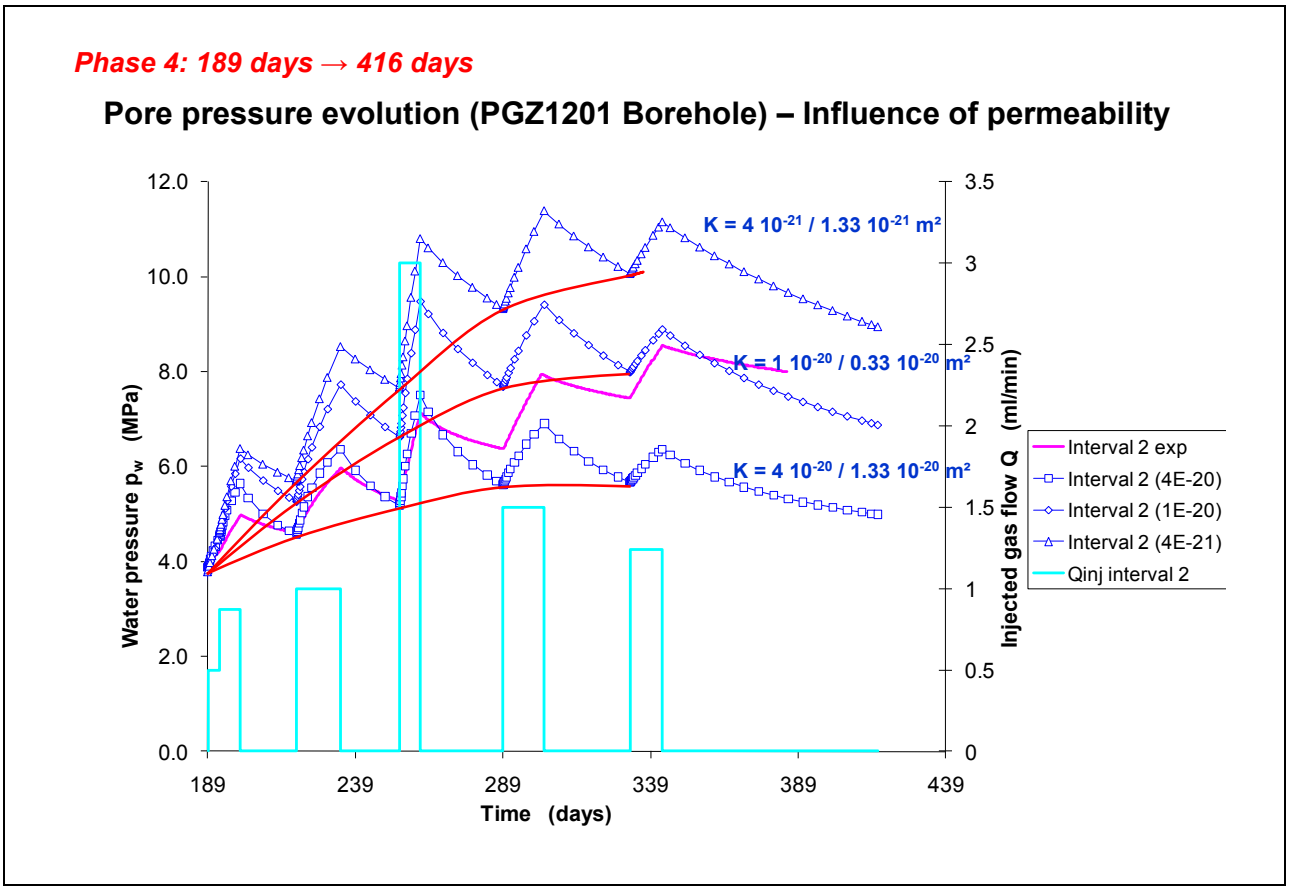

Figure 24 : Pore pressure evolution during the phase 4 – Influence of permeability.

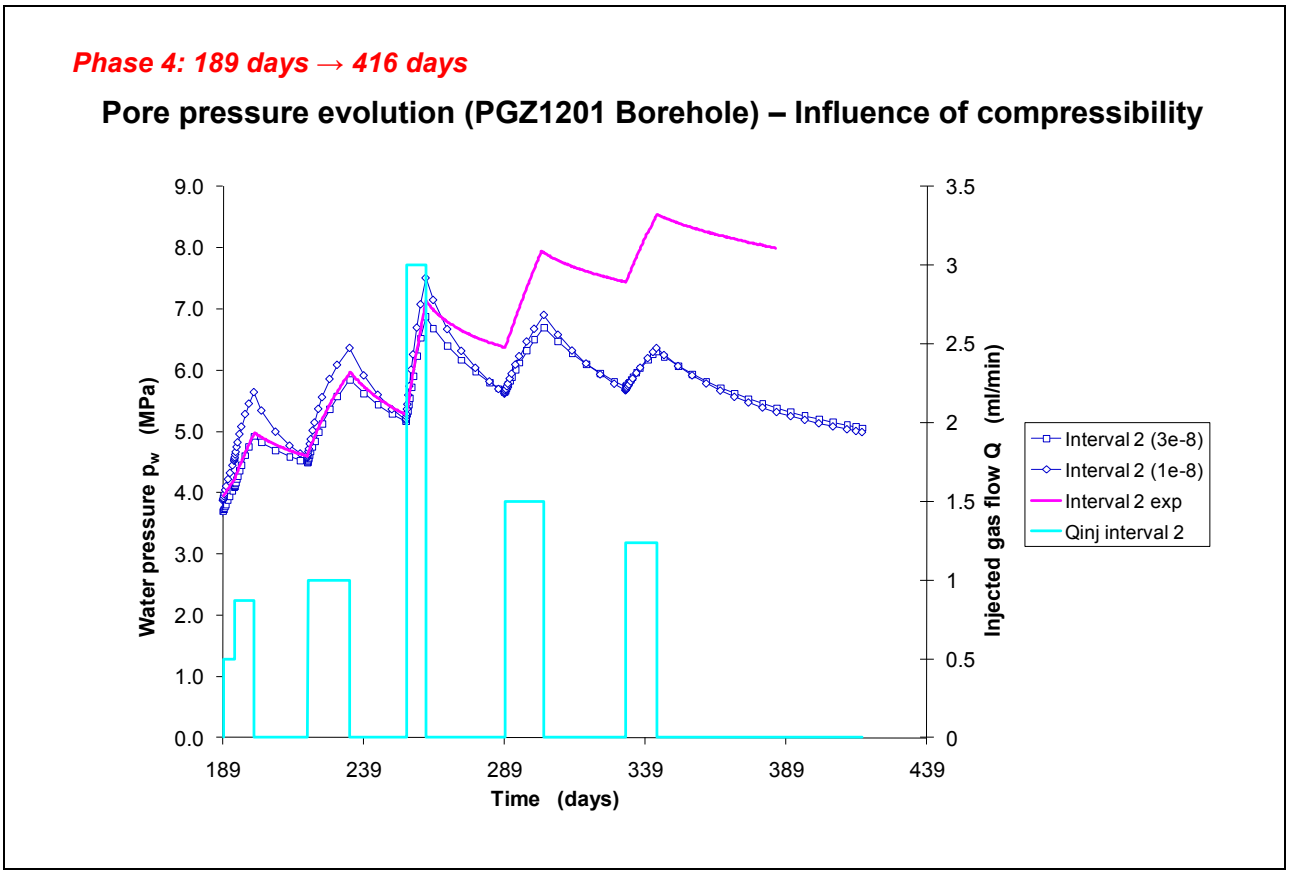

Figure 25 : Pore pressure evolution during the phase 4 – Influence of compressibility.

6.4 Phase 3: waiting phase – influence of PGZ1031 borehole drainage

Figure 26 presents now, for the 3 intervals, the evolution of the experimental pore pressure during the phase 3 (from 1 to 189 days). We can note, especially for the interval 2, a pore pressure decrease during this phase; for the intervals 1 and 3, this decrease is much lower.

It is possible that pore pressure decrease during the phase 3 comes perhaps from a drainage effect of the PGZ1031 borehole. This drainage effect was numerically tested. ***Figure 27*** presents the 3D perspective view end the x-y plane view of the mesh, with the location of the PGZ1031 borehole. The gap between this borehole and the end of interval 2 is 136 mm in the x-y plane view. That PGZ1031 borehole was not really discretised in the mesh, but we imposed that all the nodes within a radius of 25 cm from the PGZ1031 borehole axis had a water pressure equal to the atmospheric pressure 0.1 MPa during the phase 3. ***Figure 28*** gives the repartition of the water pore pressure at the end of the phase 3, where we see the drainage effect of the PGZ1031 borehole. The influence zone of this drainage may perhaps seem high (R = 25 cm) but was necessary because there were very few nodes in the mesh in the actual area of 10.13 cm diameter borehole, where the water pressure could be imposed.

Figure 30 compares the numerical and experimental pore pressure evolutions during the phase 3, with high drainage effect of the PGZ1031 borehole. We can observe that manifestly the experimental curves of the intervals 1 and 2 are not correctly reproduced (the experimental decay is significantly lower than that obtained numerically, especially for the interval 2). Only the curves for the interval 3 have a similar decrease numerically and experimentally. Let's remark that anisotropy in the permeability tensor is of course involved in these results. So, a drainage effect of the PGZ1031 borehole, even large, does not seem to numerically reproduce the experimental decrease in the pore pressure curves obtained in the phase 3.

As mentioned previously, PGZ1031 borehole was not really discretised in the mesh. Drainage is thus only imposed on some nodes of the mesh, along the PGZ1031 borehole axis or more precisely close to that axis. The mesh is relatively coarse at about the axis of the PGZ1031 borehole so that drainage to 0.1 MPa is imposed only on some points and certainly not uniformly along the borehole axis. It is certainly that finding which does not allow to correctly reproduce the experimental measurements response. To improve the numerical answer due to a draining effect of the PGZ1031 borehole, other simulations will be performed later, taking into account this time a three-dimensional mesh of revolution around the PGZ1031 borehole axis.

Figure 31 and ***Figure 32*** compare, respectively in the PGZ1201 and PGZ1202 borehole, the numerical and experimental pore pressure evolutions during the phase 3 and 4, with drainage effect of the PGZ1031 borehole.

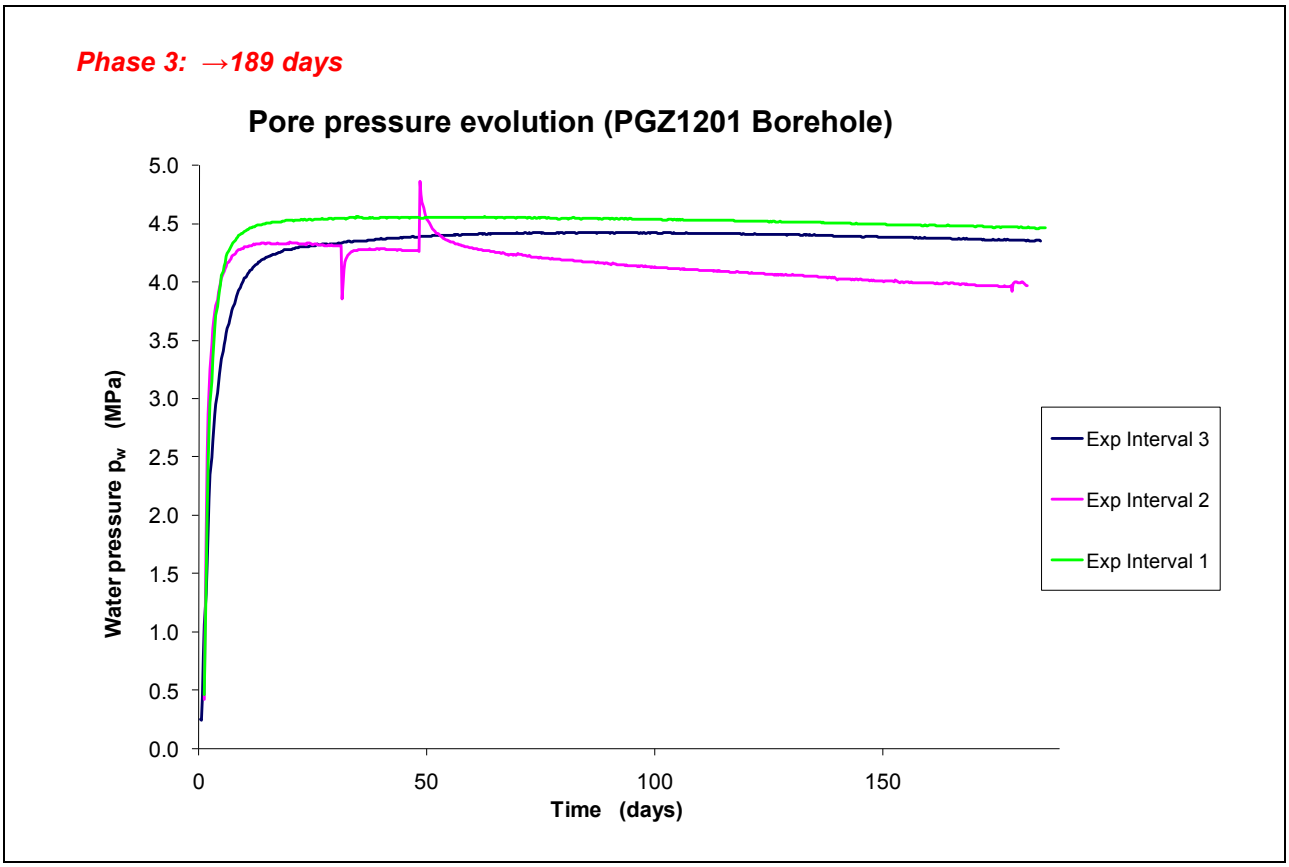

Figure 26 : Experimental pore pressure evolution during the phase 3.

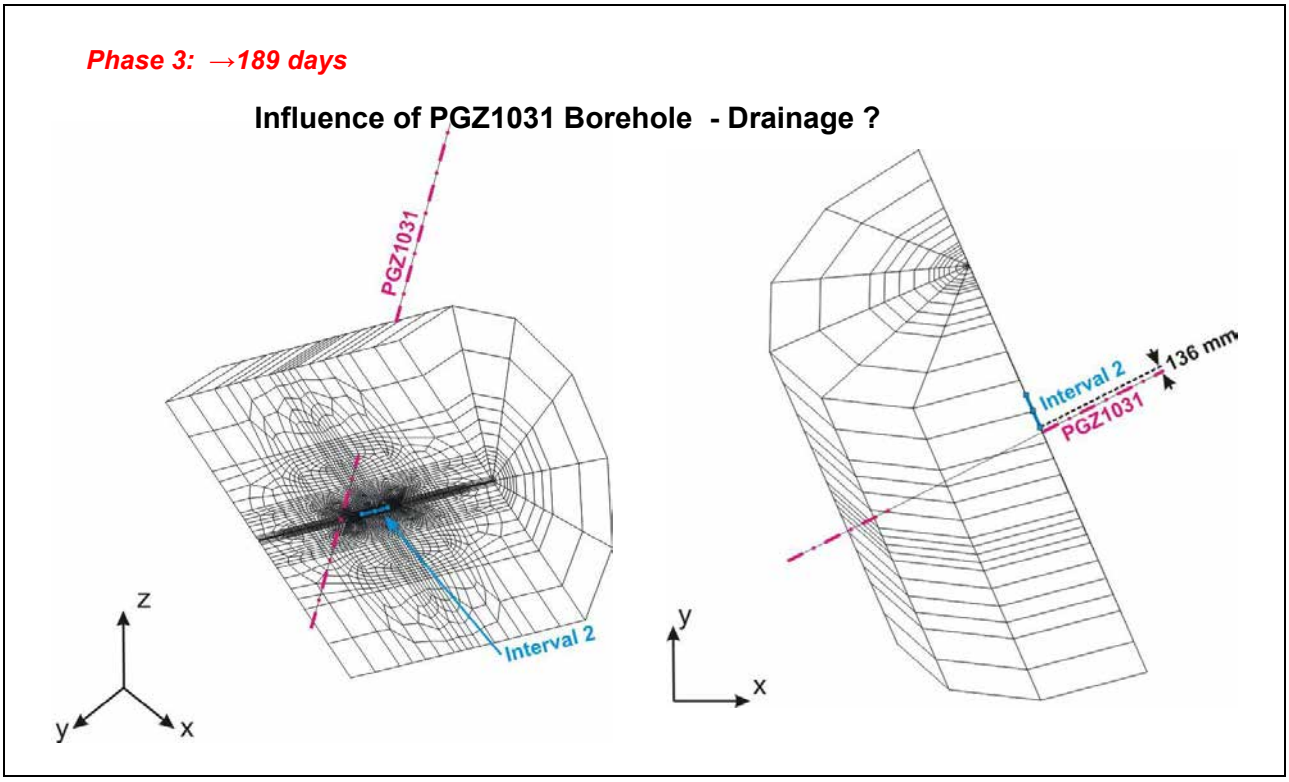

Figure 27 : Perspective and x-y plane views with location of the PGZ1031 borehole.

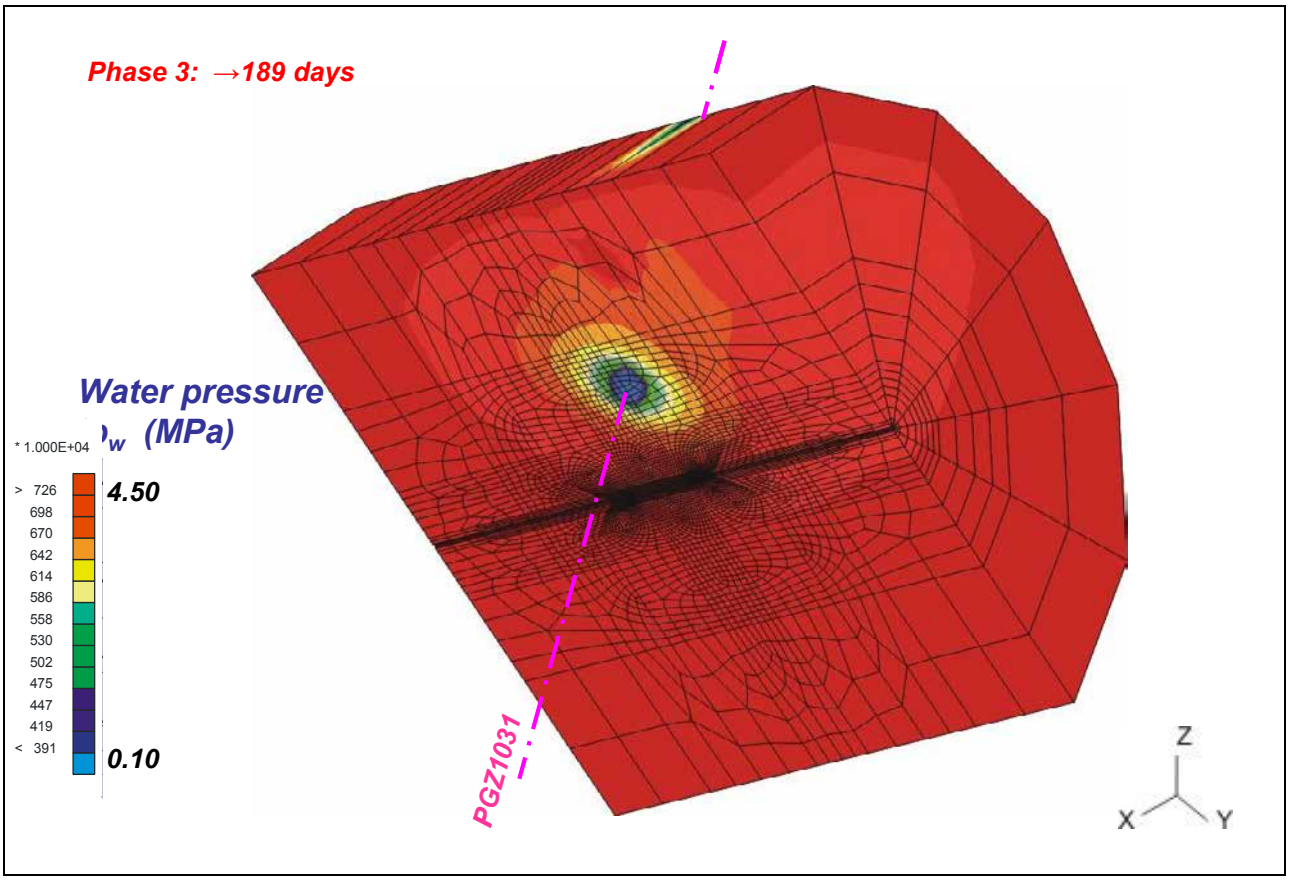

Figure 28 : Water pore pressure at the end of the phase 3.

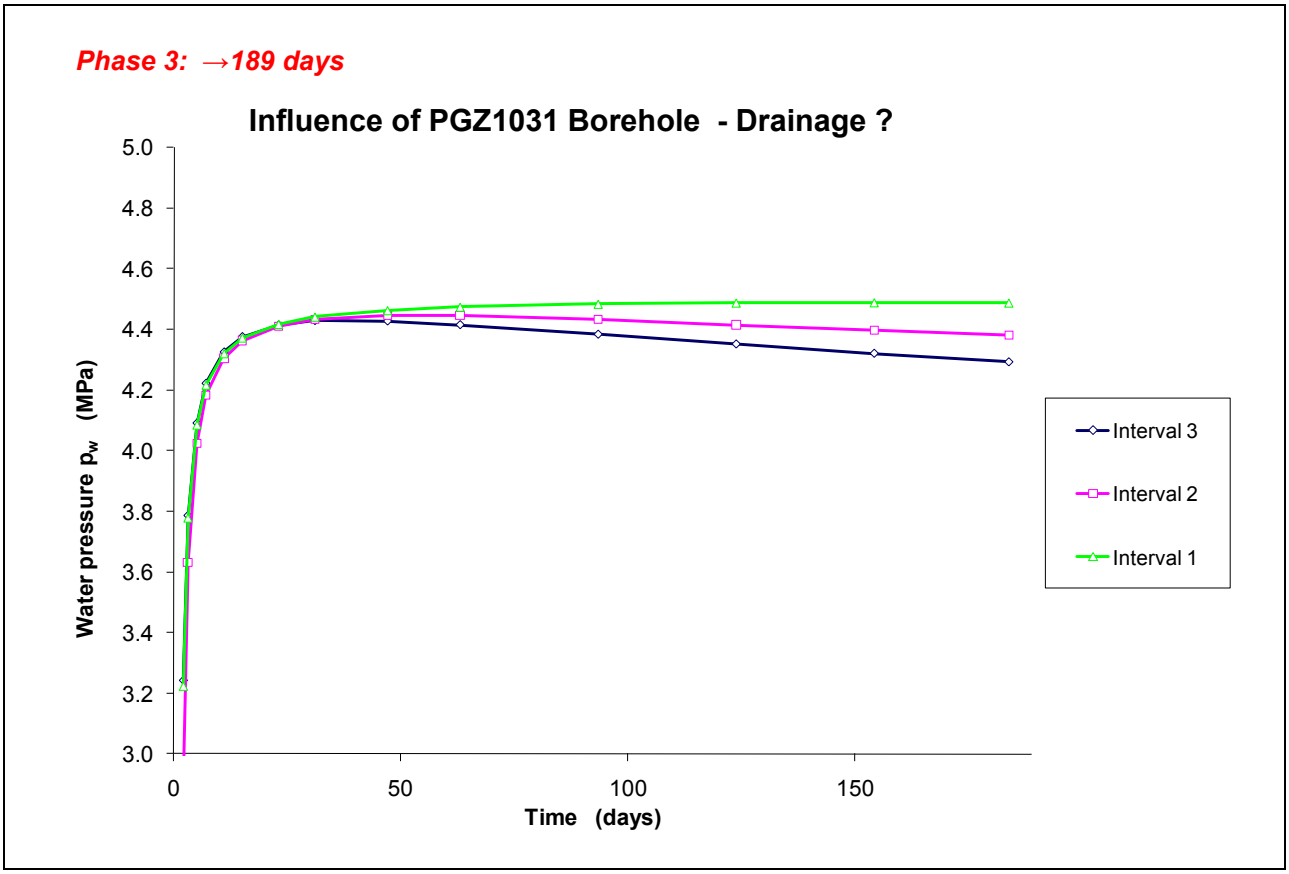

Figure 29 : Numerical water pressure evolution during the phase 3, with drainage effect of the PGZ1031 borehole.

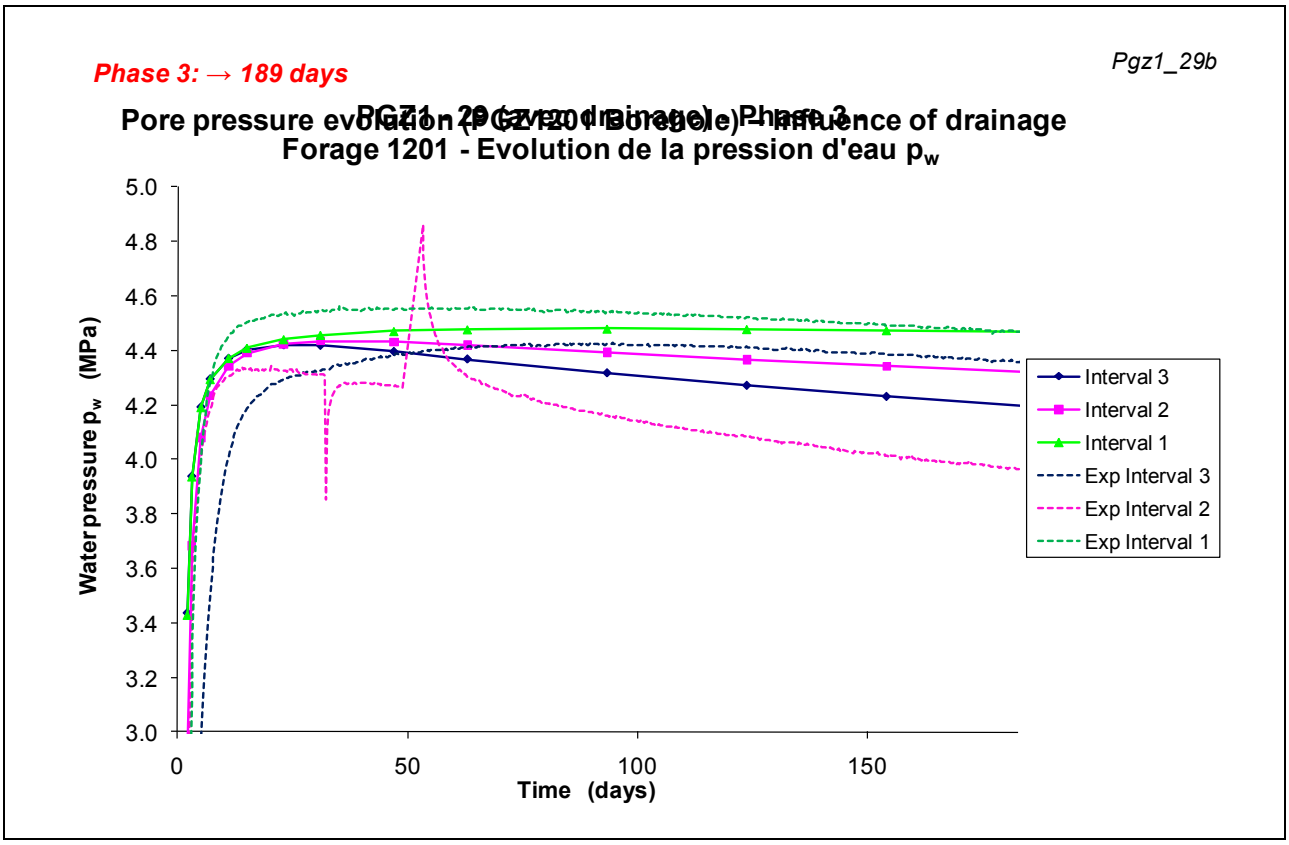

Figure 30 : Comparison of numerical and experimental pore pressure evolutions during the phase 3, with drainage effect of the PGZ1031 borehole.

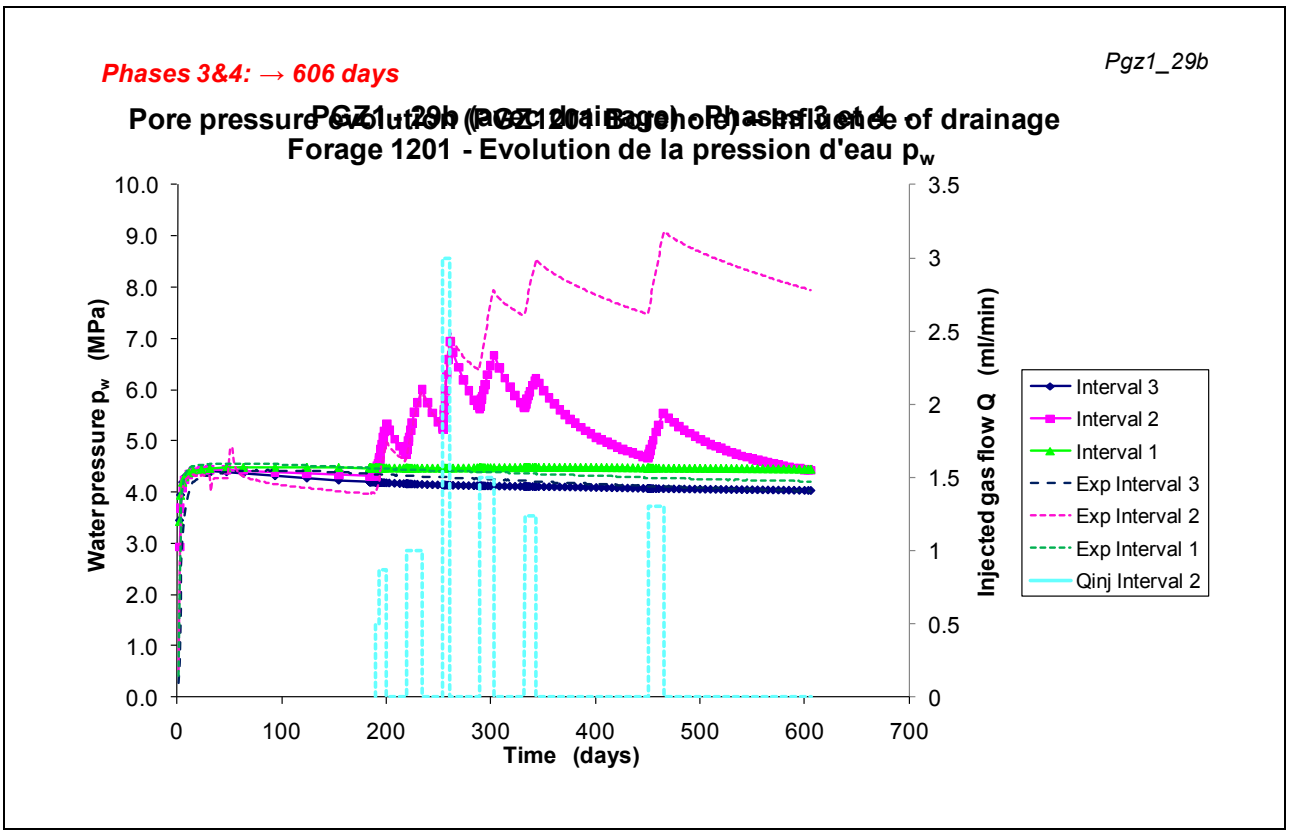

Figure 31 : Comparison of numerical and experimental pore pressure evolutions in the PGZ1201 borehole during the phases 3 and 4, with drainage effect of the PGZ1031 borehole.

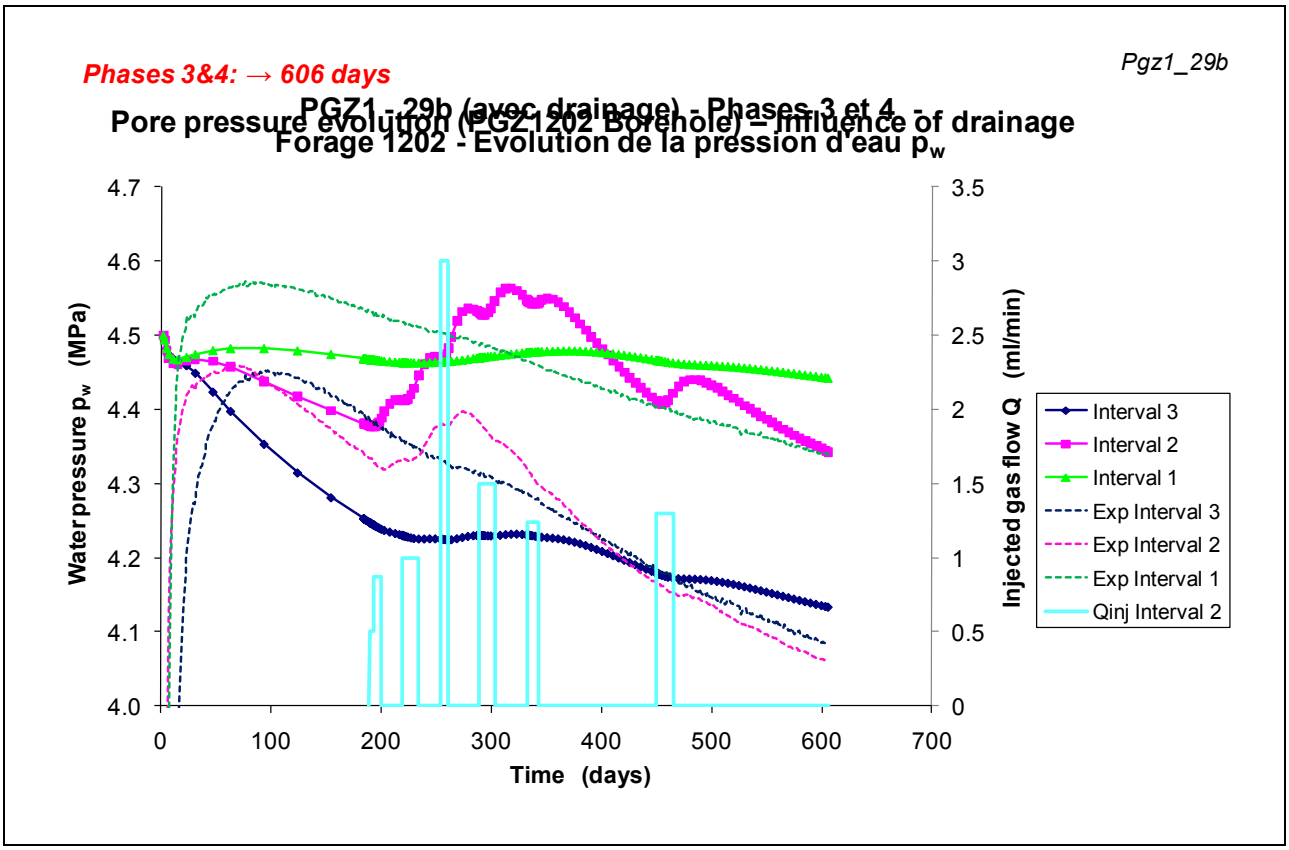

Figure 32 : Comparison of numerical and experimental pore pressure evolutions in the PGZ1202 borehole during the phases 3 and 4, with drainage effect of the PGZ1031 borehole.

6.5 Phase 3: waiting phase – influence of leakage in the injection chamber

To reproduce the experimental decrease in the interval 2 pore pressure curve which is observed in the phase 3, we can also numerically simulate a leakage in the injection chamber (interval 2). ***Figure 33*** present the experimental pore pressure evolution during the phase 3 and ***Figure 34*** present a comparison of numerical and experimental pore pressure evolutions during the phase 3, with leakage in the injection chamber linearly varying from 0 to 0.04 mm³/s at the end of the phase 3. That value of leakage was chosen to best fit the experimental curve in the interval 2. Of course, no effect is noted for the intervals 1 and 3.

Figure 35 and ***Figure 36*** compare, respectively in the PGZ1201 and PGZ1202 boreholes, the numerical and experimental pore pressure evolutions during the phases 3 and 4, with leakage in the injection chamber.

Figure 37 compares the numerical pore pressure evolutions during the phase 4, with and without leakage in the injection chamber. The case with leakage concerns then a constant leakage of 0.04 mm³/s during the phase 4. It clearly appears on ***Figure 37*** that leakage only affects very little the pore pressure curve during the phase 4.

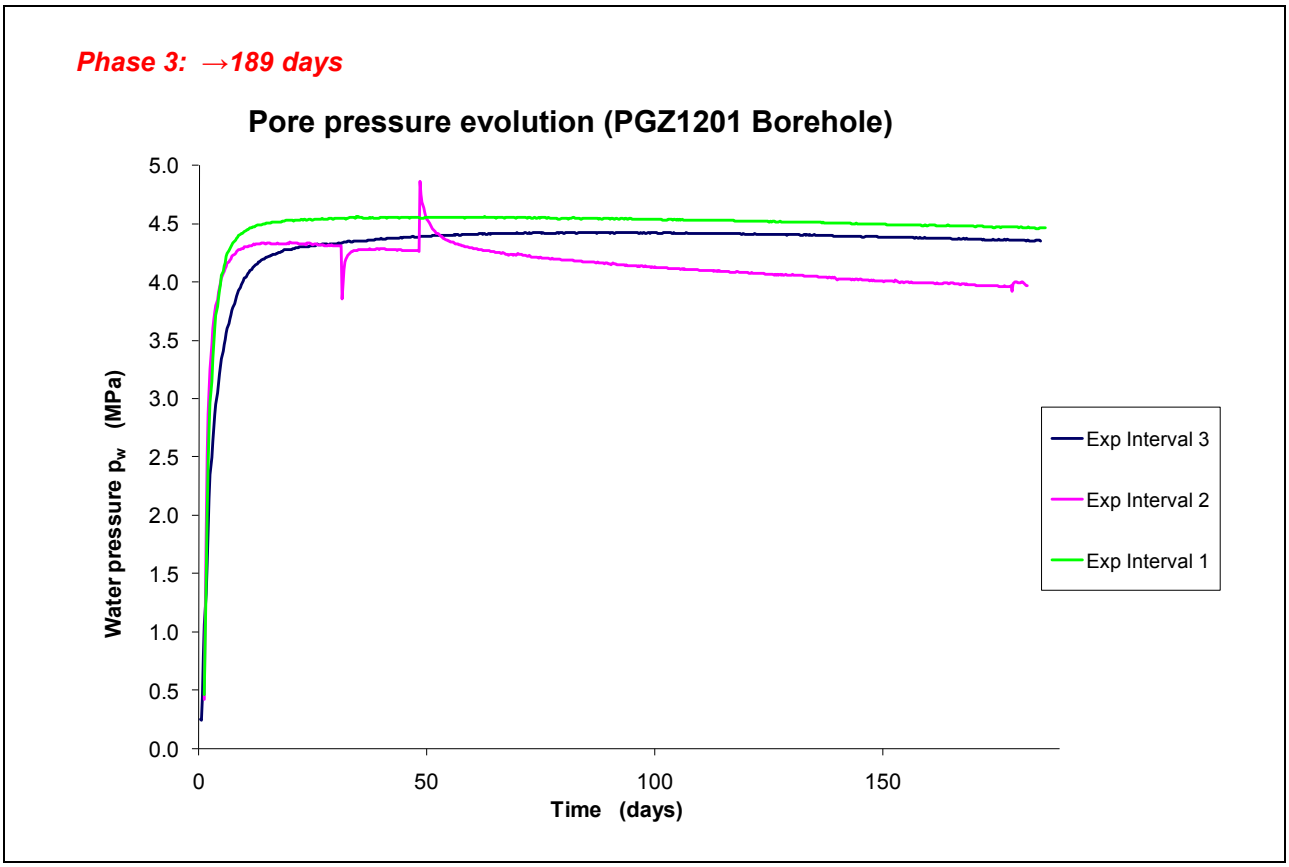

Figure 33 : Experimental pore pressure evolutions during the phase 3.

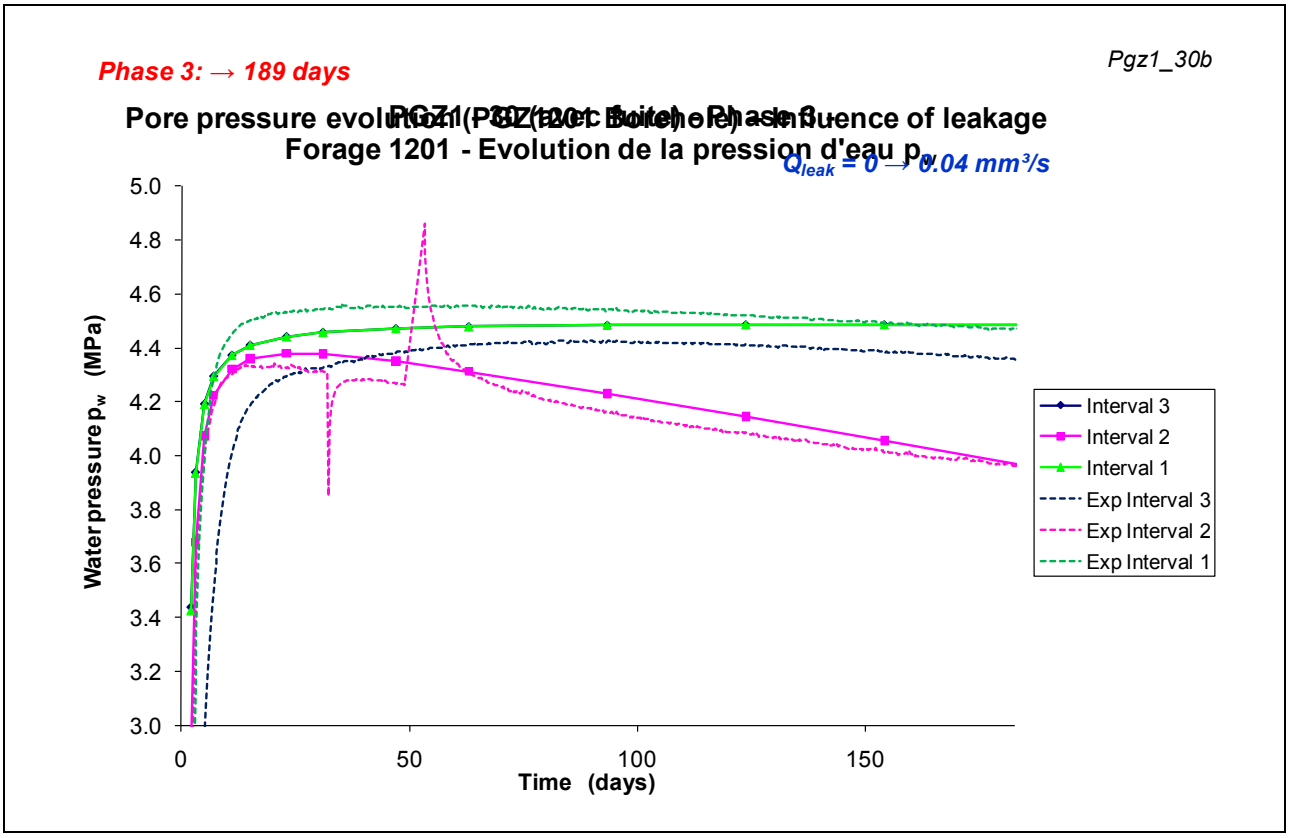

Figure 34 : Comparison of numerical and experimental pore pressure evolutions during the phase 3, with leakage in the injection chamber.

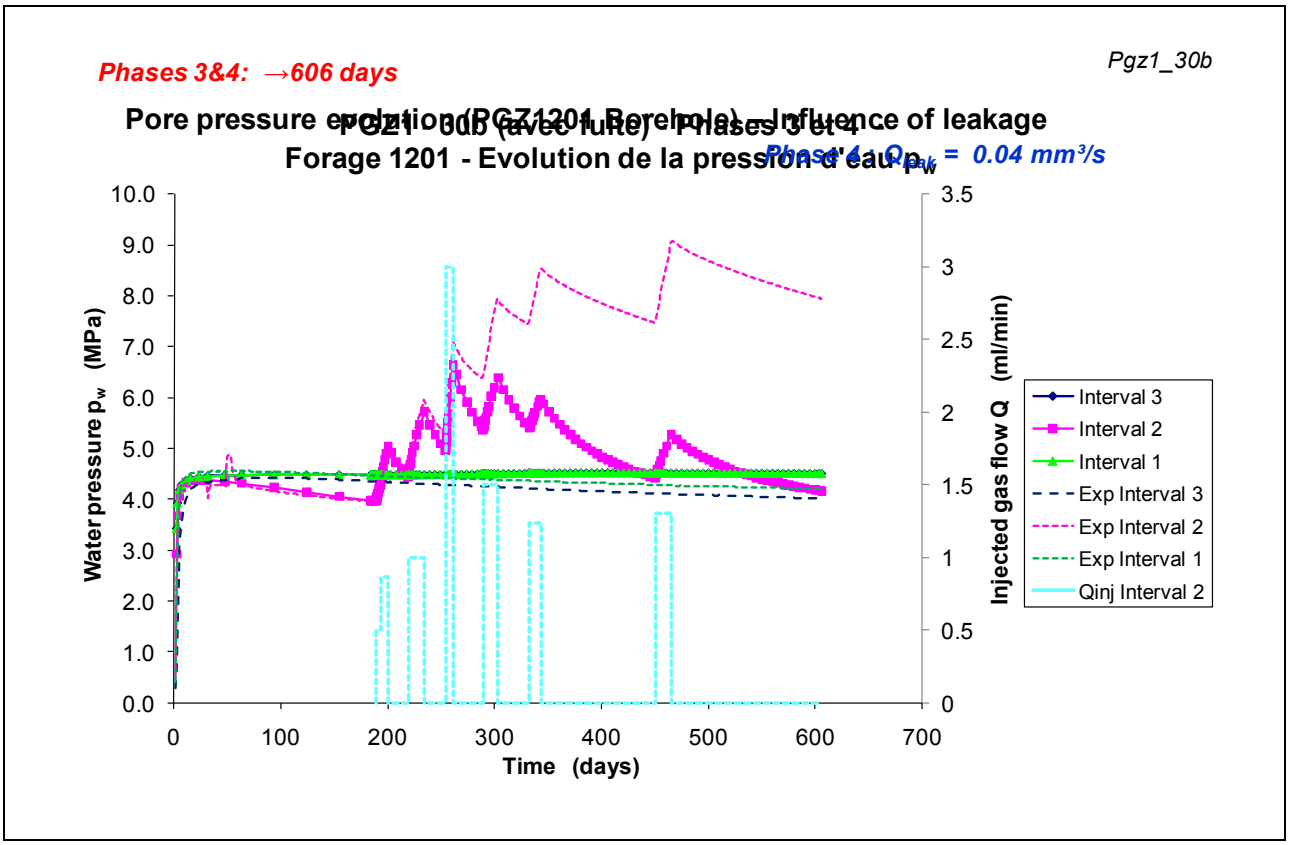

Figure 35 : Comparison of numerical and experimental pore pressure evolutions in the PGZ1201 borehole during the phases 3 and 4, with drainage leakage in the injection chamber.

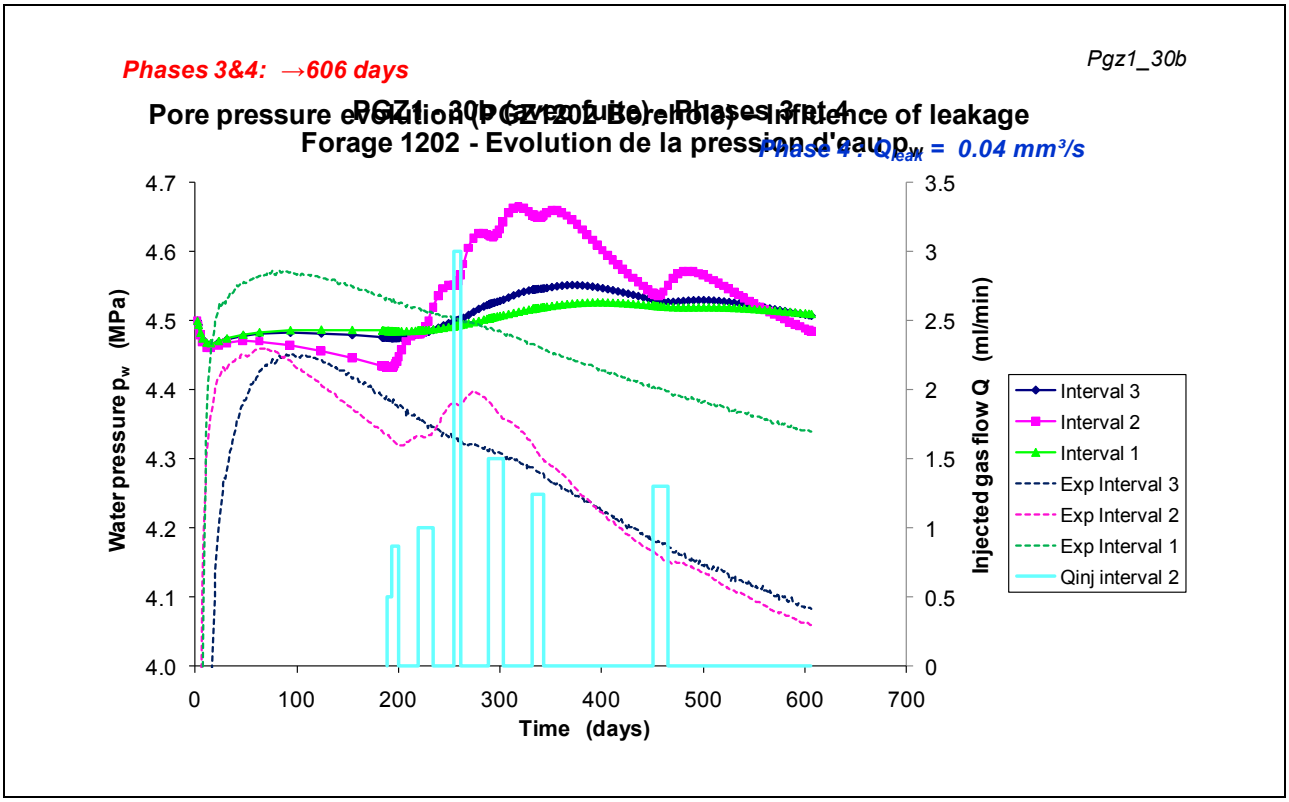

Figure 36 : Comparison of numerical and experimental pore pressure evolutions in the PGZ1202 borehole during the phases 3 and 4, with leakage in the injection chamber.

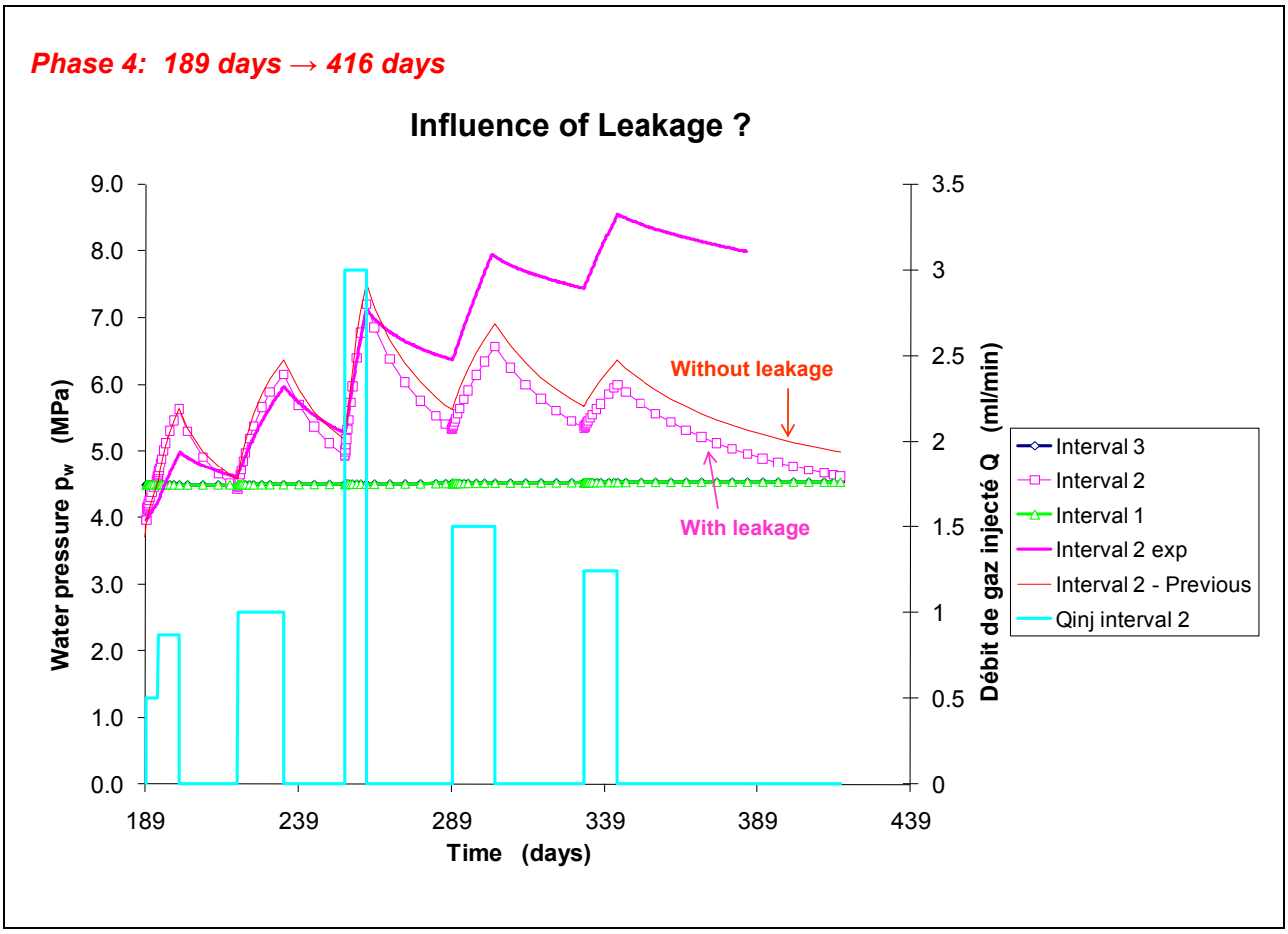

Figure 37 : Comparison of numerical pore pressure evolutions during the phase 4, with and without leakage in the injection chamber.

6.6 Phase 4: gas injection –decreasing of argillite permeability after 3rd peak

Choosing a good set of argillite permeability (4.10^{-20} m² horizontally and 1.33 10^{-20} m² vertically) and a value of the injection chamber compressibility of 3 10^{-8} Pa^{-1}, we showed that it is quite possible to reproduce the experimental evolution of the pore pressure until the end of the 3rd gas injection peak (***Figure 38***). Nevertheless it is possible to better reproduce the end of the injection experiment, brutally modifying from the end of the 3rd gas injection peak the argillite permeabilities in the whole mesh. ***Figure 39*** shows the results obtained with argillite permeabilities of 4.10^{-21} m² horizontally and 1.33 10^{-21} m² vertically from the 3rd peak, so 10 times lower values than permeabilities used for the beginning of the phase 4. That figure shows a good agreement between experimental and numerical results

Figure 40 and ***Figure 41*** compare, respectively for the case without and with modification of the argillite permeabilities after the 3rd peak, the numerical and experimental pore pressure evolutions in the PGZ1202 borehole during the phase 3 and 4. It clearly appears that, with the eventual modification of the argillite permeabilities, the corresponding numerical response in the PGZ1202 borehole is worse than that obtained before without permeabilities modification: after the 3rd peak there is no longer any peak noted in the numerical response of the interval 2 of the PGZ1202 borehole (***Figure 41***).

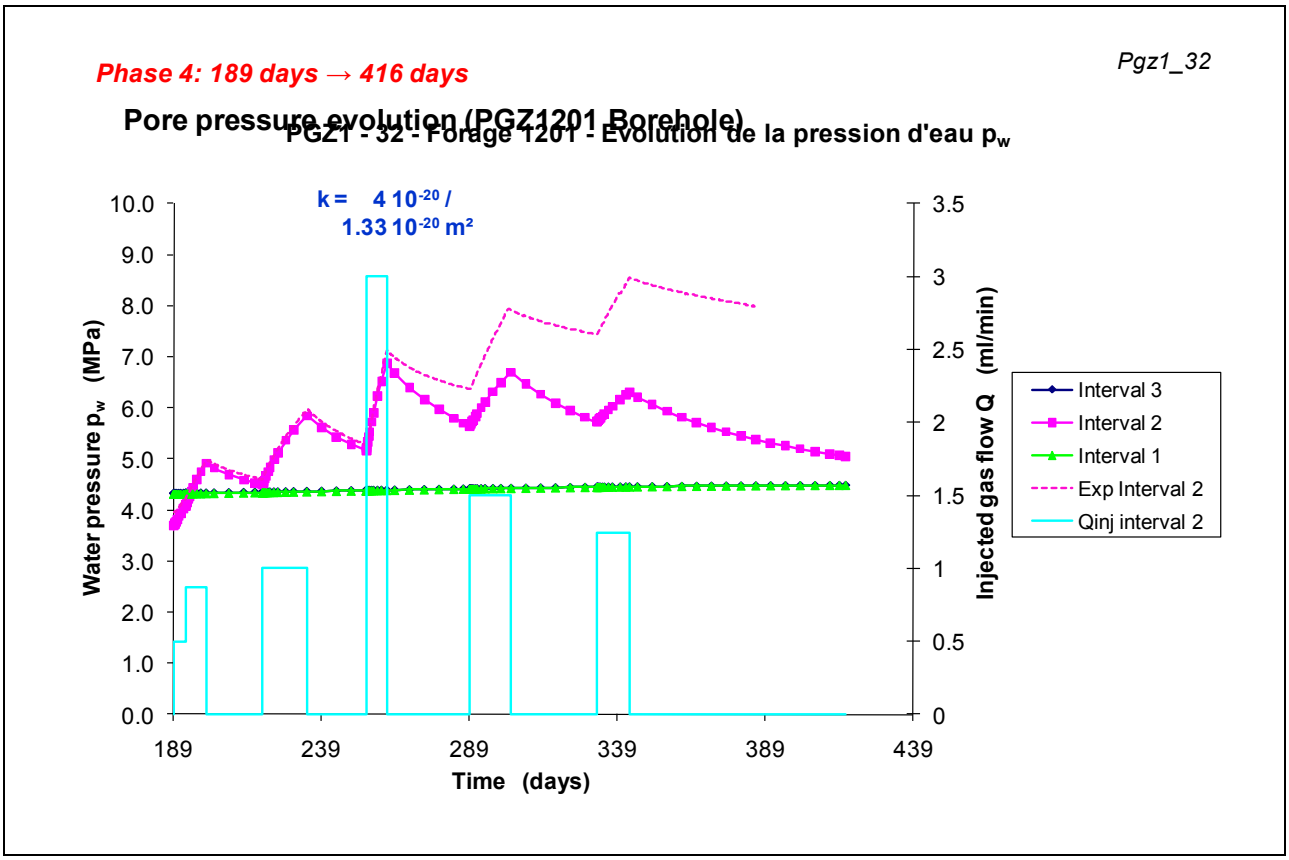

Figure 38 : Comparison between numerical and experimental water pressure evolutions in the PGZ1201 borehole during the beginning of the phase 4.

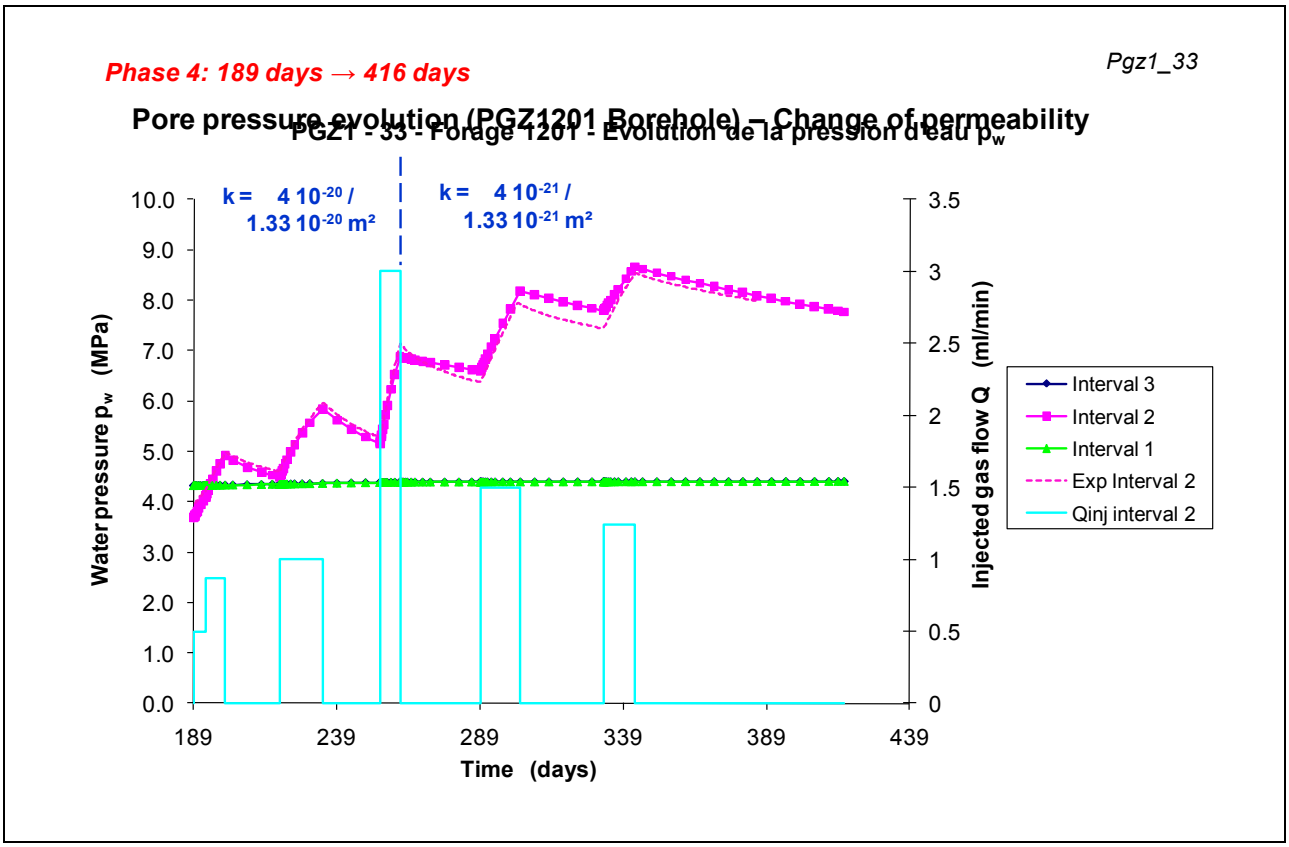

Figure 39 : Comparison between numerical and experimental water pressure evolutions in the PGZ1201 borehole during the phase 4, with modification of argillite permeabilities after 3rd peak.

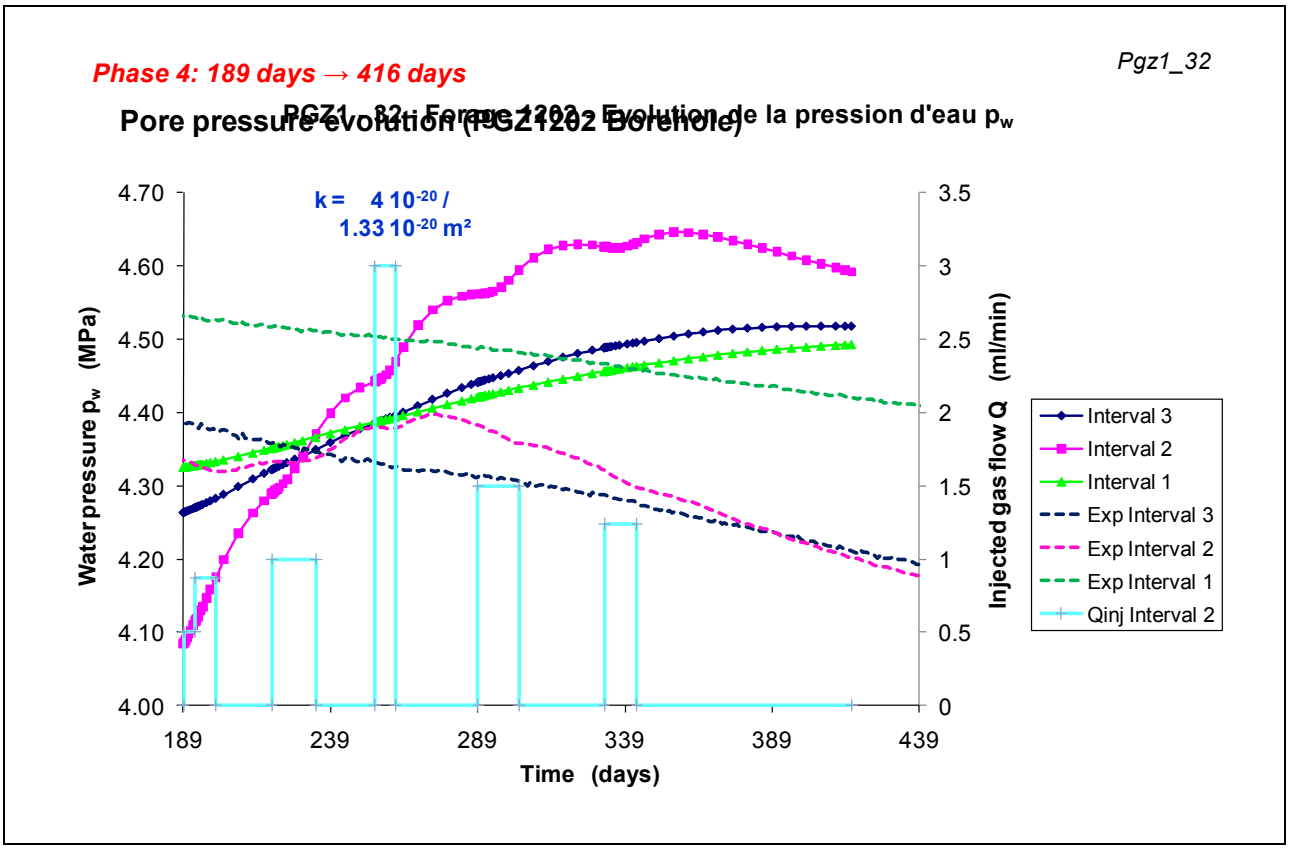

Figure 40 : Comparison between numerical and experimental water pressure evolutions in the PGZ1202 borehole during the beginning of the phase 4.

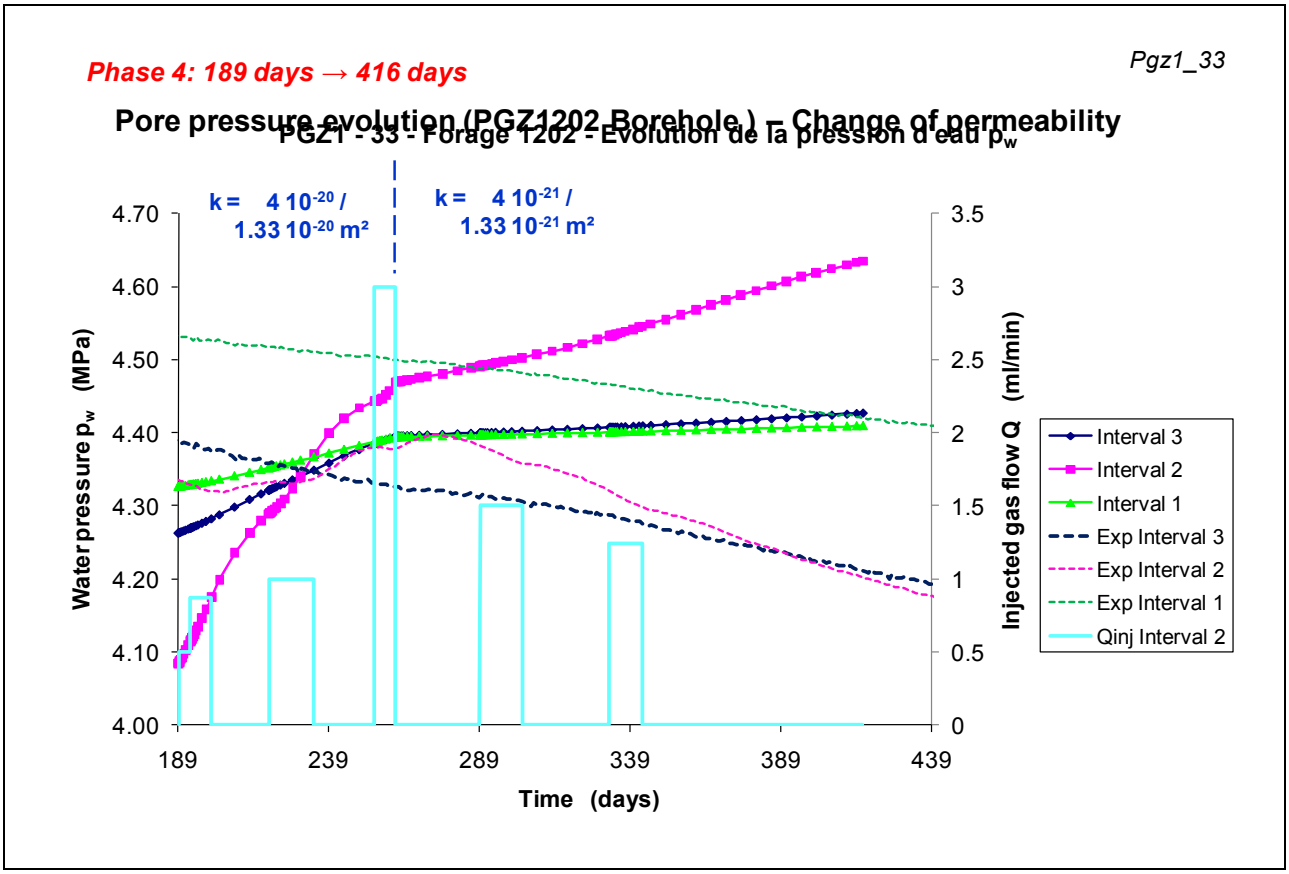

Figure 41 : Comparison between numerical and experimental water pressure evolutions in the PGZ1202 borehole during the phase 4, with modification of argillite permeabilities after 3rd peak.

6.7 Phase 4: gas injection – influence of unresined space betwwen packers

Another experimental hypothesis can also be tested numerically: the space between two packers might not be fully saturated and some fluxes can appear between the interval 2 and the unresined space, till the two volumes are at the same pressure (***Figure 42***).

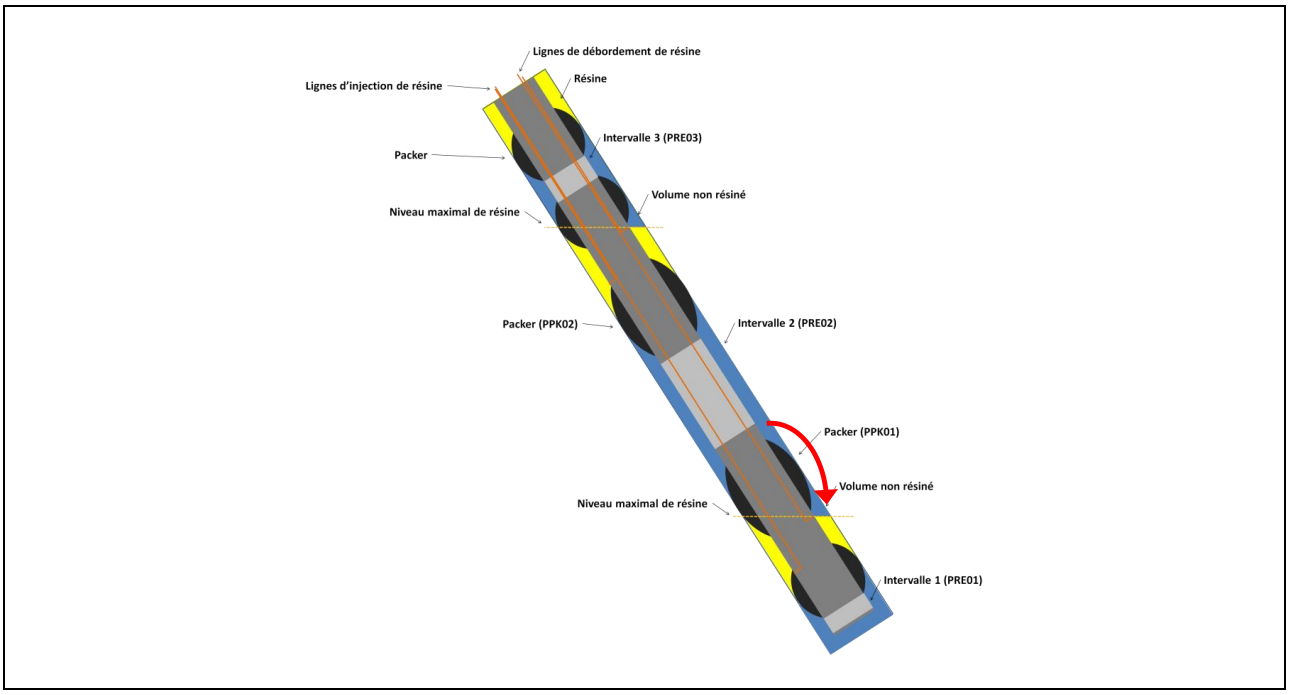

Figure 42 : Schematic view of the end of PGZ1201 borehole, with 3 intervals, packers and unresined volumes.

How can we model this possible effect, knowing that only the interval 2 is modelled? One may assume a "leakage" from the interval 2 which should depend on the pressure history within the interval. After gas injection 3, one may assume that the unresined volume is in equilibrium with the interval 2; so the "'leakage" is stopped.

Thus a modelling was performed with a set of argillite permeability low values (4.10^{-21} m² horizontally and 1.33 10^{-21} m² vertically) and a "leakage" growing from 0 to 0.004 mm³/sec during the phase 3 and equals to 0.08 mm/sec during the beginning of the phase 4.

The comparison of numerical and experimental pore pressure evolutions during the phase 3, with influence of unresined volume, is given on ***Figure 43***.

Figure 44 and ***Figure 45*** compare, respectively in the PGZ1201 and PGZ1202 boreholes, the numerical and experimental pore pressure evolutions during the phases 3 and 4, with a "leakage" due to the influence of unresined volume. It seems possible to improve the prediction for the PGZ1201 borehole, taking into account the effect of unresined volume and decreasing the permeability (***Figure 44***). However, the corresponding numerical response for the PGZ1202 is clearly worse than before (***Figure 45***).

For comparison, ***Figure 46*** shows the response of the pore pressure in the PGZ1201 borehole, with influence of unresined volume but with corresponding "leakage" no stopped after the 3rd peak.

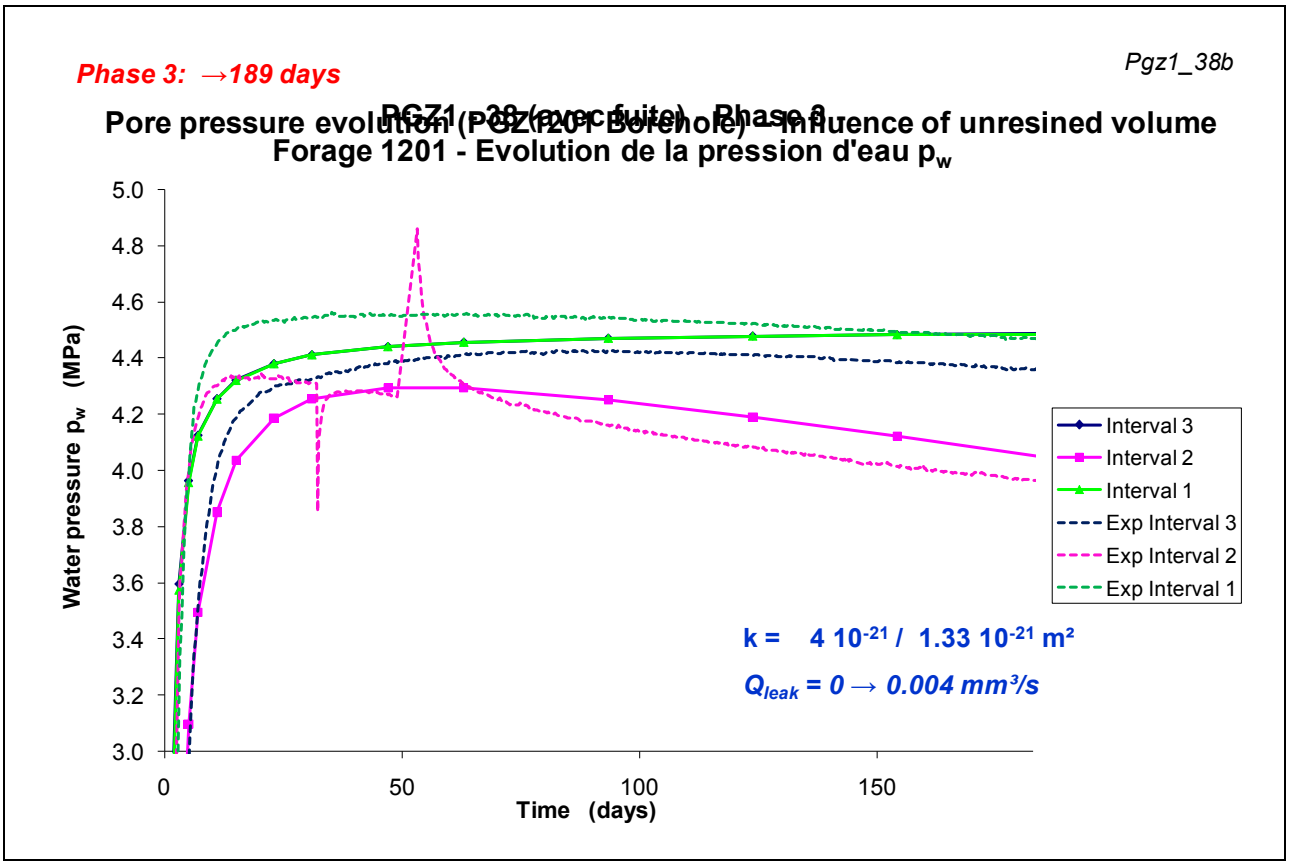

Figure 43 : Comparison of numerical and experimental pore pressure evolutions during the phase 3, with influence of unresined volume.

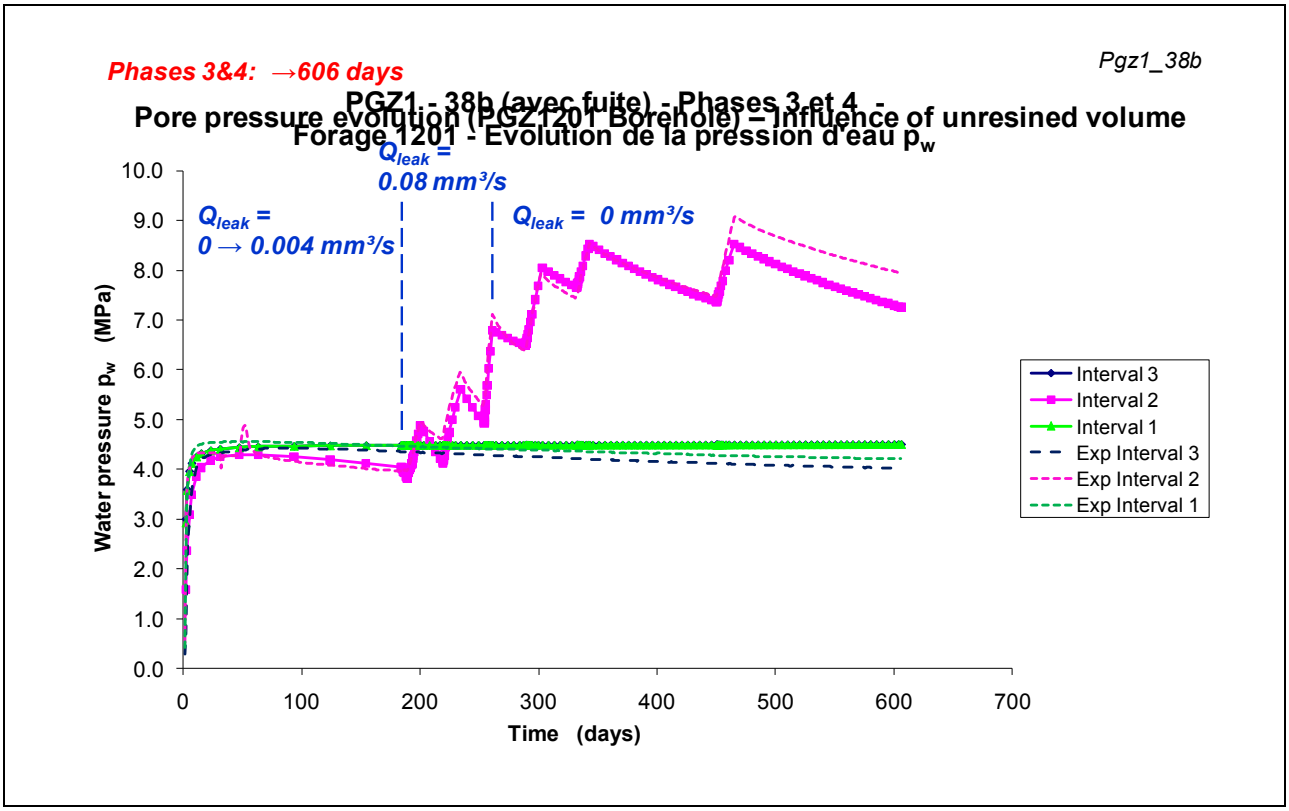

Figure 44 : Comparison of numerical and experimental pore pressure evolutions in the PGZ1201 borehole during the phases 3 and 4, with influence of unresined volume.

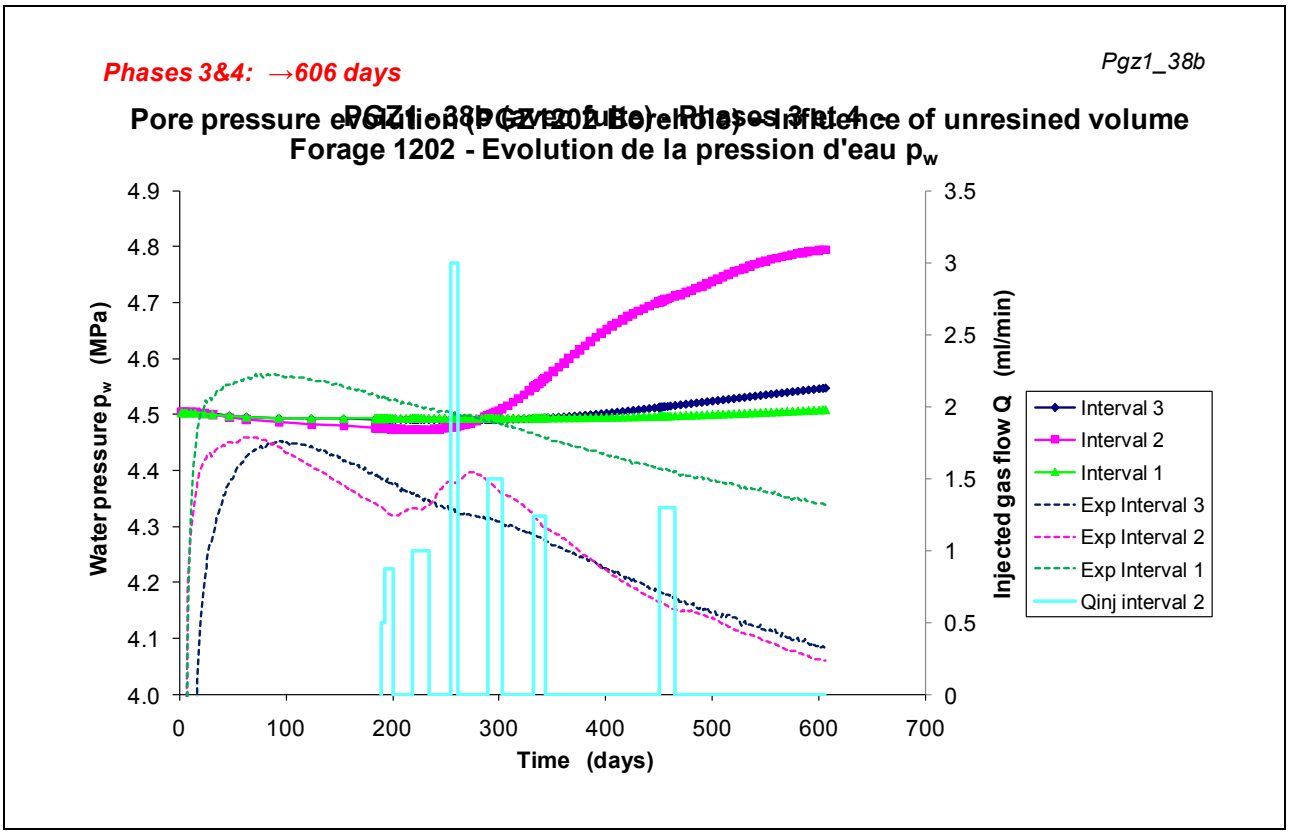

Figure 45 : Comparison of numerical and experimental pore pressure evolutions in the PGZ1202 borehole during the phases 3 and 4, with influence of unresined volume.

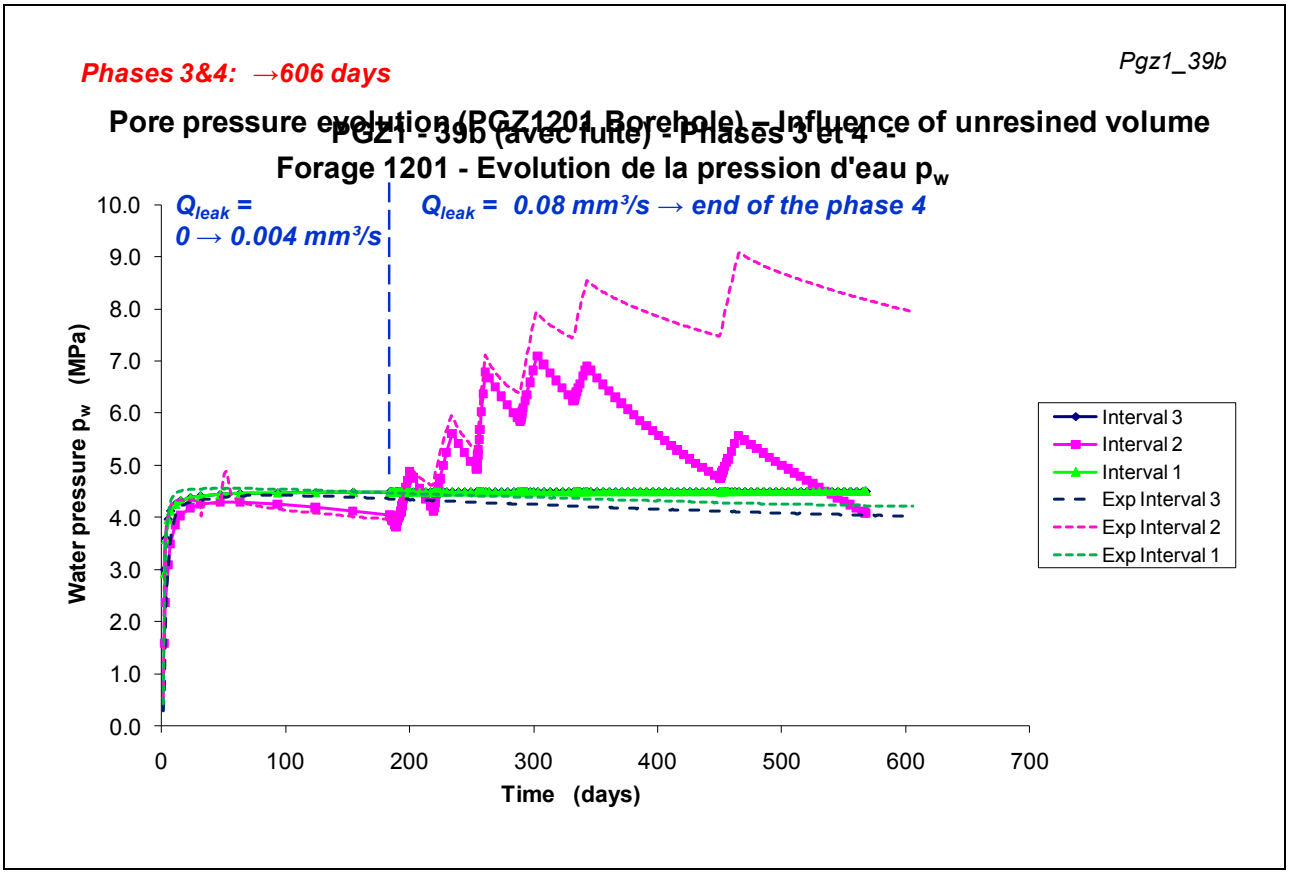

Figure 46 : Comparison of numerical and experimental pore pressure evolutions in the PGZ1201 borehole during the phases 3 and 4, with influence of unresined volume and with "leakage" no stopped after 3rd peak.

6.8 Phase 3: waiting phase – influence of PGZ1031 borehole drainage – new independent mesh

As already mentioned, taking into account the effect of drainage by PGZ1031 borehole was not really successful with the mesh considered so far. Therefore, to validate this drainage effect, a new three-dimensional mesh was created. It's now a revolution mesh around the PGZ1031 borehole axis.

For symmetry reasons, half a 3D mesh is used around the PGZ1031 borehole, inclined in x, y, z according the actual axis of the borehole. ***Figure 47*** presents the 3 plane views (x-y, y-z and z-x) and the perspective view of this mesh.

The mesh includes 70463 nodes for 65730 8-nodes brick elements. The total number of equation is 66247 (with 1 degree of freedom per node (p_w).

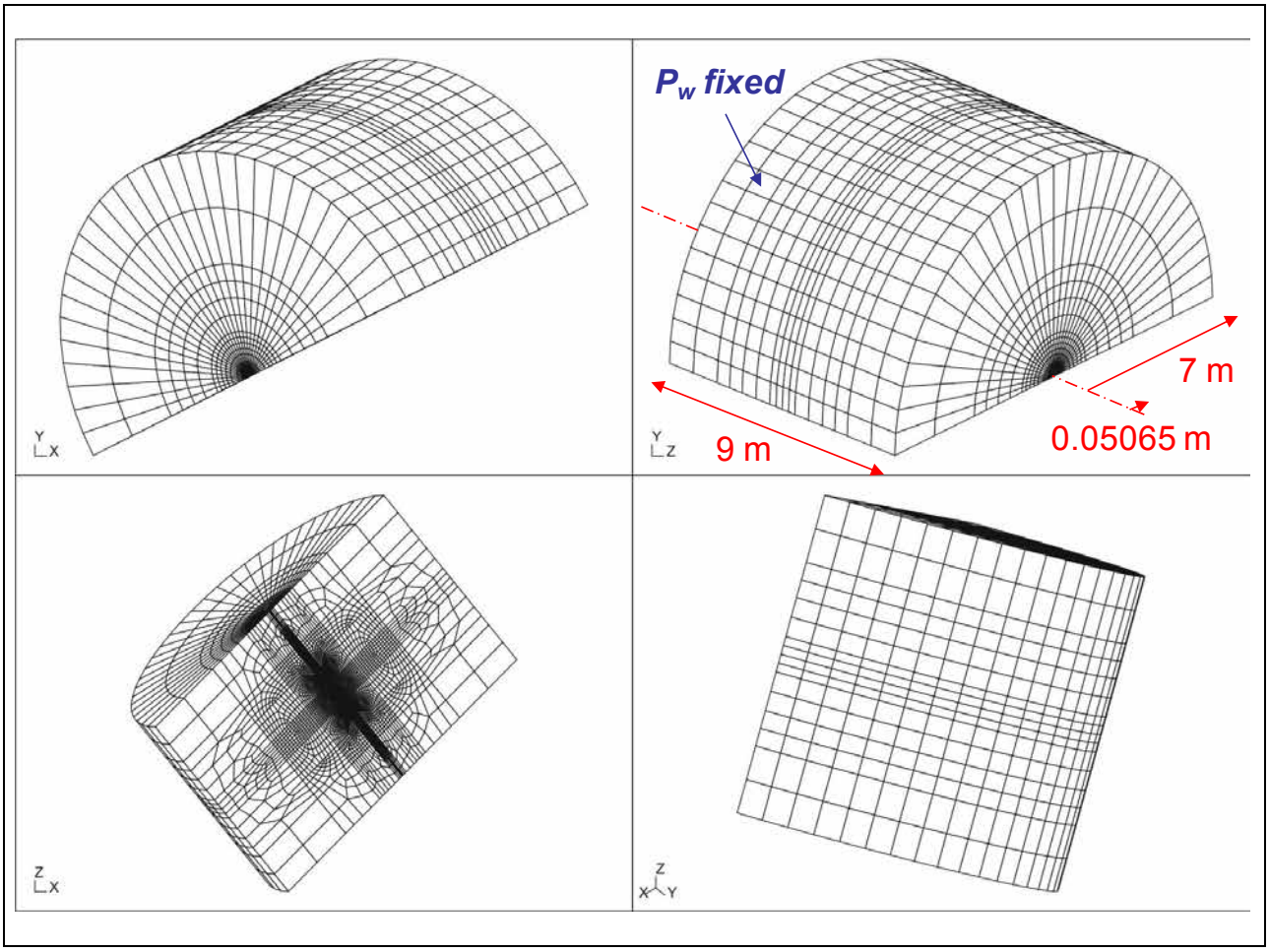

Figure 47 : Half a 3D mesh around the PGZ1031 borehole.

The extend of the mesh will be taken equal to 9 m longitudinally in the direction of the PGZ1031 borehole axis and 7 m radially from that borehole axis. The radius of the borehole is equal to 5.065 cm (***Figure 47***).

All the simulations presented hereafter are purely hydraulic. The water pore pressure p_w is fixed to its initial value (4.5 MPa) at the distant boundary. At the PGZ1031 borehole wall, this water pressure is reduced to 0.1 MPa in 1 hour and is kept constant after.

Drilling of PGZ1031 borehole took place on July 2 and 3 while drilling of PGZ1201 borehole was carried out on July 27 and 28. So there is a lag of 25 days that was considered in the simulations: compared to experimental measurements of PGZ1201 and PGZ1202 boreholes, drainage simulations of PGZ1031 borehole thus began 25 days earlier.

Figure 48 presents the 3 plane views (x-y, y-z and z-x) of the used mesh, with the locations of PGZ1201 and 1202 boreholes measurements intervals (I1, I2 and I3). Since the mesh used is only a half symmetrical 3D mesh, measurement points I1 of PGZ1201 and PGZ1202 boreholes are located outside the mesh (see ***Figure 48***, x-y plane). Therefore, these two measurement points I1 are replaced by their "symmetrical" I'1 (same z coordinate as I1 and located on the same line in x-y plane as PGZ1201 and PGZ1202 boreholes.

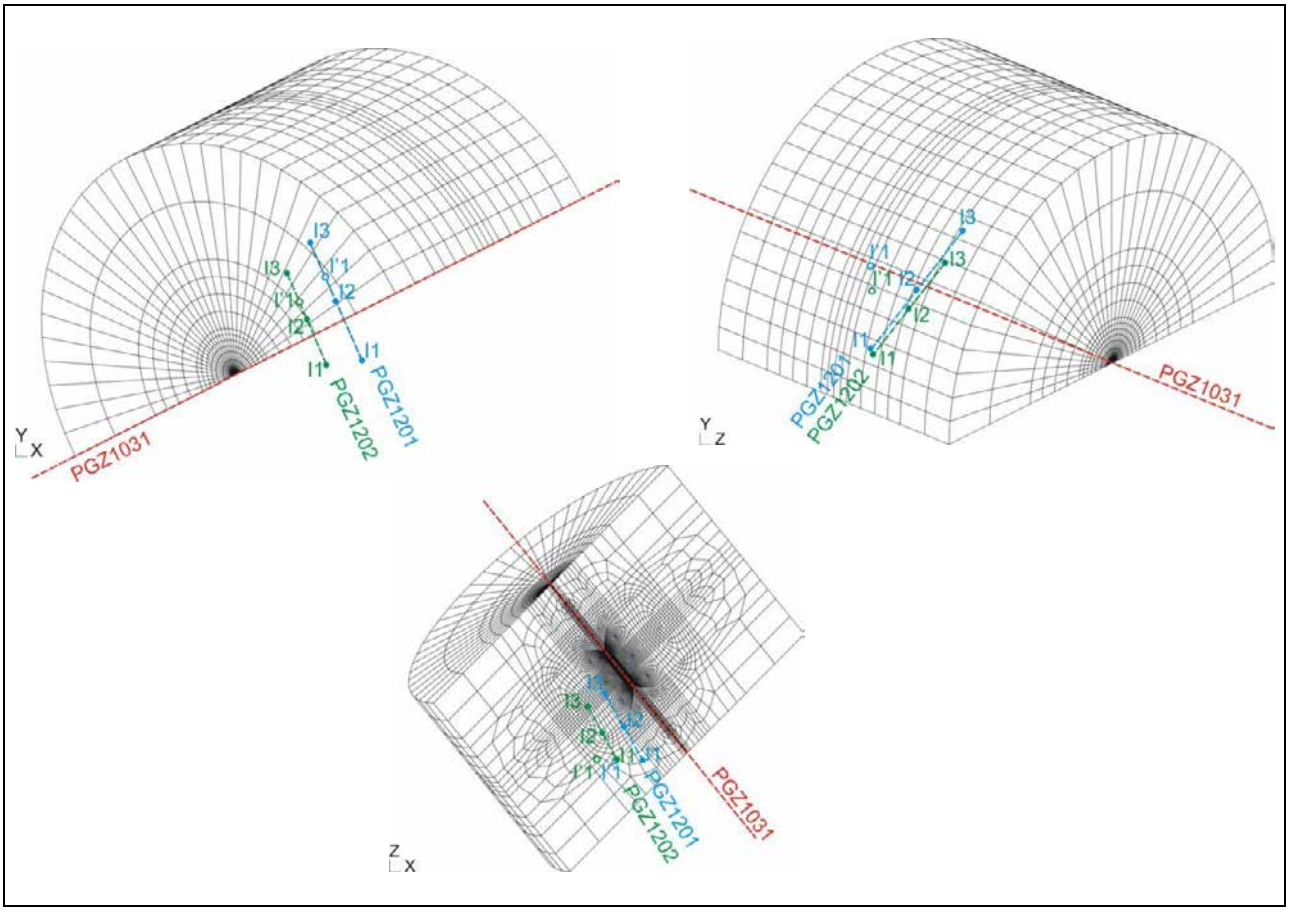

Figure 48 : Locations of PGZ1201 and PGZ1202 boreholes measurements intervals in the mesh around the PGZ1031 borehole.

Several simulations were carried out by changing the values of argillite intrinsic permeabilities:

- $K_{anisotropic} = 4\ 10^{-20}$ / $1.33\ 10^{-20}$ m²;
- $K_{anisotropic} = 4\ 10^{-21}$ / $1.33\ 10^{-21}$ m²;

- $K_{anisotropic} = 1\ 10^{-20} / 0.33\ 10^{-20}$ m²;
- $K_{isotropic} = 1\ 10^{-20}$ m².

Numerical results of this sensitivity study are respectively given on ***Figure 49*** and ***Figure 50*** for the PGZ1201 and PGZ1202 boreholes intervals. Comparisons with experimental measurements are also given on these figures. (Taking into account the dates of drilling, the range of PGZ1031 borehole numerical simulations is -25 to 189 days (so simulation of 214 days of drainage) and the range of PGZ1201 and PGZ1202 experimental measurements is 0 to 189 days.)

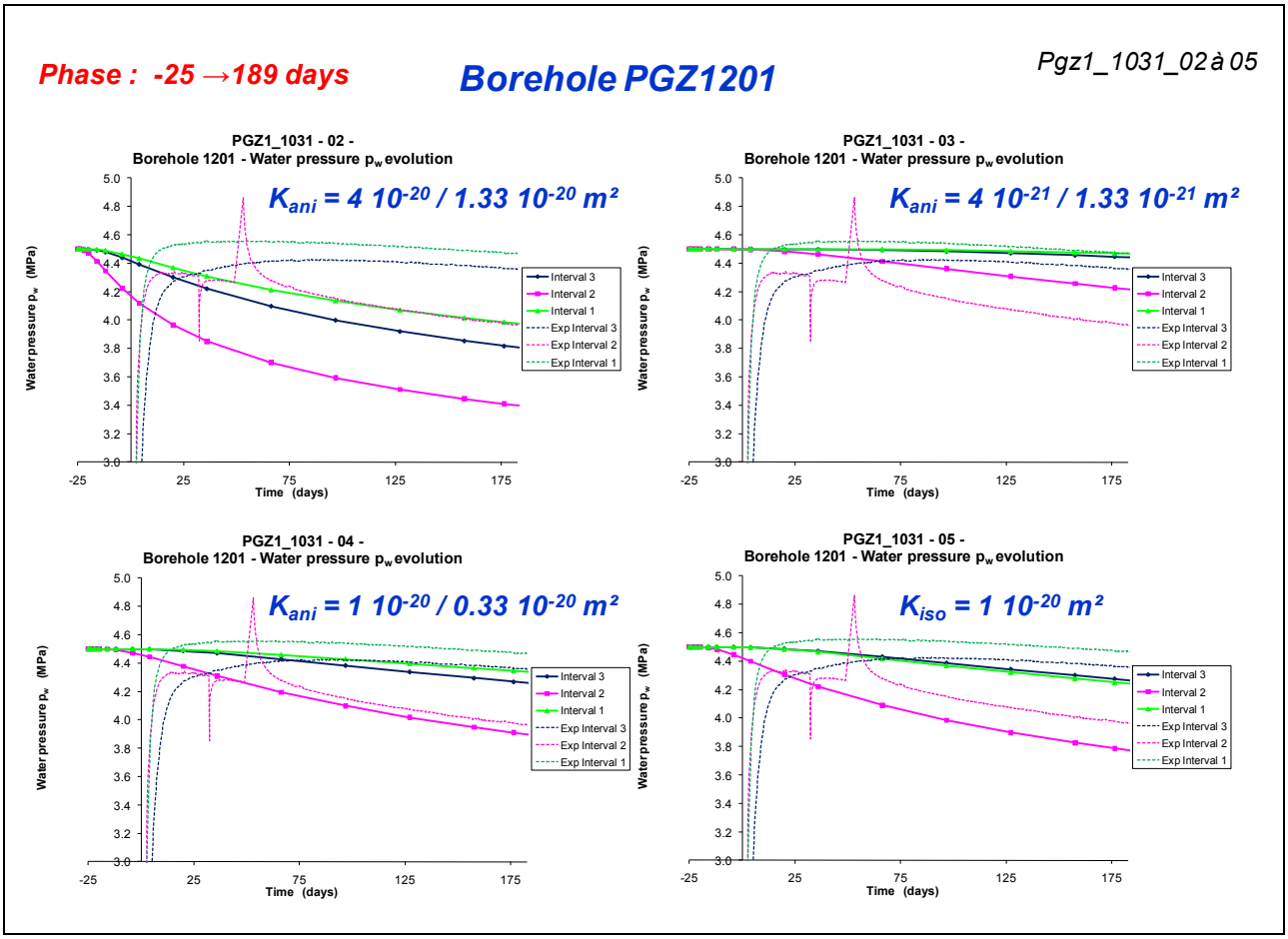

Figure 49 : Simulations of PGZ1031 borehole drainage - Numerical results of sensitivity study for PGZ1201 borehole intervals.

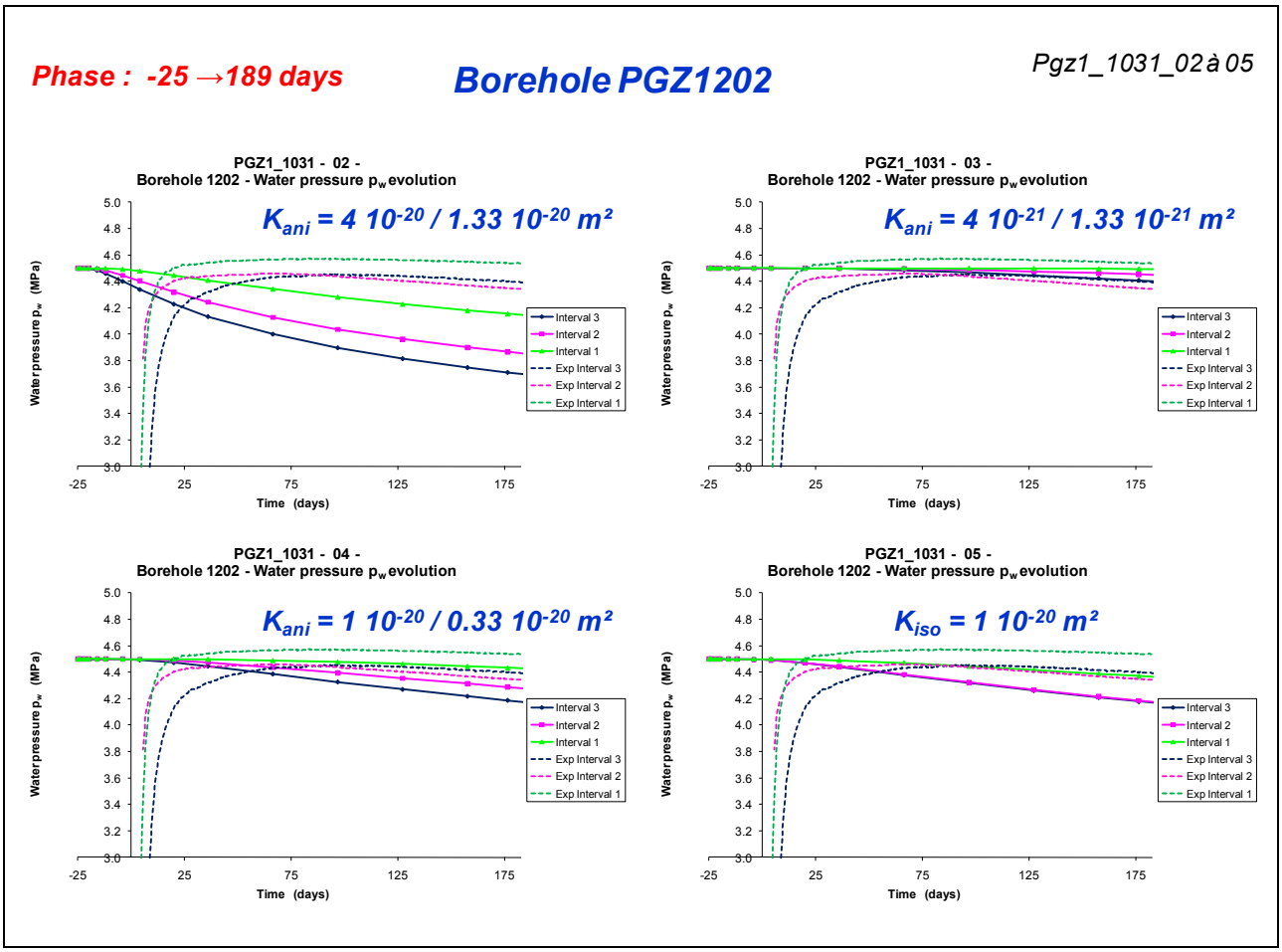

Figure 50 : Simulations of PGZ1031 borehole drainage - Numerical results of sensitivity study for PGZ1202 borehole intervals.

Finally ***Figure 51*** presents the best case fitted on experimental measurements. These results were obtained with argillite anisotropic intrinsic permeability $K_{anisotropic}$ values of 0.9 10^{-20} / 0.3 10^{-20} m². We can observe that the experimental curves of the intervals 1, 2 and 3 are now relatively correctly reproduced (the experimental and numerical decreasing slopes are similar), except perhaps for interval 3 of the PGZ1202 borehole where the numerical decreasing slope is greater than the experimental one.

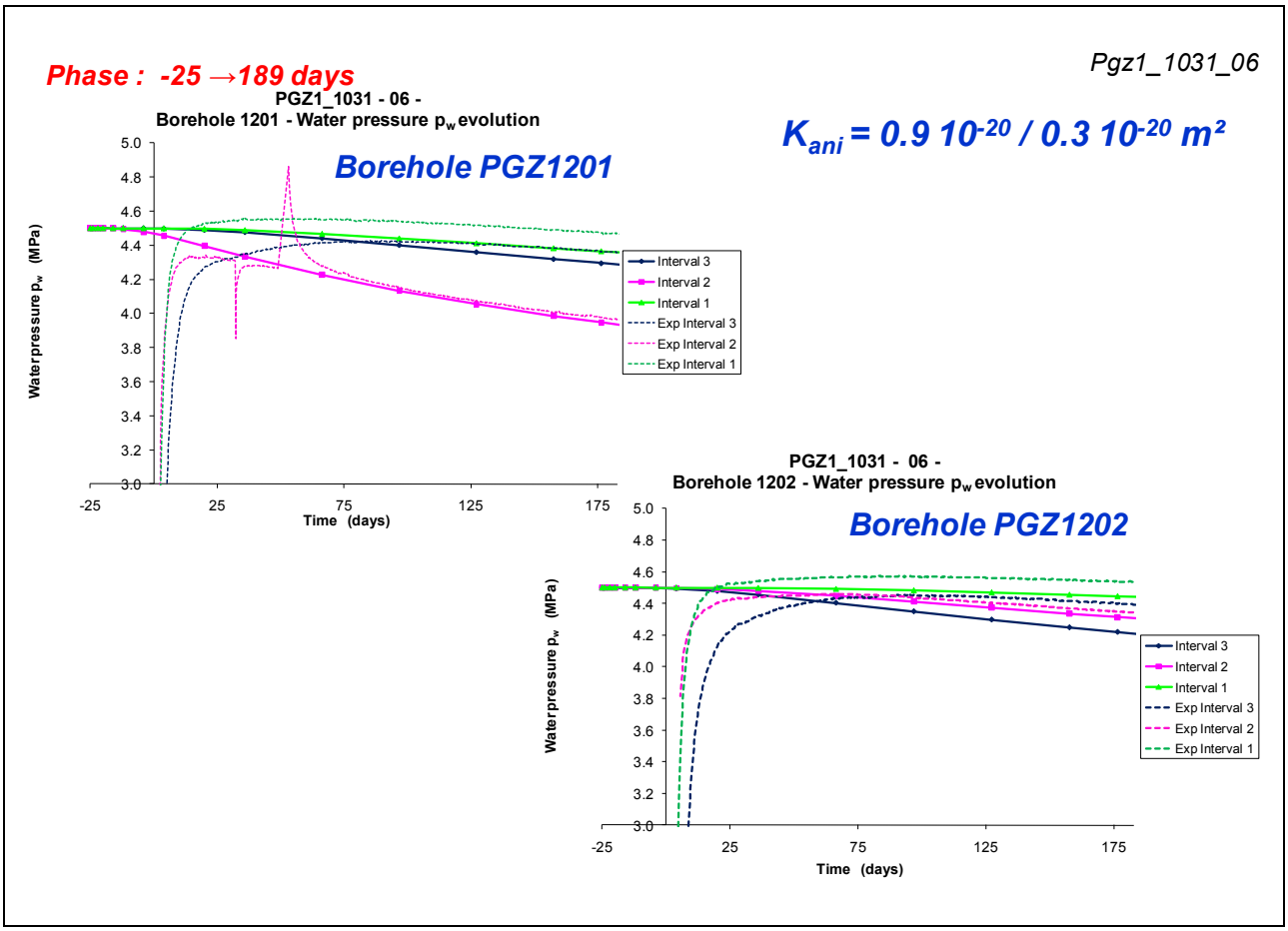

Figure 51 : Simulations of PGZ1031 borehole drainage - Numerical results of the fitted case for PGZ1201 and PGZ1202 borehole intervals.

6.9 Phase 4: gas injection – influence of EDZ

A new 3D simulation was performed taking into account of a EDZ. ***Figure 52*** shows a zoom of the used mesh perspective view, around the injection chamber.

The thickness of the EDZ is taken to 4 cm, with anisotropic permeabilities of 4 and 4/3 10^{-18} m² in front of the packers and with anisotropic permeabilities of 20 and 20/3 10^{-18} m² in front of the 3 intervals. Permeability of argillite is always equal to 4 and 4/3 10^{-20}.

Figure 53 presents the retention curves used for argillite (P_r=15MPa, n=1.49), EDZ in front of packers (P_r=8MPa, n=1.49) and EDZ in front of intervals (P_r=2MPa, n=1.49). The retention curve used for the injection chamber is now this with P_r=0,005MPa (***Figure 53***).

Only the injection gas phases ("phase 4") were simulated here, between 189 and 606 days, with, as initial conditions, a hydrostatic pressure p_w = 4 MPa in the whole model.

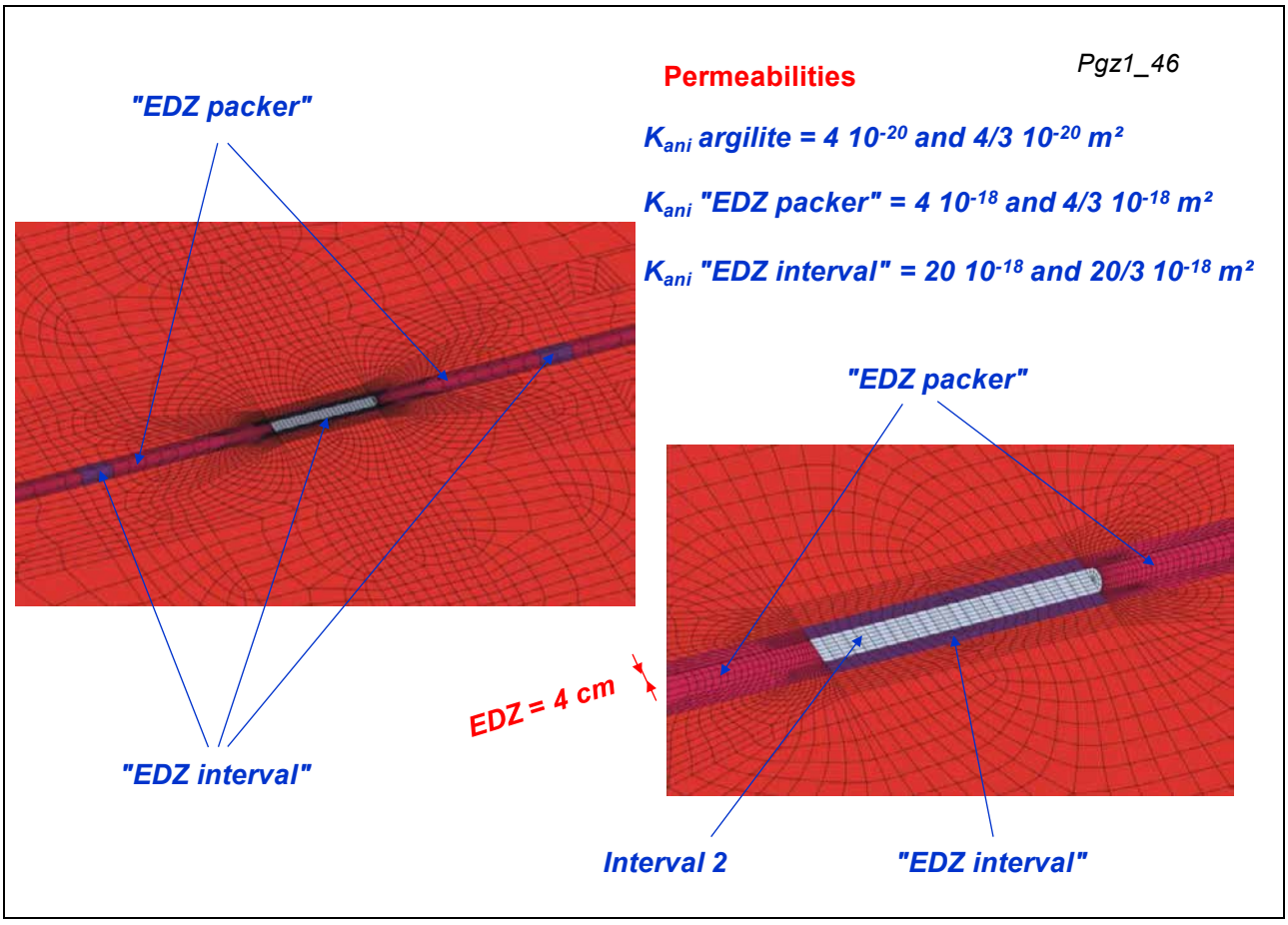

Figure 52 : Zoom on the EDZ in the perspective view around the injection chamber..

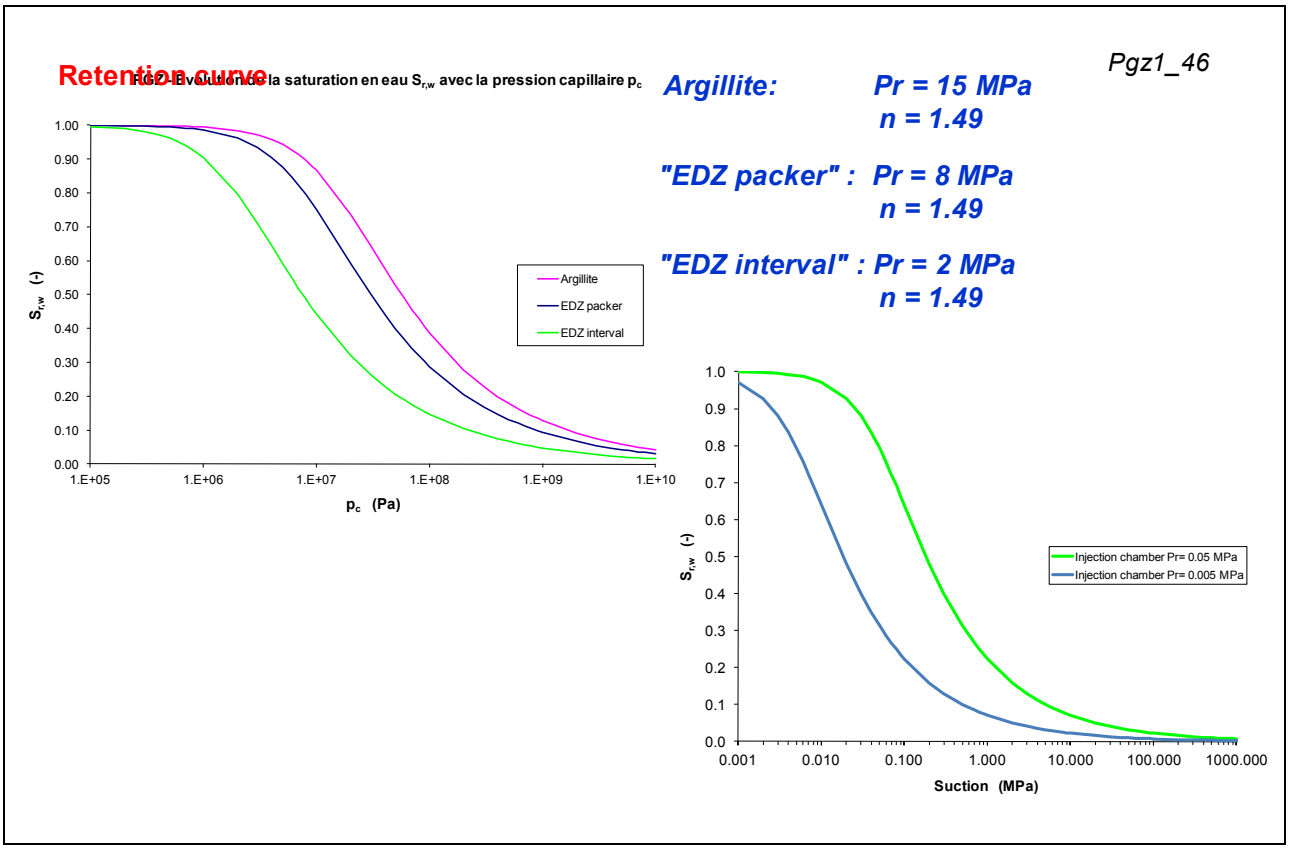

Figure 53 : Retention curves used for EDZ, argillite and injection chamber.

Figure 54 compares the numerical results of the phase 4 only, obtained with and without EDZ, for PGZ1201 and PGZ1202 borehole intervals. These results are also compared with the experimental data. It appears here that the prediction is lower with EDZ compared to the case with EDZ.

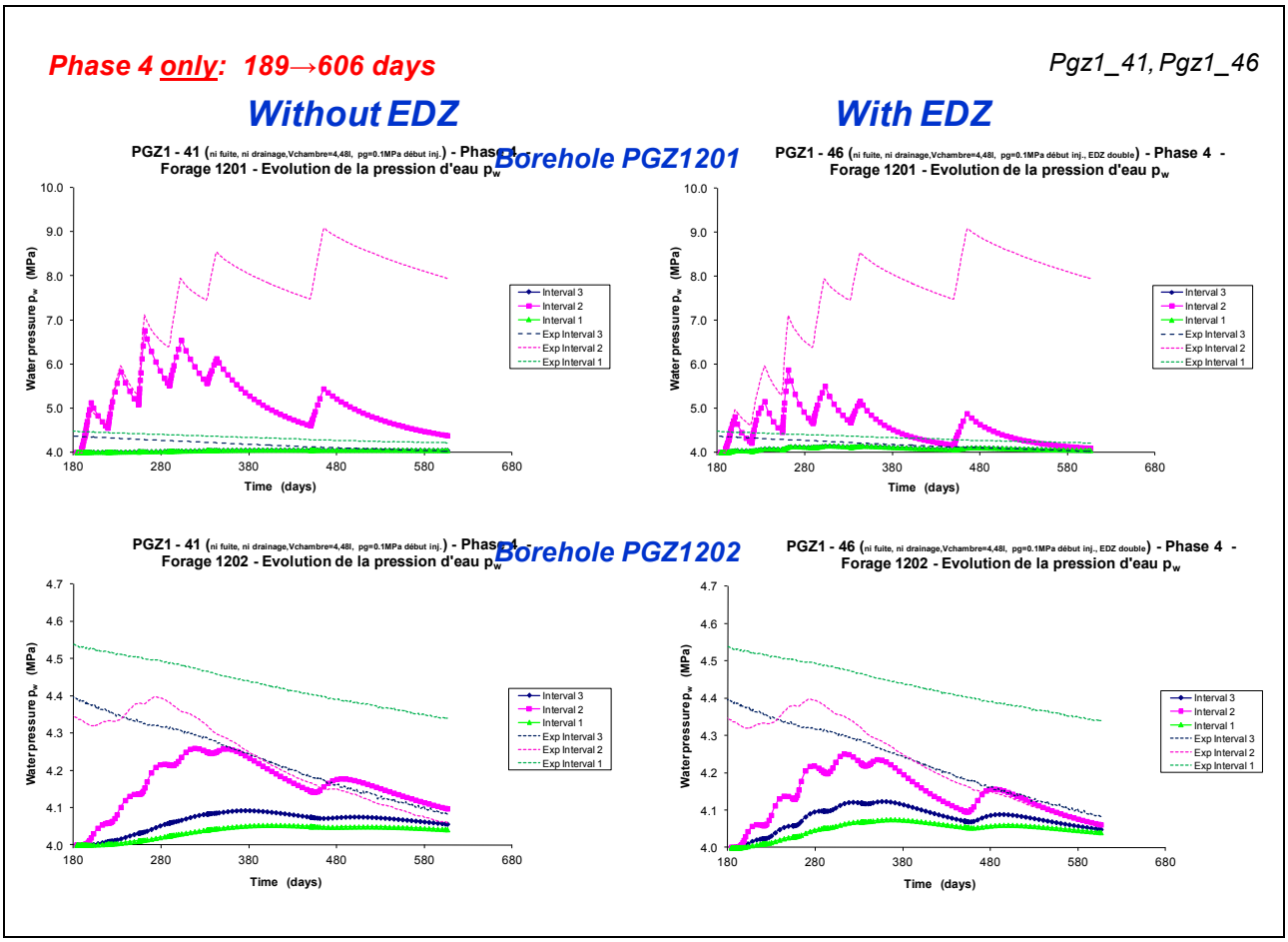

Figure 54 : Numerical results of the phase 4 only, for PGZ1201 and PGZ1202 borehole intervals, with and without EDZ, and comparison with experimental data.

Slopes due to drainage by PGZ1031 borehole can be estimated on experimental data. Different slopes, obtained on ***Figure 55***, are for PGZ1201 borehole: -6.164 10^{-4} MPa/day (interval 1, measured between 184 and 606 days), -2.356 10^{-3} MPa/day (interval 2, measured between 80 and 184 days) and -8.002 10^{-4} MPa/day (interval 3, measured between 184 and 606 days). For PGZ1202 borehole, the obtained slopes are: -4.777 10^{-4} MPa/day (interval 1, measured between 120 and 200 days), -1.092 10^{-3} MPa/day (interval 2, measured between 80 and 184 days) and -8.754 10^{-4} MPa/day (interval 3, measured between 120 and 200 days).

If it does not take into account the drainage effect in the simulations and knowing theses slopes, it is thus possible to correct the experimental data by removing the decreasing linear pressure trend, due to PGZ1031 borehole drainage.

Figure 56 compares now the numerical results, obtained with and without EDZ and for PGZ1201 and PGZ1202 borehole intervals with the corrected experimental data.

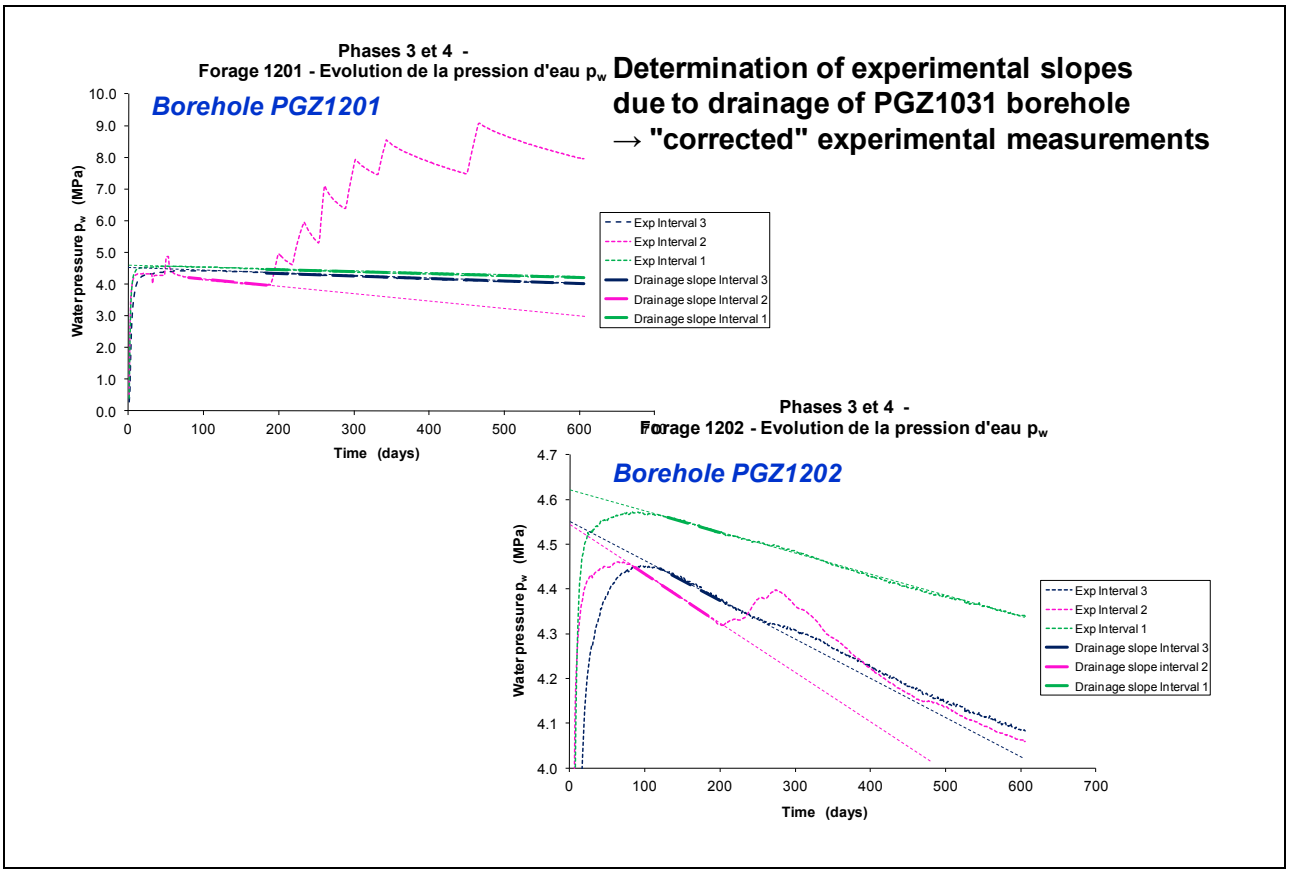

Figure 55 : Determination of experimental slopes due to drainage of PGZ1031 borehole.

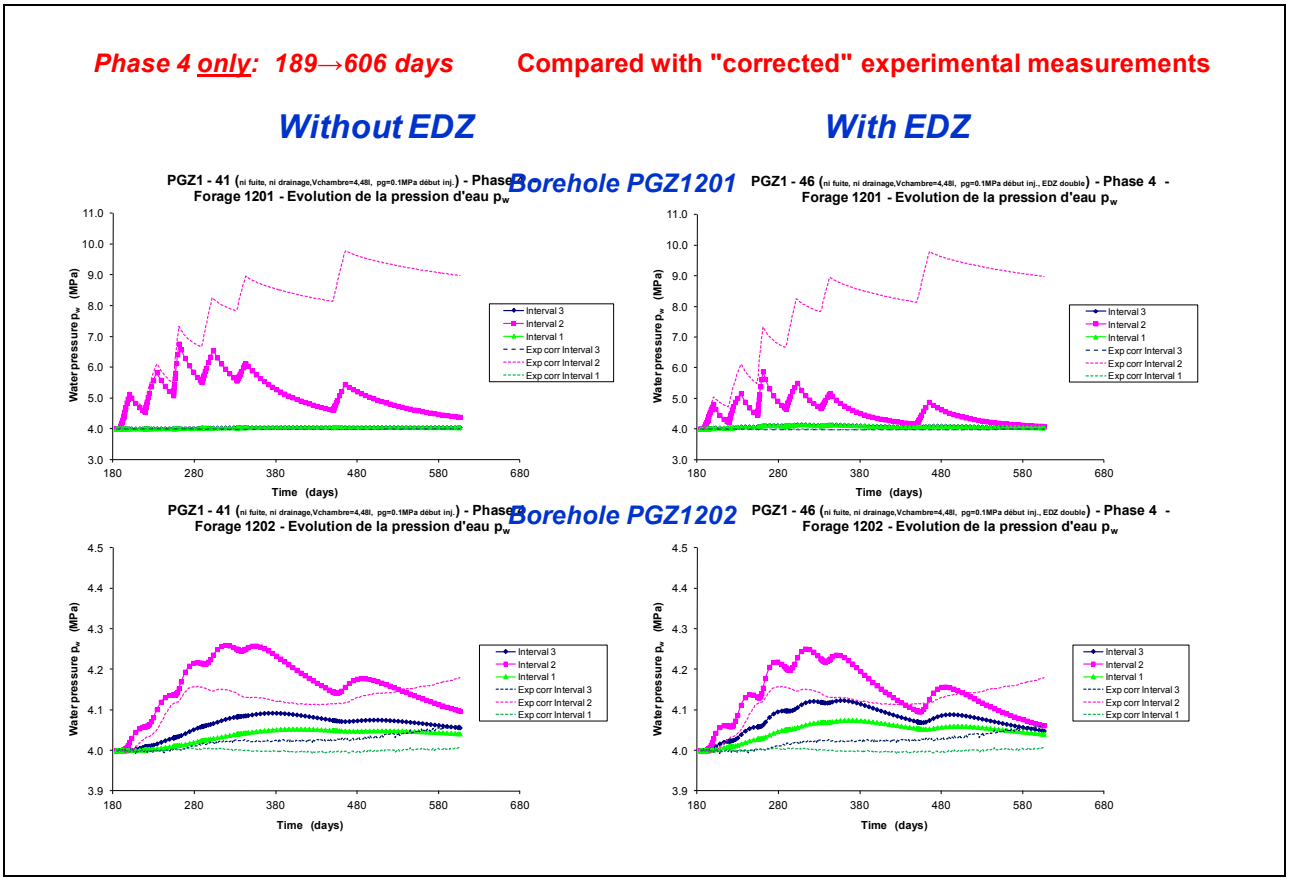

Figure 56 : Numerical results of the phase 4 only, for PGZ1201 and PGZ1202 borehole intervals, with and without EDZ, and comparison with corrected experimental data.

7 DISCRETISATION, INITIAL AND BOUNDARY CONDITIONS OF THE 1D SIMULATIONS (SET 1)

7.1 Meshing, initial and boundary conditions

In order to better understand the influence of initial conditions present in the injection chamber and the hydraulic parameters characterizing the EDZ, several one-dimensional axisymmetric simulations were performed always with the non linear finite elements code LAGAMINE. The purpose of these simulations are, with a very simple grid, to try to best reproduce the experimental measurements for PGZ1201 borehole and especially the measurements after the third injection peak gas.

Figure 57 shows the scheme of the one-dimensional axisymmetric grid. The water pressure p_w and the gaz pressure p_g are fixed at the far boundary (x=5m). The injection chamber is modelled (from 0 to 3.8 cm) by 5 elements Q8. The EDZ is meshed (from 3.8 to 7.8 cm) by 100 elements Q8, and the argillite is modelled (from 7.8 to 500 cm) by 140 elements Q8

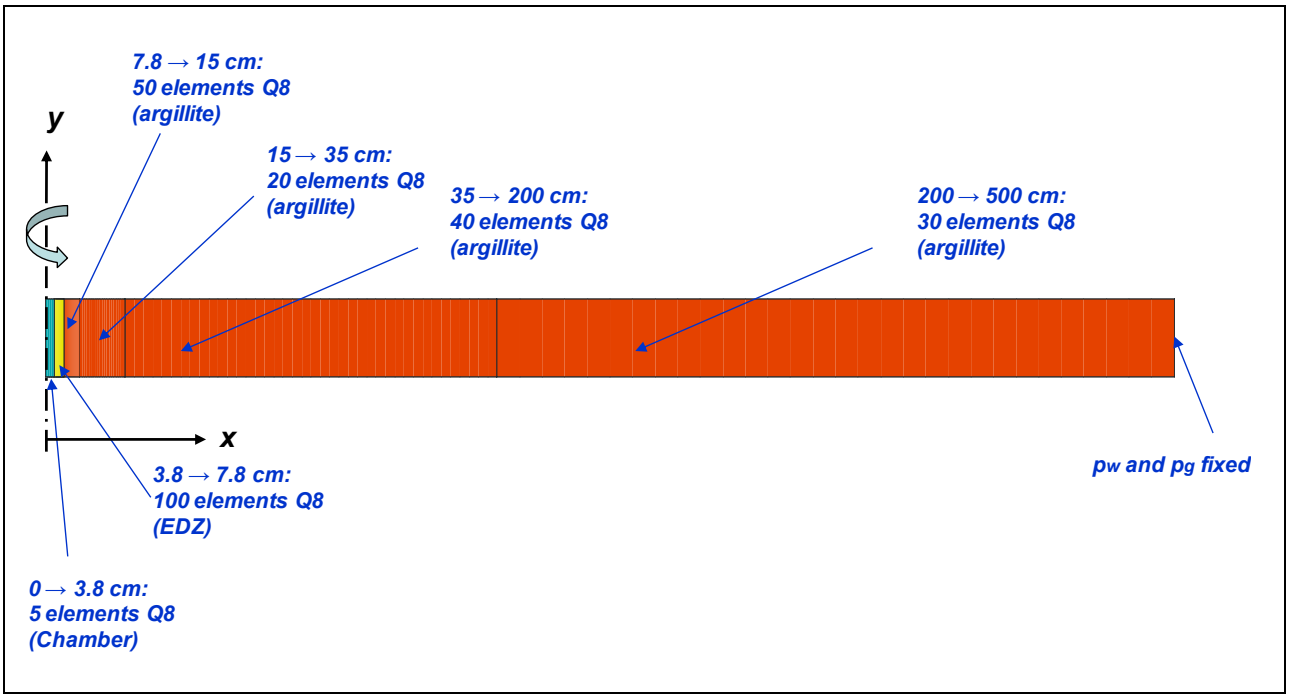

Figure 57 : Scheme of the grid and boundary conditions for the 1D simulations.

Only the injection gas phases ("phase 4") were simulated here, between 189 and 606 days, with, as initial conditions, a hydrostatic pressure p_w = 4 MPa in the whole model.

7.2 Considered cases (set 1)

Table 5 presents the different cases (set 1) and some parameters which were considered and modified in the one-dimensional modelling. All the other parameters values remain similar to

those defined previously in Table 1 to Table 4 (The value of Van Genuchten's parameter P_r for the chamber is however taken to 0.005 MPa). For each case, we note in bold the parameters values which were modified compared to the previous case.

	Chamber			Argillite	EDZ			
Case number	Initial saturation $S_{r,w}$ (-)	Volume V (l)	Compressibility $1/\chi_w$ (Pa^{-1})	Gas permeability mult. coeff. A (-)	Intrinsic permeability k (m²)	Van Genuchten's parameter P_r (MPa)	Van Genuchten's coefficient n (-)	Gas permeability mult. coeff. A (-)
1	1	**4.536**	$3\ 10^{-8}$	250	-	-	-	-
2	1	**1.040**	$3\ 10^{-8}$	250	-	-	-	-
3	1	1.040	**$2\ 10^{-7}$**	250	-	-	-	-
5	**0.221**	1.040	$3\ 10^{-8}$	250	-	-	-	-
6	0.221	1.040	**$5\ 10^{-10}$**	250	-	-	-	-
7	0.221	1.040	$5\ 10^{-10}$	**50**	-	-	-	-
8	0.221	1.040	$5\ 10^{-10}$	**1250**	-	-	-	-
9	0.221	1.040	$5\ 10^{-10}$	250	**$2\ 10^{-17}$**	**2**	**1.49**	250
10	0.221	1.040	$5\ 10^{-10}$	250	**$2\ 10^{-19}$**	2	1.49	250
11	0.221	1.040	$5\ 10^{-10}$	250	**$2\ 10^{-17}$**	**4.5**	**1.60**	250
13	0.221	1.040	$5\ 10^{-10}$	**1**	$2\ 10^{-17}$	4.5	1.60	250

Table 5: Considered cases for the 1D simulations (set 1).

8 1D NUMERICAL RESULTS (SET 1) AND COMPARISONS WITH IN-SITU MEASUREMENTS

Figure 58 presents, for the case 1 defined in Table 5, the time evolution of the water and gas pressures in the injection chamber and in the argillite close to the chamber. The experimental measurements and the corrected (by removing the linear pressure tend, decrease due to PGZ1031 borehole drainage, cfr ***Figure 55***) experimental measurements are also given on that figure. We note that the evolutions of gas and water pressure are clearly identical.

For this case, the volume of the chamber equals to $\pi.R^2.L = \pi\ 0.038^2\ 1000 = 4.356\ l$. The compressibility of the chamber is taken to 3.10^{-8} Pa^{-1} and its initial water saturation equals to 1. EDZ is not taken into account. The isotropic argillite permeability is taken to $4\ 10^{-20}$ m².

This case is to compare to the 3D case presented previously on ***Figure 54*** and ***Figure 56*** (without EDZ, borehole 1201). The results obtained in 3D and in 1D are clearly similar.

Figure 59 presents the time evolution of gas saturation: in the chamber the gas saturation varies from 0 to 0.63 and in the argillite, close to the chamber, it remains equals to 0 during all the simulation. On the space evolution of water saturation it appears that all the argillite remains saturated during all the gas injection phase. The space evolution of gas flows shows that these flows are only dissolved and there is no observed gaseous flow. Finally, ***Figure 59*** presents also the space evolutions of water and gas pressure.

Figure 60 presents, for the case 2 defined in Table 5, the time evolution of the water and gas pressures in the injection chamber and in the argillite close to the chamber. The experimental measurements and the corrected experimental measurements are also given on that figure. We note that the evolutions of gas and water pressure are identical until the 3rd peak. After the two pressures evolutions are clearly different: the water pressure drops after the 3rd peak while the gas pressure continues to rise. Until the 3rd peak, the obtained pressure peaks are greater than the observed experimental measurements.

The volume for interval 2 available for gas phase was estimated between 804 and 1540 cm^3, with a best fitting of 1040 cm^3 (cf Andra report D.NT.AMFS.11.0084, p 29 and 30). So, for this case, the geometric volume of the chamber is always equals to $\pi.R^2.L = \pi\ 0.038^2\ 1000 = 4.356$ *l*, but the porosity *n* was adapted from 1 to 0.2293 to obtained a real chamber volume of 1.040 *l*. The compressibility of the chamber is taken to 3.10^{-8} Pa^{-1} and its initial water saturation equals to 1. EDZ is not taken into account. The isotropic argillite permeability is always taken to $4\ 10^{-20}$ m^2.

Figure 61 presents the time evolution of gas saturation: in the chamber the gas saturation varies now from 0 to 0.96 and in the argillite, close to the chamber, it remains equals to 0 during the 3 first peaks and rises to maximum 0.037 after. On the space evolution of water saturation it appears that the argillite begins to desaturate after the 3rd peak, till to 20 cm depth for the 6th peak (with minimum water saturation = 0.962). Of course, gaseous flows, greater than dissolved ones, appear after the 3rd peak. Finally, ***Figure 61*** presents the space evolutions of water and gas pressure, where we note also the gap between the two pressures after the 3rd gas injection peak.

Case 3, defined in Table 5, is presented on ***Figure 62*** and ***Figure 63***. The chamber compressibility was adapted here to $2\ 10^{-7}$ Pa^{-1} to fit to experimental measurements of the 3 first peaks. After the 3rd peak, the time evolutions of the water and gas pressures in the injection chamber and in the argillite close to the chamber are similar to those obtained with the previous case 2.

Time evolution of gas saturation (in the chamber and in the argillite, close to the chamber) and space evolutions of gas flows, water saturation, water and gas pressures (***Figure 63***) are also identical to those obtained with the previous case 2.

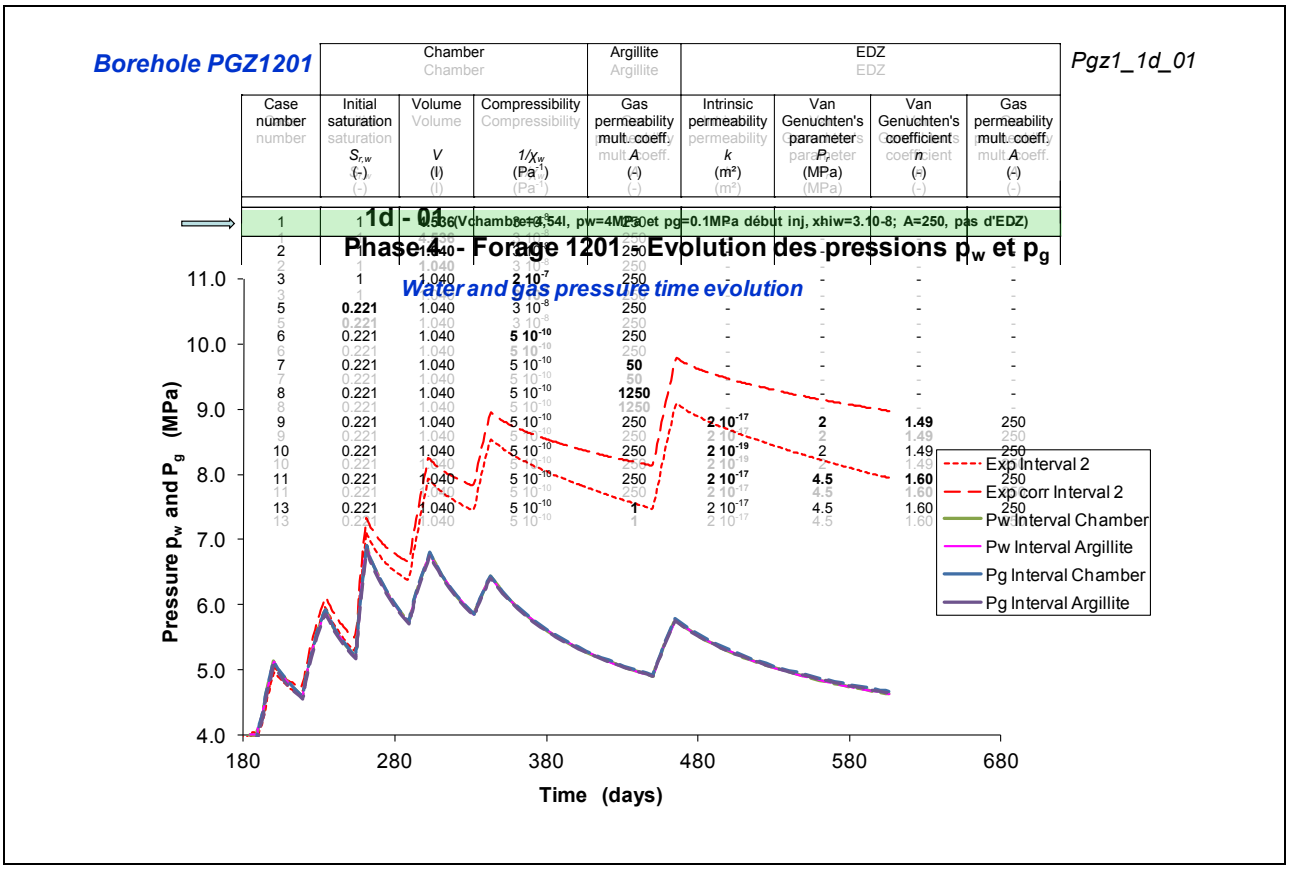

Figure 58 : Time evolution of water and gas pressures, for case 1 of 1D simulations (set 1).

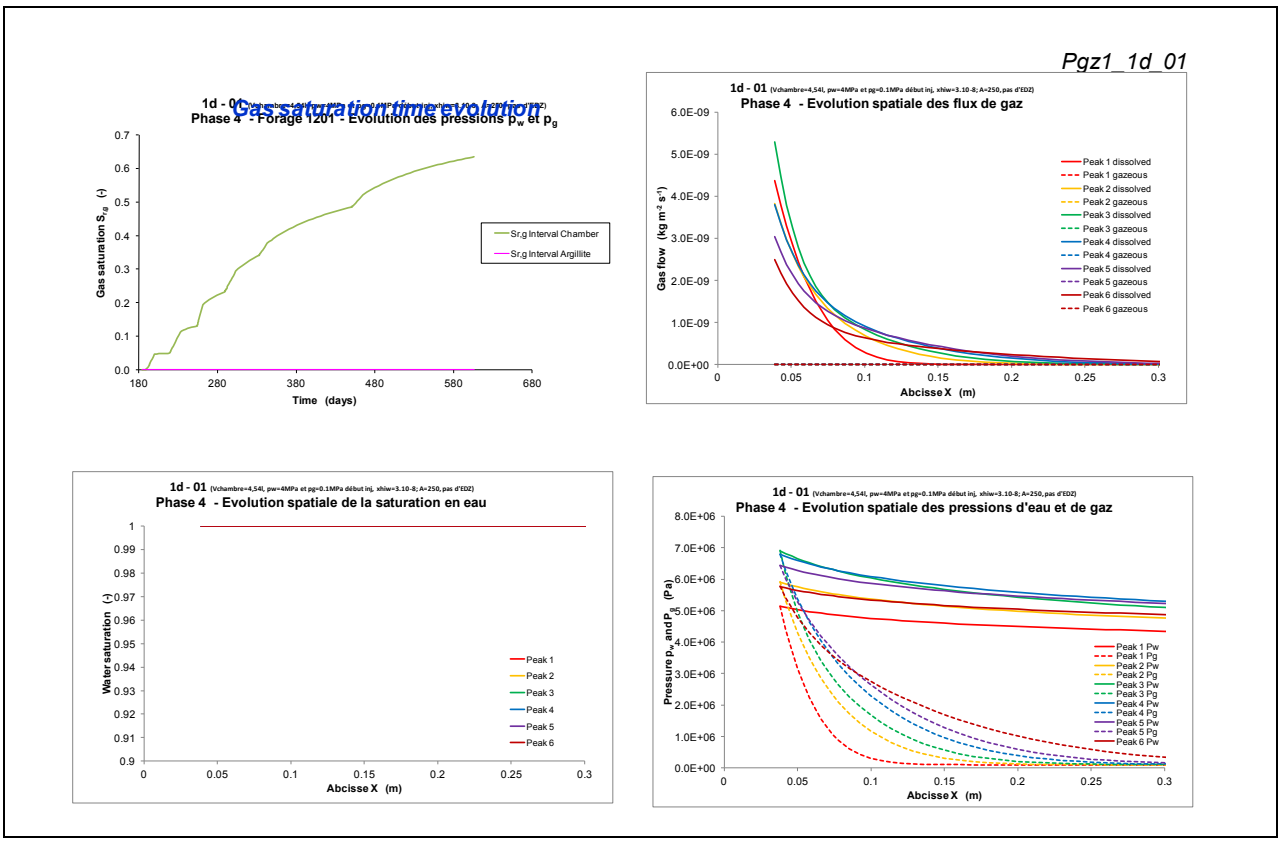

Figure 59 : Time evolution of gas saturation and space evolutions of gas flows, water saturation, water and gas pressures, for case 1 of 1D simulations (set 1).

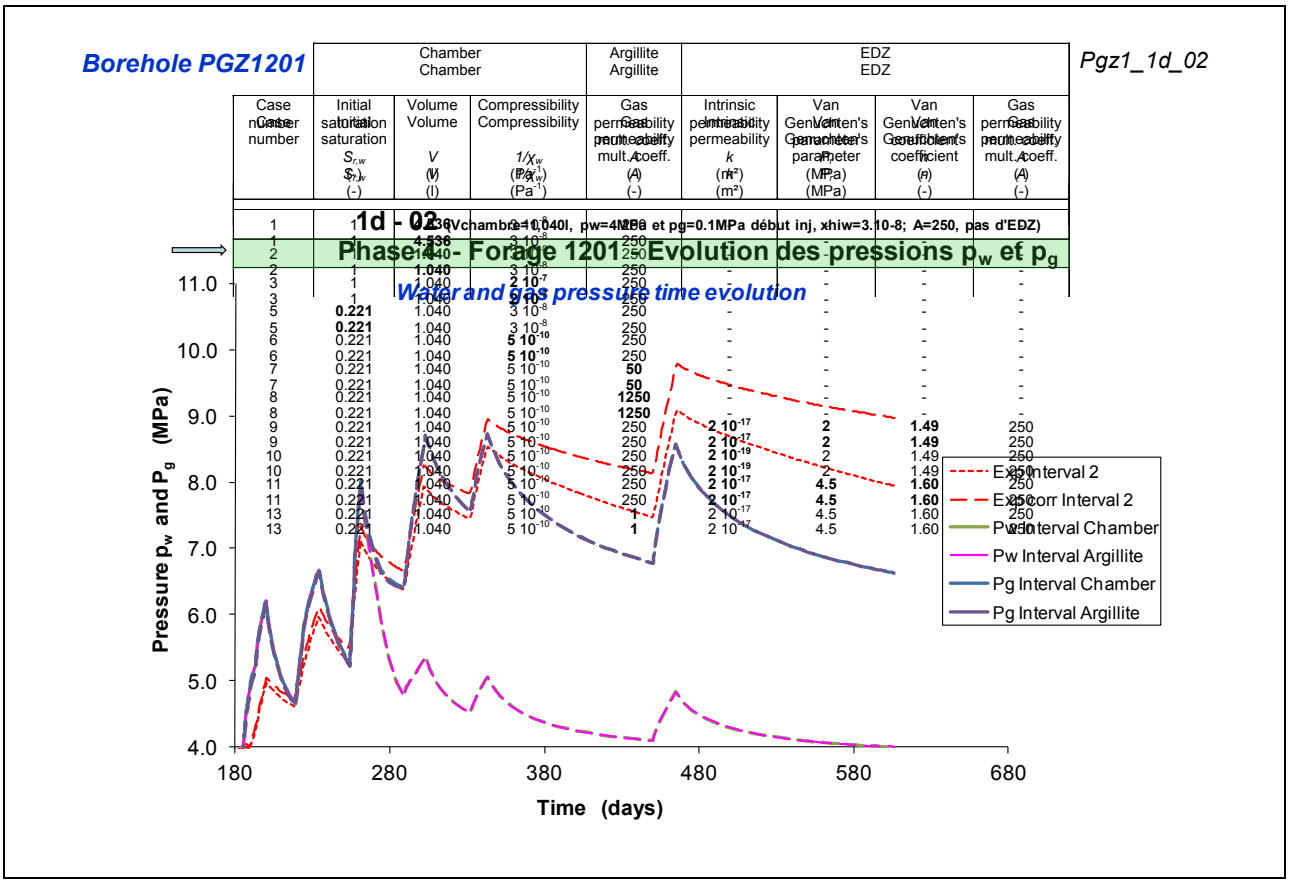

Figure 60 : Time evolution of water and gas pressures, for case 2 of 1D simulations (set 1).

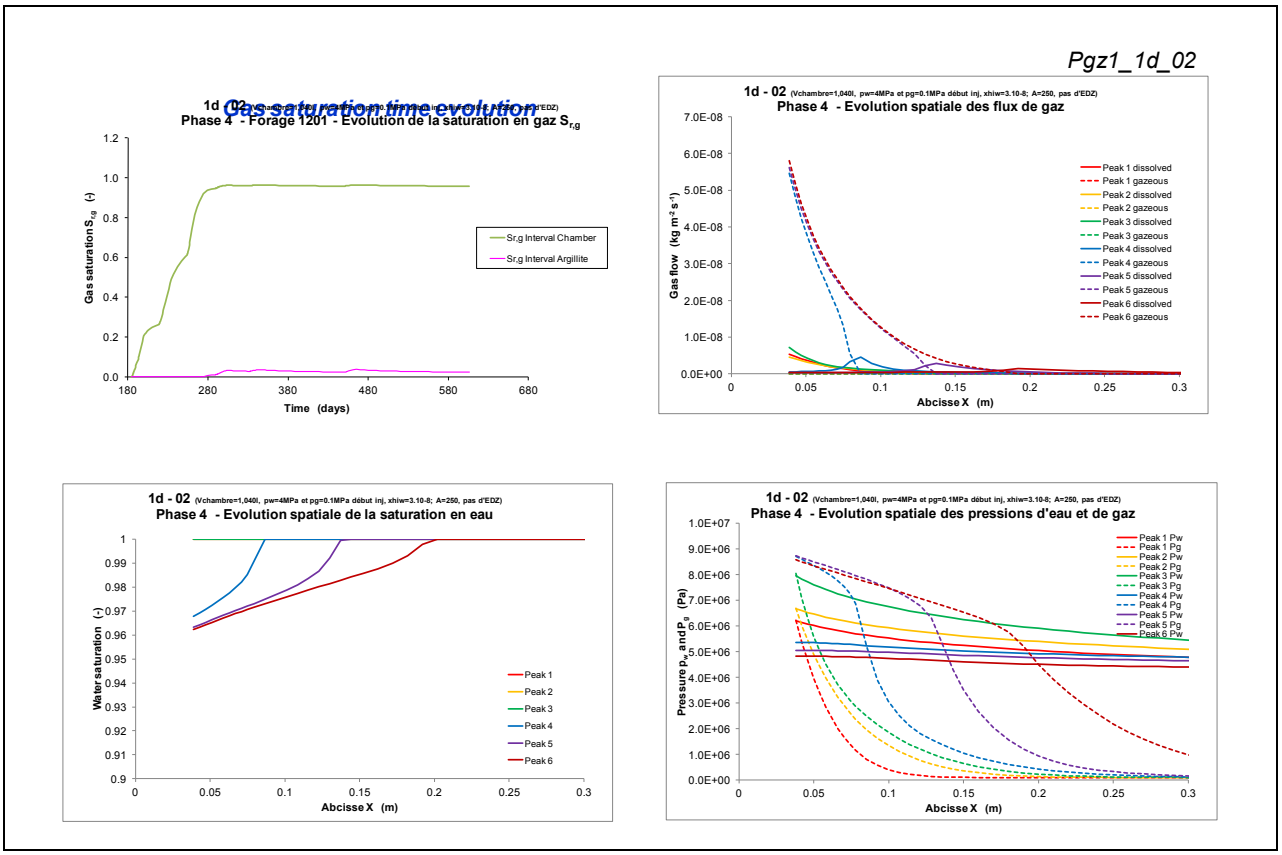

Figure 61 : Time evolution of gas saturation and space evolutions of gas flows, water saturation, water and gas pressures, for case 2 of 1D simulations (set 1).

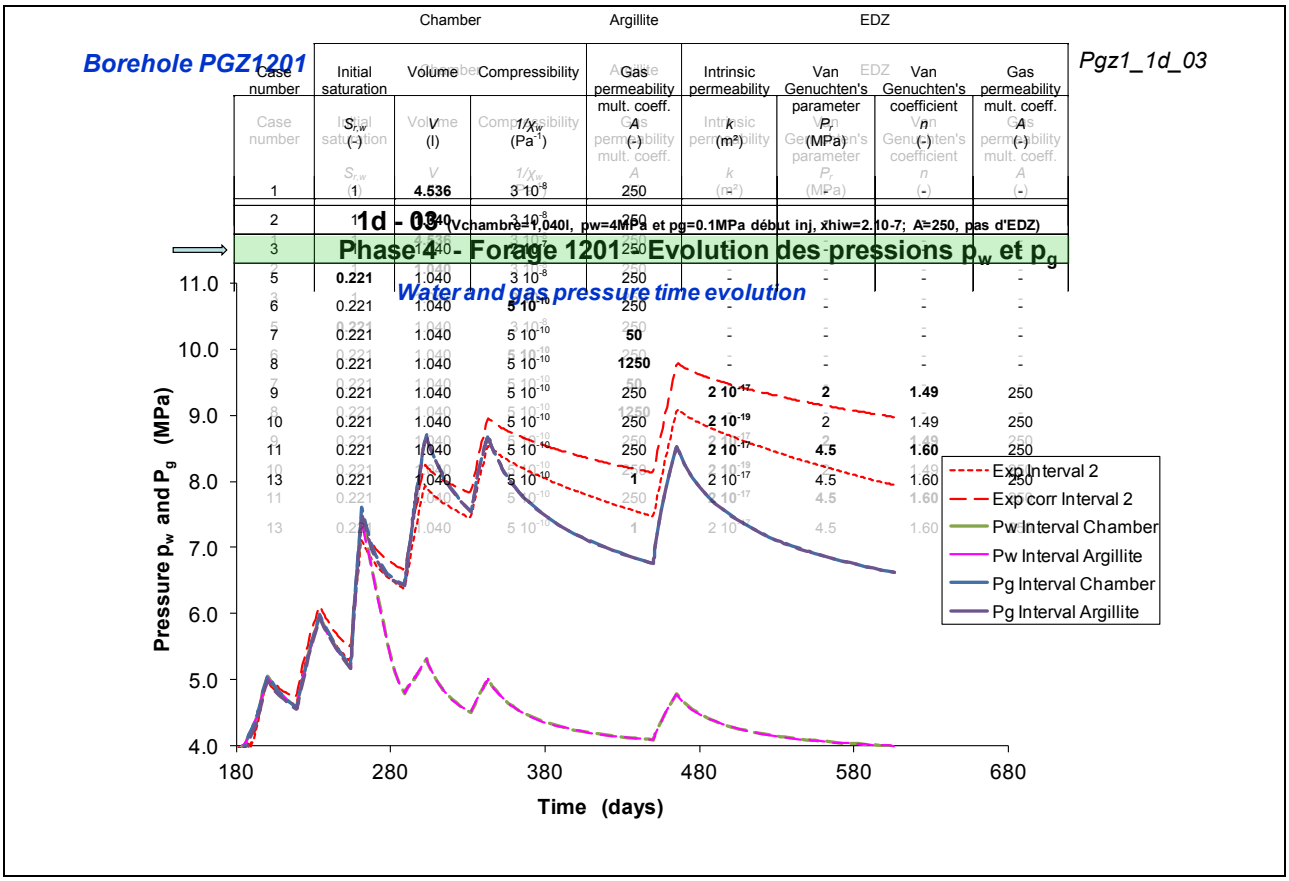

Figure 62 : Time evolution of water and gas pressures, for case 3 of 1D simulations (set 1).

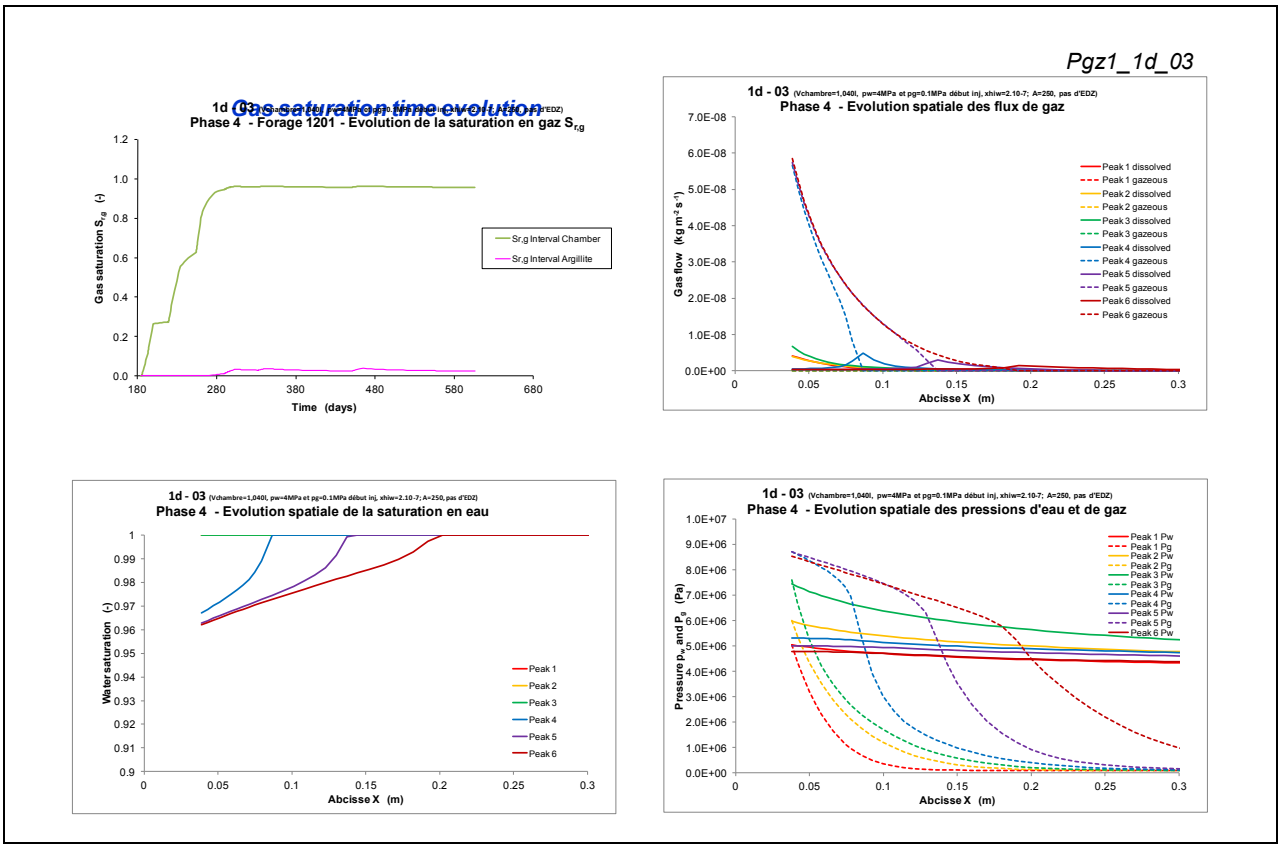

Figure 63 : Time evolution of gas saturation and space evolutions of gas flows, water saturation, water and gas pressures, for case 3 of 1D simulations (set 1).

Case 5, defined in Table 5 and presented on ***Figure 64*** and ***Figure 65***, concerns new saturation conditions in the injection chamber. The volume for interval 2 available for gas phase was estimated between 804 and 1540 cm³, with a best fitting of 1040 cm³ (cf Andra report D.NT.AMFS.11.0084, p 29 and 30). But a volume of water was extracted by blowing before the gas injection phase. This volume was measured to 810 cm³ (cf Andra report D.NT.AMFS.11.0084, p 27). Thus, we can suppose that it remains 1040 – 810 = 230 cm³ of water in the injection interval, and the initial water saturation $S_{r,w\ ini}$ = 230/1040 = 0.221. This value of initial saturation will be kept for all the following simulations. With a retention curve defined on ***Figure 53*** (P_r=0.005MPa, n=1.5) a initial water saturation $S_{r,w\ ini}$ = 0.221 correspond to a suction of 1.01 10^5 Pa (so P_w = 4 MPa and P_g = 4.101 MPa).

The compressibility of the chamber is, for this case 5, taken to 3.10^{-8} Pa^{-1} and no EDZ is taken into account. The isotropic argillite permeability is always taken to 4 10^{-20} m².

Figure 64 presents the time evolution of the water and gas pressures in the injection chamber and in the argillite close to the chamber. The experimental measurements and the corrected experimental measurements are also given on that figure. We note that from the 1st peak, the two water and gas pressures evolutions are clearly different: the water pressure changes little after the 1st peak while the gas pressure continues to rise, for the 4 first peaks, well beyond the observed experimental measurements.

Figure 65 presents the time evolution of gas saturation: in the chamber the gas saturation varies now from 0.75 to 0.96 and in the argillite, close to the chamber, it remains equals to 0 during the 2 first peaks and rises to maximum 0.040 after. On the space evolution of water saturation it appears that the argillite begins to desaturate from the 2nd peak, till to 25 cm depth for the 6th peak (with minimum water saturation = 0.960). Of course, gaseous flows, greater than dissolved ones, appear from the 2nd peak. Finally, ***Figure 65*** presents the space evolutions of water and gas pressure, where we note also the gap between the two pressures from the 2nd gas injection peak.

Figure 66 and ***Figure 67*** present the results obtained for the case 6, defined in Table 5. In that case, the compressibility of the chamber was reduced to 5.10^{-10} Pa^{-1}, which is the classical value used for water. We note on the two figures that the results are absolutely identical to those obtained with the previous case 5 and a compressibility of 3.10^{-8} Pa^{-1}. Because now the injection chamber is very desaturated initially, it is obvious that the compressibility (of water) of the chamber does not play more a major role.

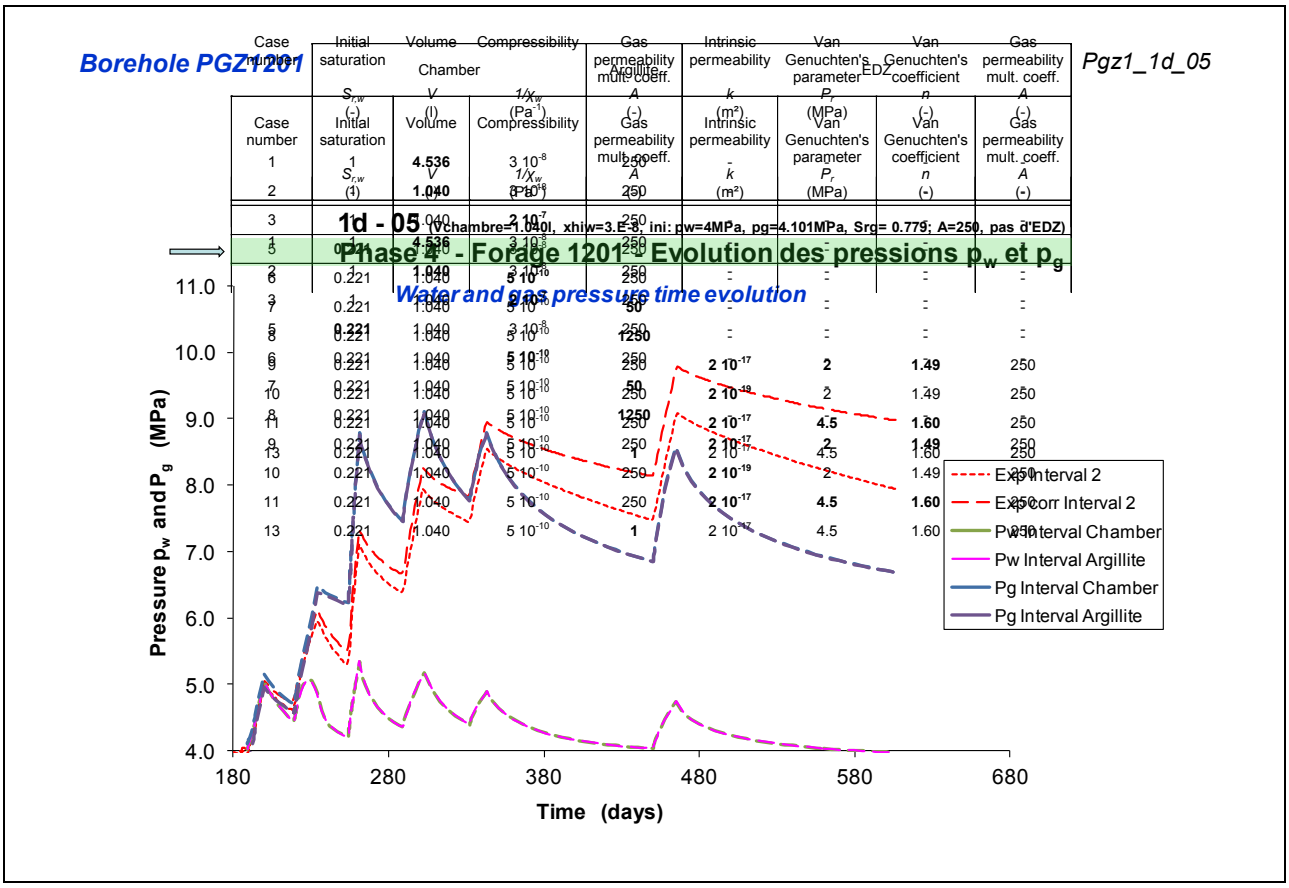

Figure 64 : Time evolution of water and gas pressures, for case 5 of 1D simulations (set 1).

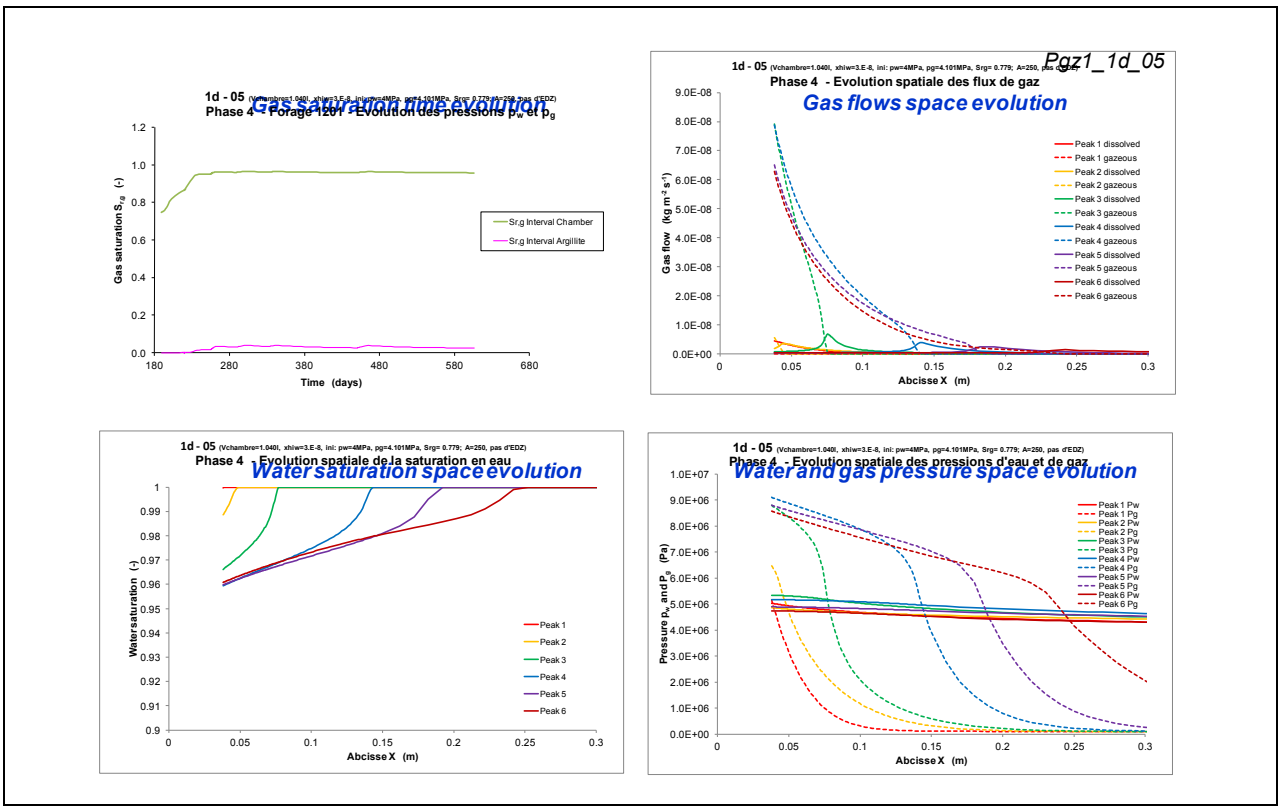

Figure 65 : Time evolution of gas saturation and space evolutions of gas flows, water saturation, water and gas pressures, for case 5 of 1D simulations (set 1).

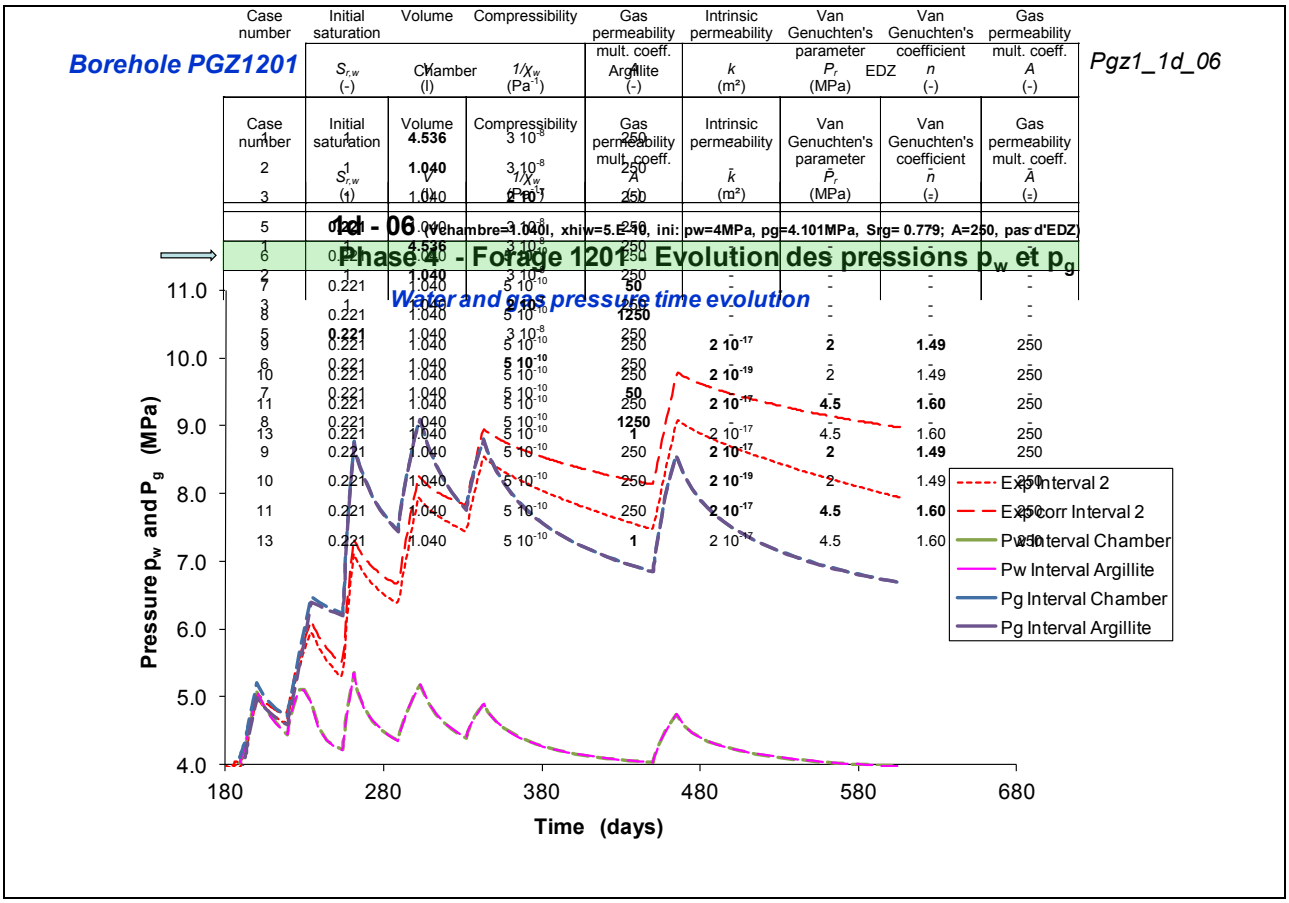

Figure 66 : Time evolution of water and gas pressures, for case 6 of 1D simulations (set 1).

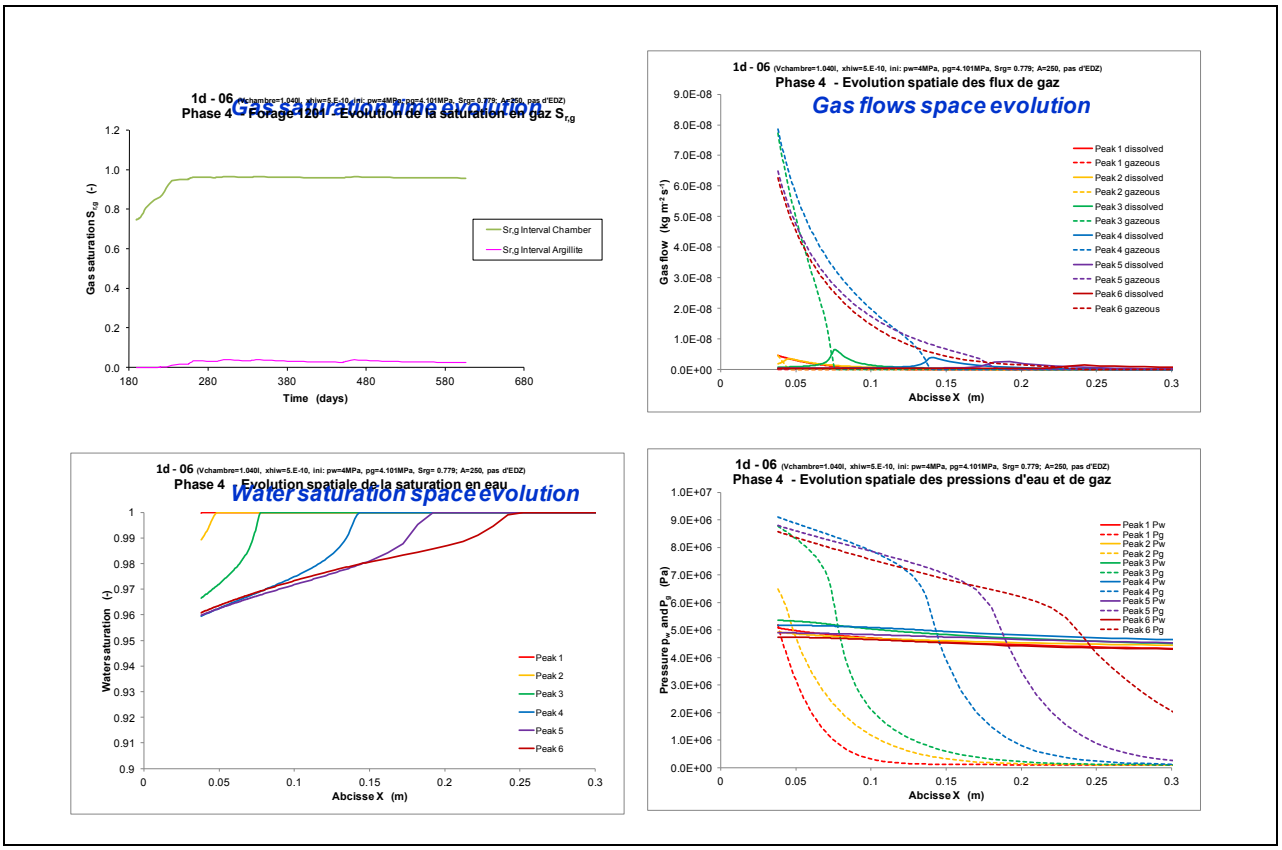

Figure 67 : Time evolution of gas saturation and space evolutions of gas flows, water saturation, water and gas pressures, for case 6 of 1D simulations (set 1).

From case 6 (with a gas permeability multiplier coefficient A = 250), two variants were performed: case 7 (with A = A/5 = 50) where results are given on ***Figure 68*** and ***Figure 69*** and case 8 (with A = A*5 = 1250) where results are given on ***Figure 70*** and ***Figure 71***.

Before peak 2, argillite is saturated and so, of course, the gas permeability multiplier has no influence. After this peak, the lower the A coefficient, the higher the rise in gas pressure (particularly the 3rd peak) (***Figure 68***). On the contrary, with a high A coefficient, the height of the gas pressure peaks are clearly lower (***Figure 70***).

Figure 69 and ***Figure 71*** present, respectively for the case A = 50 and A = 1250, the time evolution of gas saturation: in the chamber the gas saturation varies now from 0.75 to 0.97 (case A = 50) and from 0.75 to 0.96 (case A = 1250) and in the argillite, close to the chamber, it remains equals to 0 during the 2 first peaks and rises after to maximum 0.054 (case A = 50) and 0.028 (case A = 1250). On the space evolution of water saturation it appears that the argillite begins to desaturate from the 2nd peak, till to 20 cm depth for the 6th peak (with minimum water saturation = 0.945) for the case A = 50, and till to 30 cm depth for the 6th peak (with minimum water saturation = 0.972) for the case A = 1250. Of course, gaseous flows, greater than dissolved ones, appear from the 2nd peak, and are more important in the case A = 1250 than in the case with A = 50. Finally, ***Figure 69*** and ***Figure 71*** present the space evolutions of water and gas pressure, where we note always the gap between the two pressures from the 2nd gas injection peak Of course, in the case A = 1250, the values of the gas pressure is lower than in the case A = 50 but the progression of this gas in the argillite is more important.

To try to improve the comparability of results with experimental measurements, an EDZ has been introduced in all the different cases below. First in case 9, defined in Table 5, an EDZ of 4 cm thick has the following initial characteristics: isotropic intrinsic permeability $k = 2.10^{-17}$ m², Van Genuchten's parameter P_r =2 MPa and Van Genuchten's coefficient n =1.49. These values correspond to the EDZ in front of interval previously defined in 3D modelling, on ***Figure 52*** and ***Figure 53***. The isotropic argillite permeability is always taken to 4 10^{-20} m².

Figure 72 presents, for that case 9, the time evolution of the water and gas pressures in the injection chamber and in the EDZ close to the chamber. The experimental measurements and the corrected experimental measurements are always given on that figure. This case has to compare with the case 6, with identical parameters but without EDZ. We note that, for the 3 first peaks, the evolution of gas is clearly much closer to the experimental measurements than the evolution obtained with case 6 parameters (***Figure 66***). For the 3 last peaks, the obtained evolution of the gas pressure is always lower than the experimental measurements.

Figure 73 presents the time evolution of gas saturation: in the chamber the gas saturation varies now from 0.71 to 0.96 and in the EDZ, close to the chamber, it varies from 0 to maximum 0.272 after. On the space evolution of water saturation it appears that the EDZ begins to desaturate after the 1st peak and the argillite after the 2nd one, till to 18 cm depth for the 6th peak (with minimum water saturation = 0.976 in argillite and 0.734 in EDZ). Gaseous flows appear early from the 1st peak. Finally, ***Figure 73*** presents the space evolutions of water and gas pressure, where we note also the gap between the two pressures from the 2nd gas injection peak.

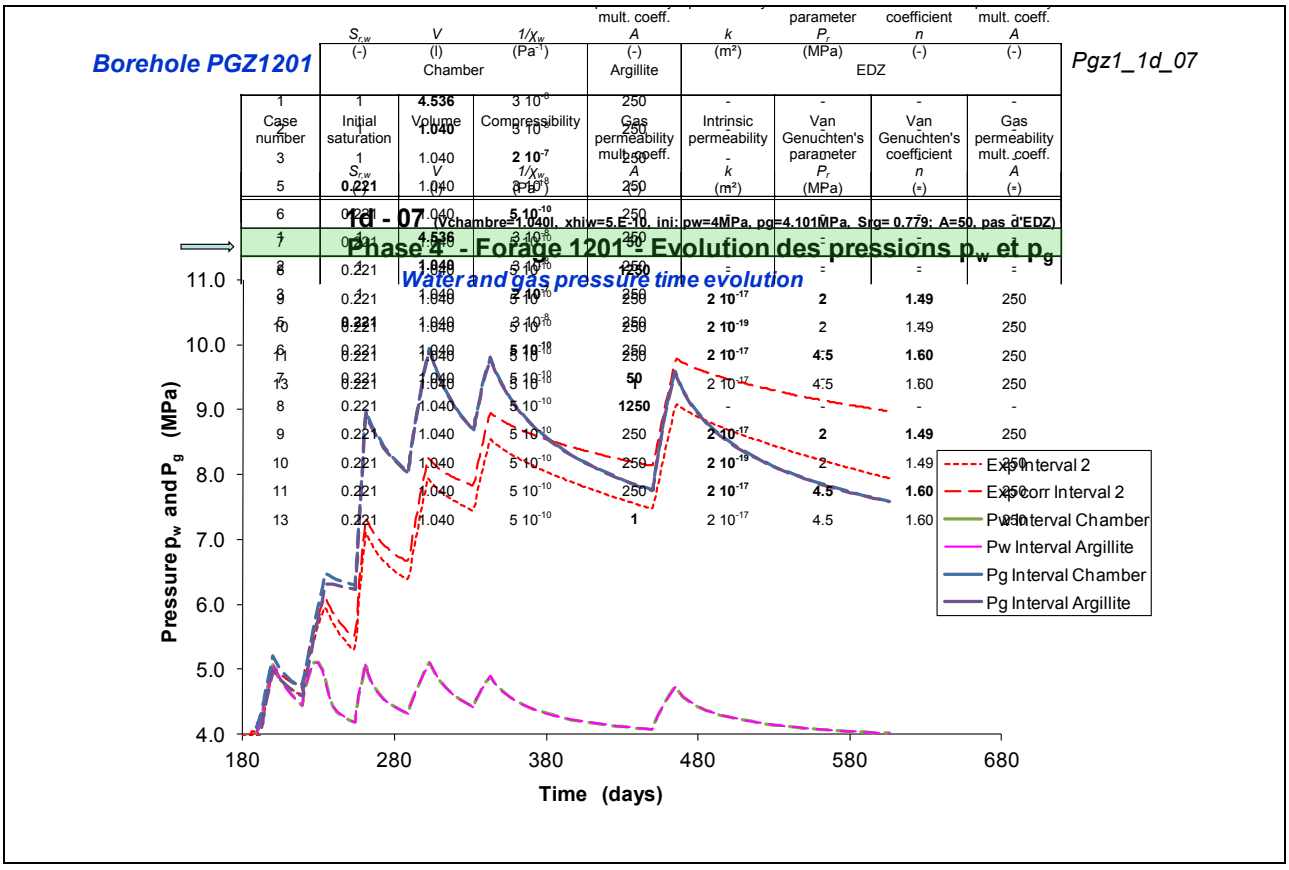

Figure 68 : Time evolution of water and gas pressures, for case 7 of 1D simulations (set 1).

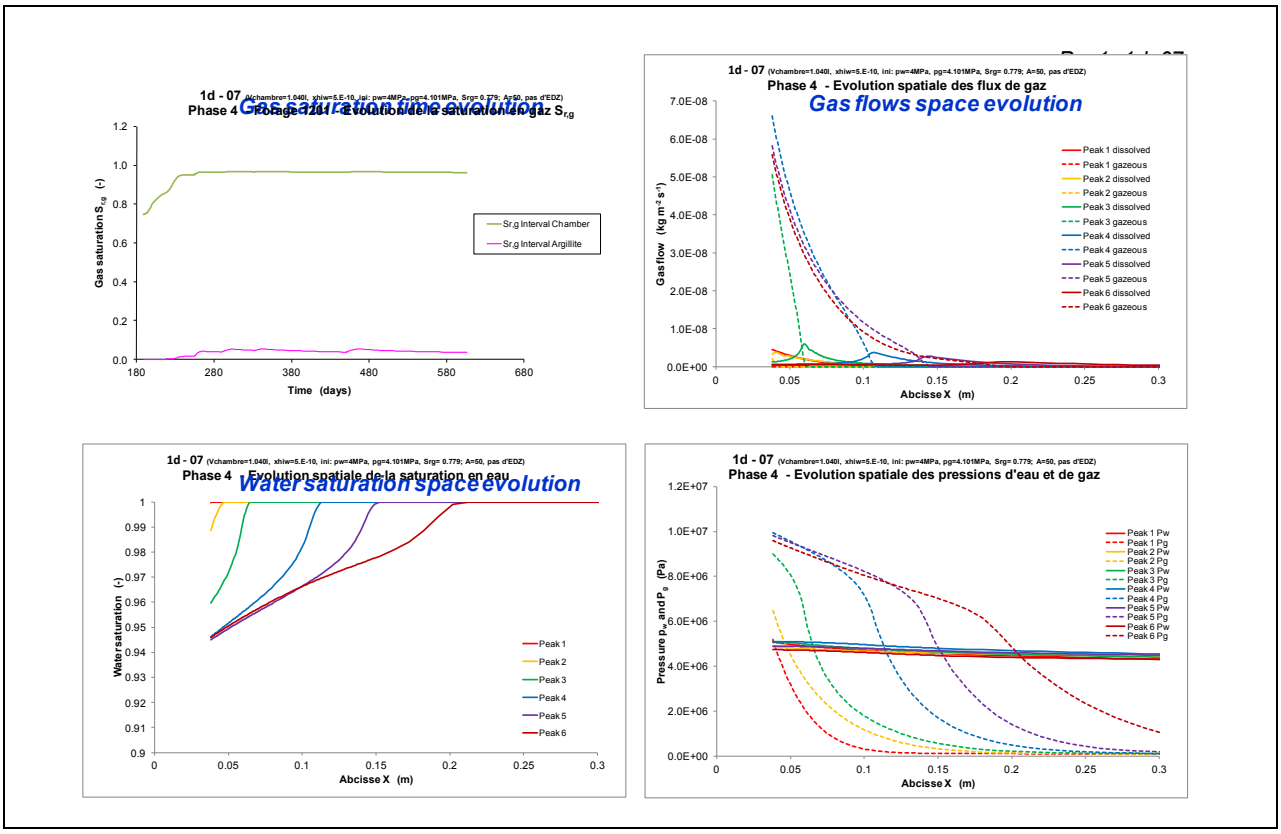

Figure 69 : Time evolution of gas saturation and space evolutions of gas flows, water saturation, water and gas pressures, for case 7 of 1D simulations (set 1).

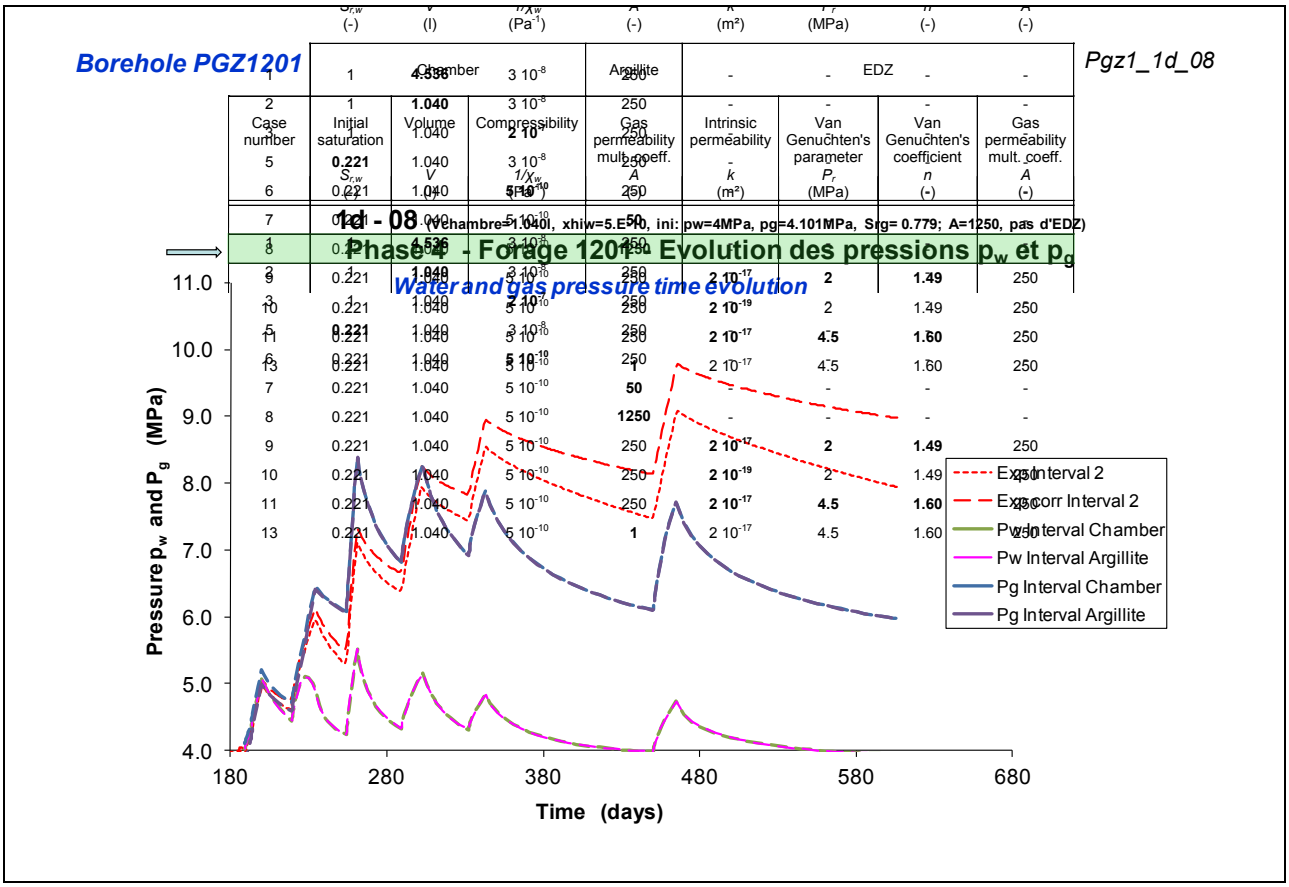

Figure 70 : Time evolution of water and gas pressures, for case 8 of 1D simulations (set 1).

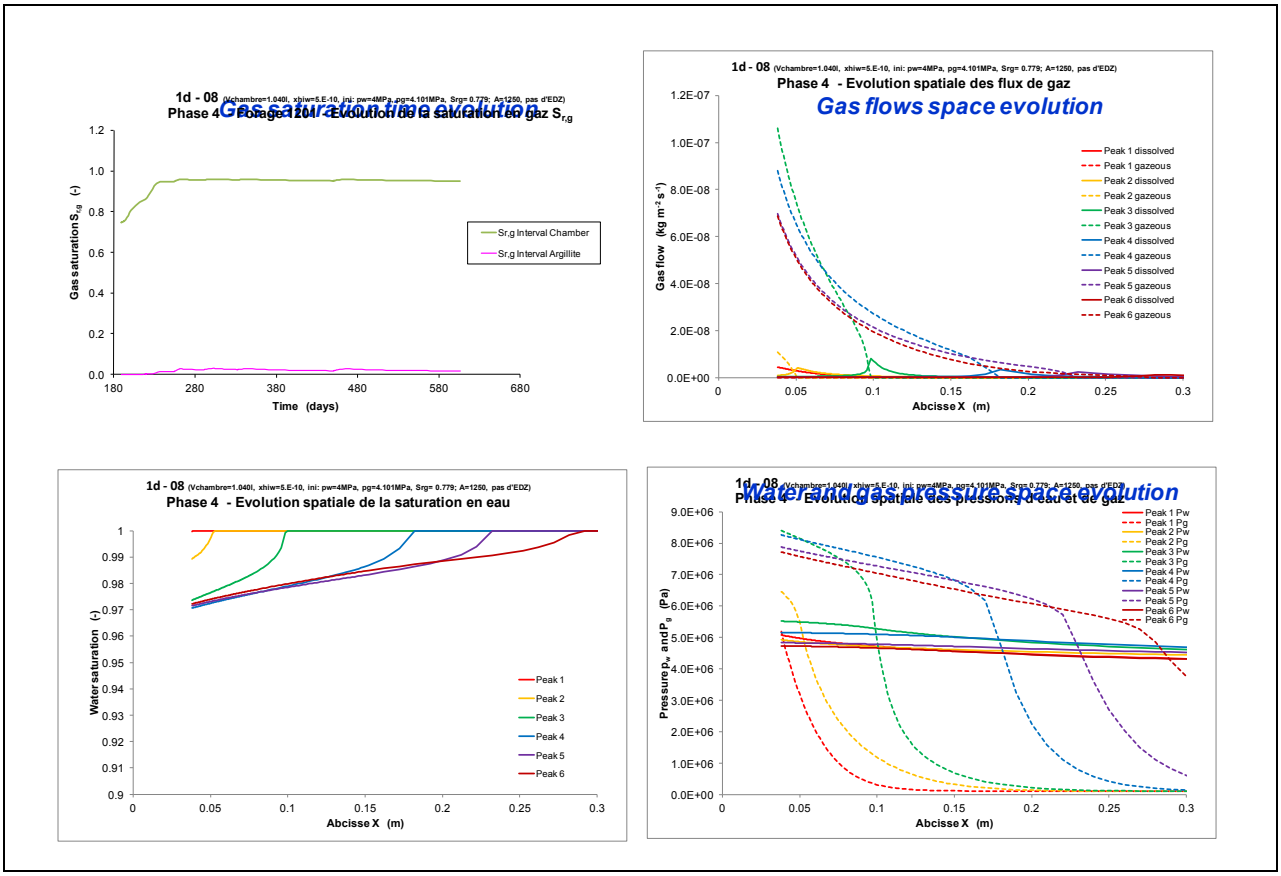

Figure 71 : Time evolution of gas saturation and space evolutions of gas flows, water saturation, water and gas pressures, for case 8 of 1D simulations (set 1).

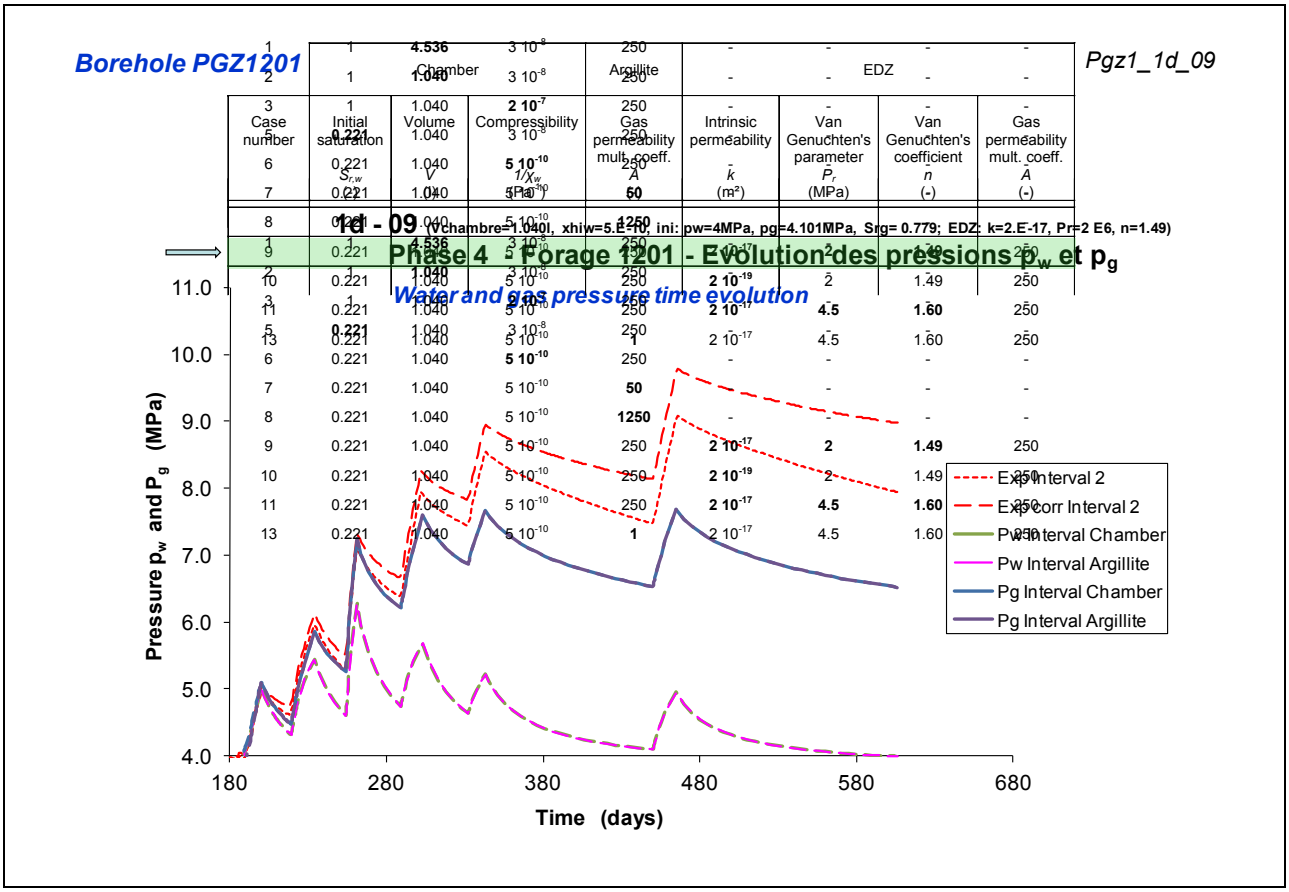

Figure 72 : Time evolution of water and gas pressures, for case 9 of 1D simulations (set 1).

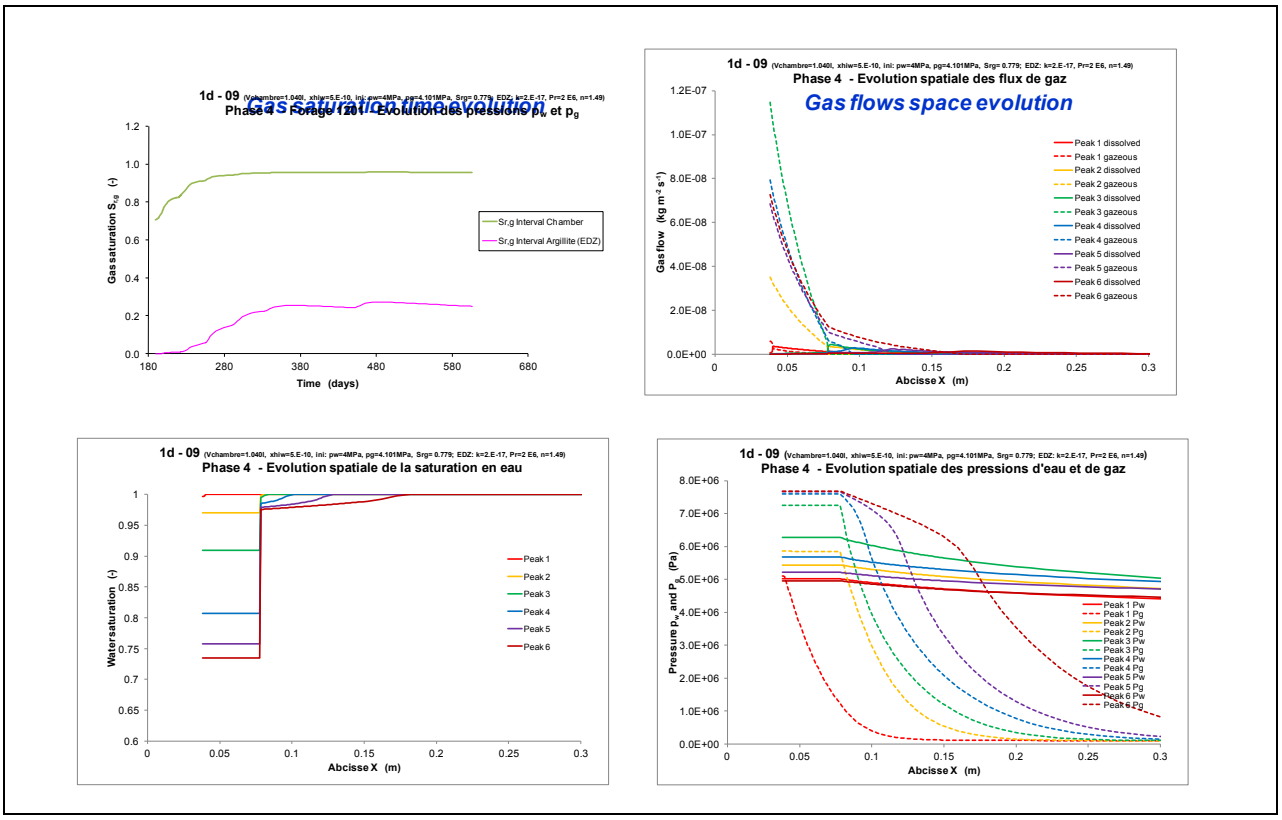

Figure 73 : Time evolution of gas saturation and space evolutions of gas flows, water saturation, water and gas pressures, for case 9 of 1D simulations (set 1).

Case 10, defined in Table 5 and presented on ***Figure 74*** and ***Figure 75***. This case is identical to the presented previous one, except for the EDZ permeability which is equal here to 2 10^{-19} m² (instead of 2 10^{-17} m² in case 9). We note that there is only very little difference between the results of two cases. For example of course the space evolution of the water saturation in EDZ on ***Figure 75*** is a little different to this shown on to ***Figure 73***, but globally the general behaviour is identical between the two cases 9 and 10.

Figure 75 presents the time evolution of gas saturation: in the chamber the gas saturation varies now from 0.75 to 0.96 and in the EDZ, close to the chamber, it varies from 0 to maximum 0.272 after. On the space evolution of water saturation it appears that the EDZ always begins to desaturate after the 1st peak and the argillite after the 2nd one, till to 18 cm depth for the 6th peak (with minimum water saturation = 0.975 in argillite and 0.730 in EDZ). Gaseous flows appear from the 2nd peak. Finally, ***Figure 73*** presents the space evolutions of water and gas pressure, where we note also the gap between the two pressures from the 2nd gas injection peak.

A new set of EDZ parameters was tested: isotropic intrinsic permeability k = 2.10^{-17} m² (identical to case 9), Van Genuchten's parameter P_r =4.5 MPa and Van Genuchten's coefficient n =1.60. ***Figure 76*** presents, for that case 11 defined in Table 5, the time evolution of the water and gas pressures in the injection chamber and in EDZ close to the chamber. The experimental measurements and the corrected experimental measurements are also given on that figure. We note that now the evolutions of gas pressure are close to the corrected experimental measurements until the 4th peak. Then when the measured pressure continues to increase, the calculated gas pressure slightly decreases for the peaks 5 and 6.

Figure 77 presents the time evolution of gas saturation: in the chamber the gas saturation varies now from 0.75 to 0.96 and in the EDZ, close to the chamber, it remains equals to 0 during the 1 first peaks and rises to maximum 0.146 after. On the space evolution of water saturation it appears that the EDZ always begins to desaturate after the 1st peak and the argillite after the 2nd one, till to 22 cm depth for the 6th peak (with minimum water saturation = 0.972 in argillite and 0.855 in EDZ). Gaseous flows appear from the 1st peak. Finally, ***Figure 77*** presents the space evolutions of water and gas pressure, where we note always the gap between the two pressures from the 2nd gas injection peak.

The case 13, defined in Table 5, is presented on ***Figure 78*** and ***Figure 79***. This case is identical to the previous one (case 11), except that the gas permeability multiplier coefficient A for argillite is reduced from 250 (cases 9, 10 and 11) to unit value. So with this set of EDZ parameters (k = 2.10^{-17} m², P_r =4.5 MPa, n =1.60) and A coefficient equal to 1 for argillite, it is possible to obtain a better agreement with the experimental measurements, especially for peaks 5 and 6 (***Figure 78***).

In the chamber the gas saturation varies now from 0.75 to 0.97 and in the EDZ, close to the chamber, it remains equals to 0 during the 1st peak and rises to maximum 0.232 after (***Figure 79***). EDZ begins always to desaturate after the 1st peak and the argillite after the 2nd one, to only 13 cm depth for the 6th peak (with minimum water saturation = 0.953 in argillite and 0.778 in EDZ). Finally, ***Figure 79*** presents the space evolutions of gas flows and water and gas pressures.

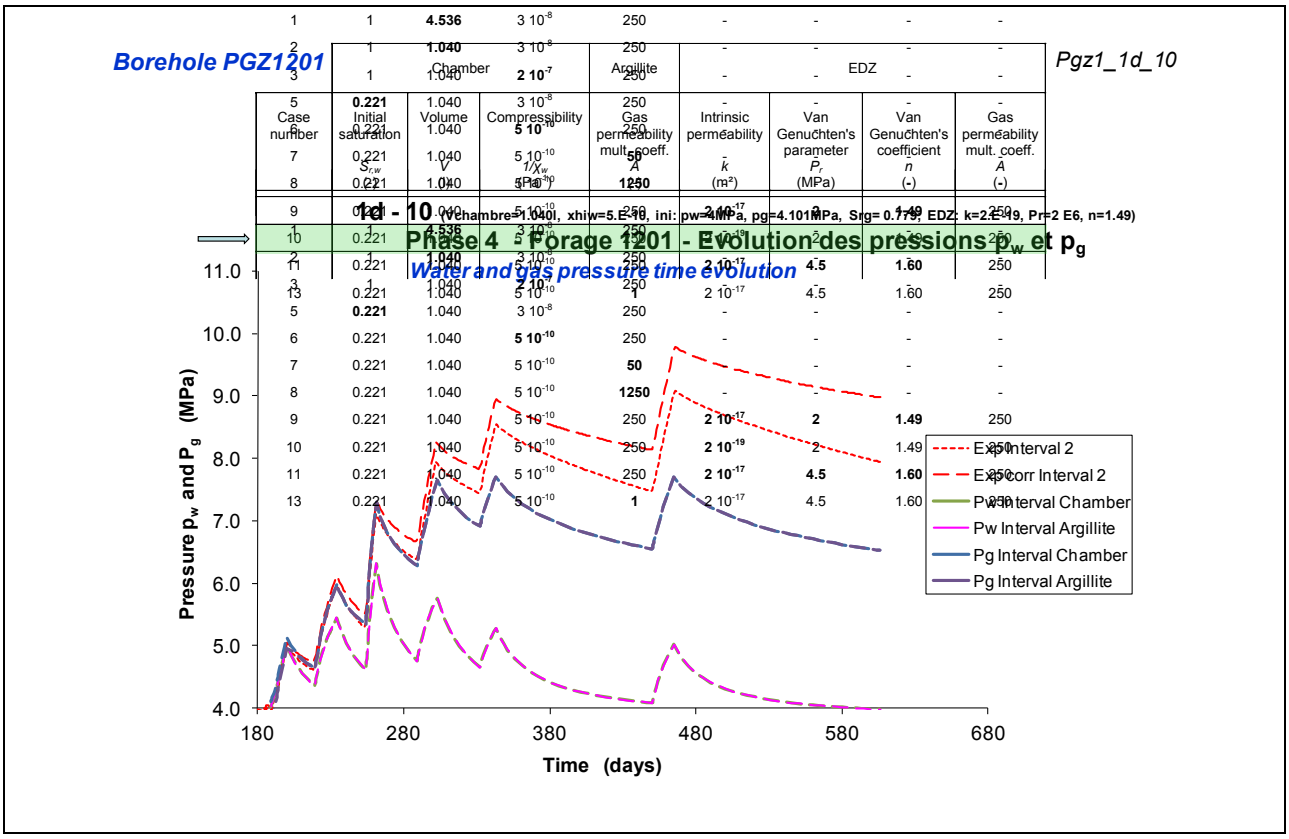

Figure 74 : Time evolution of water and gas pressures, for case 10 of 1D simulations (set 1).

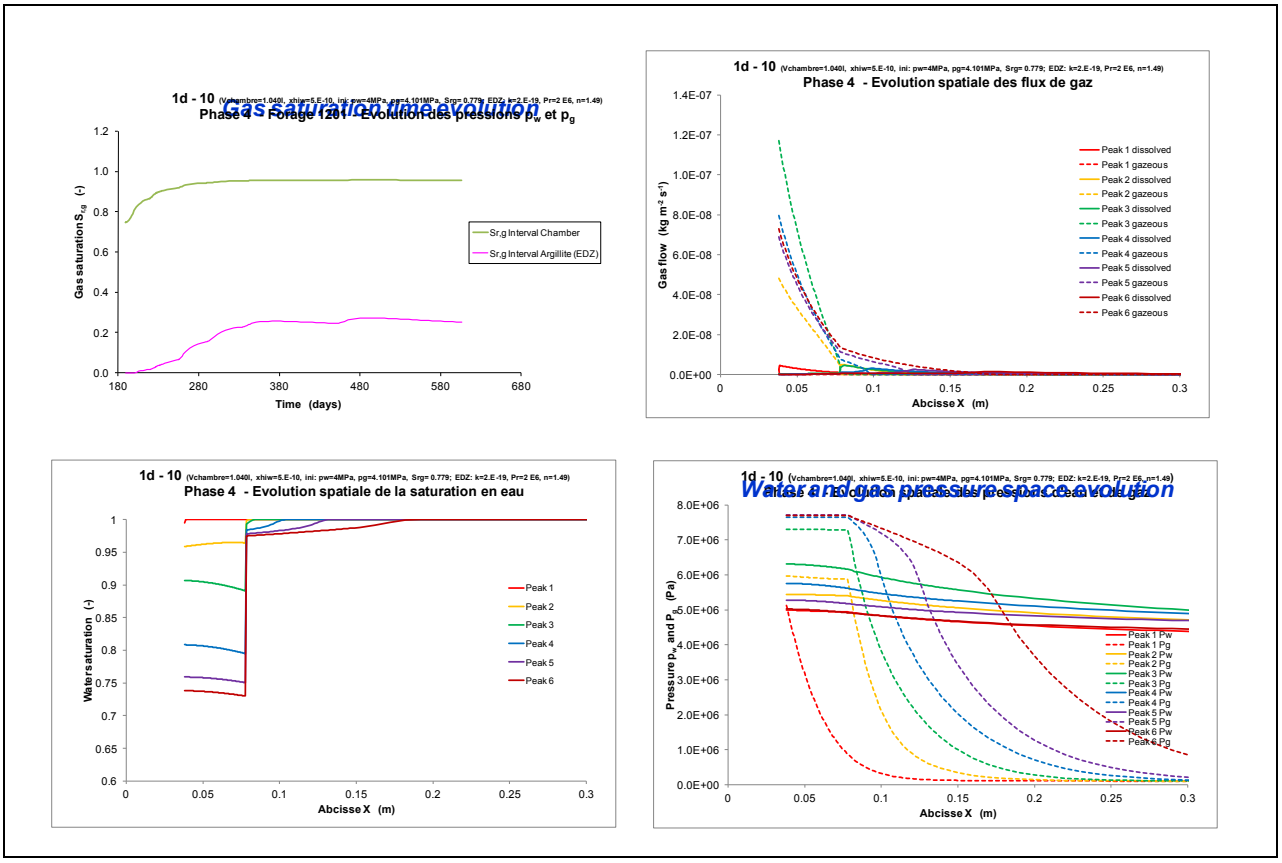

Figure 75 : Time evolution of gas saturation and space evolutions of gas flows, water saturation, water and gas pressures, for case 10 of 1D simulations (set 1).

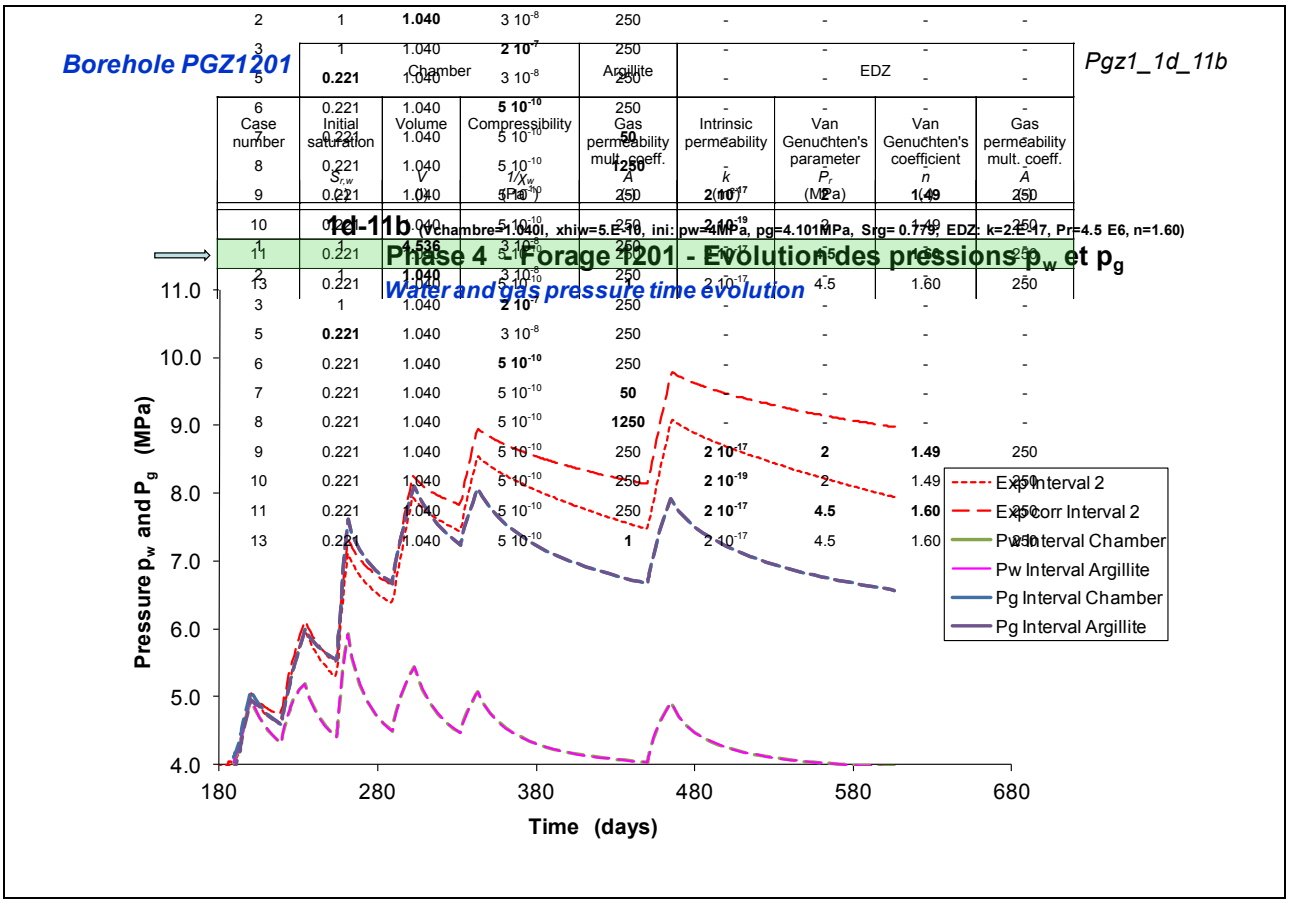

Figure 76 : Time evolution of water and gas pressures, for case 11 of 1D simulations (set 1).

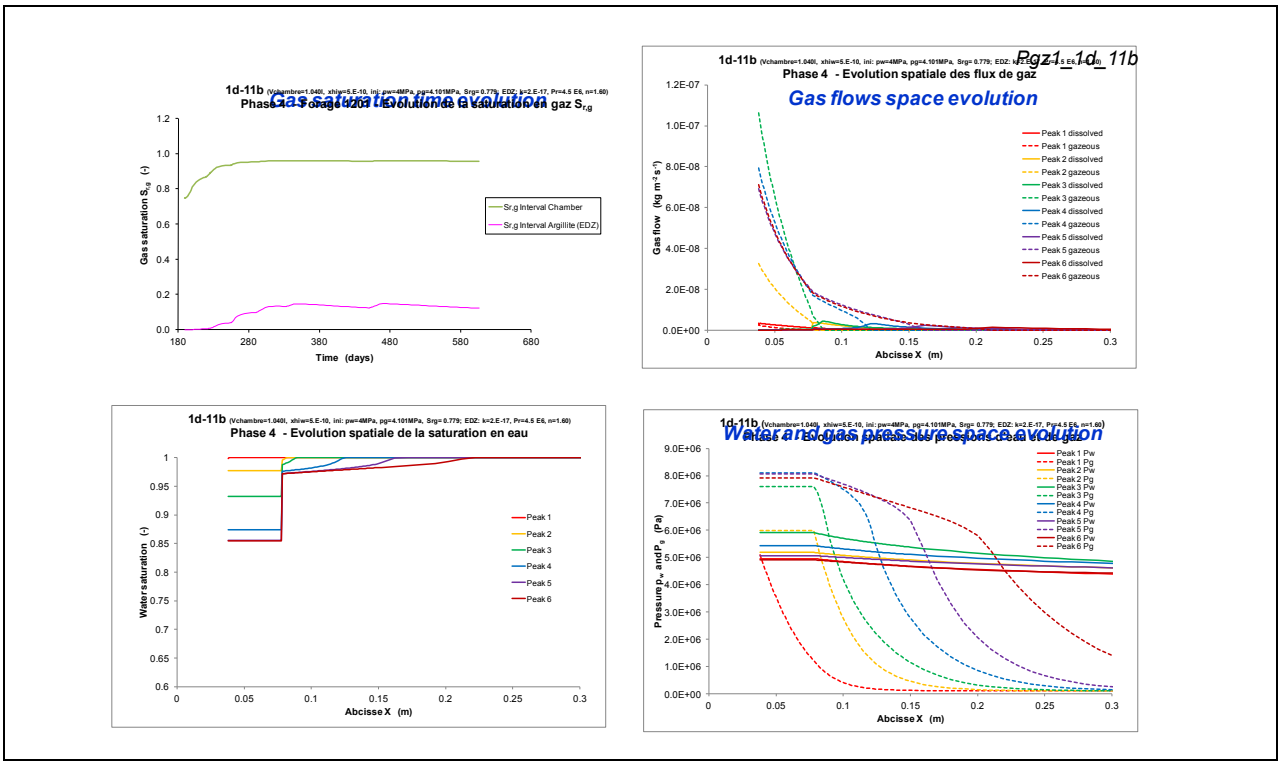

Figure 77 : Time evolution of gas saturation and space evolutions of gas flows, water saturation, water and gas pressures, for case 11 of 1D simulation (set 1)s.

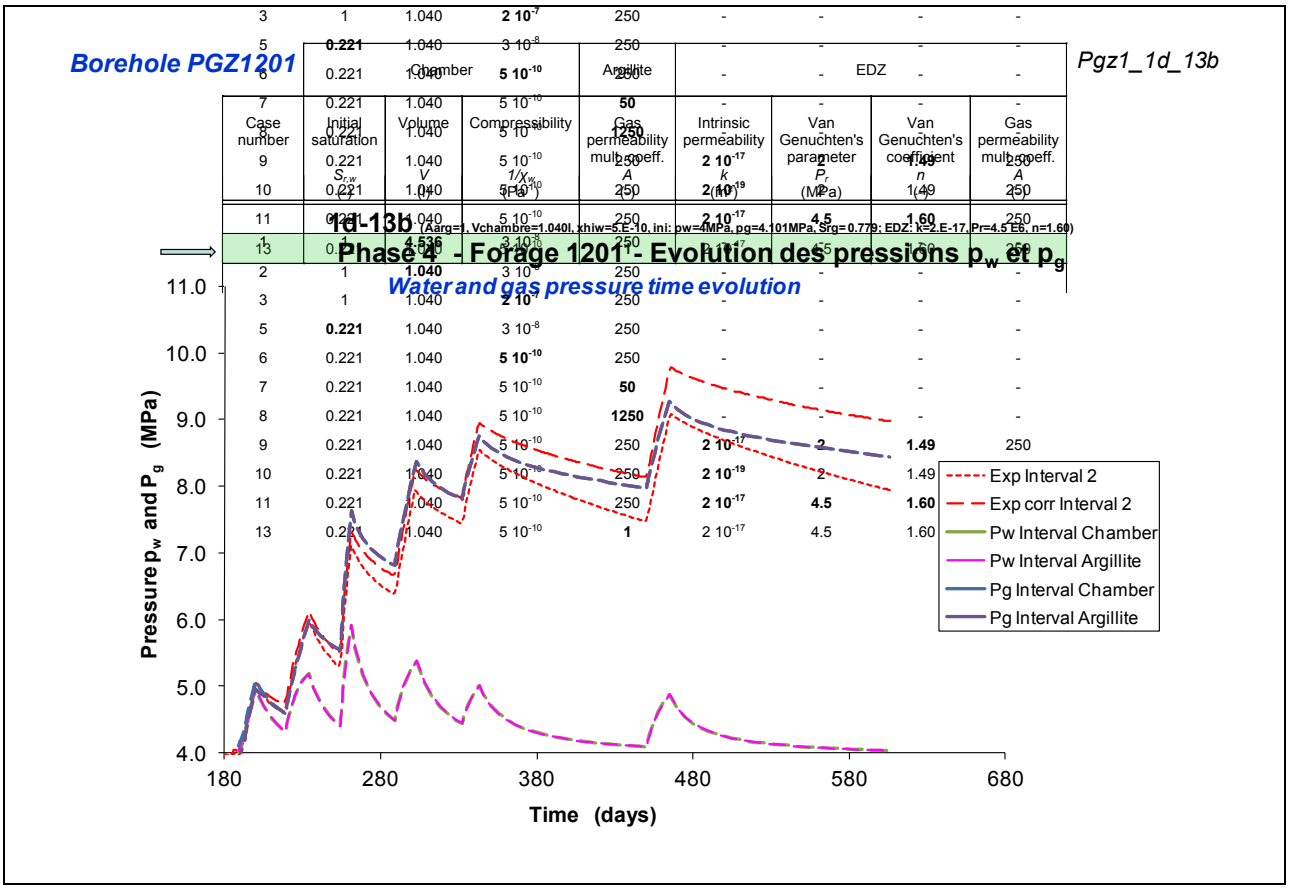

Figure 78 : Time evolution of water and gas pressures, for case 13 of 1D simulations (set 1).

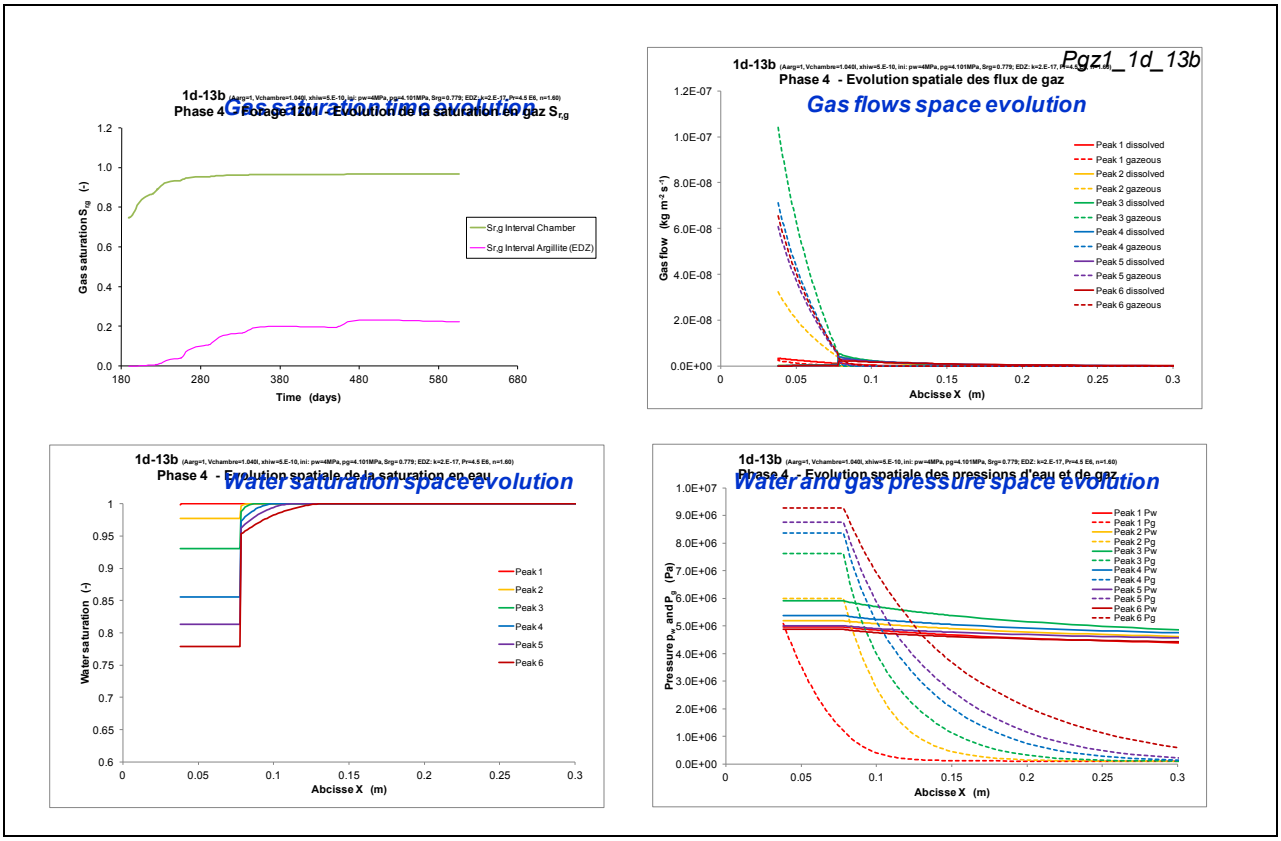

Figure 79 : Time evolution of gas saturation and space evolutions of gas flows, water saturation, water and gas pressures, for case 13 of 1D simulations (set 1).

The case 13 is the best obtained calibration on the experimental measurements. The same case (named then case 15) was also made without taking into account the diffusion/dissolution effect. Others parameters are identical between the 2 cases. The diffusion coefficient $D_{N_2}^{H_2O}$ of N_2 dissolved in water and the diffusion coefficient $D_{N_2}^{vapeur}$ of N_2 in water vapor are divided by 500 compared to the previous case 13. We note that a simple cancellation of these coefficients is not numerically possible.

Reminder, diffusion of dissolved nitrogen is integrated in the model by Fick's law:

$$\underline{i}_{(N_2)_d} = -\rho_w S_{r,w} \quad \varphi \quad \tau \quad D_{N_2}^{H_2O} \underline{\nabla}\left(\frac{\rho_{N_2}^w}{\rho_w}\right)$$

with $\rho_{N_2}^w$ the density of dissolved nitrogen [kg.m^{-3}], $D_{N_2}^{H_2O}$ the diffusion coefficient of gaseous nitrogen in the liquid water [2 10^{-9} m².s^{-1}], φ the porosity [-] and τ the tortuosity [-],. The density of dissolved nitrogen is given by Henry' law $\rho_{N_2}^w = H_{N_2}(T).\rho_{N_2}^g$ with H_{N_2} the Henry's constant pour nitrogen [0.0176].

Diffusion of nitrogen in the N_2 – water vapor mixing is given also by Fick's law:

$$\underline{i}_{(N_2)_g} = -\rho_g(1-S_{r,w})\varphi\tau \quad D_{N_2}^{vapeur} \underline{\nabla}\left(\frac{\rho_{N_2}^g}{\rho_g}\right) = -\underline{i}_{(H_2O)_g}$$

with $D_{N_2}^{vapeur}$ the diffusion coefficient of N_2 in the water vapor [m².s^{-1}], which is expressed by the following relationship $D_{N_2}^{vapeur} = D_0\left(\frac{P_0}{P_g}\right)\left(\frac{T}{T_0}\right)^{1.75}$ with D_0 = 2.42 10^{-5} m².s^{-1}, P_0 = 101 kPa and T_0 = 303 K

Figure 80 presents, for that case 15 identical to case 13 but without diffusion effects, the time evolution of the water and gas pressures in the injection chamber and in EDZ close to the chamber. The experimental measurements and the corrected experimental measurements are also given on that figure. We note that now the evolution of gas pressure is higher than in the case 13 obtained with diffusion effect.

Figure 81 presents the time evolution of gas saturation: in the chamber the gas saturation varies now from 0.75 to 0.97 and in the EDZ, close to the chamber, it remains equals to 0 during the 1 first peaks and rises to maximum 0.262 after. On the space evolution of water saturation it appears that the EDZ always begins to desaturate after the 1st peak and the argillite after the 2nd one, till to 11 cm depth for the 6th peak (with minimum water saturation = 0.944 in argillite and 0.749 in EDZ). Of course, no diffusive flux appears with that case 15. Finally, ***Figure 81*** presents the space evolutions of water and gas pressures, where we note that in the saturated zone (so after 11 cm depth) the gas no further progress in argillite because there is now no diffusive effect taken into account.

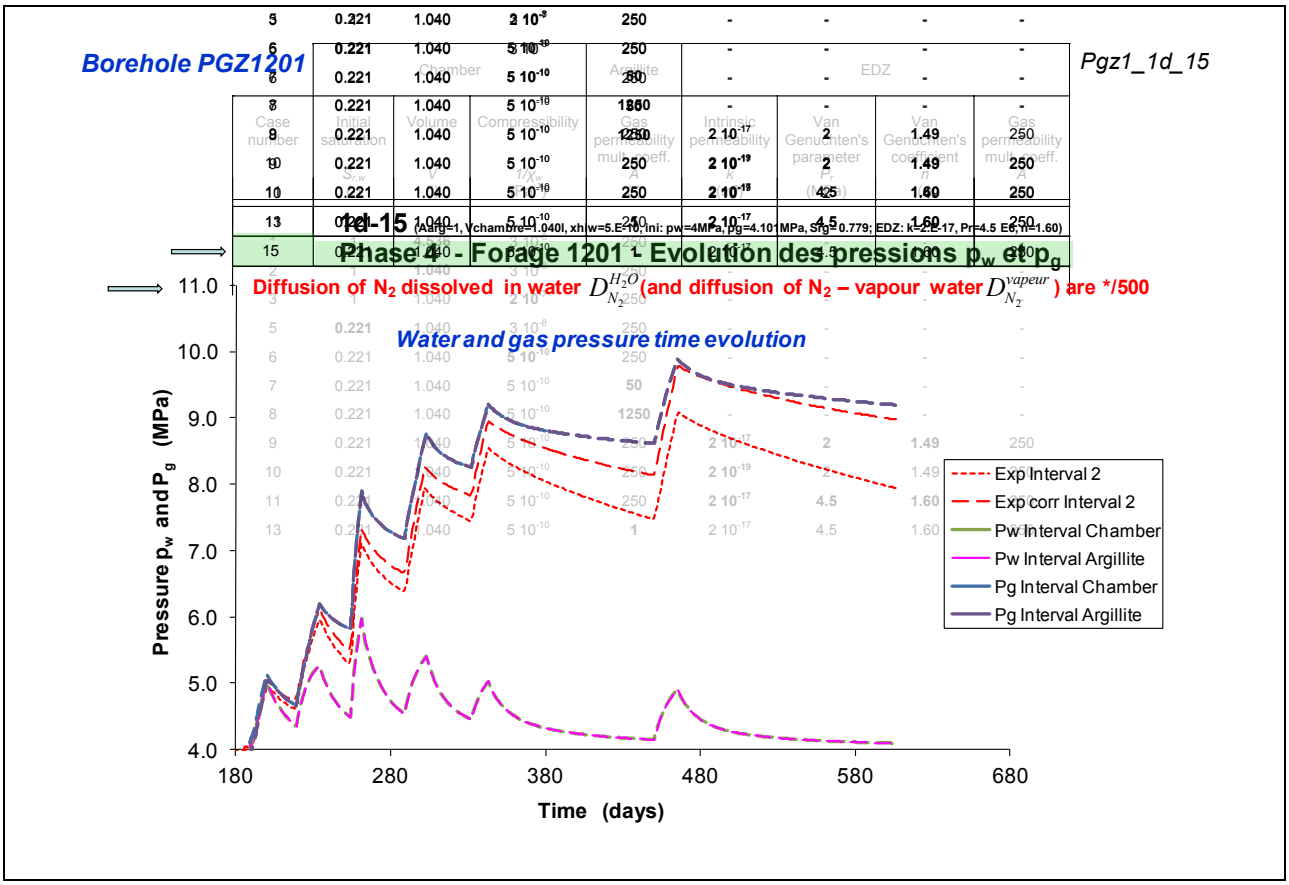

Figure 80 : Time evolution of water and gas pressures, for case 15 of 1D simulations (set 1).

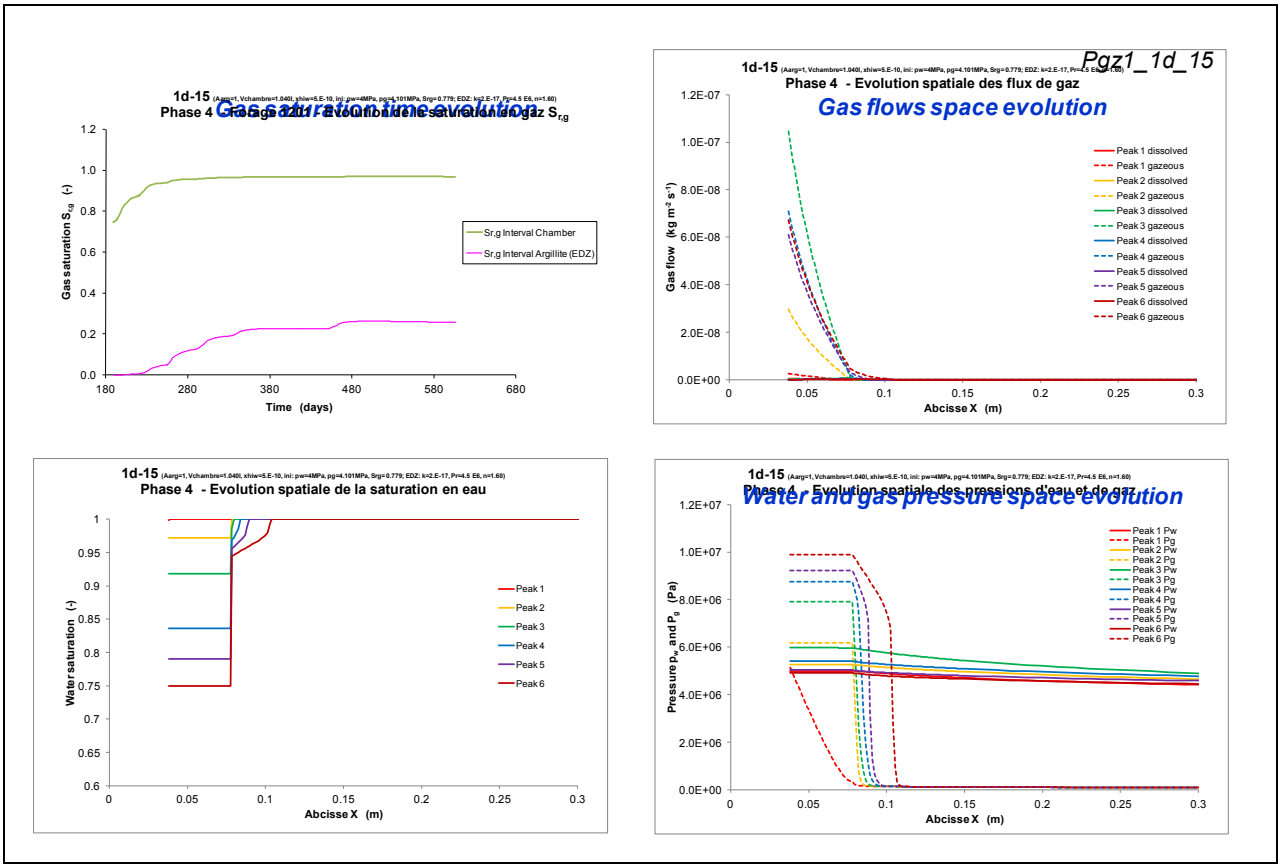

Figure 81 : Time evolution of gas saturation and space evolutions of gas flows, water saturation, water and gas pressures, for case 15 of 1D simulations (set 1).

Finally, the preceding case 13 was continued to simulate the gas extraction phase: between March 30, 2011 and April 1, 2011 (2 days: 611 to 613days) the gas flow rate is -2.9 ml/min and between April 1, 2011 and April 13, 2011 (12 days: 611 to 625 days) the gas extraction flow rate rises to -16.9 ml/min. ***Figure 82*** and ***Figure 83*** give the time evolution of water and gas pressures obtained with that gas extraction phase. We note that gas pressure drop is much larger and faster than that experimentally measured. In addition, due to numerical problems, the simulation stops after only 6 days of extraction of gas. The gas extraction flow rate which is numerically imposed seems perhaps too large to well reproduce the experimental measurements of that gas extraction phase.

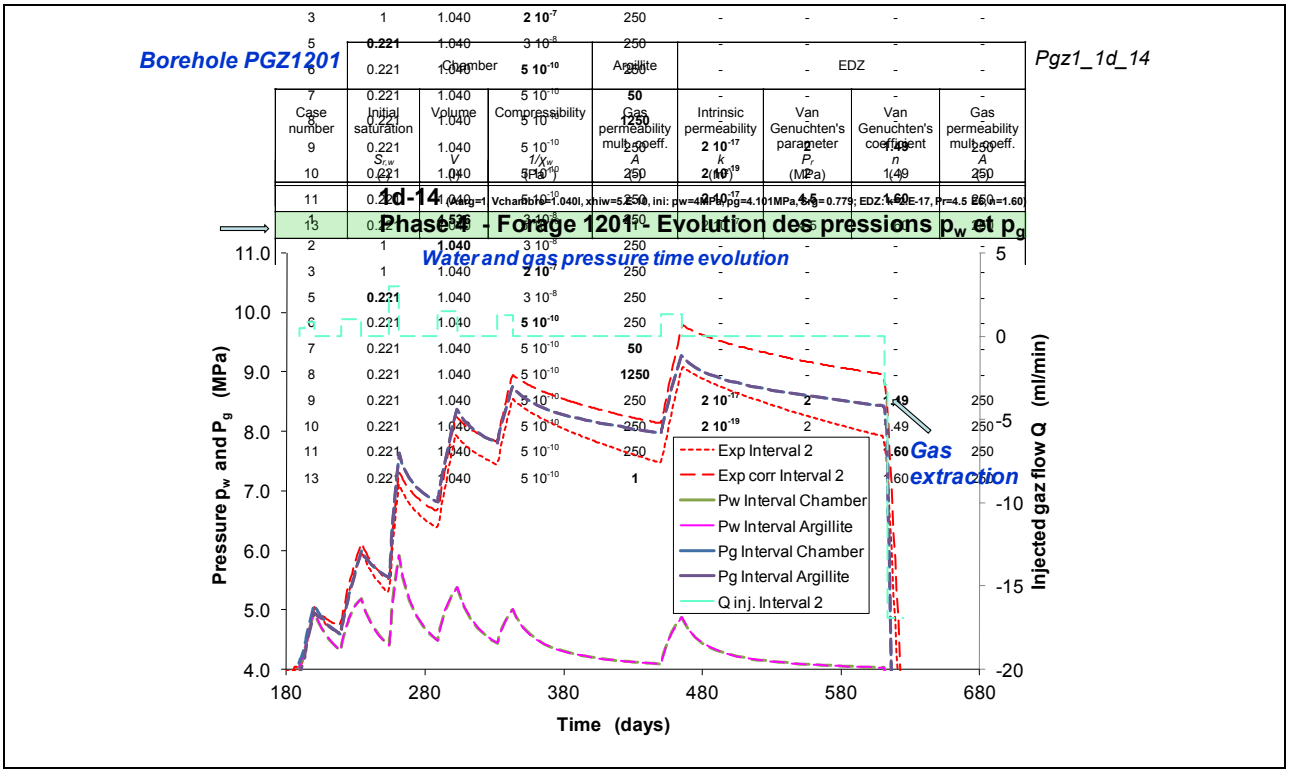

Figure 82 : Time evolution of water and gas pressures, for case 13 of 1D simulations (set 1), with gas extraction phase.

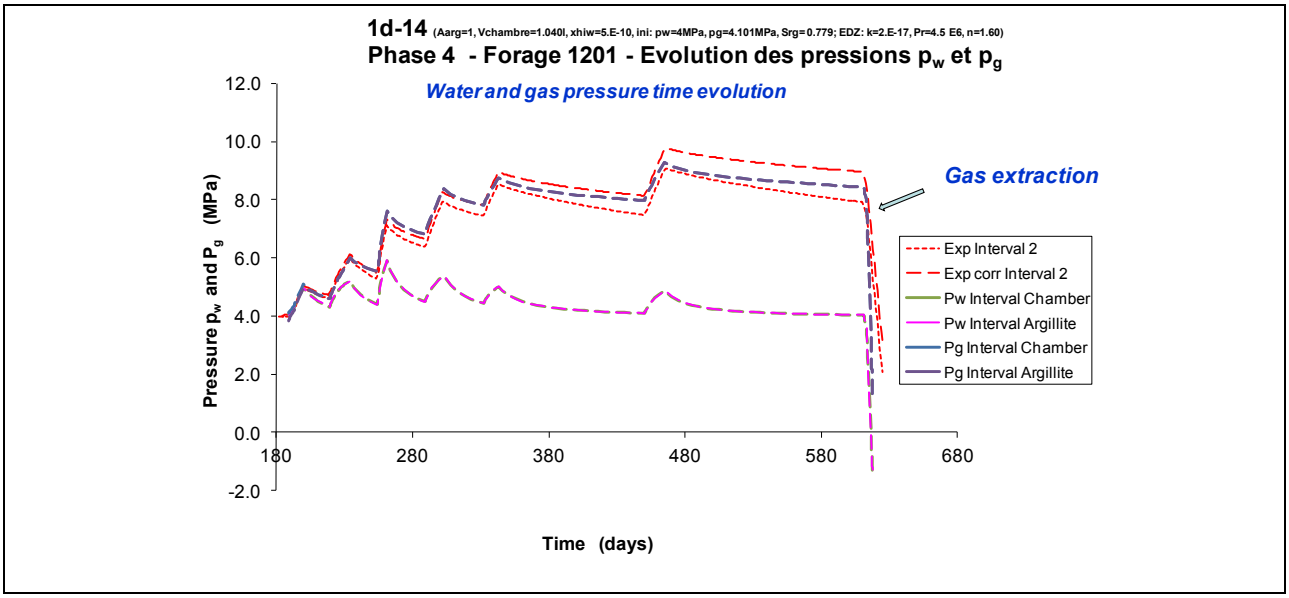

Figure 83 : Time evolution of water and gas pressures, for case 13 of 1D simulation (set 1), with gas extraction phase.

9 3D NUMERICAL RESULTS (SET 1) AND COMPARISONS WITH IN-SITU MEASUREMENTS

9.1 Phase 4: gas injection

A new 3D simulation was performed always taking into account of a EDZ of 4 cm thick (***Figure 52***). All the parameters used are those that provided the best calibration in one-dimensional simulations (set 1) (case 13, ***Figure 78*** and ***Figure 79***). EDZ permeabilities were reduced for better numerical convergence but, as that was shown during the one-dimensional simulations, it has very little influence on the numerical results (case 9, ***Figure 72*** and case 10, ***Figure 74***). So, chosen anisotropic permeabilities are 4 and 4/3 10^{-20} m² in front of the packers and 2 and 2/3 10^{-19} m² in front of the 3 intervals. Permeability of argillite is always equal to 4 and 4/3 10^{-20}.

Retention curves parameters are always P_r=15 MPa and n=1.49 for argillite, P_r=8 MPa and n=1.49 for EDZ in front of packers and P_r=4.5 MPa and n=1.60 for EDZ in front of intervals.

Only the injection gas phases ("phase 4") were simulated here, between 189 and 606 days, with, as initial conditions, a hydrostatic pressure p_w = 4 MPa in the whole model.

Figure 84 and ***Figure 85*** compare now the numerical results, obtained for PGZ1201 and PGZ1202 borehole intervals, with the (corrected) experimental data. We note that the 4 first peaks are correctly represented and the numerical response is clearly similar to that obtained in the 1d simulation with almost the same parameters (***Figure 78***). Unfortunately, the three-dimensional mesh used does not allow continuing the simulation beyond the 4th peaks.

Modifying just retention curve parameters for EDZ in front of intervals (P_r=2 MPa and n=1.49, instead of P_r=4.5 MPa and n=1.60 for the preceding simulation) it is possible to conduct the simulation until the end of the injection phase. ***Figure 86*** and ***Figure 87*** show the numerical time evolutions of water and gas pressures and comparison with corrected experiment measurements. Comparison with experimental data after the third or fourth peak is not as good here as in the one-dimensional case (***Figure 78***), but it is probably also an effect of the three-dimensional mesh.

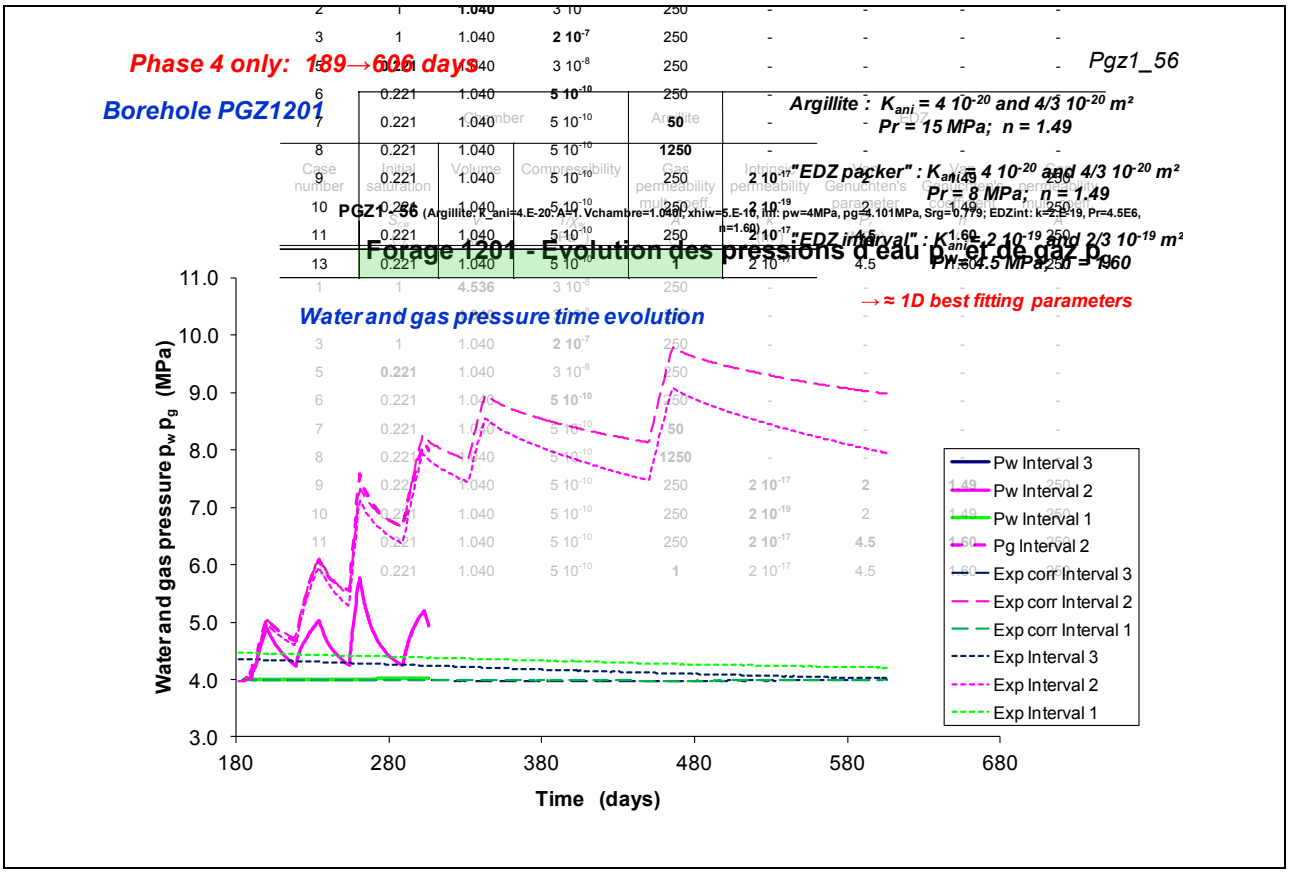

Figure 84 : Numerical results of the phase 4 only, for PGZ1201 borehole intervals, and comparison with experimental data.

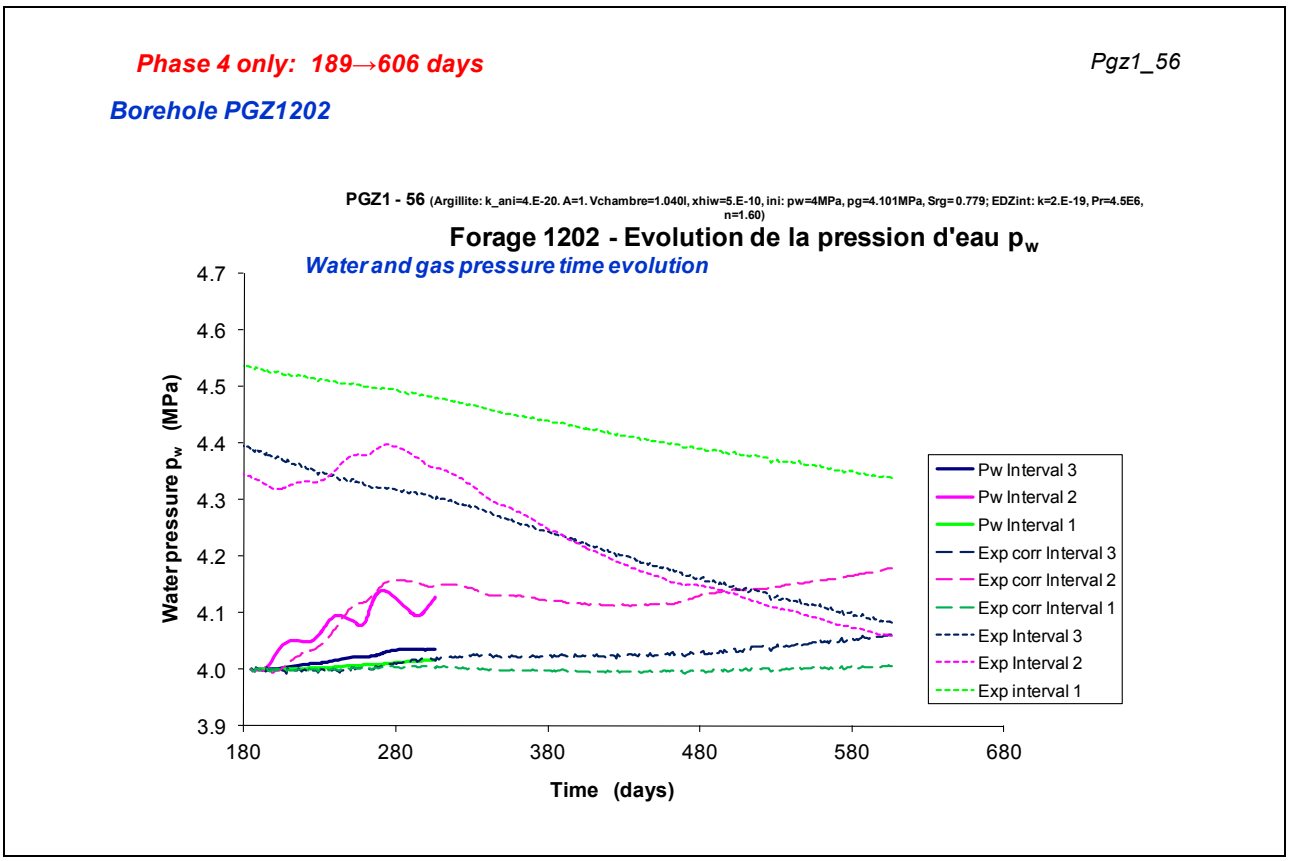

Figure 85 : Numerical results of the phase 4 only, for PGZ1202 borehole intervals, and comparison with experimental data.

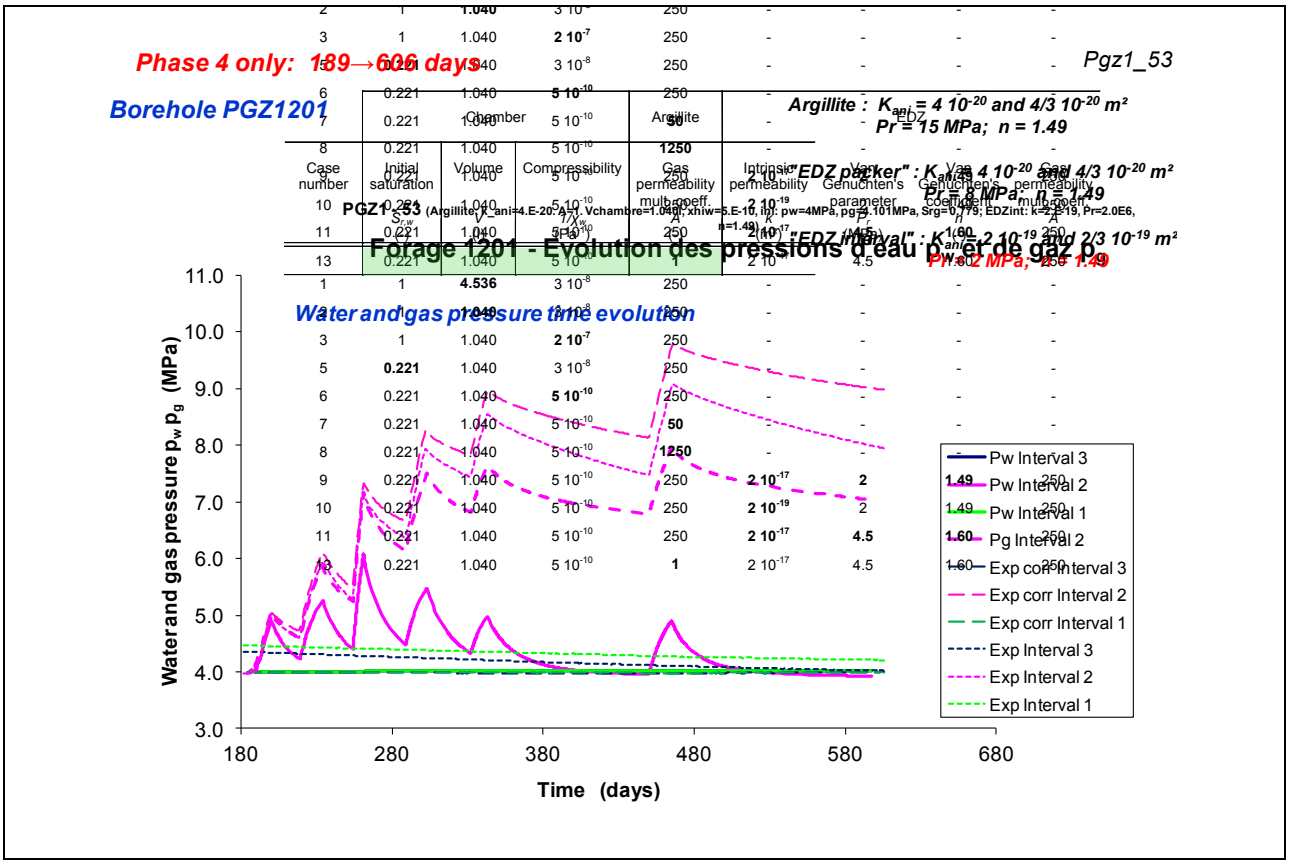

Figure 86 : Numerical results of the phase 4 only, for PGZ1201 borehole intervals, and comparison with experimental data.

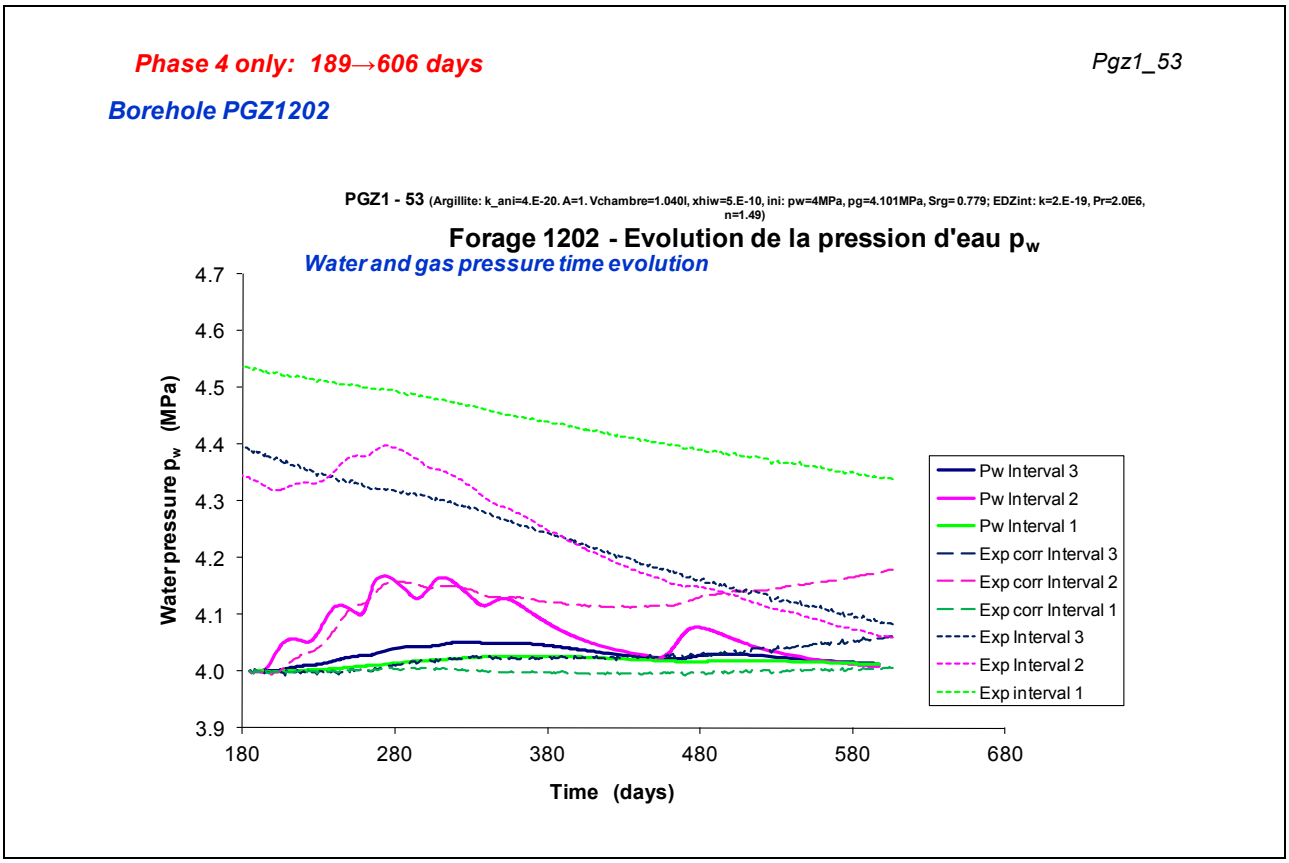

Figure 87 : Numerical results of the phase 4 only, for PGZ1202 borehole intervals, and comparison with experimental data.

10 DISCRETISATION, INITIAL AND BOUNDARY CONDITIONS OF THE 1D SIMULATIONS (SET 2)

10.1 Considered cases (set 2)

A new set of 1D simulations was performed, with more consistent parameters between argillite and EDZ (same gas relative permeability law, same gas permeability multiplier coefficient *A*, same Van Genuchten's coefficient *n*). Nevertheless, the 6 simulations of that set remain quite similar to these related to set 1.

Table 6 presents the different cases for the second set of simulations and some parameters which were considered and modified in that one-dimensional modelling set. All the other parameters values remain similar to those defined previously in Table 1 to Table 4. For each case, we note in bold the parameters values which were modified compared to the previous case.

	Chamber		Argillite	EDZ	
Case number	Initial saturation $S_{r,w}$ (-)	Volume V (l)	Gas relative permeability law (-)	Water intrinsic permeability k (m²)	Gas relative permeability law (-)
1'	1	**4.536**	Cubic	-	-
2'	1	**1.040**	Cubic	-	-
6'	0.221	1.040	Cubic	-	-
11'	0.221	1.040	Cubic	$2\ 10^{-17}$	Cubic
11b'	0.221	1.040	Cubic	**$2\ 10^{-19}$**	Cubic
15'	0.221	1.040	**Mualem – m=1.6**	$2\ 10^{-19}$	**Mualem – m=1.6**

Table 6: Considered cases for the 1D simulations (set 2).

For all these new simulations, following parameters remain constant :

Chamber :	Compressibility	$1/\chi_w$:	$5\ 10^{-10}$ Pa^{-1}	
	Van Genuchten's parameter	P_r :	0.005 MPa	
Argillite :	Gas permeability mult. coeff.	A :	100	($k_{r,min}$: 10^{-11})
	Van Genuchten's parameter	P_r :	15.0 MPa	
	Van Genuchten's coefficient	n :	1.49	
EDZ :	Gas permeability mult. coeff.	A:	100	($k_{r,min}$: 10^{-11})
	Van Genuchten's parameter	P_r :	3.0 MPa	
	Van Genuchten's coefficient	n :	1.49	

11 1D NUMERICAL RESULTS (SET 2) AND COMPARISONS WITH IN-SITU MEASUREMENTS

The experimental measurements were already corrected by removing the linear pressure tend, decrease due to PGZ1031 borehole drainage, (cfr ***Figure 55***) and noted "Exp linear corr." on following figures. After discussion with Andra, these measurements are now corrected by removing the pressure decreasing tend, always due to PGZ1031 borehole drainage (noted "Exp decreasing corr." on following figures). For information, this pressure decreasing tend are given by Andra with following equations where t is the time in days ($t \geq 185$ days):

$\underline{Borehole\ PGZ1201:}$

$$PRE01: \quad pressure\,(bar) = 46.54559813 - 0.01176623606.t + 7.242850218.10^{-6}.t^2 - 5.391795745.10^{-10}.t^3 - 5.990370683.10^{-13}.t^4$$

$$PRE02: \quad pressure\,(bar) = 44.49227043 - 0.03468704189.t + 4.721757633.10^{-5}.t^2 + 3.054931475.10^{-8}.t^3 + 7.897159211.10^{-12}.t^4$$

$$PRE03: \quad pressure\,(bar) = 45.44343394 - 0.01057973069.t - 6.271681805.10^{-7}.t^2 + 7.604753236.10^{-9}.t^3 - 3.005405014.10^{-12}.t^4$$

$\underline{Borehole\ PGZ1202:}$

$$PRE01: \quad pressure\,(bar) = 46.04934234 - 0.00204367367.t - 1.349516222.10^{-5}.t^2 + 2.174966727.10^{-8}.t^3 - 1.253585218.10^{-11}.t^4 + 2.561774519.10^{-15}.t^5$$

$$PRE02: \quad pressure\,(bar) = 45.64732834 - 0.01266238561.t - 2.161196915.10^{-6}.t^2 + 2.097600023.10^{-8}.t^3 - 1.667358399.10^{-11}.t^4 + 4.092553405.10^{-15}.t^5$$

$$PRE03: \quad pressure\,(bar) = 45.46301732 - 0.005760331934.t - 2.168963242.10^{-5}.t^2 + 4.444634826.10^{-8}.t^3 - 2.95773806.10^{-11}.t^4 + 6.727064754.10^{-15}.t^5$$

Figure 88 presents, for the case 1' defined in Table 6, the time evolution of the water and gas pressures in the injection chamber and in the argillite close to the chamber. The experimental measurements and the corrected ones are also given on that figure. We note that the evolutions of gas and water pressure are clearly identical.

For this case, the volume of the chamber equals to 4.356 *l* and its initial water saturation equals to 1. EDZ is not taken into account. The isotropic argillite permeability is always taken to 4 10^{-20} m² and the gas relative permeability law is cubic.

Figure 89 presents the time evolution of gas saturation: in the chamber the gas saturation varies from 0 to 0.64 and in the argillite, close to the chamber, it remains equals to 0 during all the simulation. On the space evolution of water saturation it appears that all the argillite remains saturated during all the gas injection phase. The space evolution of gas flows shows that these

flows are only dissolved and there is no observed gaseous flow. Finally, ***Figure 59*** presents also the space evolutions of water and gas pressure.

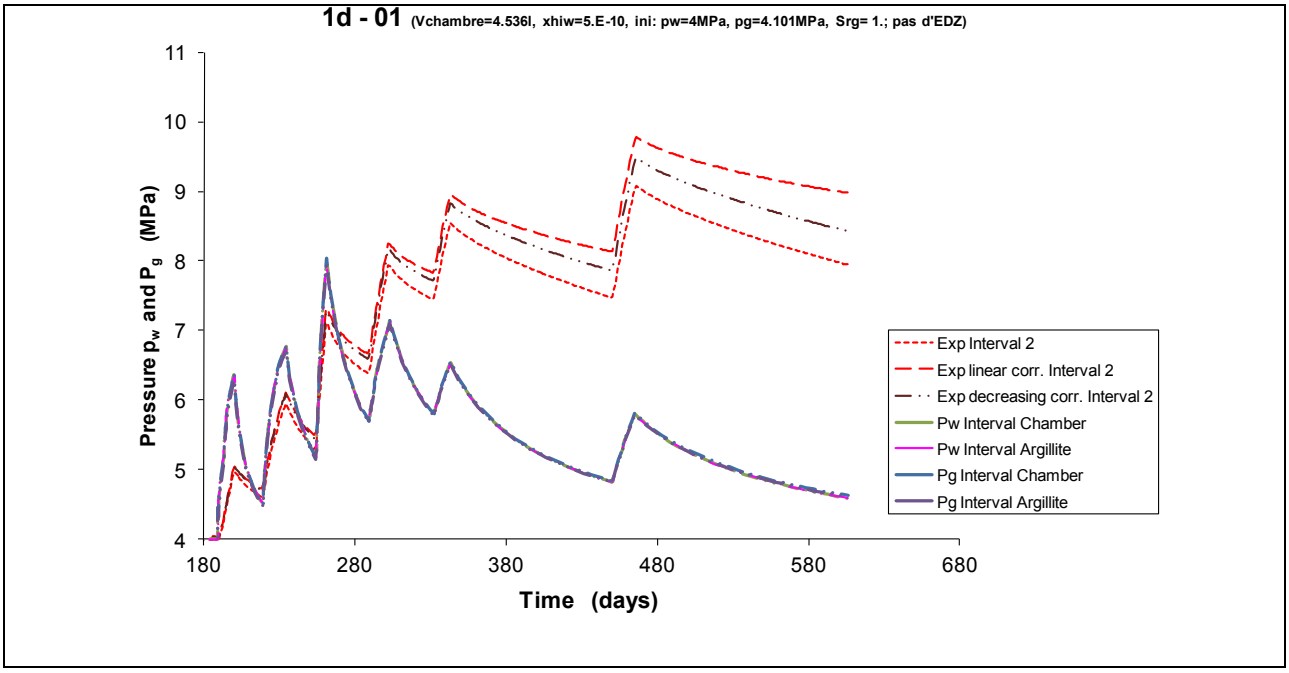

Figure 88 : Time evolution of water and gas pressures, for case 1' of 1D simulations (set 2).

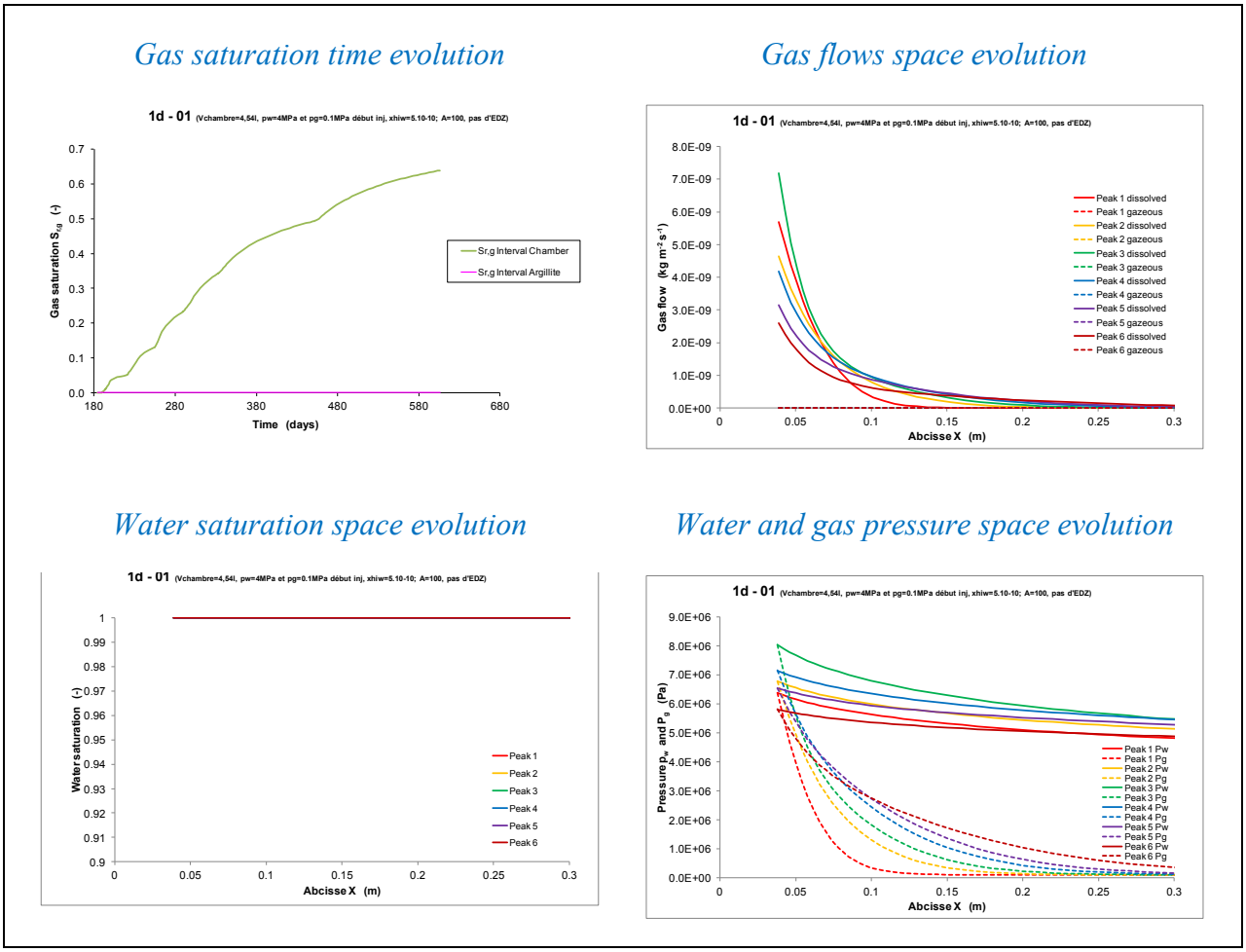

Figure 89 : Time evolution of gas saturation and space evolutions of gas flows, water saturation, water and gas pressures, for case 1' of 1D simulations (set 2).

Figure 90 presents, for the case 2' defined in Table 6, the time evolution of the water and gas pressures in the injection chamber and in the argillite close to the chamber. The experimental measurements and the corrected experimental measurements are also given on that figure. We note that the evolutions of gas and water pressure are identical until the 3rd peak. After the two pressures evolutions are clearly different: the water pressure drops after the 3rd peak while the gas pressure continues to rise. Until the 3rd peak, the obtained pressure peaks are greater than the observed experimental measurements.

For this case, the volume of the chamber equals to 1.040 *l* and its initial water saturation equals to 1. EDZ is not taken into account. The isotropic argillite permeability is always taken to 4 10^{-20} m² and the gas relative permeability law is cubic.

Figure 91 compares the time evolution of gas pressure for the cases 1' and 2'.

Figure 92 presents the time evolution of gas saturation: in the chamber the gas saturation varies now from 0 to 0.96 and in the argillite, close to the chamber, it remains equals to 0 during the 3 first peaks and rises to maximum 0.040 after. On the space evolution of water saturation it appears that the argillite begins to desaturate after the 3rd peak, till to 18 cm depth for the 6th peak (with minimum water saturation = 0.960). Of course, gaseous flows, greater than dissolved ones, appear after the 3rd peak. Finally, ***Figure 92*** presents the space evolutions of water and gas pressure, where we note also the gap between the two pressures after the 3rd gas injection peak.

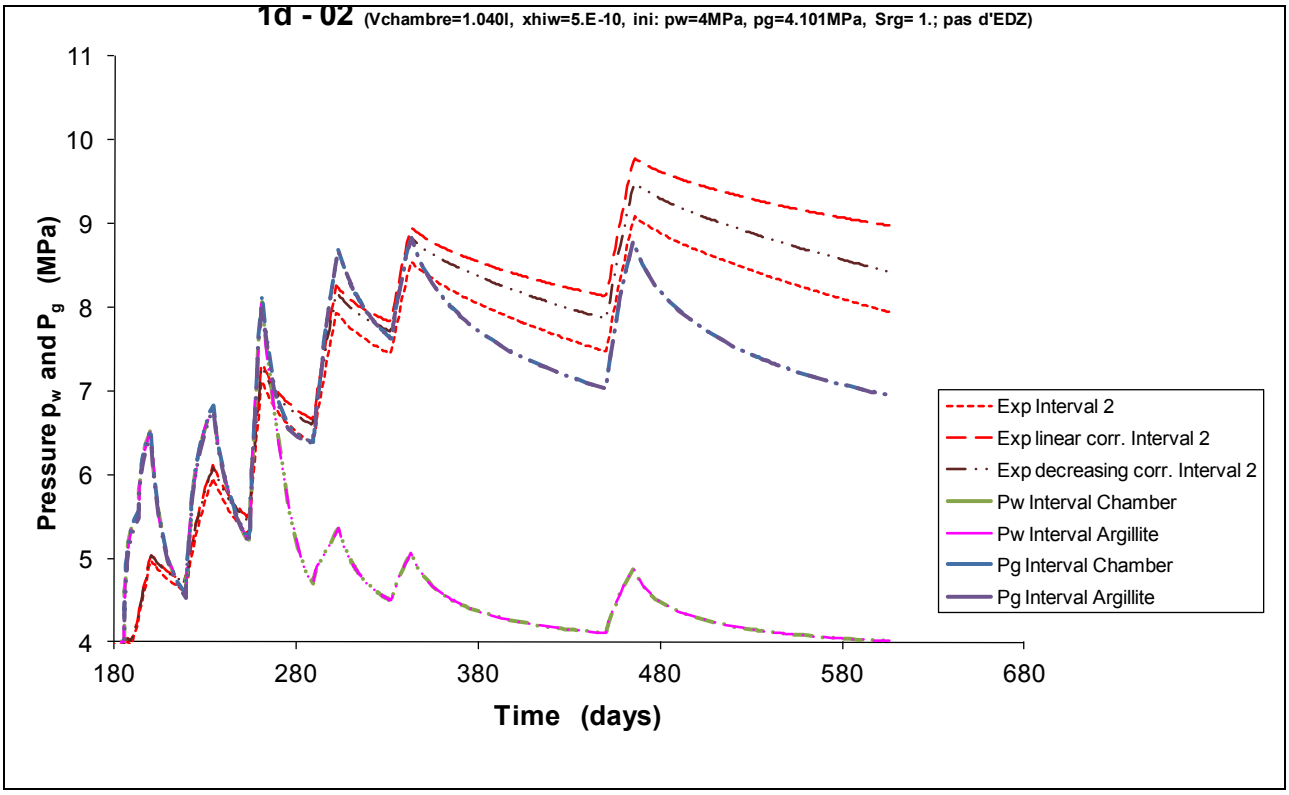

Figure 90 : Time evolution of water and gas pressures, for case 2' of 1D simulations (set 2).

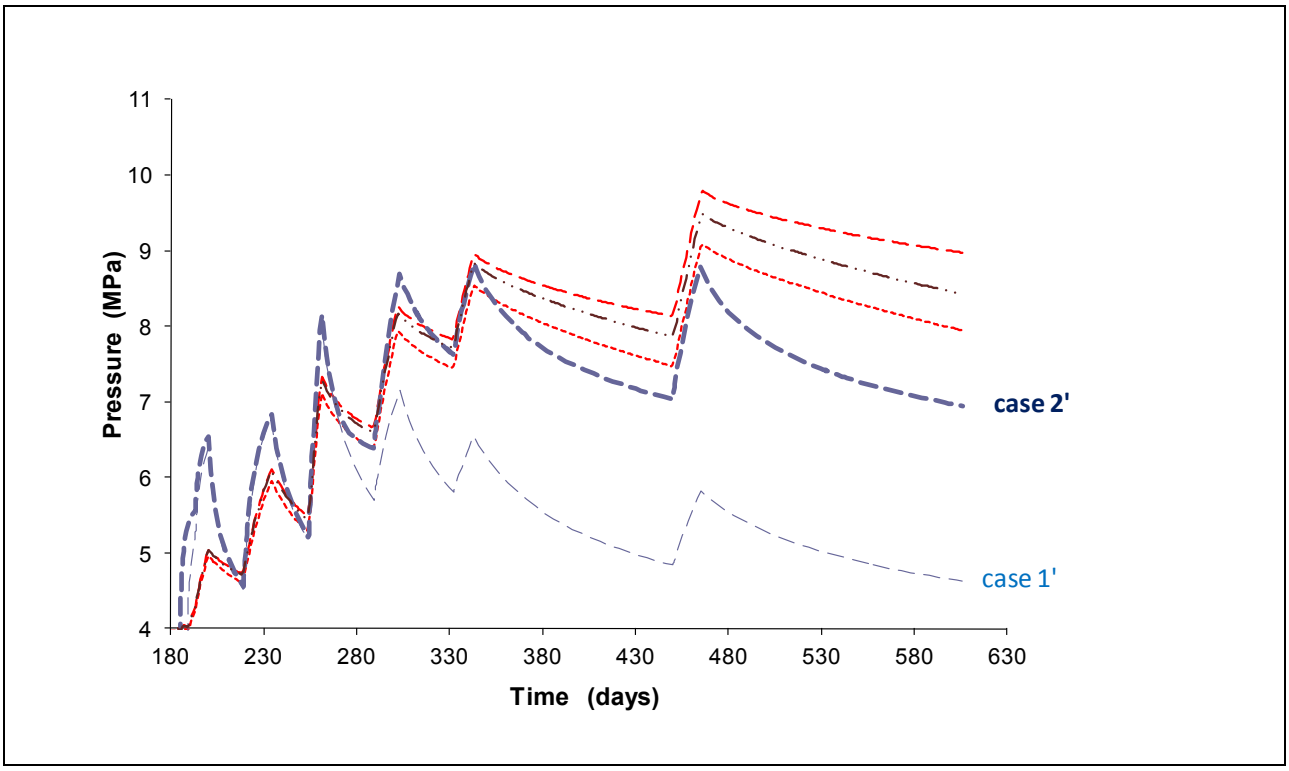

Figure 91 : Comparison of time evolution of gas pressure, between case 1' and case 2'.

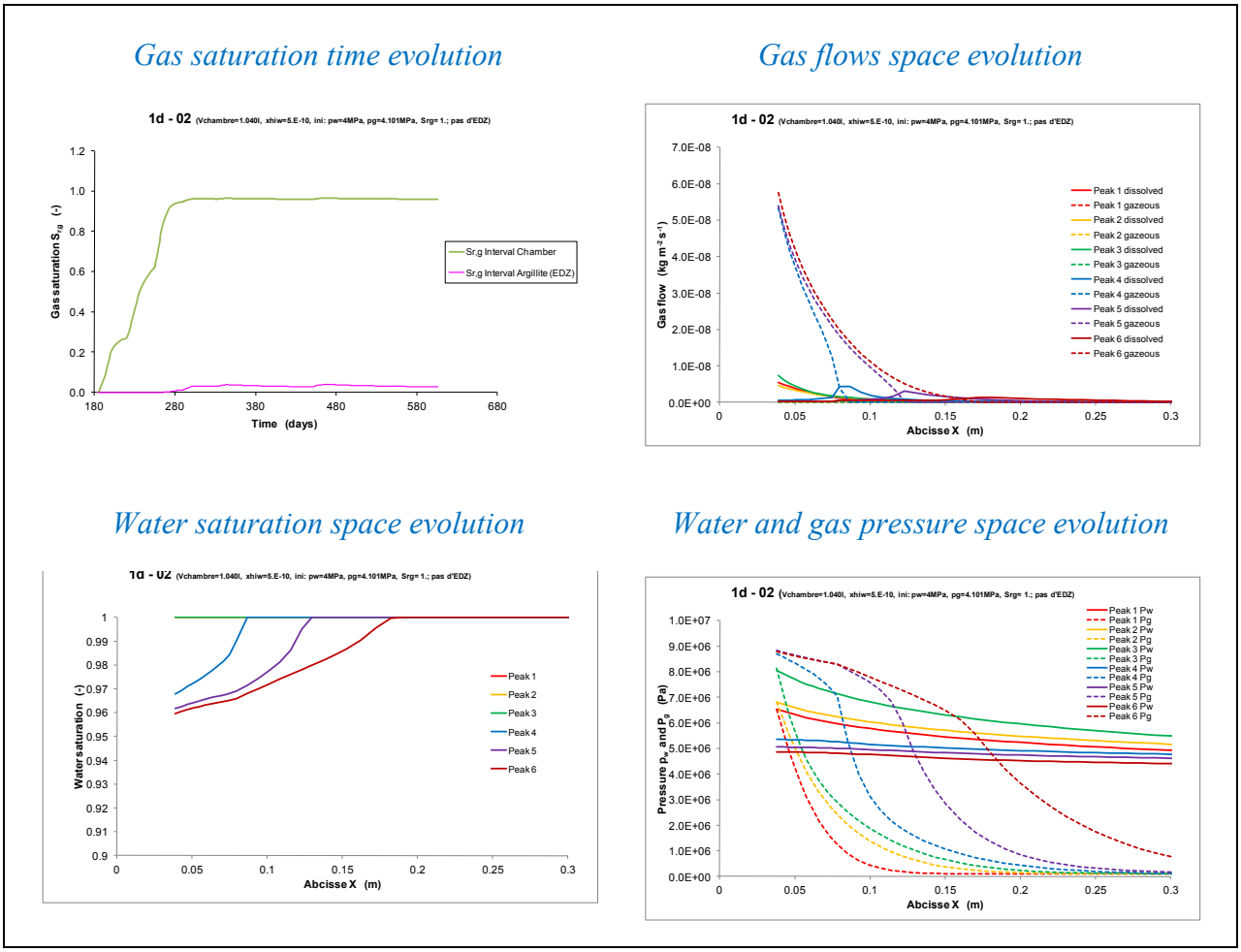

Figure 92 : Time evolution of gas saturation and space evolutions of gas flows, water saturation, water and gas pressures, for case 2' of 1D simulations (set 2).

Figure 93 presents, for the case 6', defined in Table 6, the time evolution of the water and gas pressures in the injection chamber and in the argillite close to the chamber. The experimental measurements and the corrected experimental measurements are also given on that figure. We note that from the 1st peak, the two water and gas pressures evolutions are clearly different: the water pressure changes little after the 1st peak while the gas pressure continues to rise, for the 4 first peaks, well beyond the observed experimental measurements.

For this case, the volume of the chamber equals to 1.040 *l* and its initial water saturation equals to 0.221. EDZ is not taken into account. The isotropic argillite permeability is always taken to 4 10^{-20} m² and the gas relative permeability law is cubic.

Figure 94 compares the time evolution of gas pressure for the cases 2' and 6'.

Figure 95 presents the time evolution of gas saturation: in the chamber the gas saturation varies now from 0.78 to 0.96 and in the argillite, close to the chamber, it remains equals to 0 during the 2 first peaks and rises to maximum 0.039 after. On the space evolution of water saturation it appears that the argillite begins to desaturate from the 2nd peak, till to 25 cm depth for the 6th peak (with minimum water saturation = 0.960). Of course, gaseous flows, greater than dissolved ones, appear from the 2nd peak. Finally, ***Figure 95*** presents the space evolutions of water and gas pressure, where we note also the gap between the two pressures from the 2nd gas injection peak.

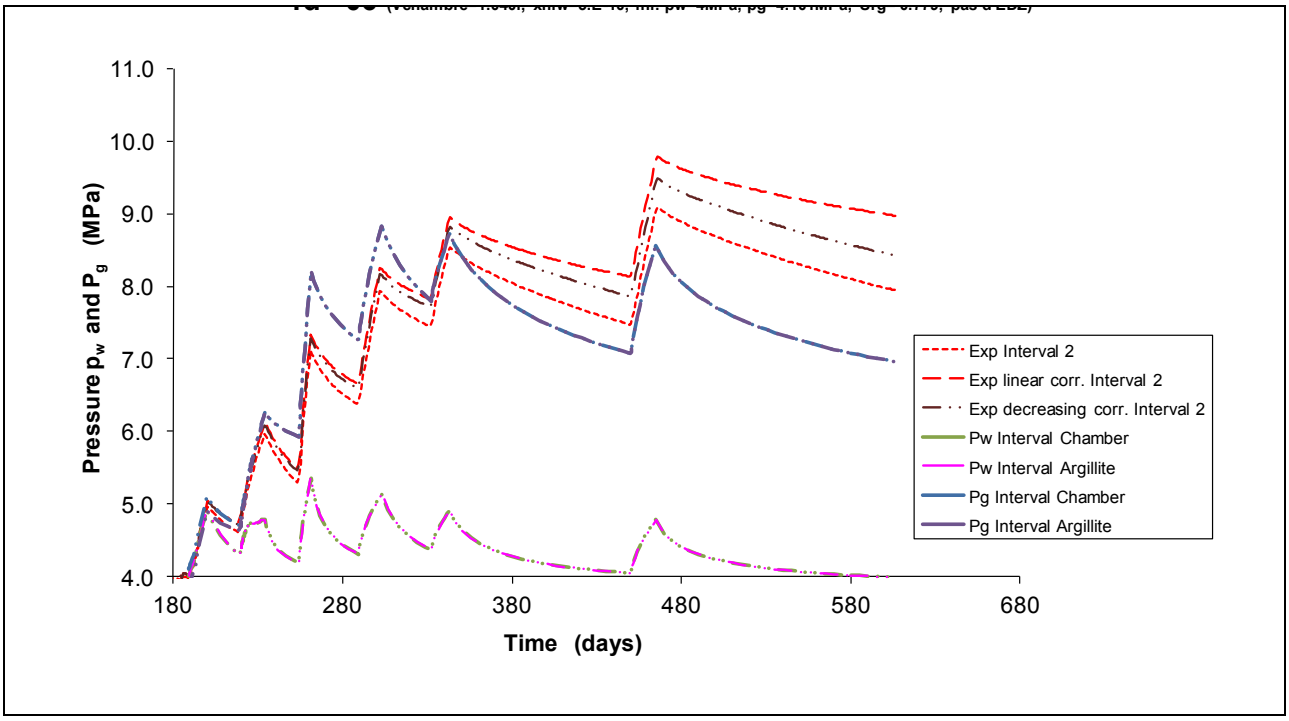

Figure 93 : Time evolution of water and gas pressures, for case 6' of 1D simulations (set 2).

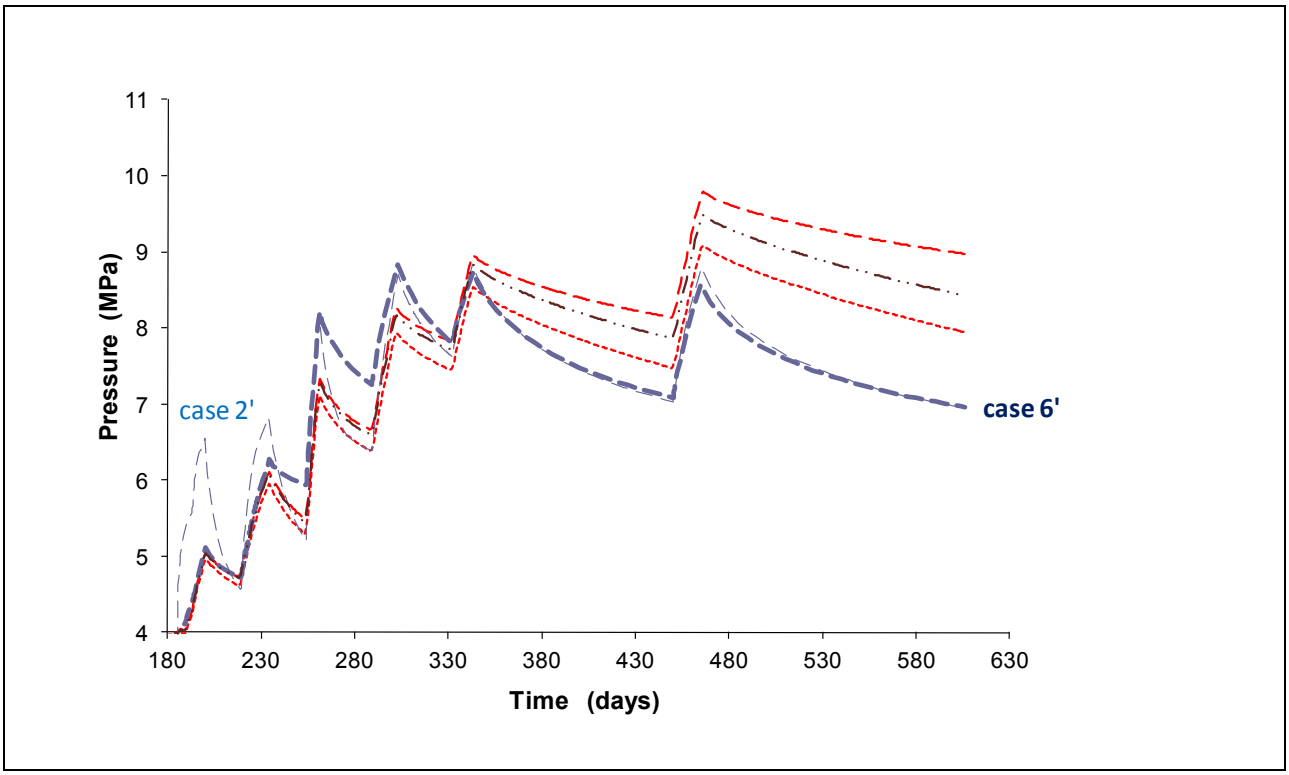

Figure 94 : Comparison of time evolution of gas pressure, between case 2' and case 6'.

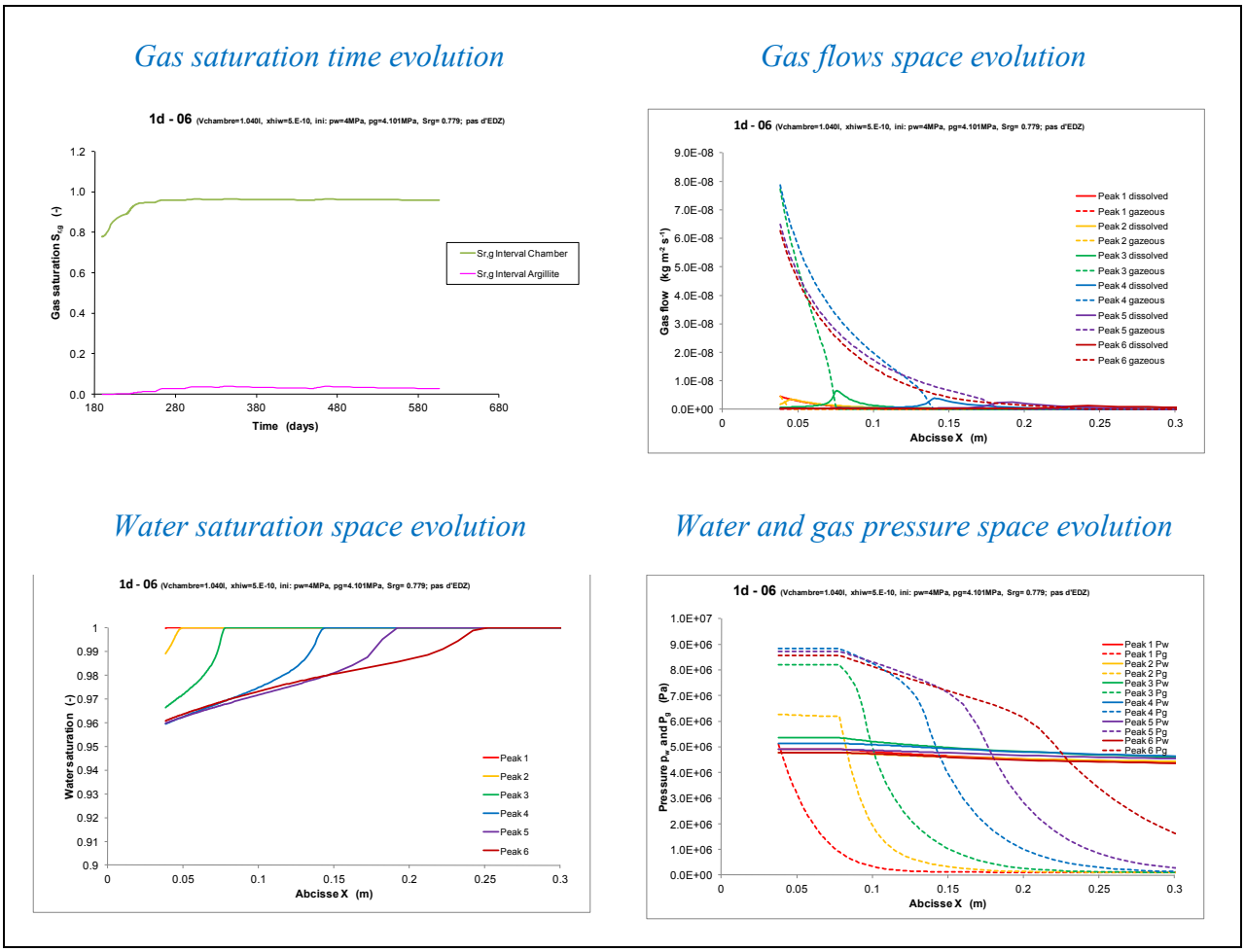

Figure 95 : Time evolution of gas saturation and space evolutions of gas flows, water saturation, water and gas pressures, for case 6' of 1D simulations (set 2).

For the case 11', defined in Table 6: Considered cases for the 1D simulations (set 2)., the volume of the chamber equals to 1.040 *l* and its initial water saturation equals to 0.221. The isotropic argillite permeability is always taken to 4 10^{-20} m² and the gas relative permeability law is cubic. EDZ of 4 cm thick is now taken into account, with a water intrinsic permeability of 2 10^{-17} m² , a cubic gas relative permeability law, a Van Genuchten's parameter P_r =2 MPa and a Van Genuchten's coefficient n =1.49.

Figure 96 presents, for that case 11', the time evolution of the water and gas pressures in the injection chamber and in the EDZ close to the chamber. The experimental measurements and the corrected experimental measurements are always given on that figure. This case has to compare with the case 6', with identical parameters but without EDZ (***Figure 97***). We note that, for the 3 first peaks, the evolution of gas is clearly much closer to the experimental measurements than the evolution obtained with case 6' parameters For the 3 last peaks, the obtained evolution of the gas pressure is always lower than the experimental measurements.

Figure 98 presents the time evolution of gas saturation: in the chamber the gas saturation varies now from 0.78 to 0.96 and in the EDZ, close to the chamber, it varies from 0 to maximum 0.22 after. On the space evolution of water saturation it appears that the EDZ begins to desaturate after the 1st peak and the argillite after the 2nd one, till to 18 cm depth for the 6th peak (with minimum water saturation = 0.969 in argillite and 0.784 in EDZ). Gaseous flows appear early from the 1st peak. Finally, ***Figure 98*** presents the space evolutions of water and gas pressure, where we note also the gap between the two pressures from the 2nd gas injection peak.

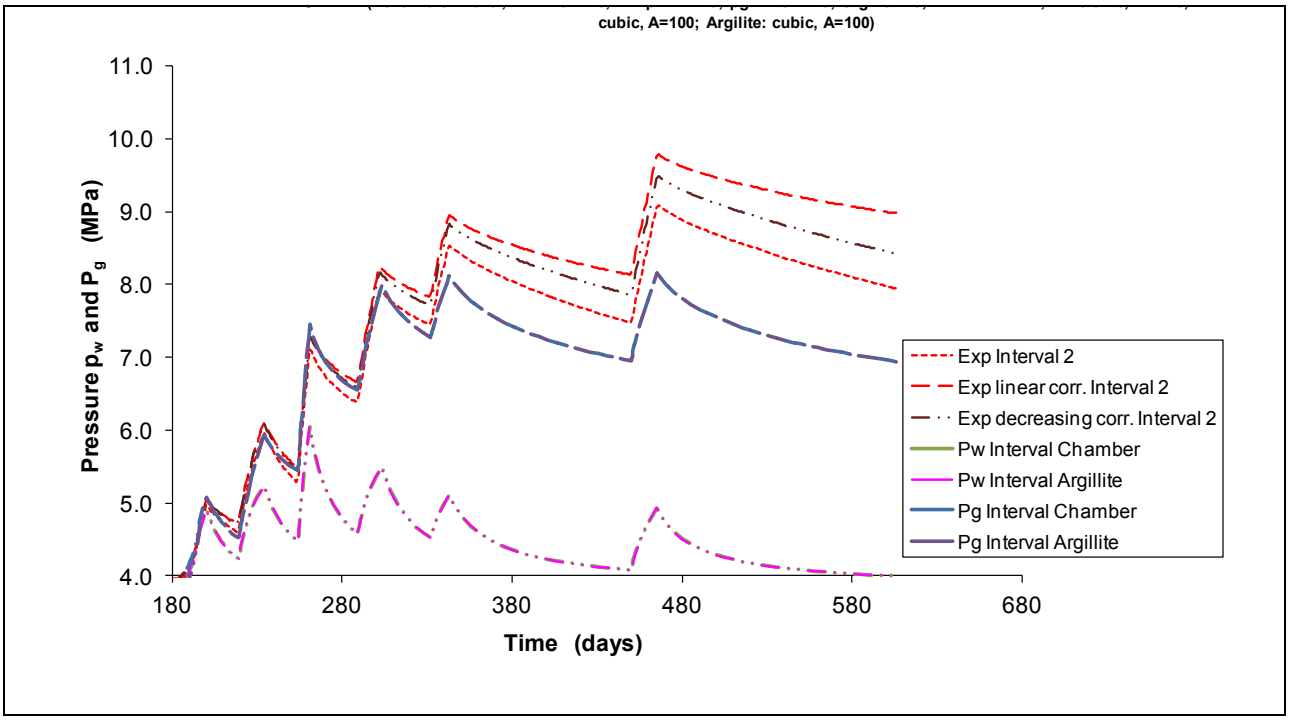

Figure 96 : Time evolution of water and gas pressures, for case 11' of 1D simulations (set 2).

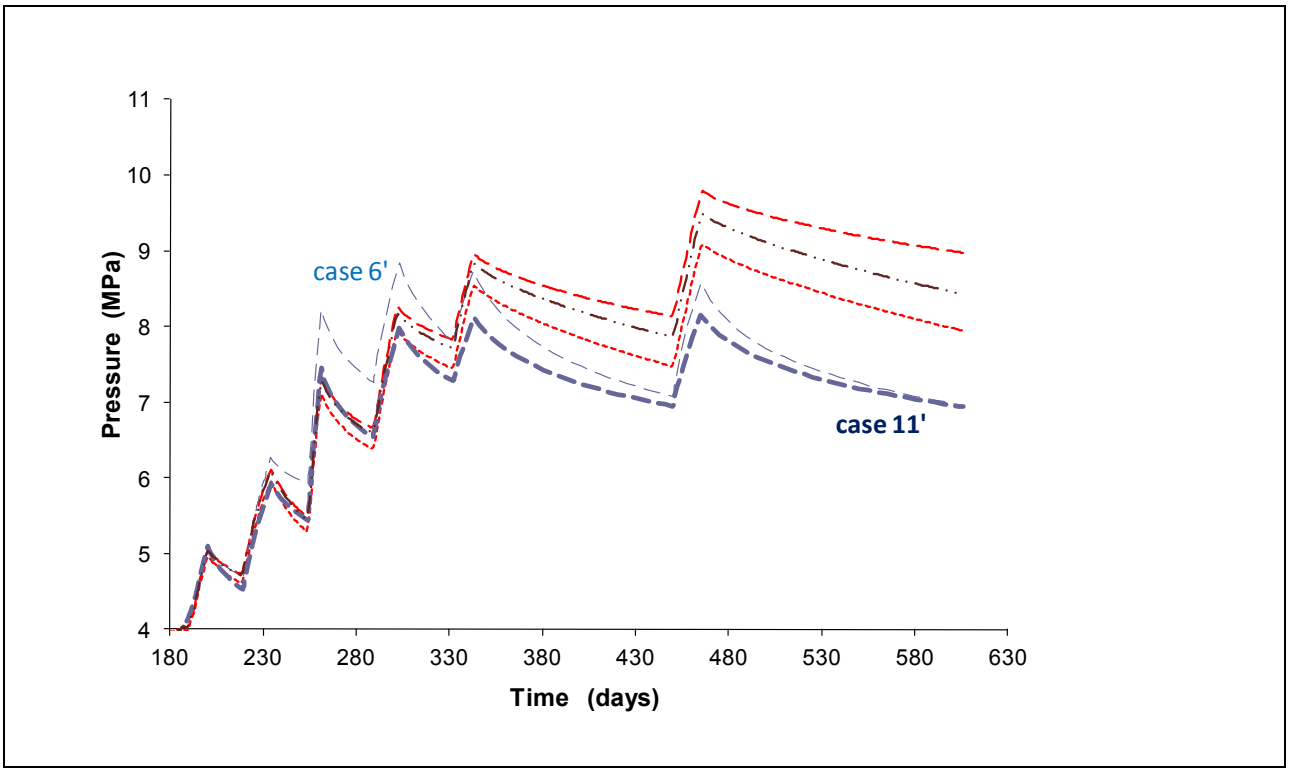

Figure 97 : Comparison of time evolution of gas pressure, between case 6' and case 11'.

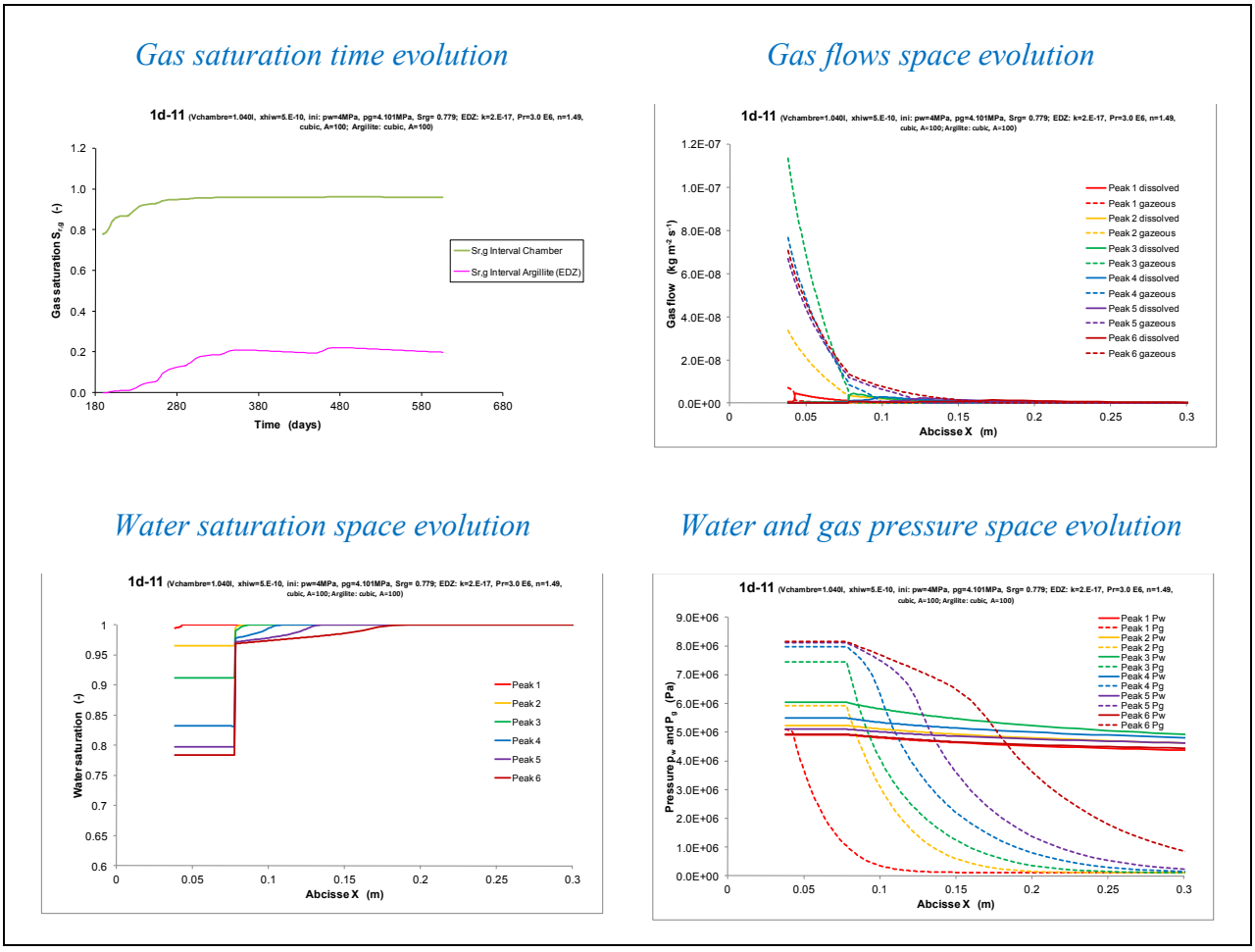

Figure 98 : Time evolution of gas saturation and space evolutions of gas flows, water saturation, water and gas pressures, for case 11' of 1D simulations (set 2).

Case 11b', defined in Table 6 and presented on ***Figure 99 : Time evolution of water and gas pressures, for case 11b' of 1D simulations (set 2).*** and ***Figure 101***. This case is identical to the presented previous one, except for the EDZ permeability which is equal here to 2 10^{-19} m² (instead of 2 10^{-17} m² in case 6'). We note that there is only very little difference between the results of two cases (***Figure 100***), but globally the general behaviour is identical between the two cases 6' and 11b'.

Figure 101 presents the time evolution of gas saturation: in the chamber the gas saturation varies now from 0.78 to 0.96 and in the EDZ, close to the chamber, it varies from 0 to maximum 0.22 after. On the space evolution of water saturation it appears that the EDZ always begins to desaturate after the 1st peak and the argillite after the 2nd one, till to 18 cm depth for the 6th peak (with minimum water saturation = 0.969 in argillite and 0.783 in EDZ). Gaseous flows appear from the 2nd peak. Finally, ***Figure 101*** presents the space evolutions of water and gas pressure, where we note also the gap between the two pressures from the 2nd gas injection peak.

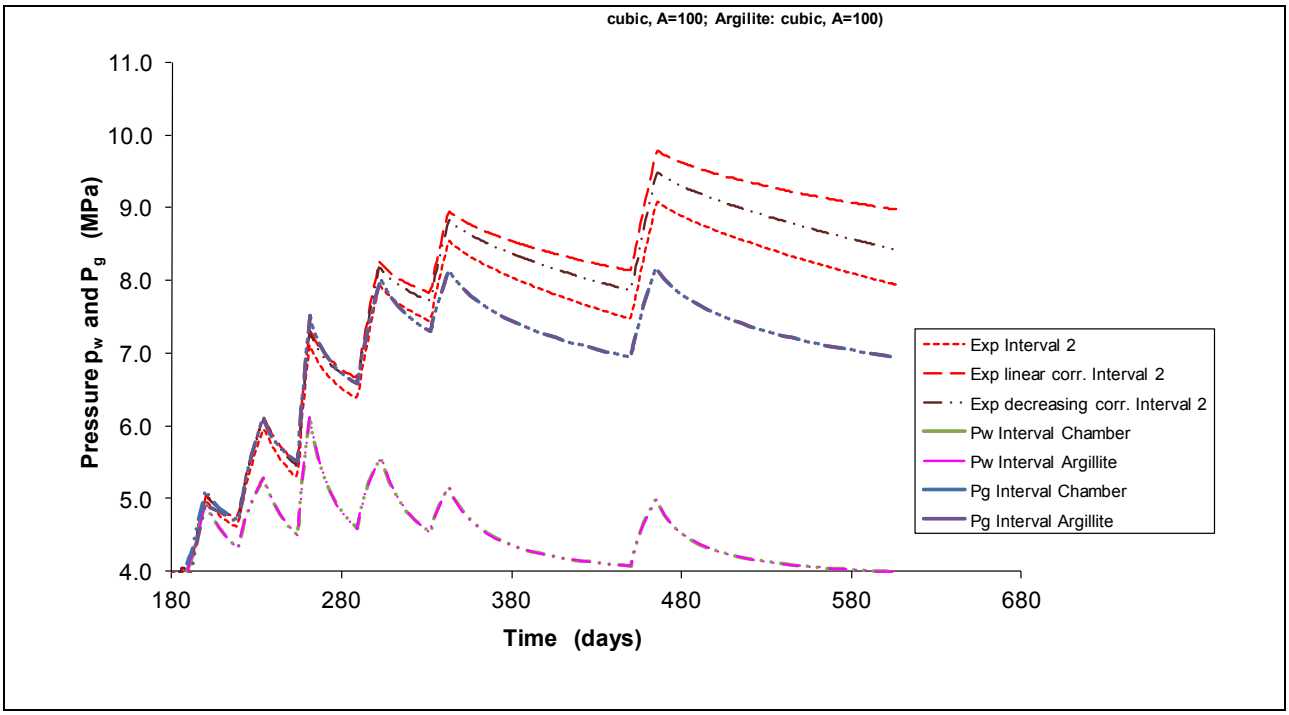

Figure 99 : Time evolution of water and gas pressures, for case 11b' of 1D simulations (set 2).

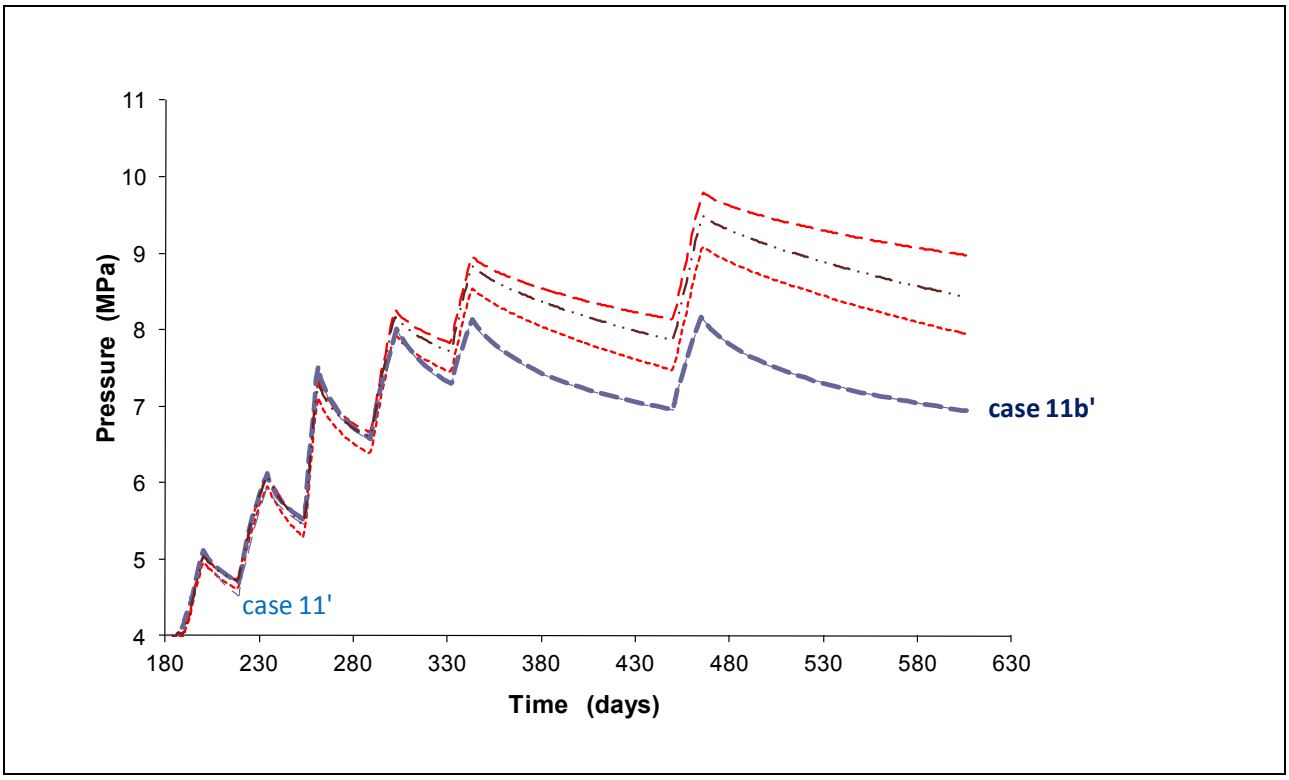

Figure 100 : Comparison of time evolution of gas pressure, between case 11' and case 11b'.

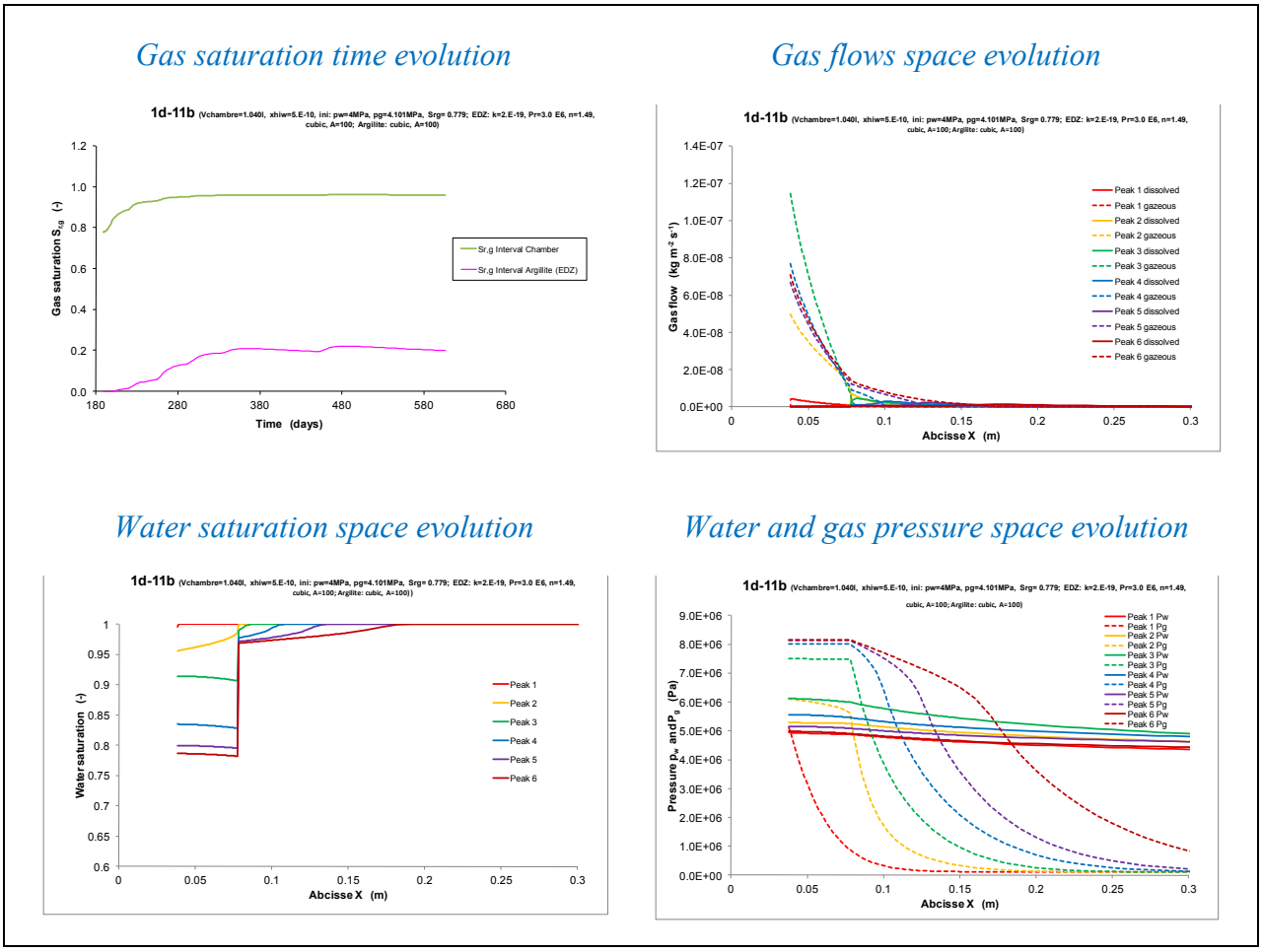

Figure 101 : Time evolution of gas saturation and space evolutions of gas flows, water saturation, water and gas pressures, for case 11b' of 1D simulations (set 2).

The case 15', defined in Table 6, is presented on ***Figure 103*** and ***Figure 105***. This case is identical to the previous one (case 11b'), except that the gas relative permeability law is now the Mualem's law (with *m*=1.6 and *A* equals always 100) instead of the cubic law previously used. This Mualem's law is used for both argillite and EDZ. So with that modification, it is possible to obtain a better agreement with the experimental measurements, especially for peaks 5 and 6 (***Figure 103***).

Figure 102 compares the Mualem's law ($k_{r,g} = A.\sqrt{1-S_{r,w}}.\ 1-S_{r,w}^{\frac{1}{m}}{}^{2.m}$) and the cubic law ($k_{r,g} = A.\ 1-S_{r,w}{}^{3}$) used for gas relative permeability.

Figure 104 compares the time evolution of gas pressure for the cases 11b' and 15'.

In the chamber the gas saturation varies now from 0.78 to 0.97 and in the EDZ, close to the chamber, it remains equals to 0 during the 1st peak and rises to maximum 0.273 after (***Figure 105***). EDZ begins always to desaturate after the 1st peak and the argillite after the 3rd one, to only 13 cm depth for the 6th peak (with minimum water saturation = 0.958 in argillite and 0.736 in EDZ). Finally, ***Figure 105*** presents the space evolutions of gas flows and water and gas pressures.

This case 15' is, for the 1D simulations set 2, the best obtained calibration on the experimental measurements.

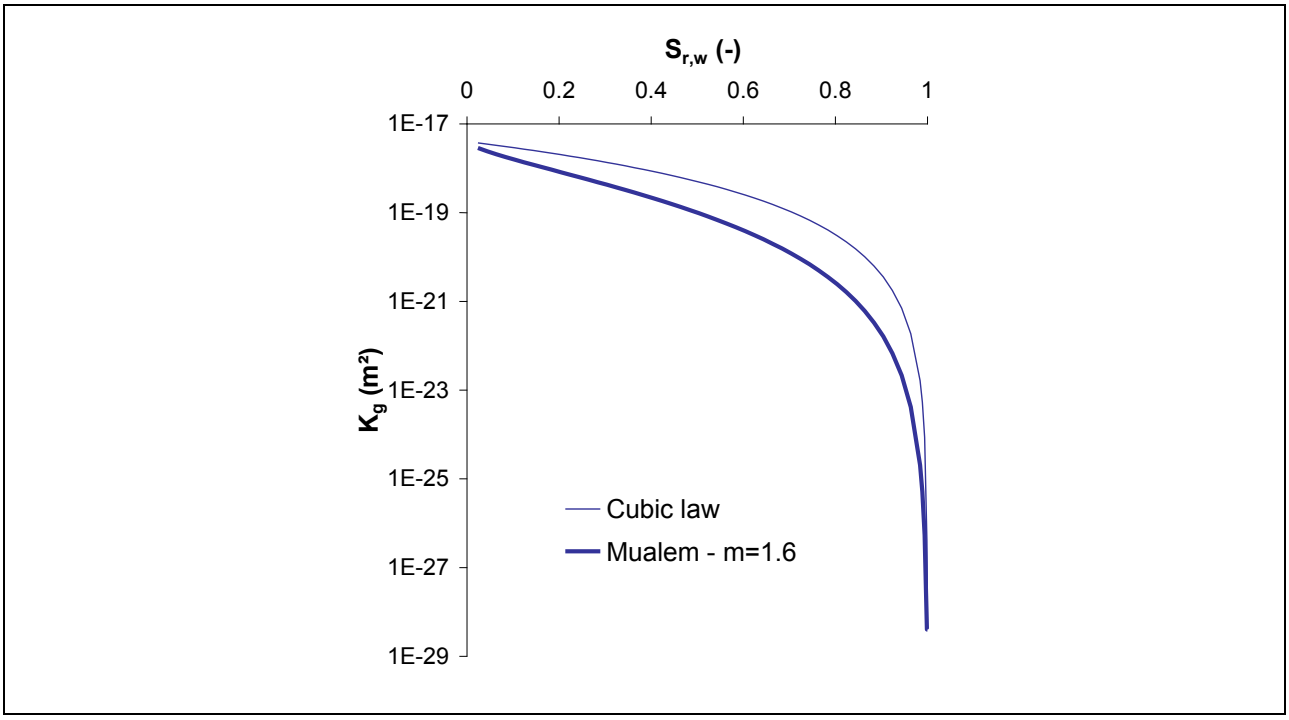

Figure 102 : Comparison of Mualem and cubic laws for gas relative permeability.

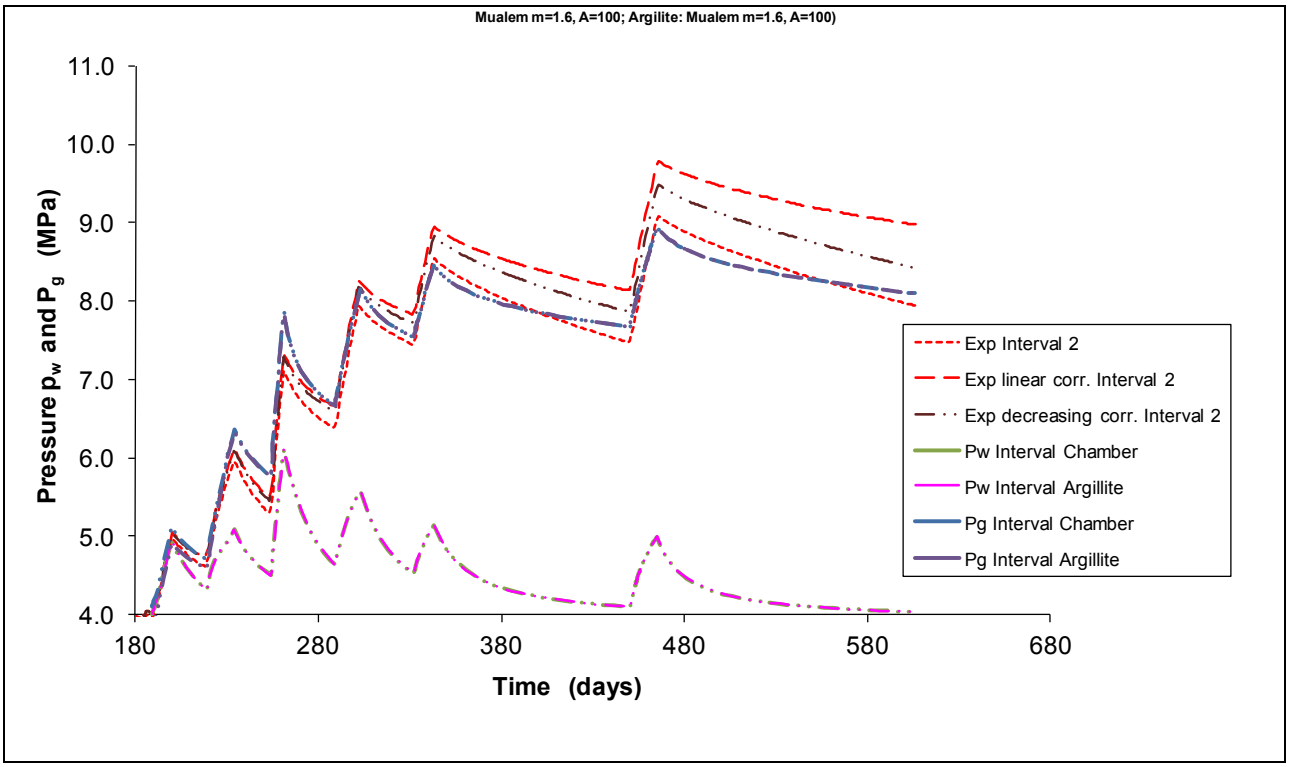

Figure 103 : Time evolution of water and gas pressures, for case 15' of 1D simulations (set 2).

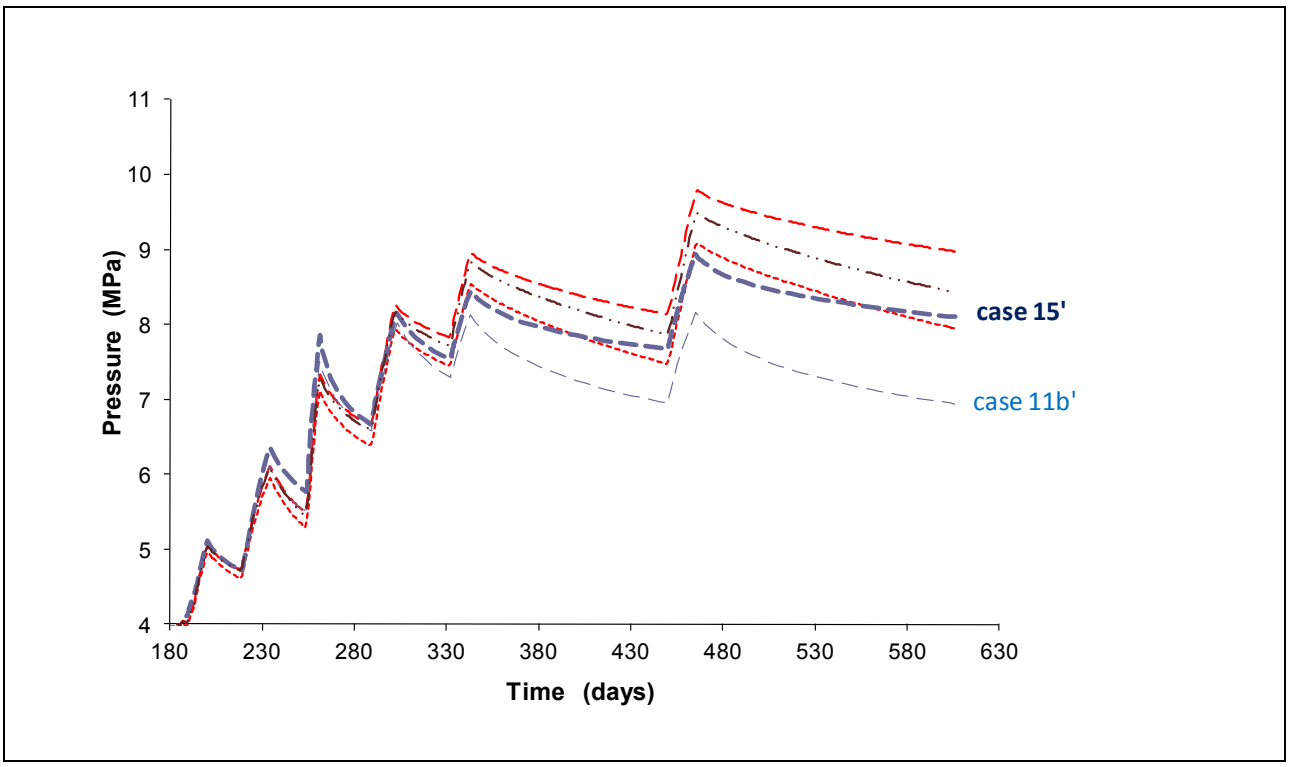

Figure 104 : Comparison of time evolution of gas pressure, between case 11b' and case 15'.

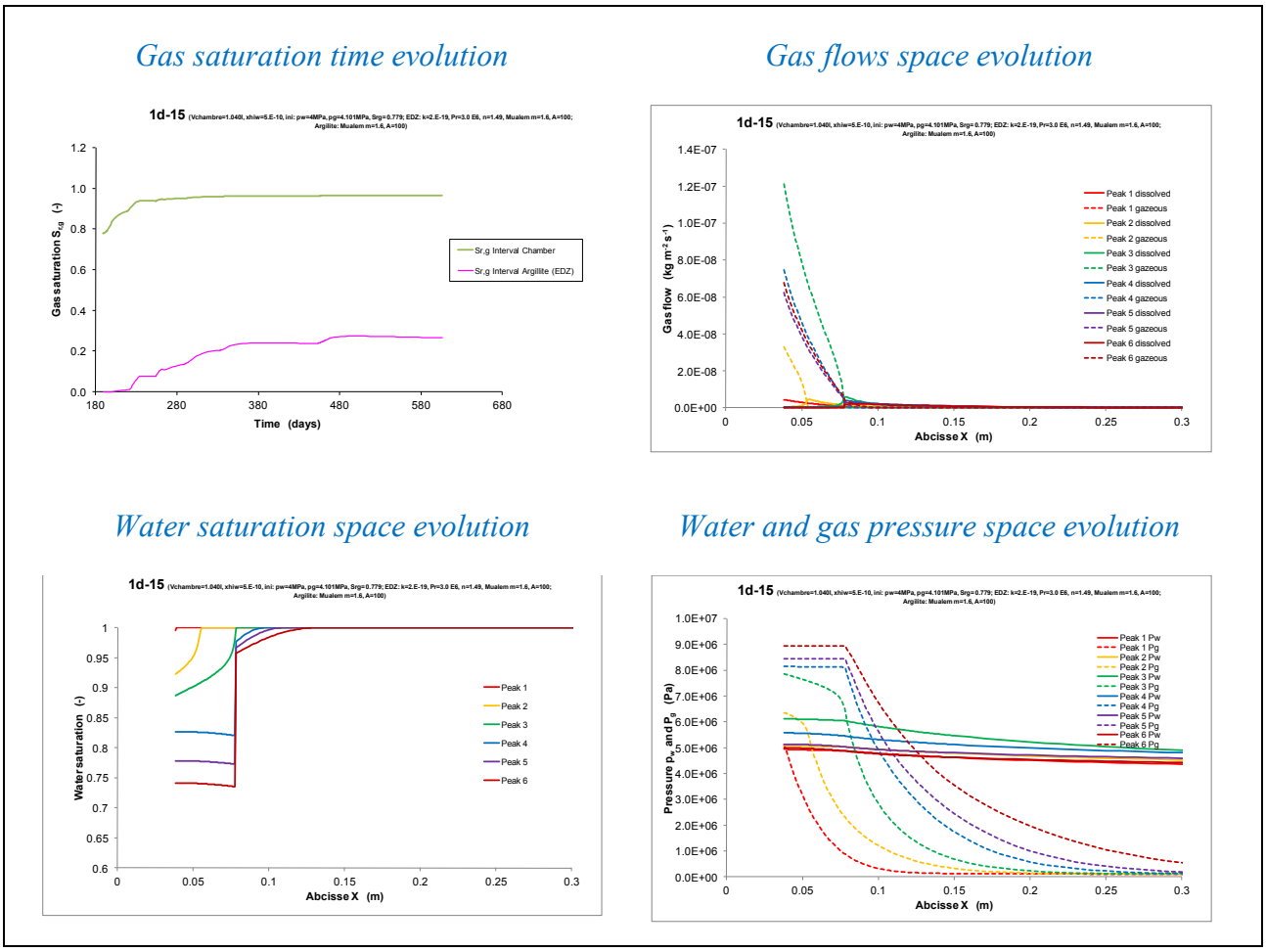

Figure 105 : Time evolution of gas saturation and space evolutions of gas flows, water saturation, water and gas pressures, for case 15' of 1D simulations (set 2).

In summary, ***Figure 106*** presents an estimation of the time ranges related to the effect of the chamber, of the EDZ and of the argillite, and so their range of influence on the obtained pressure at the PGZ1201 borehole.

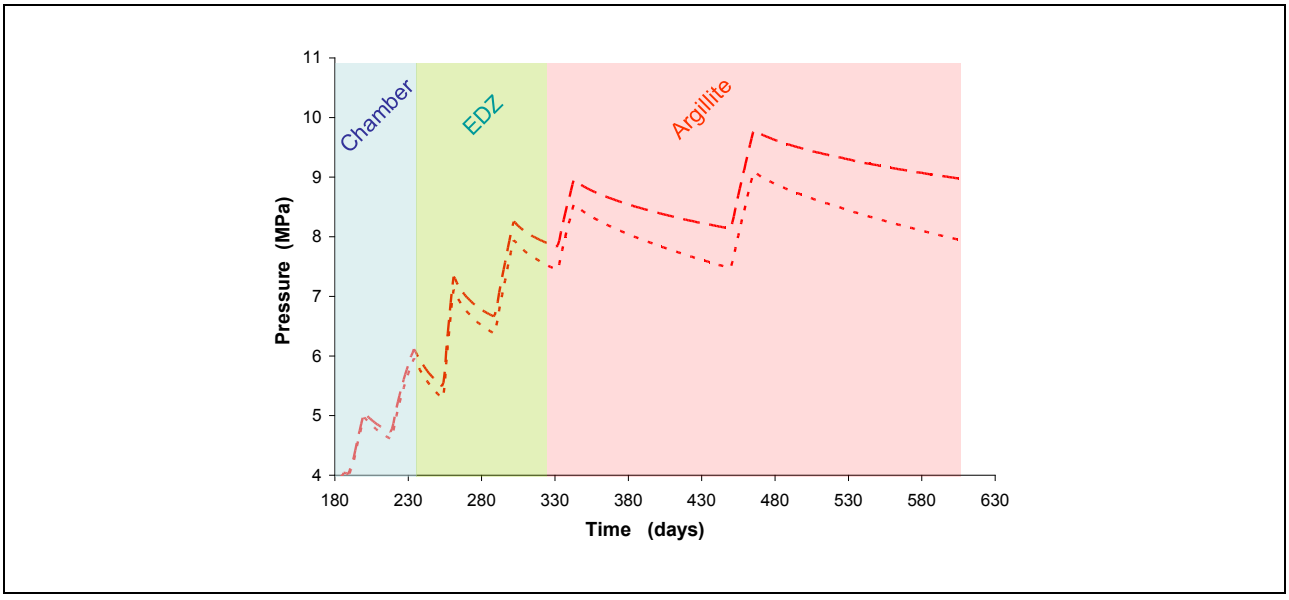

Figure 106 : Summary of time ranges related to the effect of the chamber, of the EDZ and of the argillite.

As confirmed by the gas flows profiles obtained from the best 1D modelling in a domain where the gaseous transfers are predominant (***Figure 107***), the first injection phase tests only the behaviour of the injection interval, whilst the response of the second and the third peaks are also influenced by the excavated damaged zone. It is only from the fourth peak that nitrogen reaches the undisturbed claystone and the pore pressures measurements are then influenced by its behaviour.

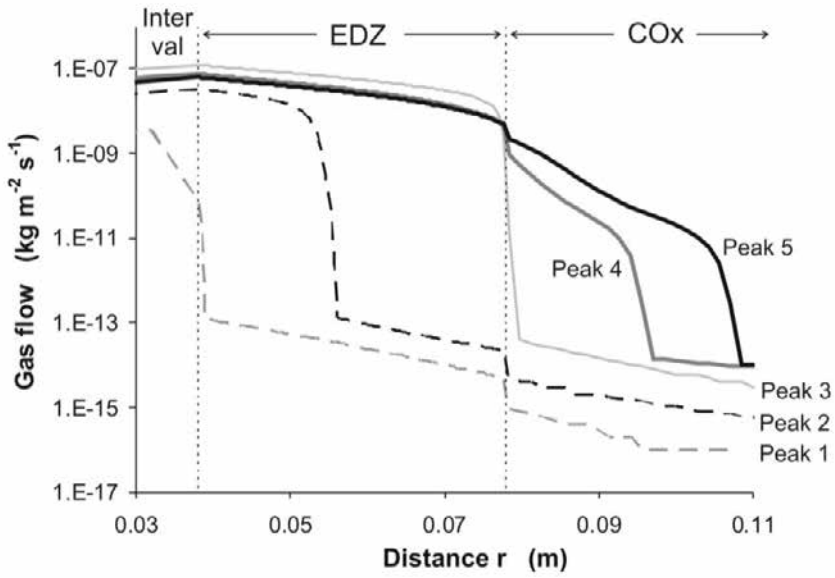

Figure 107 : Gas flows profiles at different gas injection peaks, for case 15' of 1D simulations (set 2).

For this case 15', the gas extraction phase was also simulated. That phase consists to a gas extraction flow rate of -2.9 mLn/min during 2 days (from March 30, 2011 to April 1, 2011) followed by a flow rate of -16.9 mLn/min during 12 days (from April 1, 2011 to April 13, 2011). Then a phase with constant pressure (20 bars) during 22 days is performed (from April 13, 2011 to May 5, 2011). That 3rd phase was not numerically modelled. Durant the extraction phase, an additional volume must be taken into account (see report D.NT.AMFS.11.0084, p.58). This additional volume has been estimated to 4137 cm³ (average between 4144 cm³ (extraction on small flowmeter during 2 days) and 4130 cm³ (extraction on medium flowmeter during 14 days)). Finally, for the gas extraction phase, the volume of the chamber (interval 2) has been modified and taken to 1040 + 4137 = 5177 cm³.

Figure 108 and ***Figure 109*** present the time evolution of the water and gas pressures in the injection chamber and in the argillite close to the chamber. The experimental measurements, the corrected experimental measurements and the injected/extracted gas flow are also given on these figures. We note that now, with that new interval volume, the gas extraction phase is very well represented, including a quite correct slope.

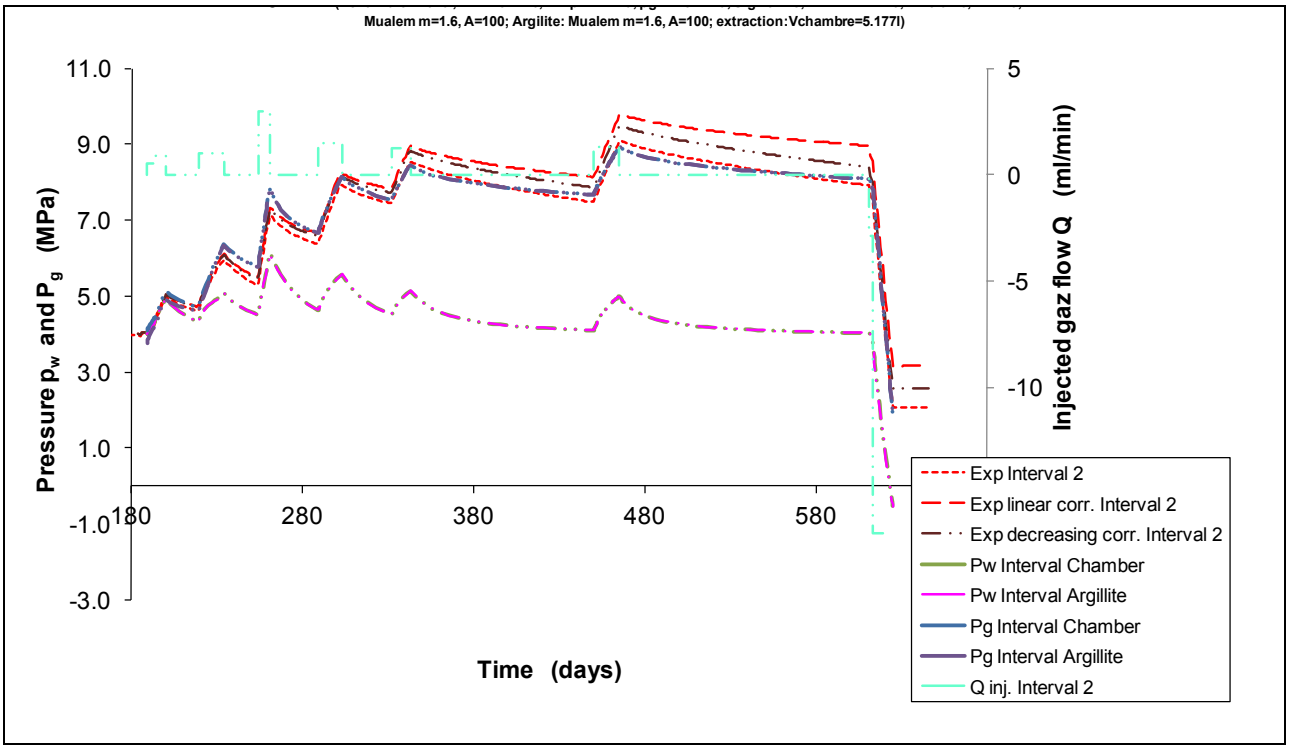

Figure 108 : Time evolution of water and gas pressures, for case 15' of 1D simulations (set 2) with extraction phase.

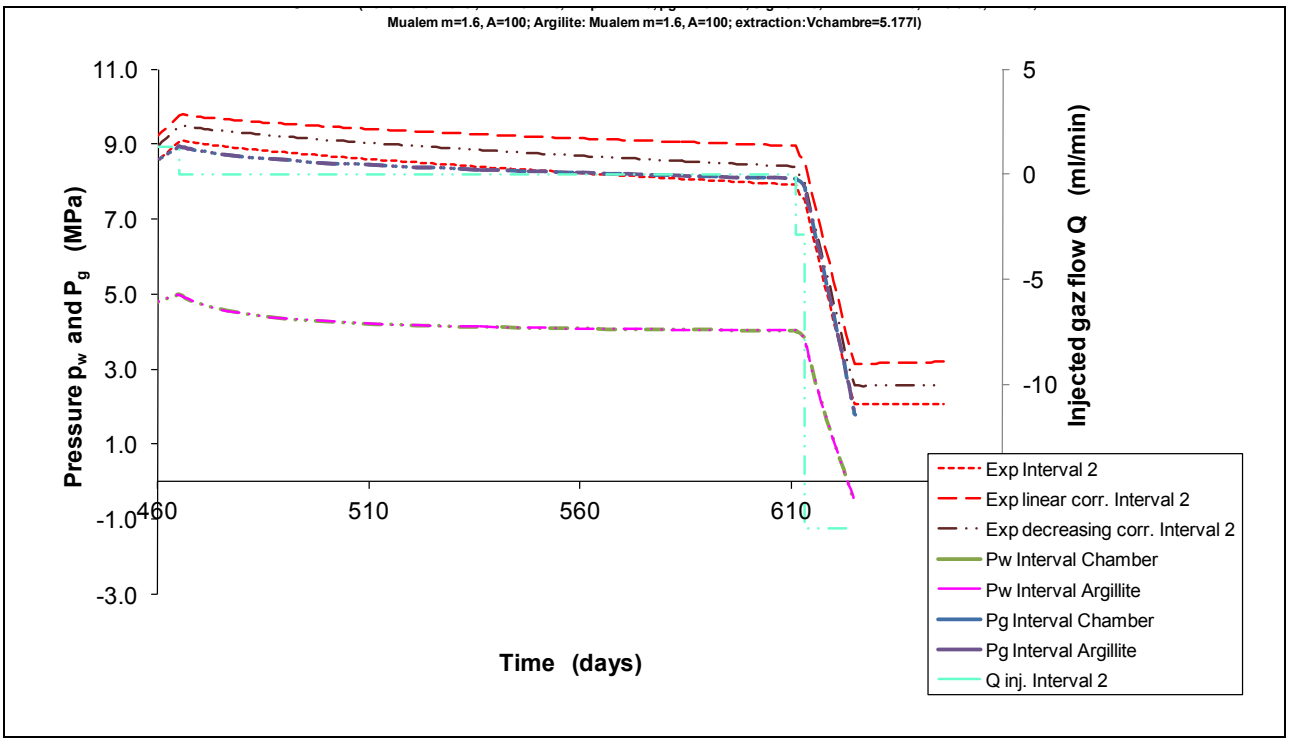

Figure 109 : Time evolution of water and gas pressures, for case 15' of 1D simulations (set 2) with extraction phase (zoom).

12 3D NUMERICAL RESULTS (SET 2) AND COMPARISONS WITH IN-SITU MEASUREMENTS

12.1 Phase 4: gas injection

Two new 3D simulations were performed taking into account of the results of the 1D simulation of set 2. For the PGZ1_74 simulation, all the parameters are identical to these of the 1D simulation 15', so the best fitting 1D calibration. For the PGZ1_70 simulation, EDZ ("interval" and "packer") parameters were slightly modified from those of the PGZ1_74 simulation.

Only the injection gas phases ("phase 4") were always simulated here, between 189 and 606 days, with, as initial conditions, a hydrostatic pressure p_w = 4 MPa in the whole model.

The main parameters for argillite, EDZ "interval" and EDZ "packer" are given in Table 7. The differences between the 2 simulations, only in EDZ parameters, are noted in bold.

		PGZ1_70	*PGZ1_74*
Argillite	Gas relative permeability law	Mualem (m=1.6)	Mualem (m=1.6)
	Anisotropic intrinsic permeability k	4 10^{-20} / 4/3 10^{-20} m²	4 10^{-20} / 4/3 10^{-20} m²
	Gas permeability mult. coeff. A	100	100
	Van Genuchten's parameter P_r	15 MPa	15 MPa
	Van Genuchten's parameter n	1.49	1.49
	Min. gas relative permea. $k_{r,min}$	10^{-11}	10^{-11}

EDZ "Interval"	Gas relative permeability law	**Cubic**	**Mualem (m=1.6)**
	Anisotropic intrinsic permeability k	$2\ 10^{-19}$ / $2/3\ 10^{-19}$ m²	$2\ 10^{-19}$ / $2/3\ 10^{-19}$ m²
	Gas permeability mult. coeff. A	**250**	**100**
	Van Genuchten's parameter P_r	**4.5 MPa**	**3 MPa**
	Van Genuchten's parameter n	**1.60**	**1.49**
	Min. gas relative permea. $k_{r,min}$	$\mathbf{10^{-9}}$	$\mathbf{10^{-11}}$

EDZ "Packer"	Gas relative permeability law	**Cubic**	**Mualem (m=1.6)**
	Anisotropic intrinsic permeability k	$4\ 10^{-20}$ / $4/3\ 10^{-20}$ m²	$4\ 10^{-20}$ / $4/3\ 10^{-20}$ m²
	Gas permeability mult. coeff. A	**250**	**100**
	Van Genuchten's parameter P_r	15 MPa	15 MPa
	Van Genuchten's parameter n	1.49	1.49
	Min. gas relative permea. $k_{r,min}$	$\mathbf{10^{-9}}$	$\mathbf{10^{-11}}$

Table 7: 3D simulations main parameters.

Figure 110 to ***Figure 114*** compare, first for the PGZ1_70 simulation, the numerical results, obtained for PGZ1201 and PGZ1202 borehole intervals, with the experimental data and the experimental data corrected by removing the pressure decreasing tend (due to PGZ1031 borehole drainage and noted "Exp decreasing corr." on following figures).

We note that the 4 first peaks are correctly represented and the agreement with experimental data for the two last peaks is quite satisfactory (***Figure 110***). For the intervals 1 and 3 of the PGZ1201 borehole (***Figure 111***), and for the three intervals of the PGZ1202 borehole (***Figure 112*** to ***Figure 114***), the experimental trends are also well reproduced (the vertical scale of pressure is obviously different from that of ***Figure 110***).

Finally, ***Figure 115*** to ***Figure 120*** present the numerical results, and the comparison with (corrected) experimental data, for the PGZ1_74 simulation (with gas extraction phase) whose parameters fully correspond to the best fitting 1D calibration. We note that these results are almost as good as those obtained with the PGZ1_70 simulation, with this time a set of parameters more consistent between argillite and EDZ (same gas relative permeability law, same gas permeability multiplier coefficient *A*, same Van Genuchten's coefficient *n*).

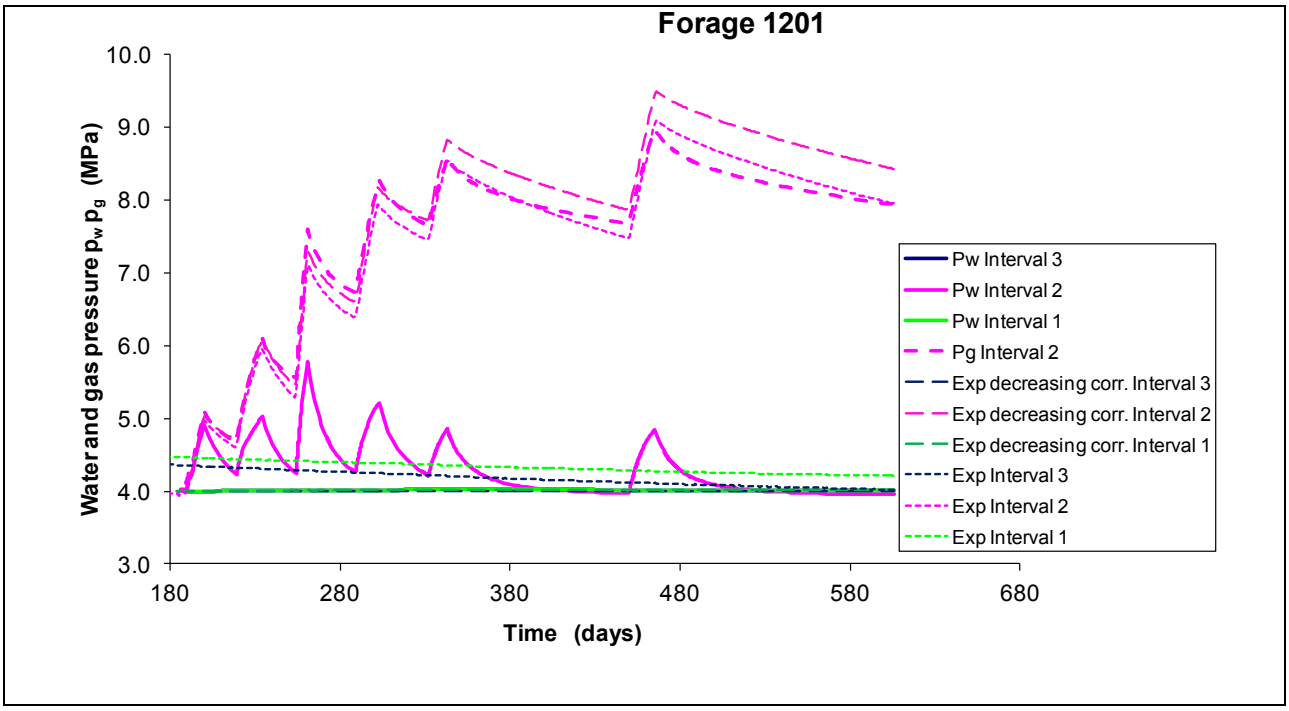

Figure 110 : Numerical results of 3D simulation PGZ1_70, for PGZ1201 borehole intervals, and comparison with experimental data.

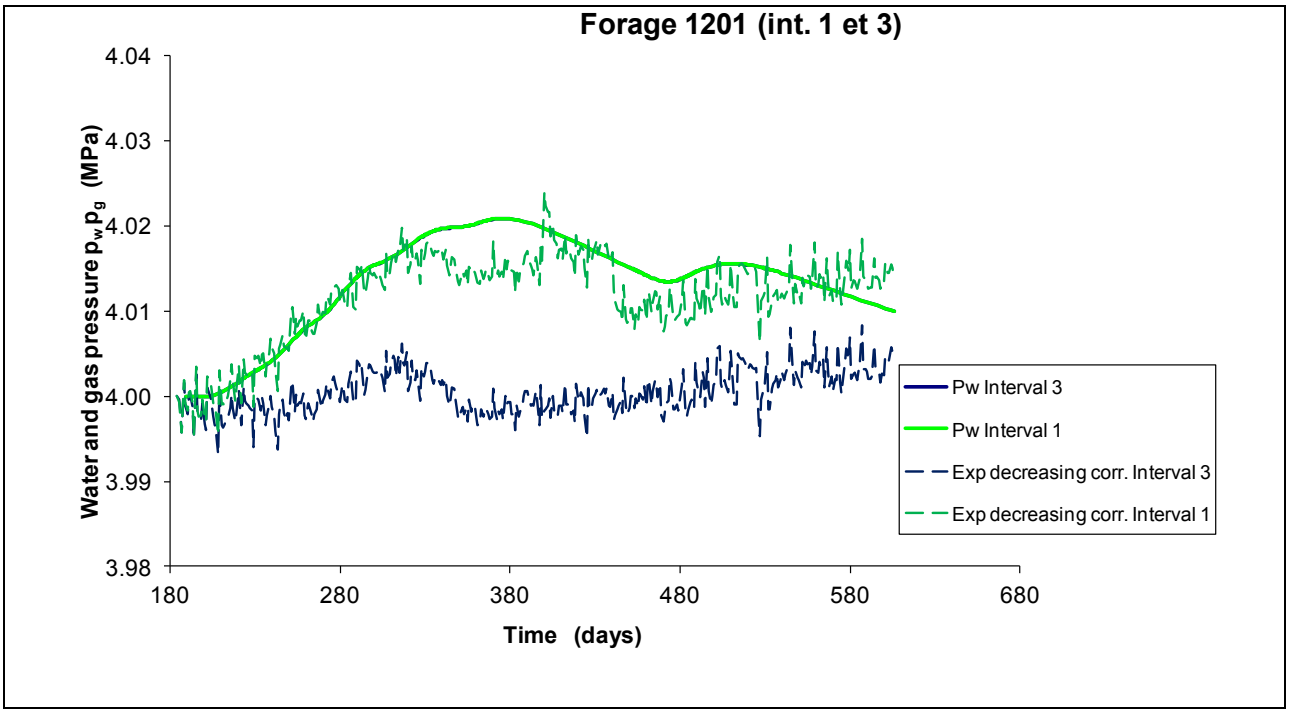

Figure 111 : Numerical results of 3D simulation PGZ1_70, for PGZ1201 borehole 1 and 3 intervals, and comparison with experimental data.

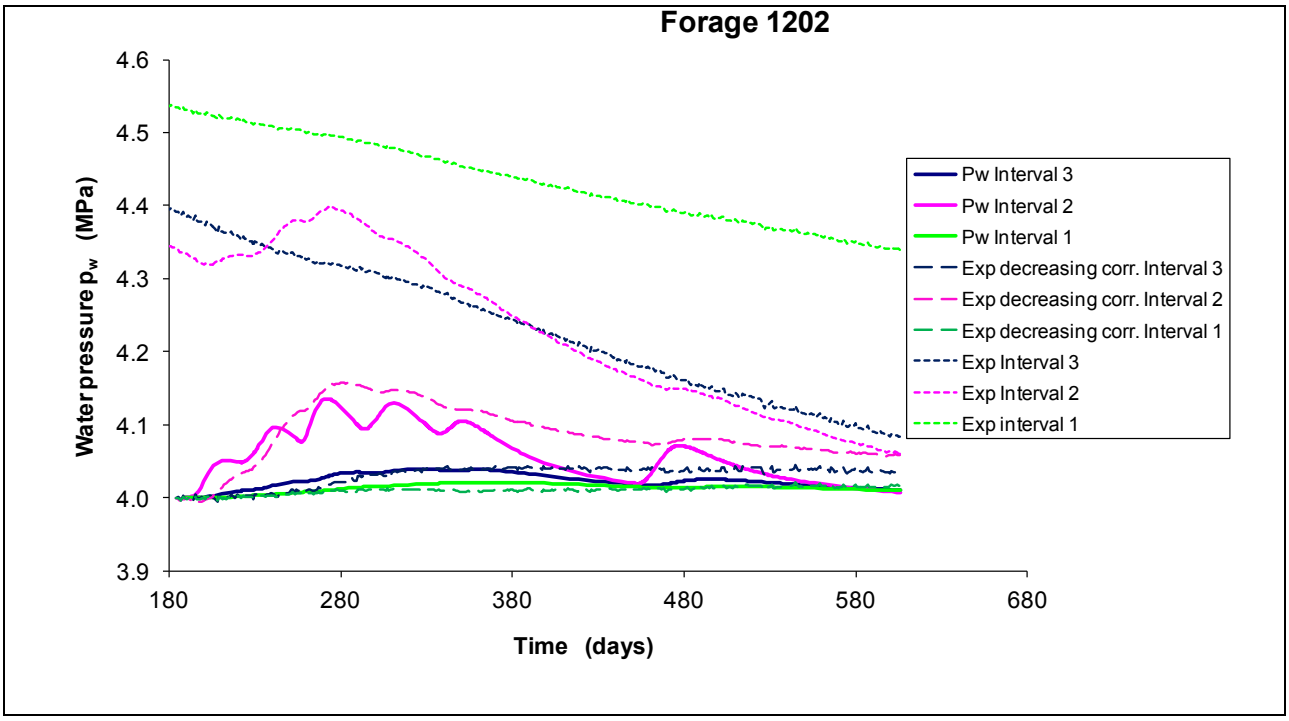

Figure 112 : Numerical results of 3D simulation PGZ1_70, for PGZ1202 borehole intervals, and comparison with experimental data.

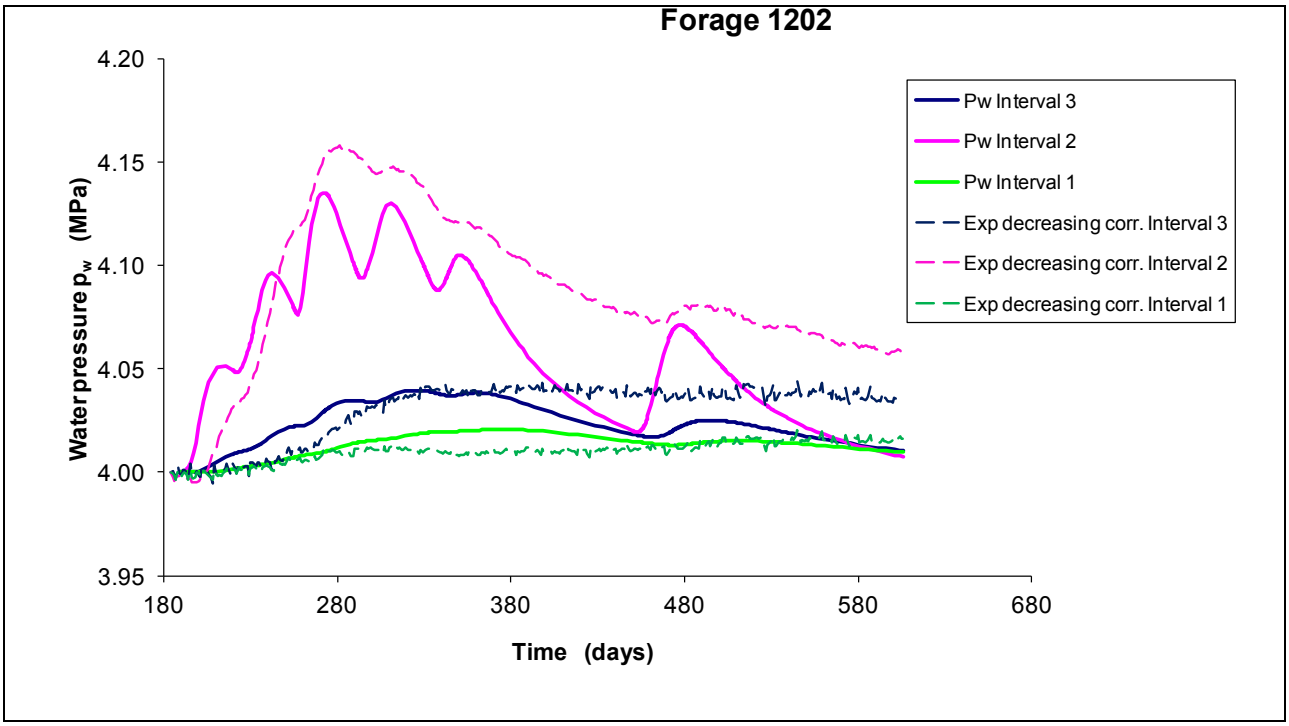

Figure 113 : Numerical results of 3D simulation PGZ1_70, for PGZ1202 borehole intervals, and comparison with experimental data.

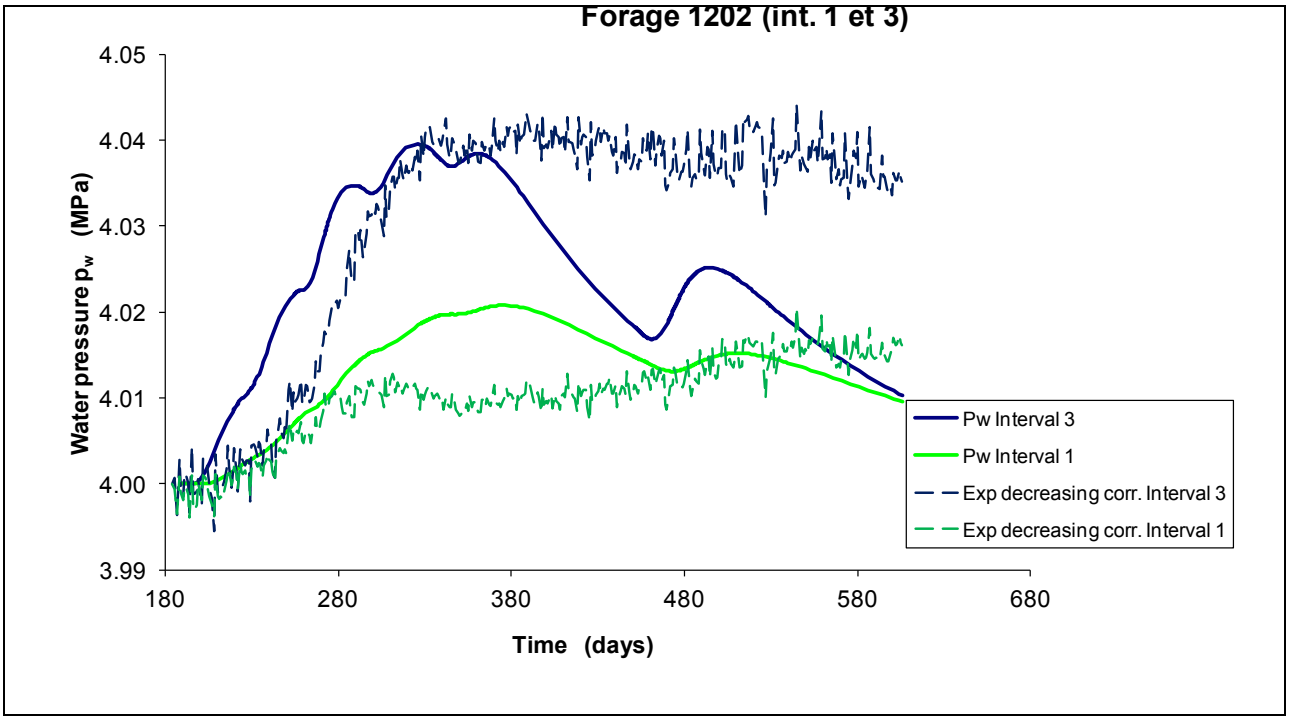

Figure 114 : Numerical results of 3D simulation PGZ1_70, for PGZ1202 borehole 1 and 3 intervals, and comparison with experimental data.

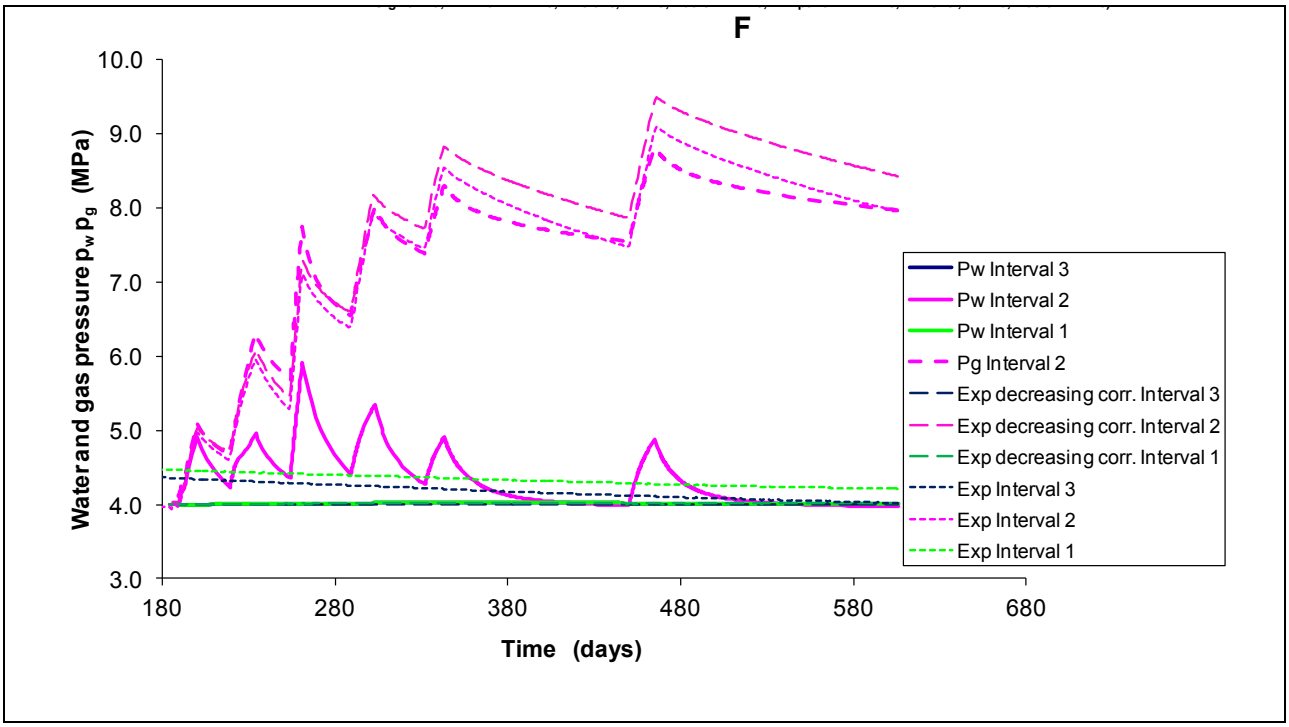

Figure 115 : Numerical results of 3D simulation PGZ1_74, for PGZ1201 borehole intervals, and comparison with experimental data.

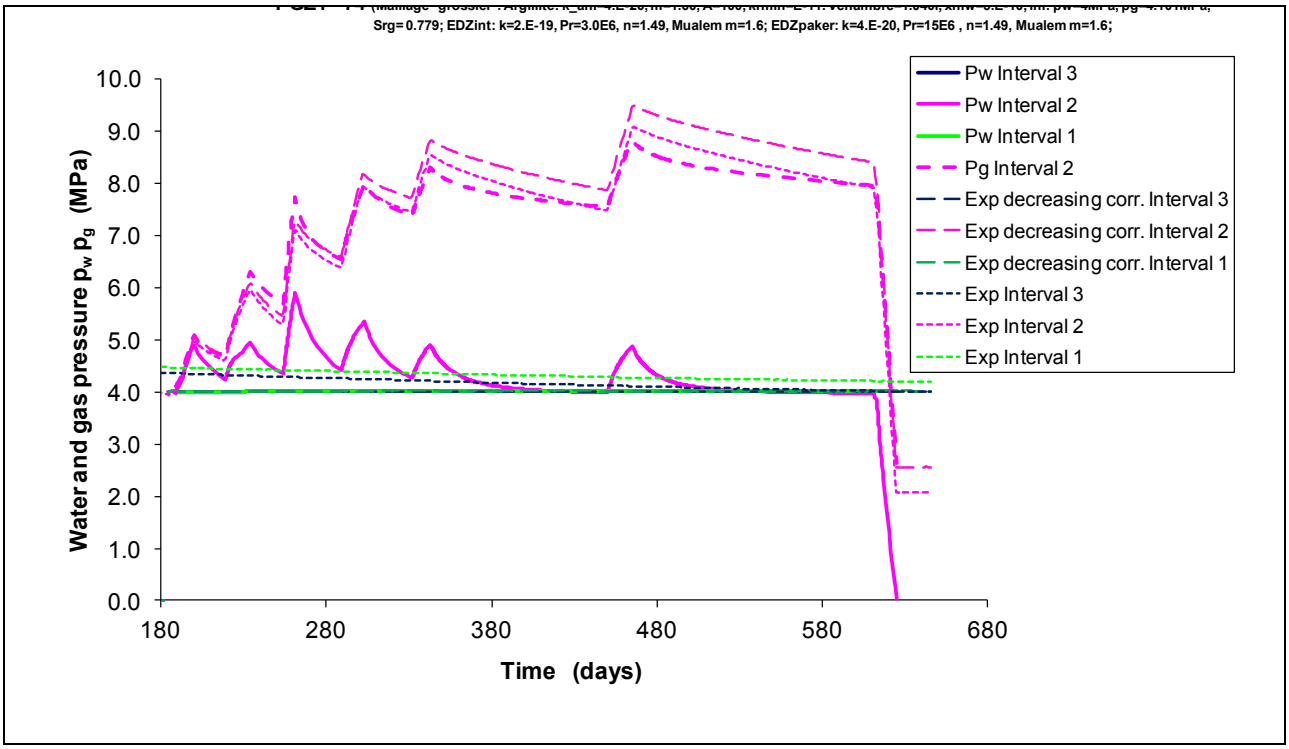

Figure 116 : Numerical results of 3D simulation PGZ1_74 (with gas extraction phase), for PGZ1201 borehole intervals, and comparison with experimental data.

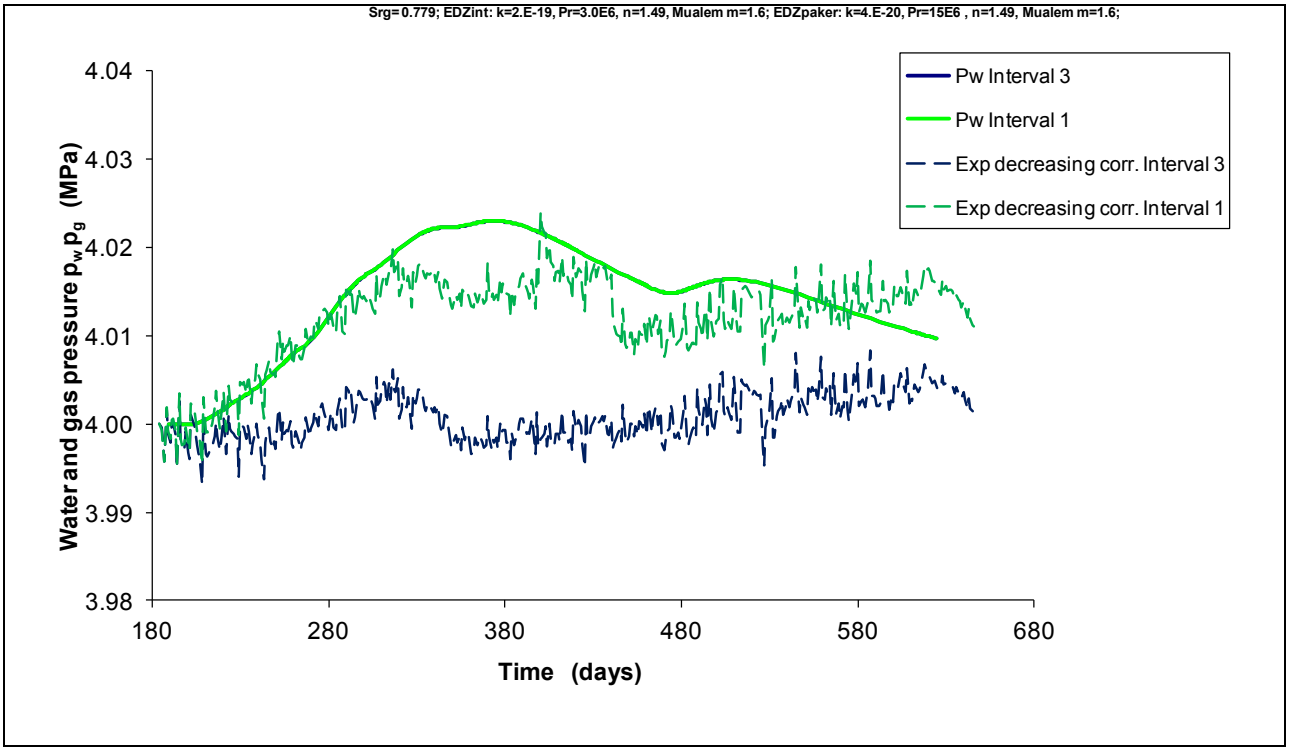

Figure 117 : Numerical results of 3D simulation PGZ1_74 (with gas extraction phase), for PGZ1201 borehole 1 and 3 intervals, and comparison with experimental data.

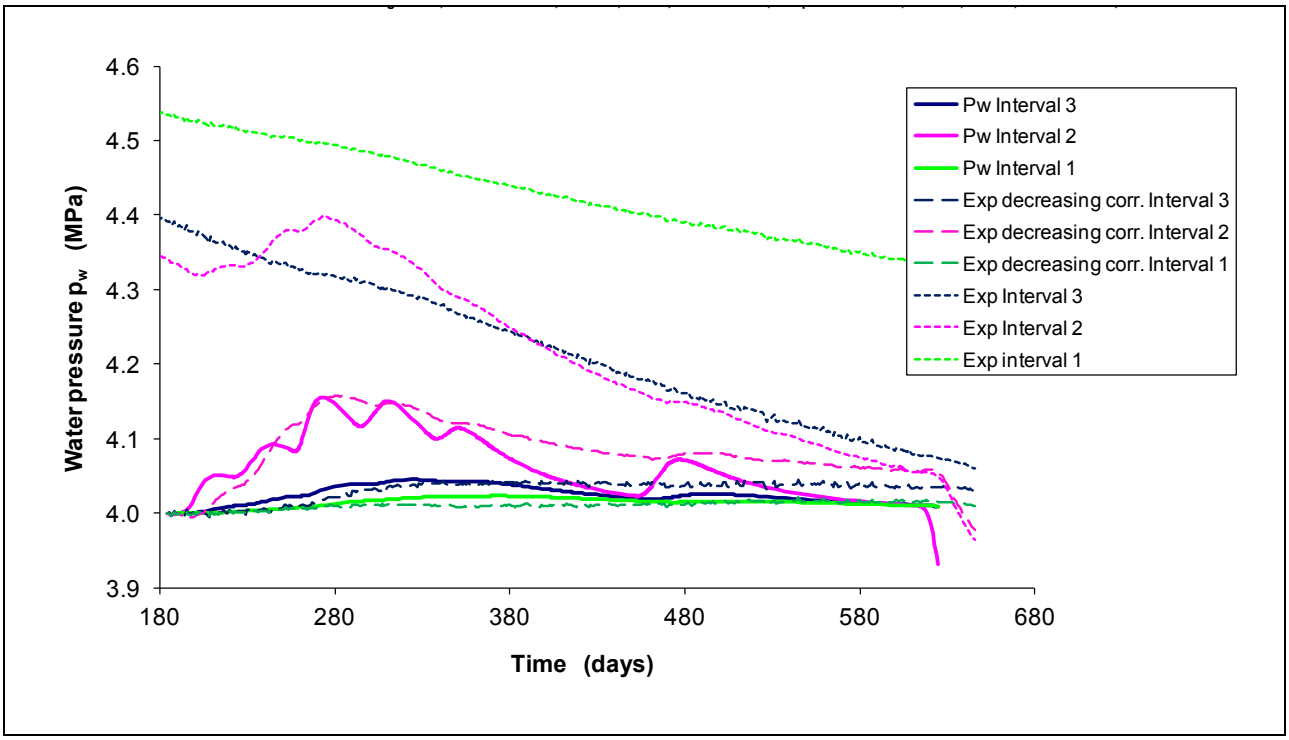

Figure 118 : Numerical results of 3D simulation PGZ1_74 (with gas extraction phase), for PGZ1202 borehole intervals, and comparison with experimental data.

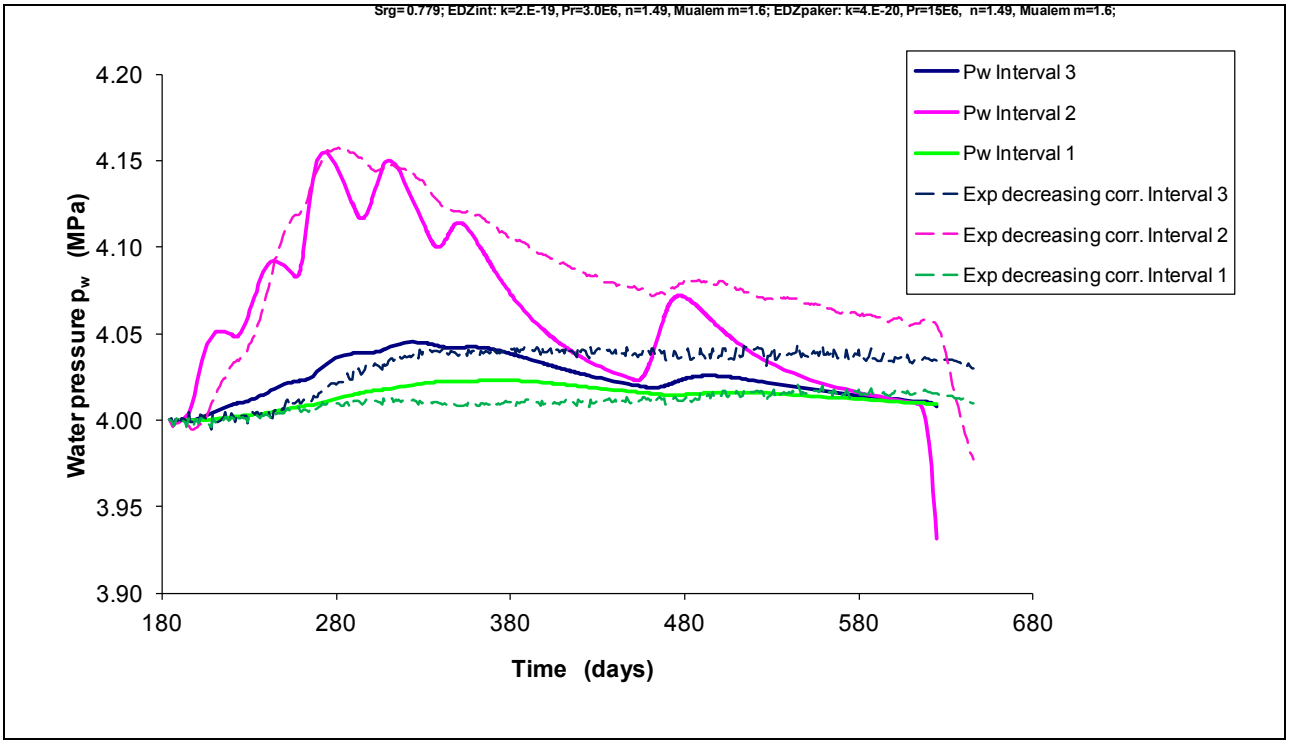

Figure 119 : Numerical results of 3D simulation PGZ1_74 (with gas extraction phase), for PGZ1202 borehole intervals, and comparison with experimental data.

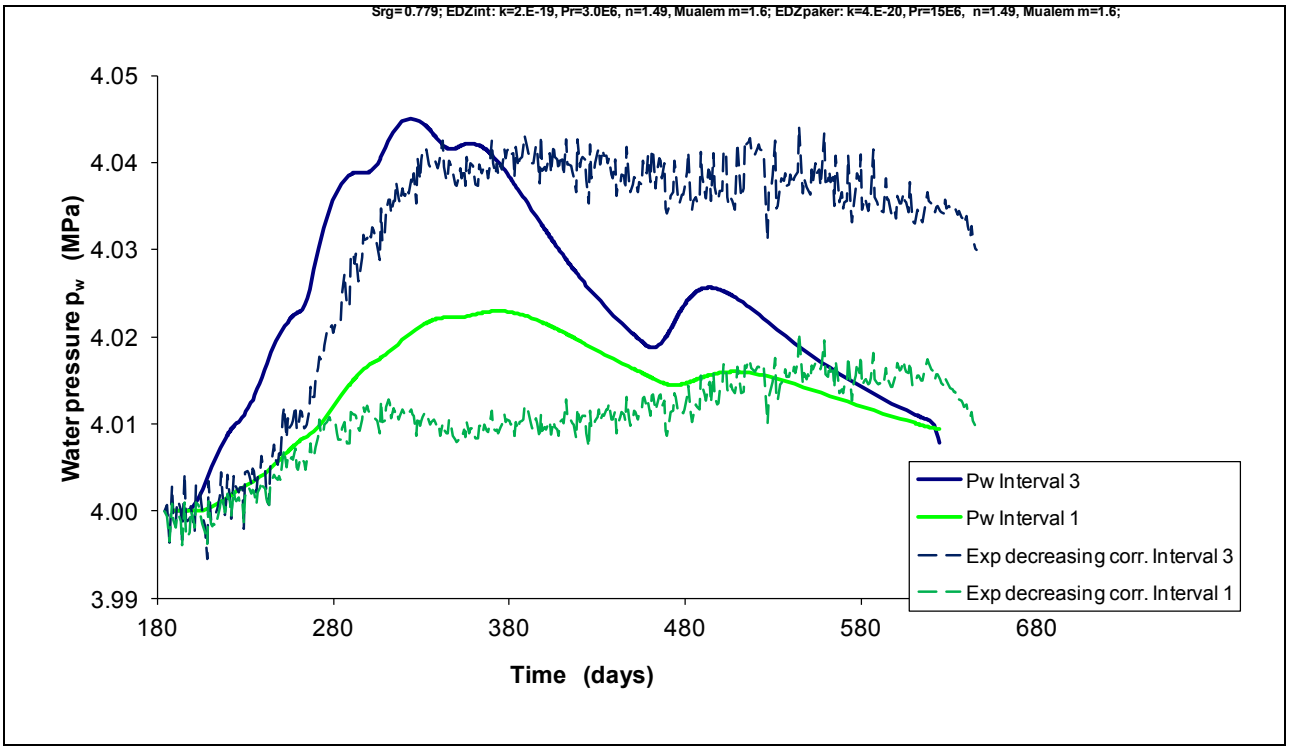

Figure 120 : Numerical results of 3D simulation PGZ1_74 (with gas extraction phase), for PGZ1202 borehole 1 and 3 intervals, and comparison with experimental data.

13 CONCLUSIONS AND DISCUSSION

A fully coupled 3D model was used for the modelling of the PGZ1 in-situ experiment. We globally noted that the gas transport was mainly dissolved gas diffusion.

The influence of a drainage effect of the PGZ1031 borehole and of a possible leakage in the injection chamber was investigated. Probably due to an imperfect implantation of that drainage effect in an insufficient mesh, the experimental curves of the PGZ1021 borehole intervals are not correctly numerically reproduce.

Nevertheless, by means of a new revolution 3D mesh around the PGZ1031 borehole axis, that drainage effect was clearly validated: the experimental curves of the intervals 1, 2 and 3 are now relatively correctly reproduced with this new model.

The influence of a possible leakage in the injection chamber was also investigated.

Choosing a good set of argillite permeability (4.10^{-20} m² horizontally and 1.33 10^{-20} m² vertically) and a value of the injection chamber compressibility of 3 10^{-8} Pa^{-1}, it was quite possible to reproduce the experimental evolution of the pore pressure in the PGZ1201 borehole until the end of the 3rd gas injection peak. After, the gap between experimental measurements and numerical results becomes very important. Nevertheless it was possible to better reproduce the end of the injection experiment, brutally modifying from the end of the 3rd gas injection peak the argillite permeabilities in the whole mesh (10 times lower values than permeabilities used for the

beginning of the gas injection phase). We obtained so a good agreement between experimental and numerical results.

It seemed also possible to improve the prediction for the PGZ1201 borehole, taking into account a "leakage" due to the influence of unresined volume and low values of argillite permeability (4.10^{-21} m² horizontally and 1.33 10^{-21} m² vertically). However, the corresponding numerical response for the PGZ1202 was clearly worse than before.

Consideration of an EDZ, taken different in front of packers and in front of intervals, was also envisaged in the 3D mesh but it does not improve the comparison with experimental data: all other parameters remaining constant, the numerical response with EDZ is even worse than without EDZ.

Then, to better understand the influence of initial conditions present in the injection chamber and the hydraulic parameters characterizing the EDZ, several one-dimensional axisymmetric simulations were performed. The purpose of these simulations was, with a very simple grid, to try to best reproduce the experimental measurements for PGZ1201 borehole and especially the measurements after the third injection peak gas. Starting from the 3D case giving, without changing parameters during the calculation, the best agreement with experimental measurements, about fifty 1D simulations were able to progressively and significantly improve the response, mainly for the last 3 peaks.

Finally, a 3D model, with a set of parameters consistent between argillite and EDZ (same gas relative permeability law, same gas permeability multiplier coefficient *A*, same Van Genuchten's coefficient *n*) was proposed, which reproduce very well, for the 6 gas injection peaks and the gas extraction, the experimental results obtained in the 2*3 intervals of the PGZ1201 and PGZ1202 boreholes.

More generally, the analysis of the numerical results has shown the importance to know and to take into account accurately each component of the experiment system, as the volume and the initial conditions in the injection interval, the presence of a disturbed zone around the boreholes and the rock mass characteristics. In particular, the way that water is removed from the injection interval or pushed in the rock mass influences strongly the analysis of the experimental observations. The numerical results are strongly dependent on the definition of the gas relative permeability in the quasi saturated domain.

The following conclusions can be deduced from the experimental observations and from the different numerical modelling. The gas transfers are strongly dependent on the gas permeability in the quasi-saturated domain, where few experimental data are unfortunately available nowadays. The presence of an excavated damaged zone around the boreholes makes easier the gas entry in the rock mass and has to be considered in order to explain the experimental observations. In this disturbed domain, it is first the decrease of the gas entry pressure induced by the micro-fracturing rather than the increase of permeability that plays a major role on the gas transfers. The modelling has also confirmed previous experimental results illustrating that gas permeability in dried conditions is higher than water permeability in saturated conditions. Finally, such results show that a predictive model as two-phase flow approach is able to reproduce experimental observations in large scale system, as far as the injection flow rate and the gas

pressures remain moderate. Taking into account the development of gas preferential pathways is certainly a crucial issue in the description of laboratory experiment, but seems to be neglected for such field test.

More generally, the PGZ1 experiment has shown that gas would remain mainly confined in the borehole disturbed zone. Even though gas penetrates in the sound claystone, the quantities remain low and located near the injection interval with such gas injection conditions.